TECHNICAL REPORT STANDARD PAGE

1. Title and Subtitle
Incorporating the Site Variability and Laboratory/ In-situ Testing Variability of Soil Properties in Geotechnical Engineering Design

2. Author(s)
Murad Abu-Farsakh, Md. Habibur Rahman, and Abu Hakim Faisal

3. Performing Organization Name and Address
Louisiana Transportation Research Center
4101 Gourrier Avenue
Baton Rouge, LA 70808

4. Sponsoring Agency Name and Address
Louisiana Department of Transportation and Development
P.O. Box 94245
Baton Rouge, LA 70804-9245

5. Report No.
FHWA/LA. 22/673

6. Report Date
August 2023

7. Performing Organization Code
LTRC Project Number: 16-6GT
SIO Number: DOTLT1000112

8. Type of Report and Period Covered
Final Report
July 2017 – March 2022

9. No. of Pages
328

10. Supplementary Notes
Conducted in Cooperation with the U.S. Department of Transportation, Federal Highway Administration

11. Distribution Statement
Unrestricted. This document is available through the National Technical Information Service, Springfield, VA 21161.

12. Key Words
Resilient modulus, permanent deformation, cyclic plate load test, weak subgrade, wet subgrade, class C Fly ash, Hydrated Lime, Portland Cement Type I

13. Abstract
The properties of geomaterials usually vary from one location to another within the same site, in both the vertical and horizontal directions. The variability of soil properties is a complex phenomenon that results from several sources of uncertainties, including inherited spatial variability, measurement error, statistical error, and model bias error. This study aimed at investigating the different methods and techniques used to evaluate the spatial variability of soil properties; the different sources of geotechnical variability; quantifying the variability of soil properties for inclusion in analysis; and design of different geotechnical engineering applications. This included conducting in-box tests and field tests on constructed sections at the Accelerated Load Facility (ALF) site and under-construction sections from different projects using different devices, such as Dynamic Cone Penetrometer (DCP), Light Falling Weight Deflectometer (LFWD), and Geogauge. Typical laboratory tests, such as

Atterberg limits, unconsolidated undrained (UU) triaxial, small direct shear, consolidation, and California bearing ratio (CBR) tests, were also conducted to evaluate the specimen and operator-related variability of different soil properties. In addition, the specific site variability was also evaluated using the results from soil borings with laboratory tests and/or the results of in-situ tests such as cone penetration test (CPT) and standard penetration tests (SPT).

The spatial variability of soil properties can be expressed in terms of mean, coefficient of variation, scale of fluctuation, and correlation length. Several statistical techniques such as X-Bar/R, ANOVA, second moment (SM) analysis, semivariogram, Bayesian, probabilistic analysis can be used to characterize and evaluate the soil variability. The results from laboratory, in-box, and field testing programs were analyzed using the Gauge R&R, ANOVA, and SM analysis; and the variability of soil properties were expressed in terms of standard deviations and coefficient of variations (COV).

The results of laboratory, in-box, and field tests showed that the COVs from SM analysis are smaller than the COVs from ANOVA method. The operator-related variations showed lower values of COVs than those generated from location/specimen-related variability. Additionally, analyses of variability from in-box tests indicated lower COVs than the field tests. The COVs for the under-construction sections were higher than the COVs for the constructed sections at ALF site. In the case of laboratory tests, the specimen-related variability had higher COVs than the operator-related variability.

The semivariogram approach was used to evaluate the site variability of six sites from CPT tests and four sites from soil boring data. The vertical and horizontal correlation ranges were determined for each site and used to evaluate the reduction factor and the spatial COV for evaluating the resistance factors for the load and resistance factor design (LRFD) of pile foundations.

A two-level Bayesian analyses were used to update the mean bias and standard deviation of the measured/predicted pile capacity variables estimated using the Laboratoire Central des Ponts et Chausees (LCPC) Pile-CPT method for three sites. In Level 1, the state variables were updated from the national data; while in Level 2, the site variables were updated from state data. The updated mean bias and standard deviation for each specific site were used to calibrate the resistance factors for LRFD design of pile foundations.

The probabilistic method was used to analyze the CPT data obtained from LA 1 site with 13 CPT tests using the Stanford Geostatistical Modeling Software (SGeMS) software, which provides confidence intervals (0 to 100%) of the estimated data between the tested points. The probability that the estimated CPT data fall between ± standard deviation were calculated and further used to update the spatial variability and the LRFD resistance factor of LCPC Pile-CPT method.

The effect of variability in soil properties in the slope stability analysis was investigated using the Slide 2018 2D software. Different scenarios were modeled for drained and undrained conditions. The

results showed that the factor of safety decreases with increasing the COV of cohesion and friction angle and with increasing the vertical and horizontal correlation lengths.

The effect of site variability on shallow and deep foundations was investigated for single and multiple soil borings with different distances from the foundation using Fenton and Griffiths and Naghibi and Fenton approaches. The results showed that the ultimate bearing capacity and the resistance factor decreases with increasing the COV of soil properties and the distance between the foundation and soil boring.

Project Review Committee

Each research project will have an advisory committee appointed by the LTRC Director. The Project Review Committee is responsible for assisting the LTRC Administrator or Manager in the development of acceptable research problem statements, requests for proposals, review of research proposals, oversight of approved research projects, and implementation of findings.

LTRC appreciates the dedication of the following Project Review Committee Members in guiding this research study to fruition.

LTRC Administrator/Manager

Zhongjie "Doc" Zhang, Ph.D., P.E.
Pavement and Geotechnical Research Manager

Members

Francisco Gudiel, Mark Sehon, Chris Nickel,
Jesse Rauser, Kristy Smith, Marta Vasquez, Clay Gottschalck, Arturo Aguirre, Johnny Sanford, and Brandon Johnson

Directorate Implementation Sponsor

Christopher P. Knotts, P.E.
DOTD Chief Engineer

Incorporating the Site Variability and Laboratory/In-situ Testing Variability of Soil Properties in Geotechnical Engineering Design

By
Murad Y. Abu-Farsakh
Md. Habibur Rahman
Abu Hakim Faisal

Louisiana Transportation Research Center
4101 Gourrier Avenue
Baton Rouge, LA 70808

LTRC Project No. 16-6GT
SIO No. DOTLT1000112

conducted for
Louisiana Department of Transportation and Development
Louisiana Transportation Research Center

August 2023

Abstract

The properties of geomaterials usually vary from one location to another within the same site—in both the vertical and horizontal directions. The variability of soil properties is a complex phenomenon that results from several sources of uncertainties, including inherited spatial variability, measurement error, statistical error, and model bias error. This study aimed at investigating the different methods and techniques used to evaluate the spatial variability of soil properties; the different sources of geotechnical variability; quantifying the variability of soil properties for inclusion in analysis; and design of different geotechnical engineering applications. This included conducting in-box tests and field tests on constructed sections at the Accelerated Load Facility (ALF) site and under-construction sections from different projects using different devices, such as Dynamic Cone Penetrometer (DCP), Light Falling Weight Deflectometer (LFWD), and Geogauge. Typical laboratory tests, such as Atterberg limits, unconsolidated undrained (UU) triaxial, small direct shear, consolidation, and California bearing ratio (CBR) tests, were also conducted to evaluate the specimen and operator-related variability of different soil properties. In addition, the specific site variability was also evaluated using the results from soil borings with laboratory tests and/or the results of in-situ tests such as cone penetration test (CPT) and standard penetration tests (SPT).

The spatial variability of soil properties can be expressed in terms of mean, coefficient of variation, scale of fluctuation, and correlation length. Several statistical techniques such as X-Bar/R, ANOVA, second moment (SM) analysis, semivariogram, Bayesian, probabilistic analysis can be used to characterize and evaluate the soil variability. The results from laboratory, in-box, and field testing programs were analyzed using the Gauge R&R, ANOVA, and SM analysis; and the variability of soil properties were expressed in terms of standard deviations and coefficient of variations (COV).

The results of laboratory, in-box, and field tests showed that the COVs from SM analysis are smaller than the COVs from ANOVA method. The operator-related variations showed lower values of COVs than those generated from location/specimen-related variability. Additionally, analyses of variability from in-box tests indicated lower COVs than the field tests. The COVs for the under-construction sections were higher than the COVs for the constructed sections at ALF site. In the case of laboratory tests, the specimen-related variability had higher COVs than the operator-related variability.

The semivariogram approach was used to evaluate the site variability of six sites from CPT tests and four sites from soil boring data. The vertical and horizontal correlation ranges were determined for each site and used to evaluate the reduction factor and the spatial COV for evaluating the resistance factors for the load and resistance factor design (LRFD) of pile foundations.

A two-level Bayesian analyses were used to update the mean bias and standard deviation of the measured/predicted pile capacity variables estimated using the Laboratoire Central des Ponts et Chausees (LCPC) Pile CPT method for three sites. In Level 1, the state variables were updated from the national data; while in Level 2, the site variables were updated from state data. The updated mean bias and standard deviation for each specific site were used to calibrate the resistance factors for LRFD design of pile foundations.

The probabilistic method was used to analyze the CPT data obtained from LA 1 site with 13 CPT tests using the Stanford Geostatistical Modeling Software (SGeMS) software, which provides confidence intervals (0 to 100%) of the estimated data between the tested points. The probability that the estimated CPT data fall between the standard deviation were calculated and further used to update the spatial variability and the LRFD resistance factor of LCPC Pile-CPT method.

The effect of variability in soil properties in the slope stability analysis was investigated using the Slide 2018 2D software. Different scenarios were modeled for drained and undrained conditions. The results showed that the factor of safety decreases with increasing the COV of cohesion and friction angle and with increasing the vertical and horizontal correlation lengths.

The effect of site variability on shallow and deep foundations was investigated for single and multiple soil borings with different distances from the foundation using Fenton and Griffiths and Naghibi and Fenton approaches. The results showed that the ultimate bearing capacity and the resistance factor decreases with increasing the COV of soil properties and the distance between the foundation and soil boring.

Acknowledgments

This research project was funded by the Louisiana Department of Transportation and Development (DOTD) (SIO No. DOTLT1000112) and the Louisiana Transportation Research Center (LTRC Project No. 16-6GT). The help and support of Zhongjie Zhang, Ph.D., at LTRC is gratefully acknowledged.

Implementation Statement

This study aimed at evaluating the different sources of geotechnical variability that include laboratory and field testing, variability of testing devices, and quantifying the spatial variability of soil properties for incorporation into analysis and design of different geotechnical engineering applications. The findings of this study can be implemented into the design and analysis of deep foundations, shallow foundations, slope stability, and any other geotechnical application as summarized below:

1. The variability of different soil properties evaluated in terms of coefficient of variation (COV) from the laboratory and the AASHTO Materials Reference Laboratory (AMRL) test results can be implemented in reliability analysis and design for different geotechnical engineering applications.

2. The variability and spatial distribution of in-situ testing measurements of field sections, in terms of COV using the different devices, such as DCP, LFWD, Geogauge, Nuclear Density Gauge (NDG), and E-Gauge, can be implemented in forensic analysis and design of pavements, embankments, slopes, etc.

3. The semivariorgam analysis can be used to evaluate the spatial variability from multiple CPT tests and/or multiple soil borings to determine the vertical and horizontal correlation ranges of the site variability, which will be used to evaluate the spatial COV for the specific site for use in many geotechnical engineering applications. This includes specific site calibration of resistance factor for LRFD design of shallow and deep foundations, settlement calculation, and slope stability analysis.

4. The Bayesian analysis technique can be incorporated to update the mean bias and standard deviation, and hence the COV of the measured/predicted pile capacity variables as more pile load test data are available. This technique can be applied to update state variables (level 1) or specific site variables (level 2) for use to calibrate the resistance factors for LRFD design of pile foundations.

5. The application of the probabilistic analysis approach using the SGeMS software can provide us with the confidence level of estimated data between the tested points from kriging analysis, and hence the probability that the estimated data fall between ± standard deviation. The results of probabilistic analysis can be used to

update the spatial variability of the specific site for calibrating the LRFD resistance factor for different geotechnical engineering applications, such as LRFD design of pile foundation.

6. The variations of soil properties can be implemented to evaluating the slope stability analysis of slopes, embankments, and mechanically stabilized earth (MSE) walls.

7. The method proposed by Fenton and Griffiths can be implemented to incorporate the variability in soil properties and distance from soil boring(s) for analysis and design of shallow foundations.

8. The method proposed by Naghibi and Fenton can be implemented to incorporate the variability in soil properties and distance from soil boring(s) for analysis and design of deep foundations.

Table of Contents

List of Tables

List of Figures

Introduction

The subsurface soil conditions of all natural deposits are usually subjected to significant degree of variability in terms of soil type, layering, and their properties, which are rarely homogeneous. Unlike structural engineers who deal with mostly homogeneous man-made materials, such as concrete and steel, geotechnical engineers have to cope with highly variable natural materials (soils and rocks). As a result, high variance is expected in the resistance of geotechnical structures (e.g., foundations, slopes, earth-retaining structures) due to the vertical and horizontal spatial variations of soil properties for the site. Generally, the soil borings and in-situ tests are carried out at fixed-spaced locations (e.g., every 100 feet), and the laboratory tests are conducted on samples retrieved from discrete depths, which can result in special variations of soil properties for the specific site. Due to variability problem, the accuracy and reliability of the measured data to be used in the design geotechnical structure are somehow unknown. Therefore, geotechnical engineering often deals with different kinds of uncertainties that can result in either under-design, which can cause failure, or overdesign, which increases the construction cost if these uncertainties are not considered properly in the design.

Site investigation and characterization of subsurface soil conditions are very crucial for geotechnical engineering design and analysis. The scope of site exploration and investigation is mainly controlled by how much the customer and project authorities are willing to spend, rather than by what is needed to explain the subsurface soil condition. To design foundations and other geotechnical structures, specialists are preferably looking for exclusive soil properties at numerous locations. However, reaching this goal can be unlikely and expensive, since it may consume huge amounts of finance, labor, and material as well as time. Fortunately, some soil properties are spatially correlated with each other and thus can be related to many environmental issues (e.g., [1], [2], [3]).

The soil properties inherently vary spatially from point to point within the same site (both horizontally and vertically) due to several factors including depositional environment, degree of weathering, and physical processes (e.g., [4], [5]). The inherent spatial variability of soil renders inescapable uncertainty in geotechnical design [4]. Soil variability is a complex phenomenon that arises from many different sources of uncertainties. The four primary sources of geotechnical uncertainty are inherited spatial variability (horizontally and vertically) of the soil deposit during deposition, random measurement error, statistical uncertainty, and model bias uncertainty. The first source of

uncertainties results from the natural geologic processes that continuously modify the in-situ characteristics of the soil properties, which vary from location to location. Different factors such as the random mixture of various soil types and composition, variation in water content, variation in density, and variation of stress level over time contribute to the in-site variation in the soil properties. The inherent soil variability is described as a random field that can be described precisely by the mean (m), coefficient of variation (COV), and scale of fluctuation. Measurement error is caused by equipment and/or operator induced variation, which can take place from one test to another. Equipment error arises from variations when tests are set up and loads are delivered. Operator induced variation occurs when personal judgement is required to read scales and take measurement, or during sample preparation and handling. Statistical uncertainty is associated with choosing the best equation/correlation required to interpret collected data from a range of equations. Statistical uncertainty is expected to be significant because the volume of soil sampled can be a large fraction of the volume of interest. The bias model uncertainties are due to variations between the model's predictions from the measured values, which arise from transformation when the important property was not measured directly but rather projected using a credible transformation/interpretation model or other sufficiently reasonable (or measured) information (e.g., [6], [7], [8]). These sorts of uncertainties can be lumped together and termed as total site variability (e.g., [7], [8]).

Several techniques have been proposed to evaluate the site variability. These techniques involved Geographic Information Systems (GIS), geostatistical studies, multivariate statistical analysis, and other methods. The GIS was initially developed as a tool for data retrieval and displaying geographic information, and later enhanced for spatial analysis [9]. GIS with various spatial interpolation methods, including inverse distance and kriging, was used in several regional scales for soil quality survey studies (e.g., [10], [11]). The traditional interpolation techniques including inverse distance and kriging are inadequate for the uncertainty assessment with the soil variables. Kriging algorithm is apt to smooth out a local spatial variation of the variable. Goovaerts et al. [12] indicated that small values are typically overestimated and large values are underestimated, with the local error variance being the minimum and the variance of kriging estimates being six times smaller than the sample variance. However, the Sequential Gaussian Simulation (SGS) can be used to generate variable maps and reproduce actual statistics, histograms, and variograms of the spatial variability for the data without smoothing effect.

Defining the spatial variability from the measured data requires engineers to determine the correlation between data pairs that are separated by different distances (vertically and

horizontally) using different parameters. One of the main fundamental parameters used is the covariance $Cov(q_i,q_j)$ between data values q_i and q_j separated by a distance (h). The other parameter that is used to measure site variability in terms of the extent of spatial dependency between samples is known as the semi-variogram, $\gamma(h)$, which can be defined as the distance range (a) that defines the end of correlation between the data pairs. Researchers are also looking for new techniques to evaluate site variability parameters using advanced statistical methods, such as the Bayesian analysis, probability analysis, or distribution by adopting the sequential Gaussian simulation using the Stanford Geostatistical Modeling Software (SGeMS).

Several researchers in literature studied the effect of site variability for different geoterchnical engineering applications. Onyejekwe et al. [13] performed geostatistical spatial analysis to evaluate the undrained shear strength profile at any specific location within the site. Lacasse and Nadim [4] showed that the geotechnical parameters had variability in both vertical and horizontal directions with a greater inclination for the geotechnical properties. McVay et al. [14] conducted a study to evaluate the resistance factors (ϕ_R) for the Load and Resistance Factor Design (LRFD) of piles that incorporates the spatial variability of local rock and soil strength. Otero [15] performed a study to improve the LRFD resistance factors (ϕ_R) for non-redundant shaft design incorporating the new design methods for larger single shaft design. Faraone [16] presented a methodology that incorporates the framework of reliability-based design, while accounting for the site-specific spatial variability, which is applicable to several deep foundation design practices. Fenton and Griffiths [17] investigated the effect of variation in soil parameters on the bearing capacity of shallow foundations. Naghibi and Fenton [18] investigated the effect of site soil variability with varied distance from soil boring to calculate resistance factor for deep foundation. Several studies are also available in literature on the effect of spatial variability on the slope stability analysis (e.g., [19], [20], [21]).

This study aimed at evaluating the operator-induced and equipment-induced variations, evaluating the different sources of geotechnical variability from both soil boring/laboratory and in-situ testing; and quantifying the special variability of soil properties for incorporation into analysis and design of different geotechnical engineering applications such as LRFD design of pile foundations, bearing capacity shallow foundations, and slope stability analysis.

Literature Review

General

The subsurface soil deposits are usually heterogeneity in nature, which contribute to the spatial variation in soil types, soil layering, and soil properties. Therefore, the soil properties of all natural soil deposits have certain degrees of variability and vary inherently from point to point within the same site, in both the vertical and horizontal directions, due to many reasons including the depositional environment, the degree of weathering, and the physical process [e.g., [4], [5]. Looking at the microscopic level, the soils are associated with different types of phases that can include minerals, gasses, ions, and other non-mixable fluids and micro organisms. Meanwhile, at the macroscale level, the soil heterogeneity leads to geological processes of soil varying, which imparts soil spatial formation such as physical, chemical and biological weathering, deposition, consolidation, cementation, desiccation, leaching, and diagenesis.

Researchers have long recognized the necessity of assessing variability and uncertainty in geotechnical engineering design, and reliability-based design (RBD) approaches have been developed internationally over the last 30 years. For example, Terzaghi et al. emphasized the importance of uncertainty and unpredictability in geotechnical engineering design and practice [22]. Several studies have been done by various researchers (e.g., [6], [8], [14], [23], [24]) to enhance the state of knowledge in geotechnical engineering by assessing variability and uncertainty, and applying reliability-based design methodologies.

The variability of subsurface soil condition and soil properties is a complex phenomenon that results from many different sources of uncertainties. The inherent soil variability is usually described as a random field with mean (m), coefficient of variation (COV), and scale of fluctuation of data. Before examining the historical progress of the study of spatial variability in the field of geotechnical engineering, it is necessary, by way of background, to treat the various mathematical techniques used in this area of research. This section will present the work available in literature on geotechnical engineering variability and uncertainty analysis.

Variability and Uncertainty in Geotechnical Engineering

In geotechnical engineering analyses, variability is a primary source of uncertainty. Many areas of geotechnical engineering, notably the characterization of soil properties, are fraught with uncertainty. There are two types of uncertainty in geotechnical properties: aleatory and epistemic uncertainty ([4], [25], [26]). Aleatory uncertainty is a consequence of the spatial variability of the soil characteristic and indicates the property's intrinsic randomness. Lack of information and flaws in measurement and/or calculation cause epistemic uncertainty. For example, systematic inaccuracy is caused by factors such as property measurement methods, modeling errors, and the amount of available data. Human error is the third source of uncertainty. However, because it is difficult to separate and its effects on probability are frequently included in compilations of statistics on aleatory uncertainty, it is not usually considered in uncertainty assessments [27]. Figure 1 presents the schematic of the sources of uncertainty in geotechnical soil properties.

Figure 1. Sources of uncertainty in geotechnical soil properties (Adapted from [25])

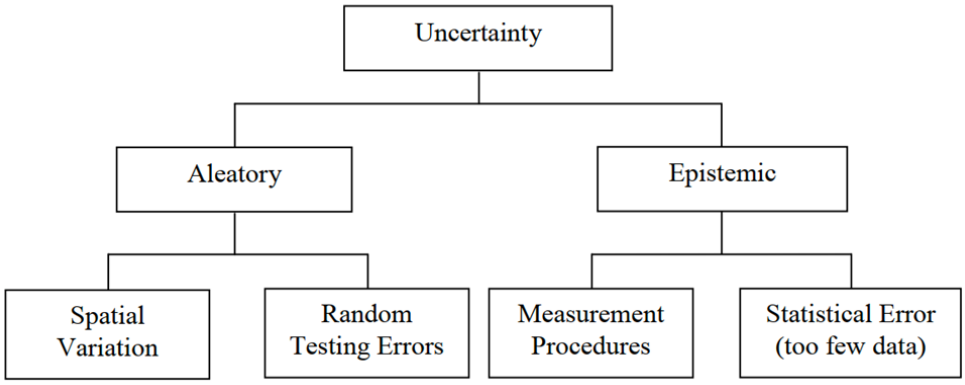

In the field of geotechnical engineering, traditional tools for dealing with soil heterogeneity have relied on a high factor of safety and local experience. This creates inconsistency in performance measurement, prompting widespread recognition of the need for more reliable techniques to incorporate soil heterogeneity into a more quantitative scheme suited to engineering design. Since the performance of geotechnical structures depends on local extremes of characteristics within a subsurface profile, it is critical to probabilistically characterize the soil profile [28]. The probabilistic classification of soil profiles offers a format for evaluating geotechnical information about subsurface soil conditions at a specific site; a foundation for performance

prediction of a geotechnical engineering structure and evaluating the probability of failure; and allows a geotechnical engineer to better evaluate various site investigation and testing programs [29].

Baecher originally described two key sources of variability in rock mass attributes, found from site investigations, as inherent spatial variation and mistakes induced by sampling and testing when conducting site characterization on rock masses [30]. Baecher and Einstein and Baecher proposed a method for coping with large amounts of uncertainty in rock mass joints based on statistical reasoning and formal inference [30], [31]. Baecher concluded that the sources of uncertainties are due to geological uncertainty resulting from site formations, geometry, and previous history; model uncertainty caused by physical model offerings; parametric uncertainty arising from spatial variability, measurement error, and estimation bias; and finally, uncertainty arising from omissions or overlooking geological details [30], [32], [33], [34].

Geotechnical variability is a complex attribute that results from many disparate sources of uncertainties. As shown in Figure 2, Christian et al. [35] classified the uncertainty in soil/rock parameters into two groups: (1) data scatter, which includes spatial variation of the soil deposit and random testing/measurement errors; and (2) systematic error, which includes statistical error and measurement bias. The spatial variability usually results from the natural geologic processes and deposits that produced and continuously modify the in-situ characteristics of soil, which makes the soil properties to vary, horizontally and vertically, from place to place. Different parameters (e.g. the mixture of various soil, water content, density, stress level) contribute to the change of soil properties.

Measurement errors are caused by equipment or operator-induced variation, which can take place from one test to another. Operator-induced variation occurs when personal judgement is required to read scales, take measurements, or during sample preparation and handling and possible soil disturbance. Equipment error arises from variations in the way tests are set up, loads are delivered, or soil response is sensed. For example, in the light falling weight deflectometer (LFWD) tests, the load plate of LFWD may be situated on the material to be tested differently in succeeding tests. Drop height and rod resistance may vary slightly from one drop to another, and temperature changes can affect the damping properties of the rubber buffer.

Statistical error is predominantly caused by the use of a small number of measurements; whereas the model bias arises when a correlation model is selected to interpret specific data.

Figure 2. Uncertainty in soil properties [35]

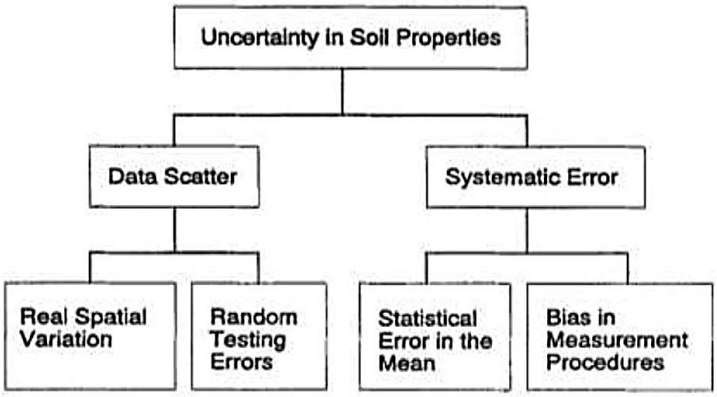

Baecher and Christian [36] adopted Hacking's terminology [37] for two basic forms of uncertainty: aleatory and epistemic uncertainty, which reflect natural variability and lack of information, respectively. As illustrated in Figure 3, Baecher and Christian [36] categorized the uncertainty in geotechnical engineering design into three broad groups: natural variability (temporal, spatial), knowledge uncertainty (model, parameters), and decision model uncertainty (objectives, values, and time preferences).

Figure 3. Categories of uncertainty in risk analysis [36]

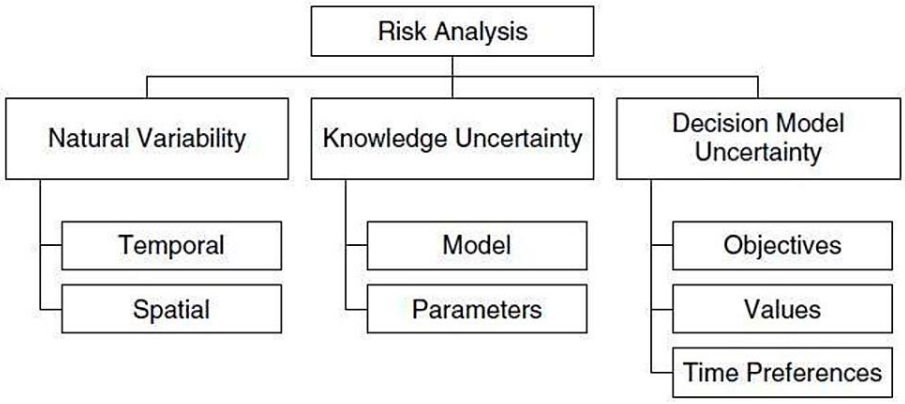

As defined by Baecher and Christian [36], the natural variability is the variability of soil qualities across time and space, expressed as variability at a single place with changes in time (temporal) and variability throughout space at a single time (spatial). Another name for natural variability is the aleatory uncertainty. Since it has been introduced into the design due to a lack of information, data, and understanding, Baecher and Christian's knowledge uncertainty is known as subjective uncertainty. It is also known as epistemic uncertainty. Figure 3 describes how the model and parameter uncertainties can be

subdivided from the knowledge uncertainty. In geotechnical design, Baecher and Christian's decision model uncertainty, which comprises of objectives, values, and time preferences, entails implementing designs that reflect both aleatory and epistemic uncertainties.

Phoon and Kulhawy ([6], [7], [38]) evaluated three key types of uncertainty in geotechnical variability: (1) inherent variability, (2) model uncertainty, and (3) measurement error. The generic depiction of uncertainty for soil parameters studied by Kulhawy and his co-authors is shown in Figure 4. For a homogeneous random field model, the inherent variability is represented using the coefficient of variation and scale of fluctuation [38]. Unlike the model uncertainty, the transformation model uncertainty considered by Kulhawy and Phoon reflects uncertainty originating from the application of empirical models or correlation models to convert indirect measurements to required design parameters [7]. The equipment, procedural/operator, and random testing effects all contribute to measurement error during the measurement procedure [6].

Figure 4. Uncertainty in soil property estimates [38]

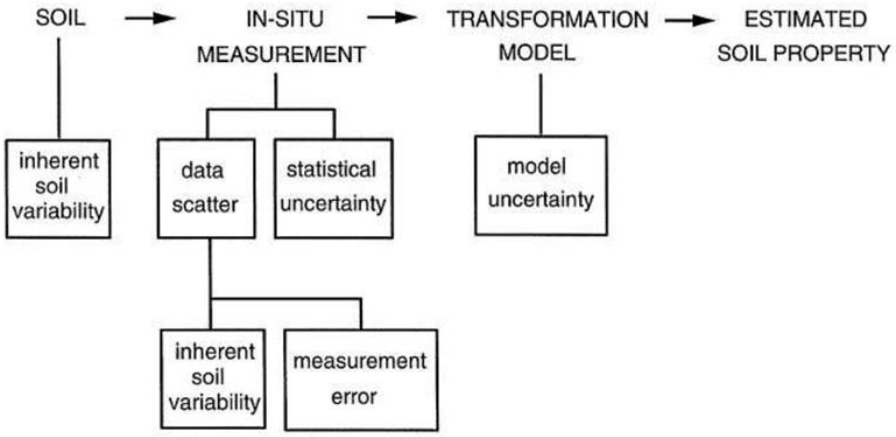

Unlike most prior researchers, Griffiths and Fenton [19] concentrated on aleatory uncertainty, soil fluctuation that occurs naturally. Their research focuses on the spatial variability of soil parameters and the application of random field finite element models for reliability-based design. Vanmarcke's random field theory, which uses the correlation structure of one-dimensional random processes in terms of a variance function and a scale of fluctuation, was adopted by Griffiths and Fenton [39]. The random field theory aids in the construction of models for studying soil spatial variability and is the foundation of Griffiths and Fenton's reliability analysis. Griffiths and Fenton use a positive connection between soil parameters obtained at near distances to reflect the soil

information at a given place. Griffith et al. [24] also developed the random finite element method (RFEM) in reliability-based design by combining random field theory and the finite element approach with Monte Carlo simulation methodologies. Fenton researched quantifying soil qualities in order to create spatial correlation structures that might be used to make inferences about other locations with similar soil engineering properties ([40], [41]). Fenton used the fractal model to examine the tip resistance measurements from cone penetration tests (CPT) and constructed a global correlation model to characterize the spatial variability of tip resistance [23].

Onyejekwe et al. [13] conducted a research study with the goal of statistically describing the variability of geotechnical factors in order to increase geotechnical engineers' adoption of reliability-based design (RBD). The first and second statistical moments, as well as the coefficient of variation (COV) were used to describe the geotechnical characteristics. Their probability distributions and fluctuation scales, were also calculated. The degree of fit of study data to known empirical correlations was studied. Correlations between difficult-to-obtain parameters and more easily-obtain parameters were generated. They revealed that the Semivariogram Function (SVF) is better suitable for determining the scale of variation from widely dispersed, noncontinuous, irregular data received from laboratory testing than the Autocorrelation Function (ACF). A framework was suggested in his research that combines the spatial averaging impact of parameters computed from widely dispersed, irregular, and non-continuous data using the scale of fluctuation and variance reduction factor.

McVay et al. [14] noted that the Florida Department of Transportation (FDOT) and the Federal Highway Administration (FHWA) use a constant load and resistance factored design (LRFD) for deep foundation design, which depend on redundancy and independent of pile or shaft dimension. They stated that the properties of soil differ from one location to another and are often spatially associated. Since the skin friction (and end bearing) need spatial averaging of the soil properties across the pile shaft, the resulting total shaft resistance variability (CV_R) will not be the same as the soil/rock field measurement variability (CV_q). The varying degree of spatial correlation, as expressed by a covariance function, and the correlation length (a) will also affect the total shaft resistance variability (CV_R). They showed that while CV_R is a function of pile/shaft dimensions, CVq value and spatial correlation, the value of resistance factors (ϕ_R) is not constant for any given location. They provided four quadrant iterative design charts for single and group pile/shaft layouts, which consider side and tip resistances as well as layered systems, which were produced to assist the designer.

Faraone [16] debated that AASHTO specifies resistance factors (ϕ_R) for use in a variety of design approaches, foundation types, and levels of field verification in current reliability-based design practice for deep foundations (e.g., load testing). These values of ϕ are calibrated using databases of measured vs anticipated resistances and are based on defined target reliabilities. This calibration has the drawback of not accounting for the varying degrees of design parameter variability that can be seen across different sites (i.e., homogeneous versus heterogeneous sites). He introduced a reliability-based design methodology that he thinks accounts for site-specific spatial variability and may be applied to a variety of deep foundation design practices. Through stochastic modeling, geostatistical tools are employed to describe site heterogeneity and quantify uncertainty of either foundation resistance or rock mass modulus.

Data Scatter

The first source of uncertainties results from the natural geologic processes that continuously modify the in-situ characteristics of soil. The soil properties vary from place to place. Different parameters (e.g. the mixture of various soil, water content, density, stress level) contribute to the change of soil properties. Measurement error is caused by equipment- or operator- induced variation, which can take place from one test location to another. Operator-induced variation occurs when personal judgement is required to read scales, take measurements, or during sample preparation and handling. Equipment error arises from variations when tests are set up and loads are delivered. For example in the case of the LFWD, drop height, rod resistance, and seating of the load plate can vary from one drop to another, and the rubber buffer can be influenced by temperature change. Collectively, these two sources can be described as data scatter ([6], [7], [8]).

Various geologic, physical-chemical, and environmental processes contribute to the development of soil deposit. Some of these processes continue for long periods of time and can modify the soil characteristics. Due to the ongoing natural processes, soil properties will vary in both the horizontal and vertical directions The spatial variability can be depicted precisely by the central trend, the COV, and the scale of fluctuation.

Soil Profile

The spatial variation of soil properties can be classified into a deterministic trend component "f" and a random component "ε". The relationship can be formulated as follows ([7], [42], [43]):

$$sp(z) = f(z) + \varepsilon(z) \quad [1]$$

where sp is the soil property, z is the depth, and the vertical spatial soil variability is represented by the random component. First, the random component is measured by all geostatistical operations, and the deterministic component is added later.

While quantifying spatial variability, it is required to model sp(z) as a homogeneous random function or field [44]. Two considerations are required to maintain when the function sp(z) is considered statistically homogeneous: (1) there are no change in mean trend and variation of "ε" along the depth; and (2) the correlation is a function only of the deviations between two separation distances, rather than their absolute position. When data is collected from a homogenous soil layer, fluctuations in the soil property profile are probably considered to be uniform. Figure 5 presents the spatial soil variability with depth along soil profile.

Coefficient of Variation

The standard deviation of inherent soil variability (σ_w) for a homogeneous variability function sp(z) can be defined as follows [42]:

$$\sigma_w = \sqrt{\frac{1}{n-1}\sum_{i=1}^{n}[\varepsilon(z_i)]^2} \quad [2]$$

where, n is the number of data points, and $\varepsilon(z_i)$ is the fluctuation at depth z_i. Dimensionless representation of inherent soil variability known as the coefficient of variation (COV_w) can be more useful by normalizing σ_w with respect to the mean soil property trend (f) as follows:

$$COV_w = \frac{\sigma_w}{f} \quad [3]$$

Figure 5. Spatial soil variability ([6], [7])

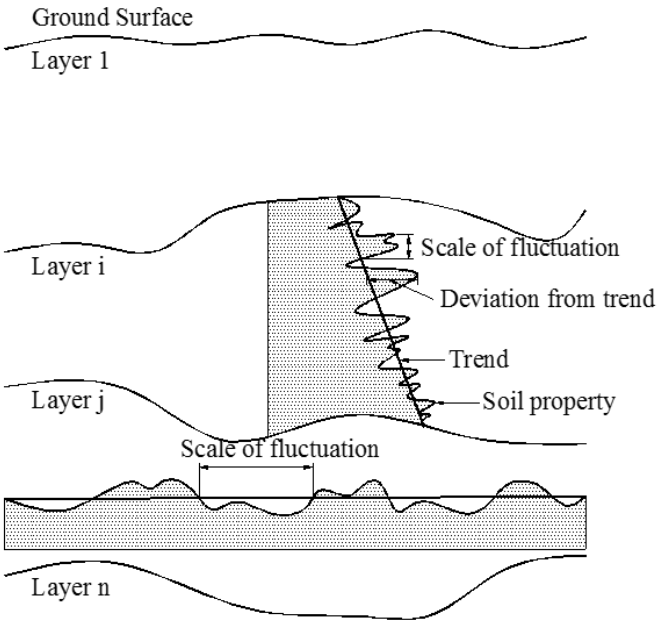

Scale of Fluctuation

Another statistical parameter that is required to describe site variability is the correlation distance or scale of fluctuation, δ_v, as shown in Figure 6, which can provide a specific indication of the property values that show a strong correlation.

$$\delta_v = 0.8\ \bar{d} \qquad [4]$$

where, δ_v is the vertical scale of fluctuation, and $\bar{d}$ is the average distance between the intersections of the profile of fluctuating property and its trend function, as shown in Figure 6.

Figure 6. Estimation of vertical scale of fluctuation ([6], [7])

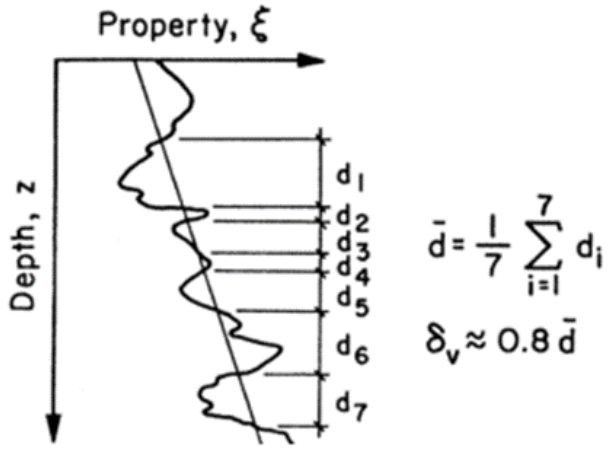

Measurement Error

The second source of uncertainties, which are measurement-related uncertainties, can be divided into three categories: accuracy, repeatability (precision) and reproducibility [45]. The accuracy is referred to the average of individual measurements as compared with the true value, which is influenced by the resolution, bias, stability (change in bias over time), and linearity (change in bias over normal operating range) of the measurements [45]. Figure 7 illustrates the accuracy, stability, and linearity of the measurements. Repeatability is defined as the variation that occurs when the same operator repeatedly measures the same sample using the same devise under the same conditions (see Figure 8a) [45]. Reproducibility is related to the variations that occur between two or more operators or devises measuring the same sample using the same measurement method in a stable environment (see Figure 8b) [45].

Repeatability and reproducibility (R&R) can be estimated using the Gauge R&R (GRR) analysis method. The Gauge is any device that can be used to obtain measurement. The R&R is defined as the coordination of the device variability (repeatability) and operator variability (reproducibility). The concept of GRR is illustrated in Figure 8c. The results of a Gauge R&R study are EV (repeatability or equipment variability), AV (reproducibility or the operator variability), and SV (specimen variability) [43].

Figure 7. Illustration of accuracy, stability, and linearity of measurements [45]

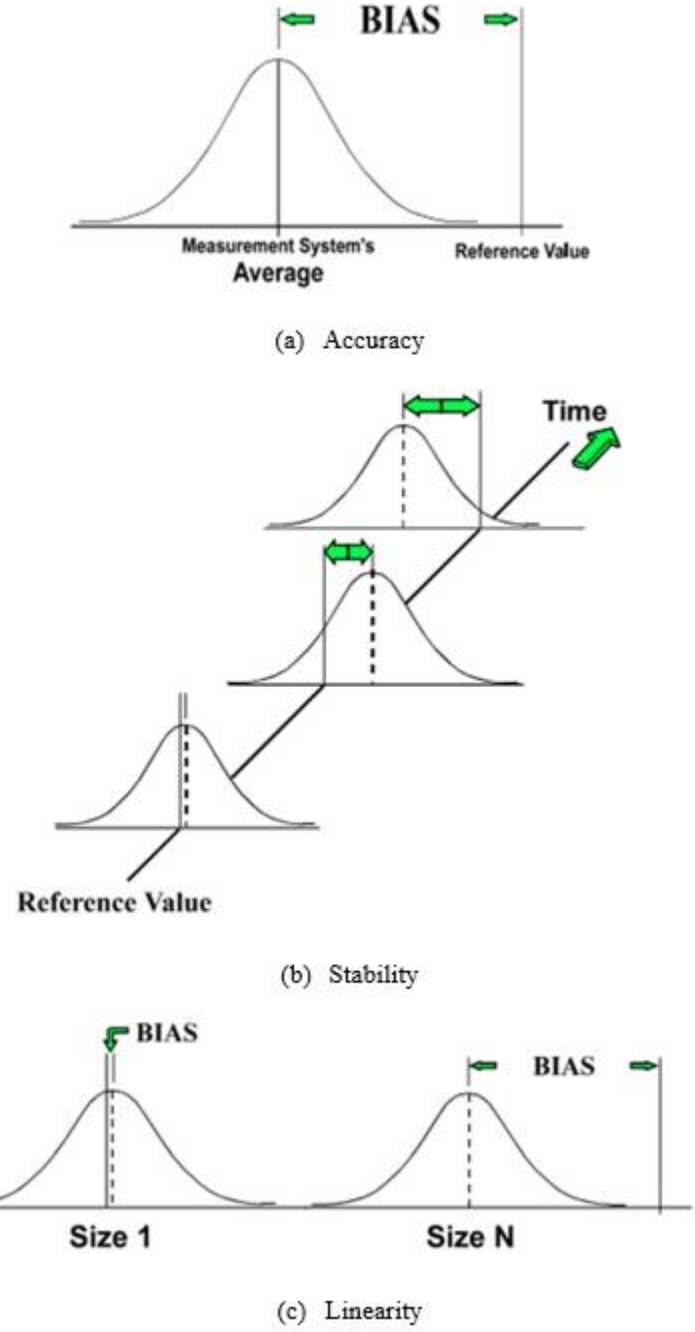

Systematic Error

The third source of uncertainty in geotechnical measurements is the statistical errors that result from the limited amount of information. When it is required to estimate the mean trend of measurements, the use of limited number of tests can lead to possible statistical

error. This type of measurement uncertainty can be minimized by performing tests on more soil samples [6], [8], [38].

The fourth source of uncertainty, known as the model bias, is introduced when empirical or other correlation models are used for field or laboratory measurements, which are consequently transformed into design soil properties. This bias uncertainty can be estimated empirically by comparing the model predictions made from the measured values against the observed values. Collectively, these two sources can be described as the systematic error [8].

Figure 8. Illustration of repeatability, reproducibility, and GRR of measurements [45]

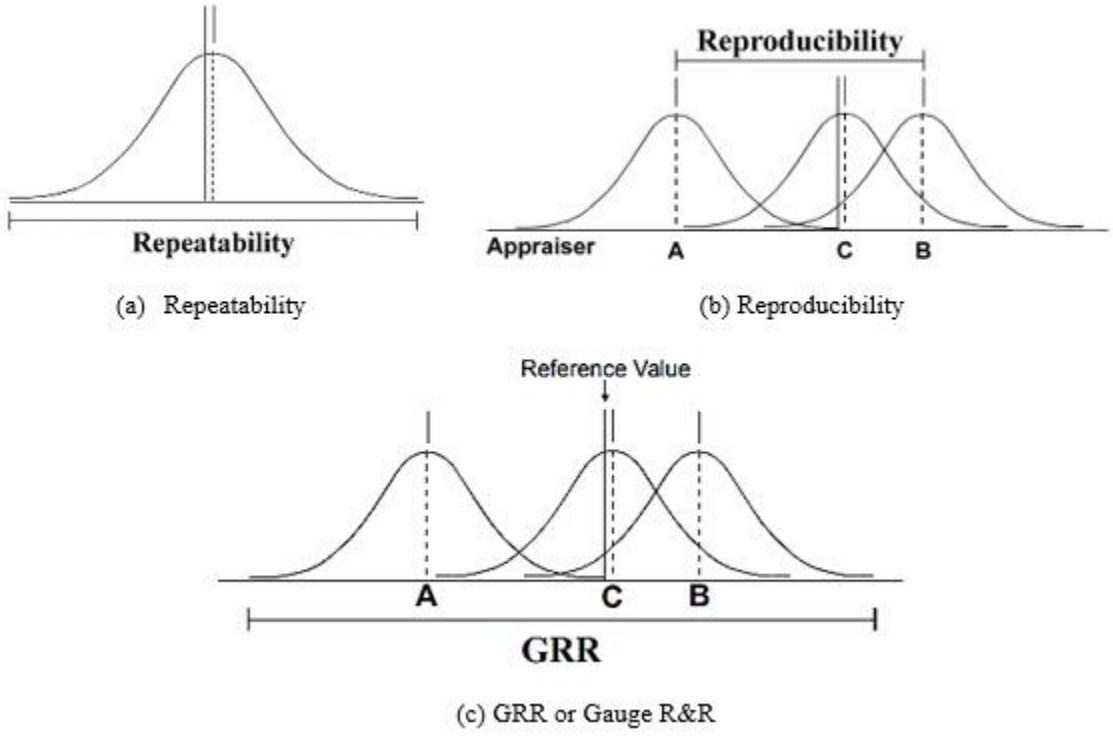

Methods and Techniques for Evaluating Site Variability

As stated earlier, the in-situ properties of all soil deposits, by nature, are usually subjected to certain degree of variability (spatially in both the vertical and horizontal directions) within the same site, which was inherited with time since soil deposition. The variation of soil properties can be statistically characterized by the mean, m, and standard deviation, σ. The dimensionless representation of inherent soil variability, known as the coefficient

of variation, COV, can be useful by normalizing the standard deviation, σ, with respect to the mean of the soil property trend, m, as follows:

$$\text{COV} = \frac{\sigma}{\text{m}} \quad [5]$$

Orchant et al. [46] combined all possible error sources in one term using the following equation:

$$\sigma^2_{measure} = \sigma^2_{equip} + \sigma^2_{op/proc} + \sigma^2_{random} \quad [6]$$

where: $\sigma^2_{measure}$= total variance of measurement, σ^2_{equip}= variance of equipment effects, $\sigma^2_{op/proc}$ = variance of operator / procedural effects, and σ^2_{random} = variance of random testing effects. If the operator has a good experience and the machine is well maintained and calibrated, the associated errors are expected to be substantially reduced. Orchant et al. [46] evaluated the variation of CPT data from different sites and found out that the total measurement error of the CPT is normally within the range of 5% to 15%.

Different methods and techniques have been introduced in literature to evaluate the spatial variability of soil properties of a specific site from either the soil borings with laboratory testing or from in-situ testing. The following sub-sections will present several evaluation methods and their potential application in many geotechnical engineering analysis and design.

X-Bar/R and ANOVA Analyses

Several methods and techniques can be used to perform the Gauge R&R analysis, which includes the average and range (X-Bar/R) method and the analysis of variance (ANOVA) method. The X-Bar/R method allows repeatability, reproducibility and specimen-to-specimen variability where device-operator interaction is not considered. On the other hand, ANOVA method is more precise in considering the interaction between the operator and the device [43].

The equations used in the X-Bar/R and ANOVA methods are presented in Table 1 and Table 2, where m replicate measurements that are performed by p operators on n specimens. The parameter y_{ijk}, which refers to the measurement made using the device (i) by operator (j) on specimen (k), can be expressed using the following equation [43]:

$$y_{ijk} = x_i + u_j + w_{ij} + \varepsilon_{ijk} \quad [7]$$

where, x_i is the actual value of the desired parameter; u_j represents the operator variation; w_{ij} represents the interaction between the specimen and operator; and ε_{ijk} represents the repeatability error. The Gauge R&R value can be obtained from the following expression [43]:

$$GRR = \sqrt{EV^2+AV^2} \quad [8]$$

where, EV represents the repeatability of equipment variation, and AV represents the reproductively of the operator variation. The total variation (TV) of a measurement system can be calculated by adding the Gauge R&R variations to the specimen variation (SV) as follows [43]:

$$TV = \sqrt{EV^2+AV^2+SV^2} \quad [9]$$

Table 1. Equations used to calculate variability parameters - X-Bar/R Method according to AIAG Guidelines (Measurement System Analysis Manual, 4th Edition)

Repeatability -Equipment Variation (EV)	Reproducibility - Operator Variation (AV)	Repeatability & Reproducibility (GRR)	Specimen Variation (SV)	Total Variation (TV)
$\frac{\overline{R}}{d_2}$	$\sqrt{\left[\frac{R_O}{d_2^*}\right]^2 - \left(\frac{EV^2}{nr}\right)}$	$\sqrt{EV^2+AV^2}$	$\frac{R_S}{d_2^*}$	$\sqrt{GRR^2+SV^2}$

[a]Automotive Industry Action Group (AIAG), $\overline{R}$ = average range of measurements, d_2 = bias correction factor obtained from statistical Tables, R_O = range of the operator averages, d_2^* = correction factor for estimating variances obtained from statistical Tables, *n*= number of specimens, *r* = number of measurement repetitions, R_S = range of the specimen average.

Table 2. Equations used to calculate variability parameters - ANOVA Method (Measurement System Analysis Manual, 4th Edition)

Source of Variation	Degree of Freedom	Sum of Squares, SS	Mean Sum of Squares, MSS	Estimate of Variance Component	Expected Value of Variance Estimate**
Specimens	n-1	$mp\sum_{i=1}^{n}(\bar{y}_{i..}-\bar{y}_{...})^2$	$\frac{SSO}{n-1}$	$\frac{MSSO-MSSI}{mp}$	υ^2
Operators	p-1	$nm\sum_{j=1}^{p}(\bar{y}_{.j.}-\bar{y}_{...})^2$	$\frac{SSA}{p-1}$	$\frac{MSSA-MSSI}{mn}$	θ^2
Interaction	(n-1)(p-1)	SSI = SST-SSO-SSA-SSE	$\frac{SSI}{(n-1)(p-1)}$	$\frac{MSSI-MSSE}{m}$	α^2
Error	np(m-1)	$\sum_{i=1}^{n}\sum_{j=1}^{p}\sum_{k=1}^{m}(y_{ijk}-\bar{y}_{ij.})^2$	$\frac{SSE}{np(m-1)}$	MSSE	σ^2

var(y_{ijk})=$\upsilon^2 + \theta^2 + \alpha^2 + \sigma^2$, SSO = Sum of Squares of Objects, SSA = Sum of Squares of Operators, SSI = Sum of Squares of Interactions, SSE = Sum of Squares of Errors, MSSO = Mean Sum of Squares of Objects, MSSI = Mean Sum of Squares of Interactions, MSSA = Mean Sum of Squares of Operators, MSSE = Mean Sum of Squares of Errors. $\bar{y}_{i..}$ represents the average of the measurements from the i^{th} object (the "dot" symbol shows averaging over the second and third indices, j and k).

Second Moment Probabilistic Method

In the second moment probabilistic methods, the uncertainty in a random variable are usually evauated through its first two moments, i.e. the mean (a central tendency parameter) and the variance (a dispersion parameter). The second moment method and their modeling of soil parameters are widely used in the geotechnical literature because of their efficiency in transmitting important properties of datasets. Phoon and Kulhawy [6] used the second moment probabilistic approach to statistically estimate the site soil variability and measurement error in an extensive manner. They applied the second moment approach (using the mean and coefficient of variation) to combine the inherent soil variability, measurement error, and the transformation uncertainty.

A summary of the COVs of inherent variability, scale of fluctuation, and measurement error for various test measurements were presented in their study. They found out that the vertical and horizontal scale of fluctuation of index parameter were the greatest. They performed several laboratory tests (e.g. undrained shear strength, friction angle, liquid and plastic limit, total and dry unit). In case of measurement error, they also reported that the COVs of measurement error for most laboratory strength tests were estimated to be between 5% and 15%. They also found out that the COVs of clay properties are greater than sand soil.

A detailed analysis of the measurement error has been conducted by Kulhawy and Trautmann [47] for the field test measurements. They performed regression analyses to determine the amount of variation assignable to each test parameter. They applied the second moment statistics (mean and coefficient of variation) to estimate the random testing errors where replicate data were available.

In modeling uncertainty in the second moment probabilistic method, it is necessary to assume that uncertainty propagation techniques (such as Monte Carlo simulation) are compatible with the random variables [48]. The first-order second-moment (FOSM) method has been effectively used in literature to investigate the propagation of second moment uncertainties by calculating an approximate estimate of the central tendency parameter (e.g., mean) and the dispersion parameter (e.g., standard deviation) of a random variable that is a function of other random variables [48].

Spatial Correlation and Semivariogram

Geotechnical design engineers frequently fail to recognize the spatial variability of the collected geotechnical data and its potential inverse impact on geotechnical engineering applications, such as improper and/or unsafe design of shallow and deep foundations, and slope stability analysis. The simple evaluation of mean values from soil borings or in-situ testing within a zone or layer is a useful measure of the spatial variability of the intended soil property/parameter. Differences in soil parameters are strongly related to the spatial variability throughout a site, resulting in corresponding variations in the design value of geo-structure, such as the axial capacities of deep foundation. Additionally, since spatial variability has a degree of correlation that decreases with distance, the recommended LRFD resistance factors for design of geo-structures (such as foundation) based on data within the footprint versus data outside the footprint can be significantly different.

Correlation in Soil Properties

In geotechnical engineering, using correlations and empirical relationships to predict the value of one parameter based on the value of another (perhaps more easily obtained parameter) can be considered a quick and cost-effective approach, provided that the relevant correlations are used. The quantification of the correlation between two or more soil qualities can provide a more accurate assessment of design parameter uncertainty and an indicator of the degree of independence between the parameters in probabilistic analysis (i.e., [48], [49], [50]).

The correlation between two or more soil attributes has been found to be influenced by soil type, the testing method used to get the numerical value of the parameter, and the homogeneity of the soil to variable degrees [48]. There have been a lot of correlations between soil parameters that have been published. Over 50 of these connections are presented in an article by Kulhawy and Mayne [51].

Histogram, Mean and Variance

The data for each soil layer or zone needs be plotted in a histogram once the site has been divided into layers or zones and the data has been de-trended for stationarity criteria. An engineer can see the frequency ranges of data as well as its distribution using the histogram (e.g., mode and mean align, etc.). The presence of several peaks or modes in the histogram can also be utilized to determine whether multiple distributions do exist inside each zone or layer.

Both the mean (μ) and variance (σ^2) of the dataset (q_i) should be first determined in addition to the histogram. For example,

$$\mu = \frac{1}{n}\sum_{i=1}^{n} q_i \quad [10]$$

$$\sigma^2 = \frac{1}{n-1}\sum_{i=1}^{n}(q_i - \mu)^2 \quad [11]$$

The coefficient of variation (COV) is a dimensionless measure of the inherent soil variability that can be made more helpful by normalizing the standard deviation with regard to the mean soil property trend, μ, as follows:

$$\text{COV} = \frac{\sigma}{\mu} \quad [12]$$

where, μ is the dataset's mean, n is the number of data points, q_i are the data values, and σ is the dataset's standard deviation. The spread or dispersion of data around the mean is represented by COV, a dimensionless number.

Engineers should select the best probability distribution function (PDF) that best represents the observed data based on the shape of the histogram's distribution (e.g., uniform, triangular, normal, lognormal, etc.) as well as summary statistics (mean vs. mode, etc.). Almost all soil parameters (e.g., strength, modulus, etc.) have no negative values and a wide range of positive values, resulting in considerable disparities in mode (most frequent) vs mean values and are best described by lognormal distribution.

Following the discussion of second moment statistics (mean, standard deviation, coefficient of variation (COV), and probability distribution) and correlation in soil properties, it can be concluded that second moment statistics are heavily dataset dependent, with data distribution heavily influenced by soil type and in-situ state. Published values, with their wide range of values, frequently fail to adequately represent the local circumstances and, as a result, may fail to produce efficient, cost-effective outcomes. As a result, site-specific second moment statistics must be developed.

Spatial Variability Analysis

The geographical variability of the parameters is not taken into consideration by the second-moment-based methodologies for characterization the uncertainty in geotechnical parameters. Geotechnical parameters are known to have lateral and depth-dependent relationships. They vary spatially, with a larger tendency for close neighbors to have similar values than distant neighbors. This is why the second moment statistics alone are insufficient to characterize the geotechnical parameter uncertainty ([4], [27], [48]). Figure 9 shows why the second moment statistics alone are insufficient to quantify the uncertainty of geotechnical parameter. The figure depicts the simulated spatial data with identical distributions (top and bottom left) but distinct magnitudes of spatial correlation: weak correlation (top right) and strong correlation (bottom right) [52].

Figure 9. Spatial data with similar distributions (top and bottom left) but different magnitudes of spatial correlation [52]

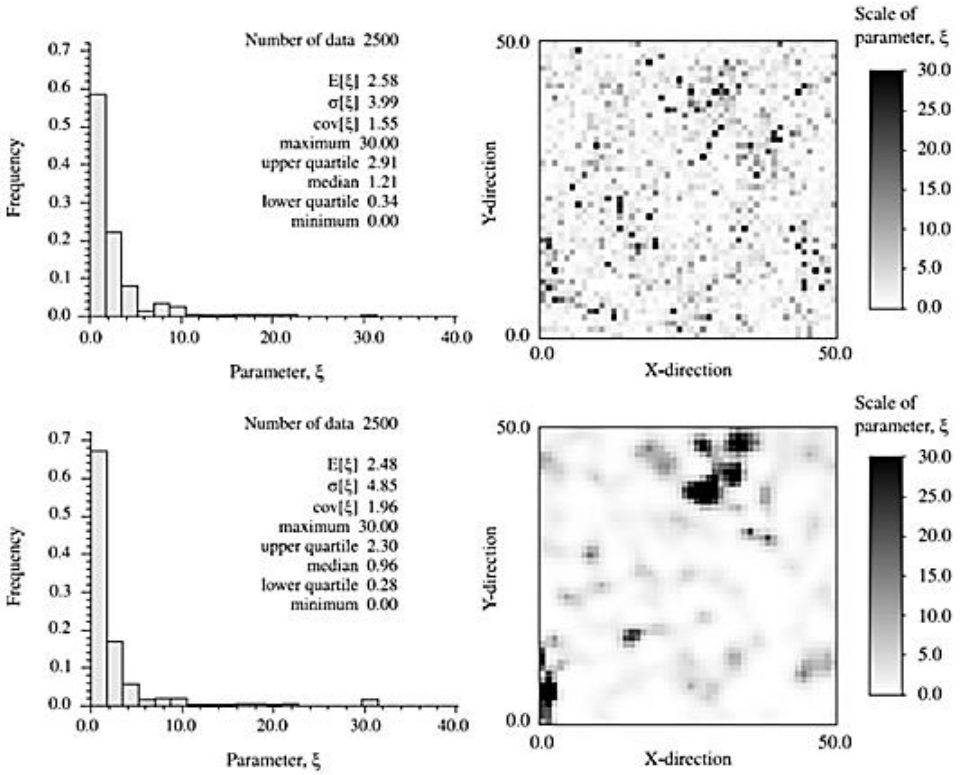

Geostatistics is based on regionalized variables with properties that are partly random and partly spatial, and that are consistent from one point to another point [53]. The semivariogram, which is used to quantify the degree of spatial dependency between samples along a certain orientation and to illustrate the degree of continuity of the characteristic in question, is one of the most basic statistical measures in geostatistics.

The stationarity of data is required in order to undertake geostatistical analysis. If the following conditions are met, data is said to be stationary: (a) there is no trend in the data; (b) the variance is constant with distance (homoscedastic); (c) there are no seasonal variations; and (d) there are no irregular fluctuations. In time series analysis, the need for stationarity is more severe than in geostatistics. It is common practice, in both random field theory and geostatistics, to convert a nonstationary dataset into a stationary one by removing a low-order polynomial trend, usually no more than a quadratic, using the Ordinary Least Squares (OLS) approach ([29], [48]).

In semivariogram analysis, engineers must first assess the correlation between data/sets separated by different distances using different factors in order to define the spatial variability from measured data. The covariance C(h) between data values q_i and q_j separated by a distance h is one of the most important fundamental parameters used. The covariance C(h) is calculated as follows:

$$C(h) = \frac{1}{n}\sum_{i.j=1}^{n}(q_i - \mu)(q_j - \mu) \quad [13]$$

where, q_i and q_j are the data pairings separated by h, and n is the total number of data pairs. The C(h) value equals the variance for completely correlated data (i.e., $q_i = q_j$). C(h) = 0 if there is no correlation (i.e., the product of the terms is both plus and minus and sums to zero). The correlation coefficient, ρ(h), is a dimensionless representation of the data's correlation.

$$\rho(h) = \frac{C(h)}{\sigma^2} \quad [14]$$

The limits of zero and one ($0 < \rho(h) < 1$) represent no correlation and perfect correlation, respectively. Another characterization of the spatial correlation in geostatistics is the semivariogram, γ(h), which is given by the following equation:

$$\gamma(h) = \frac{1}{2n}\sum(q_i - q_j)^2 \quad [15]$$

The variogram γ(h) can also be evaluated from the covariance C(h) and the variance of data σ^2 as follows:

$$\gamma(h) = \sigma^2 - C(h) \quad [16]$$

Figure 10 presents typical instances of C(h), ρ(h), and γ(h) as a function of h with each function indicating a decreasing correlation as h increases. The correlation function goes to zero at a distance of h = a (called the range), or the data pairings become uncorrelated. In the case of Equation 16, $\gamma(h=a) = \sigma^2$ [C(h)=0], the variogram's top value, or sill, is attained. The spatial covariance function can be predicted using a variety of theoretical models. There are four types of models: spherical, exponential, Gaussian, and circular ([6], [7]). The spherical model is the most extensively used of these models, and it is defined as follows:

$C(h_i) = 1\text{-}1.5h_i\text{+}0.5h_i^3$ for $h_i < 1$

$$C(h_i) = 0 \qquad \text{for } h_i \geq 1 \qquad [17]$$

Figure 10. Graphical examples of: (a) Spatial covariance function C(h); (b) Spatial correlation function ρ(h); and (c) Variogram γ(h) [14]

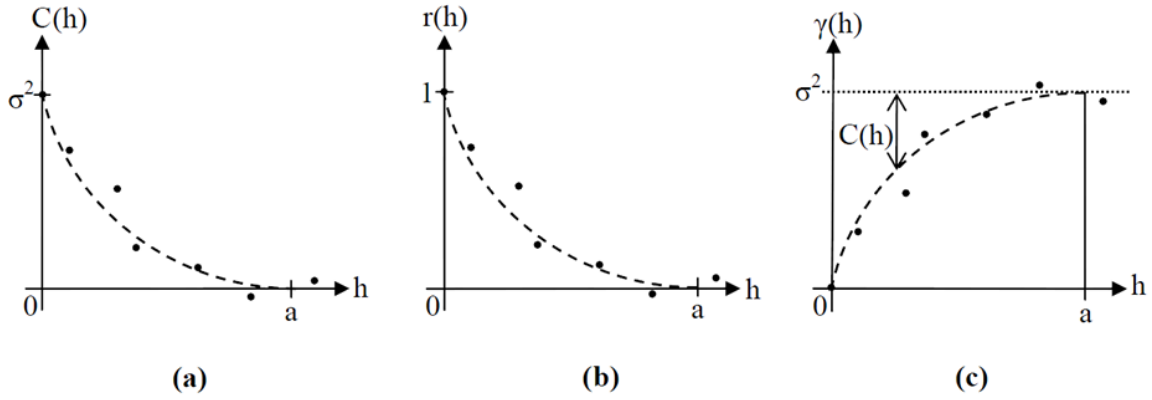

Different Component of the Semivariogram

The semivariogram curve describes the measured sample points' spatial autocorrelation. A model is fitted through each pair of locations once they have been mapped. There are some properties that are frequently used to characterize these models. Figure 11presents the three different components of the semivariogram, which include the range, sill, and nugget.

Range: Examining the model of a semivariogram, we can see that it levels out at a given distance, h, between sample/test locations. The range is defined as distance at which the model begins to flatten out. Spatial autocorrelation exists between test/sample locations separated by a distances less than the range, but not between test/sample locations farther apart than the range. The range's physical meaning is that pairs of points that are this far apart or more are not spatially connected.

Sill: The sill is the value that the semivariogram model achieves at the range (the y-axis value). The partial sill is the same as the full sill, but without the nugget.

Nugget: The semivariogram value is 0 in theory for zero separation distance (lag = 0). The semivariogram, on the other hand, frequently exhibits a nugget effect, which is a value greater than 0 at an infinitesimally small separation distance. The nugget equals 0.10, for example, if the semivariogram model intercepts the y-axis at 0.10.

Measurement mistakes; spatial sources of variation at distances smaller than the sampling interval; or both, might be blamed for the nugget effect. The mistake inherent in measuring apparatus causes measurement error. Natural events vary in spatial scale across a wide variety of scales. The nugget effect will manifest as variation at microscales smaller than the sample distances. Before you start collecting data, you need learn about the different dimensions of geographic variation.

Figure 11. Different components of the semivariogram

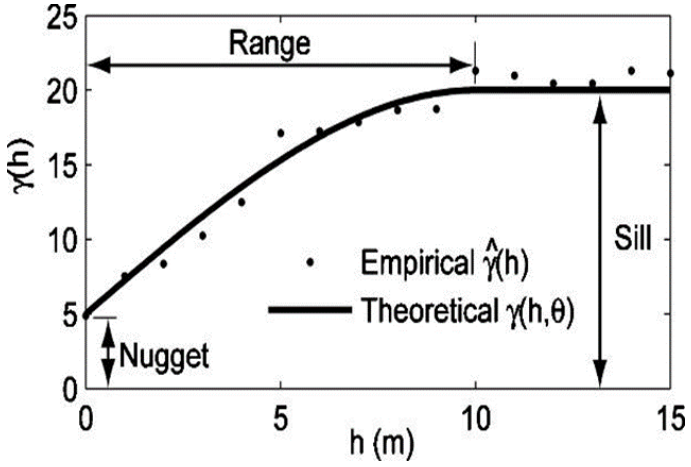

Evaluation of Scale of Fluctuation from Semivariogram

The statistics and probabilistic analysis of the geotechnical parameters are the main focus of the deployment of reliability based design (RBD). The statistics elements needed for RBD are the mean, variance, and scale of fluctuation, θ. These statistics are not only site-specific but also dataset-specific. The mean and variance are easy to compute when data is available. However, calculation of the scale of fluctuation is a bit complex, requiring more data and a well-defined soil profile [54].

In-situ field tests such as the cone penetration test (CPT) can provide sufficient data to establish a well-defined profile but are not widespread used. The more used method is the standard penetration test (SPT), which cannot provide ample data to establish a well-defined profile, which is required for computing the scale of fluctuation. The continuous Shelby tube sampling method is the alternate method and has the inherent capacity of providing sufficient data to establish a well-defined profile that can be used to compute the scale of fluctuation. Tests can be performed at a closer spacing (closer than SPT) and direct and indirect measurements of geotechnical properties can be carried out ([13], [54]).

The semivariogram is one of the best approaches to evacuate the scale of fluctuation. The experimental variogram is first plotted and a best-fit model is obtained, and the parameters of the model are determined. One of the model parameters, the range of influence, a, is then used to evaluate the scale of fluctuation using the appropriate equation for the semivariogram (Gaussian, exponential, spherical, and circular), as given in Table 3 [55].

Table 3. Relationship between range of influence and scale of fluctuation [55]

Model	Mathematical Function	Scale of Fluctuation (θ)
Gaussian	$\gamma_h = C\,(1 - e^{-h^2/a^2}) + C_o$	$\pi^{0.5}a$
Exponential	$\gamma_h = C\,(1 - e^{-h/a}) + C_o$	2a
Spherical	$\gamma_h = C\left(\frac{3h}{2a} - \frac{h^2}{2a^2}\right) + C_o$; $h \le a$ $\gamma_h = C + C_o$; $h \ge a$	3a/4
Circular	$\gamma_h = C\,(1 - (2/\pi)(\cos^{-1}(h/a) - (h/a)(1 - (h/a)2)^{1/2})) + C_o$; $0 < h \le a$ $\gamma_h = C + C_o$; $h > a$	8a/π
Notes: a = range of influence; h = lag length		

Several programs available in the market to model the semivariogram, such as VESPER and ArcGIS. The VESPER 6 program was used in this study to determine the scale of fluctuation.

Implementing site variability from semivariogram into LRFD design of piles

The ranges obtained from the semivariogram analyses are used to determine the reduction factor, α_r [14], which will be applied to calculate the spatial coefficient of variation $COV_{R,spatial}$ as a function of COVq, of the field measurements (e.g., CPT-qt, SPT-N, S_u) using the following equation:

$$COV_{R,spatial} = \sqrt{\alpha_r}\, COV_q \qquad [18]$$

Here $COV_q = \sigma/m$ is the coefficient of variation in the sample data q. For application to pile foundation design, the generalized expression for COV_R can be given as follows [14]:

$$\mathrm{COV}_{\mathrm{R,spatial}} = \frac{\sqrt{\pi^2 D^2 \sum_{j=1}^{n_L} L_{Lj}^2 \alpha_{Lj} \sigma_{Lj}^2 + \sigma_{EB}^2}}{\pi D \sum_{j=1}^{n_L} L_{Lj} m_{Lj} + m_{EB}} \qquad [19]$$

where, D is the pile diameter; L_{Lj} are the known (deterministic) length intervals of the shaft; m_{Lj} are the expected values of fs_{Lj} (and hence q) in each layer; m_{EB} is the value (expected) of end bearing resistance; α_{Lj} is the α for each layer; σ_{Lj}^2 is the variance in q for each layer; and σ_{EB}^2 is the variance in end bearing resistance. Equation 19 reduces to Equation 18 for $n_L = 1$ (single layer) and $m_{EB} = \sigma_{EB}^2 = 0$ (no end bearing) [14].

In the above equation, the reduction factor, α_r, is a function of $(\frac{L}{a_v}, \frac{D}{a_h})$, where a_v and a_h are the correlation ranges in both the vertical and horizontal directions, respectively; and L and D are the pile length and pile diameter, respectively. Since the horizontal correlation is too large compared to the pile diameter, the value of $\frac{D}{a_h}$ is usually approaching to zero, $\frac{D}{a_h} \approx 0$, in many cases. Elkateb et al. [5] derived the following equation to determine α_r for spherical model:

$$\alpha_r = 1 - \frac{L}{2\,a_v} + \frac{L^3}{20\,a_v^3} \qquad \text{For } 0 \le \frac{L}{a_v} \le 1$$

$$\alpha_r = 1 - \frac{3\,a_v}{4\,L} + \frac{a_v^2}{5\,L^2} \qquad \text{For } \frac{L}{a_v} \ge 1 \qquad [20]$$

In order to consider, both $\frac{L}{a_v}$ and $\frac{D}{a_h}$, we have to use the figure 1.8 given by McVay et al. [14]. Results from McVay et al. [14] numerical integration in terms of $\alpha_r^{1/2}$ as a function of the dimensionless variables $\frac{L}{a_v}$ and $\frac{D}{a_h}$ are presented in Figure 12 (spherical).

Once the value of spatial coefficient of variation, COV_R, is defined, the resistance factor, ϕ_R, for pile design according to the load and resistance factor design (LRFD) method can be calculated using the following modified first-order second moment method (MFOSM) calibration equation proposed by McVay et al. [14]:

$$\phi_R = \frac{\lambda_R \left(\gamma_D \frac{Q_D}{Q_L} + \gamma_L\right) \sqrt{\frac{1 + COV_Q^2}{1 + COV_R^2}}}{\left(\lambda_{QD} \frac{Q_D}{Q_L} + \lambda_{QL}\right) \exp\left(\beta_T \sqrt{\ln(1 + COV_R^2)\left(1 + COV_Q^2\right)}\right)} \qquad [21]$$

where, λ_R is the resistance bias factor; Q_D is the dead load and Q_L is the live load; β_T is the target reliability index; γ_D is the dead load factor and γ_L is the live load factor; λ_{QD} is

the dead load bias factor (measured divided by predicted) and λ_{QL} is the live load bias factor. COV_{QD} is for the dead load and COV_{QL} is for the live load. The Q_D/Q_L is the ratio of dead and live load (which is assumed to be 3 in this study).

Figure 12. Integrating $\alpha_r^{1/2}$ as a function of L/a_v and D/a_h for piles for the spherical model [14]

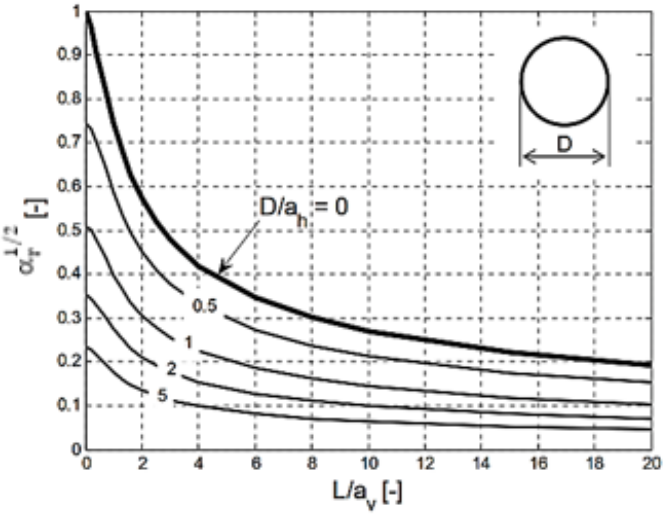

The value of the resistance bias factor, λ_R, depends on the method used to design the pile foundations. In this study, we will use the Laboratoire Central des Ponts et Chausees (LCPC) method [56] to design the piles from the CPT data. The LCPC is a direct pile-CPT method that showed one of the best performance pile-CPT methods on estimating the ultimate pile resistance in Louisiana [57]. The resistance bias factor, λ_R, and $COV_{R,method}$ for the LCPC method are 1.04 and 0.31, respectively. For design of piles using the soil borings and laboratory tests, the static analysis method recommended by the Federal Highway Administration (FHWA) will be considered. The FHWA recommends using the Nordlund method for sand layers based on results of SPT data, and the α-Tomlinson method for clay layers based on undrained shear strength, S_u. The values of λ_R and $COV_{R,method}$ for the Nordlund method are 1.02 and 0.48, respectively; and the values of λ_R and $COV_{R,method}$ for the α-Tomlinson method are 0.87 and 0.48, respectively [58].

It should be noted here that the coefficients of variation of resistance, COV_R, presented above for the different design methods (i.e., COV_R = 0.31, 0.48 or 0.48) do not include the effect of site variability, which treats the site with low variability the same as the site with high variability. In this study, we will incorporate the effect of site variability in calibrating the resistance factor, ϕ_R, for use in LRFD design of driven piles.
The value of resistance bias factor, λ_R, is calculated as:

$$\lambda_R = \frac{\sum \lambda_{Ri}}{N} \quad [22]$$

where, λ_{Ri} is the resistance bias factor for each site and N is the number of sites. The coefficient of variation of the random loads, COV_Q, was introduced by McVay et al. [14] using the following equation:

$$COV_Q = \sqrt{\frac{\frac{{Q_D}^2}{{Q_L}^2}{\lambda_{QD}}^2 COV_{QD}^2 + {\lambda_{QL}}^2 COV_{QL}^2}{\frac{{Q_D}^2}{{Q_L}^2}{\lambda_{QD}}^2 + 2\frac{Q_D}{Q_L}\lambda_{QD}\lambda_{QL} + {\lambda_{QL}}^2}} \quad [23]$$

where, COV_{QD} and COV_{QL} are the coefficient of variations (COV) for the dead load and live load, respectively. According to the FHWA [59], the dimensionless parameters in the above equations can be defined as the follows:

$$\gamma_L = 1.75;\ \lambda_{QL} = 1.15;\ COV_{QL} = 0.18;\ \gamma_D = 1.25;\ \lambda_{QD} = 1.08;\ \ COV_{QD} = 0.128$$

Bayesian Analysis

The Bayesian statistical analysis was introduced in 1763, and the Bayes' technique was adopted by Laplace and other notable probabilists at that time. However, it was not favorable during the nineteenth century due to the lack of understanding on how to appropriately handle the prior probabilities. The development of an entirely different theory, known as frequentist statistics, occurred in the first half of the twentieth century. The modern Bayesian analysis method started in the second half of the twentieth century, by Jimmy Savage in the United States and Dennis Lindley in the United Kingdom. But the Bayesian inference remained extremely difficult to implement until the late 1980s and early 1990s, when powerful computers became widely available and new computational methods were developed. The surge of interest in Bayesian statistics has resulted in considerable study in Bayesian methodology, as well as the application of Bayesian methods to pressing challenges in a variety of fields, including astrophysics, weather forecasting, health care policy, criminal justice and, engineering.

Bayesian analysis is a statistical paradigm that uses probability assertions to answer research queries regarding unknown parameters. In Bayesian analysis, rather than one fixed value, a parameter is described by a complete distribution of values, as in classical frequentist analysis. The essence of Bayesian analysis is in estimating this distribution, and the posterior distribution of a parameter of interest.

Prior Distribution

A prior probability distribution of an unknown quantity, also known as the prior in Bayesian statistical inference, is the probability distribution that would describe one's assumptions about the quantity before any evidence is taken into account. For example, the prior could be a probability distribution indicating the relative proportions of voters who will vote for a specific politician in a future election. Rather of being an observable variable, the unknown quantity could be a model parameter or a latent variable.

The posterior probability distribution, which is the conditional distribution of the unknown quantity given the data, is calculated using Bayes' theorem, which produces the renormalized pointwise product of the prior and the likelihood function. Similarly, the unconditional probability ascribed to a random event or an ambiguous claim before any relevant data is taken into consideration is known as the prior probability.

A prior can be calculated using historical data, such as previous experiments. It can also be derived from an experienced expert's completely subjective opinion. When no information is available, an uninformative prior might be generated to indicate a balance among outcomes.

Informative priors: A precise, definite information about a variable is expressed by an informative prior. A prior distribution for the temperature at noon tomorrow is an example. Making the prior a normal distribution with an expected value equal to today's noontime temperature and a variance equal to the day-to-day volatility of atmospheric temperature, or a temperature distribution for that day of the year, is a reasonable method.

This example, like many priors, has the property that the posterior from one problem (today's temperature) becomes the prior for another problem (tomorrow's temperature); pre-existing evidence that has already been taken into account is part of the prior, and as more evidence accumulates, the posterior is largely determined by the evidence rather than any original assumption, provided that the original assumption admitted the possibility of what the evidence shows. The phrases "prior" and "posterior" refer to a specific datum or observation in general.

Weakly informative priors: A variable's partial information is expressed by a weakly informative prior. For example, if the prior distribution for the temperature in St. Louis at noon tomorrow is a normal distribution with a mean of 50 degrees Fahrenheit and a standard deviation of 40 degrees, the temperature is very loosely constrained to the range

(10 degrees, 90 degrees) with a small chance of being below 30 degrees or above 130 degrees. A weakly informative prior is used for regularization, or keeping inferences within a tolerable range.

In this research, in level 1 analysis of Bayesian framework, the statistical data for Prior1 (i.e., weakly informative prior) are usually taken from previously nationwide (or statewide) testing database when available.

Likelihood function

The joint probability of the observed data as a function of the parameters of the chosen statistical model is described by the likelihood function (sometimes simply called the likelihood).

The likelihood function $p(y|\theta)$ assigns a probabilistic forecast to the observed data (y) for each given parameter value (θ) in the parameter space. The likelihood includes both the data-generating process and the missing-data mechanism that created the observed sample because it is effectively the product of sampling densities. The parameters' likelihood is not a probability density function (PDF). Meanwhile, in Bayesian statistics, the likelihood function acts as a conduit for sample information, $p(\theta|y)$, to alter the parameter's posterior probability. Fisher [60] was the first to advocate for the use of likelihood, believing it to be a self-contained framework for statistical modeling and inference. Later, Barnard and Birnbaum endorsed the likelihood principle, claiming that the likelihood function contains all the important information for inference ([61] [62]). The likelihood function, however, is important in both frequentist and Bayesian statistics [63].

Posterior probability

The conditional probability of a random occurrence or an uncertain claim is the posterior probability given the relevant data or background in Bayesian statistics. In this usage, "posterior" indicates taking into consideration all relevant evidence relating to the particular matter under investigation. The posterior probability distribution is the probability distribution of an unknown quantity that is handled as a random variable and is based on data from an experiment or survey.

A posterior distribution is made up of a prior distribution for a parameter and a likelihood model that provides parameter information based on observed data. The posterior distribution can be calculated analytically or estimated using one of the Markov chain

Monte Carlo (MCMC) methods, depending on the prior distribution and likelihood model used.

The posterior distribution is used in Bayesian inference to create various summaries for model parameters, such as posterior means, medians, percentiles, and interval estimates known as credible intervals. Furthermore, all model parameter statistical tests may be stated as probability assertions based on the predicted posterior distribution. The ability to incorporate prior information into the analysis; an intuitive interpretation of credible intervals as fixed ranges to which a parameter is known to belong with a predetermined probability; and the ability to assign an actual probability to any hypothesis of interest are all unique features of Bayesian analysis.

Bayesian inference

In Bayesian, statistical conclusions regarding a parameter θ, or unobserved data $\tilde{y}$, probability assertions are used. These probability statements are represented in our notation as p(θ|y) or p($\tilde{y}$ | y) and are conditional on the observed value of y. Bayesian inference differs from the approach to statistical inference described in many textbooks, which is based on a retrospective evaluation of the procedure used to estimate θ (or $\tilde{y}$) over the distribution of possible y values conditional on the true unknown value of θ at the fundamental level of conditioning on observed data.

Using the basic feature of conditional probability known as Bayes' rule, simply conditioning on the known value of the data y produces the posterior density:

$$p(\theta|y) = \frac{p(\theta,y)}{p(y)} = \frac{p(\theta)\,p(y|\theta)}{p(y)} \qquad [24]$$

An equivalent form of the above equation omits the factor p(y), which does not depend on θ, and with fixed y, it can be considered as a constant, resulting of the posterior density which is the right side of the following equation:

$$p(\theta|y) \propto p(\theta)\,p(y|\theta) \qquad [25]$$

where, p(θ|y) is the posterior function, p(θ) is the prior distribution, and p(y|θ) is the likelihood function.

There are many reasons to use Bayesian approaches, which can be used in a variety of domains. Several foundational theorems demonstrated that the only way to make consistent and sound decisions in the face of uncertainty is to employ the Bayesian

approaches. The pragmatic advantages of the Bayesian approach have fueled its rapid expansion over the last 20 years and are the cause for its adoption in an ever-widening range of sectors. Bayesian approaches can solve vast and complex statistical issues with relative ease due to powerful computational resources, whereas frequentist methods can only approximate or fail completely.

Bayesian analysis in geotechnical analysis

The presumption that the bias factors for the various project sites in any specific area have similar measurements and variabilities may not be generally valid. The variety in components (e.g., soil properties and workmanship) from site to site can cause the statistical analysis of the bias factor and standard deviation to be contrast in different sites within the same area [64]. The significance of the site-specific variability in the design of pile foundations based on load test database have been demonstrated in several research studies (e.g., [64], [65], [66]). They found out that the variability of the bias factor for a specific site, is usually lower than that in the regional area.

Most of the time, any interpretation model is just a guess or improvement of the present reality, model vulnerability, or uncertainty that consistently exist ([67], [68]). On the off chance that the model's uncertainties are not thought of, the model expectations, and henceforth the choices dependent on the predictions could be one-sided or biased. Tang and Gilbert [69] and Lacasse and Nadim [70] found out that the predicted failure probabilities without considering the model uncertainties were not representing the real failure probabilities of geotechnical frameworks. Inquiries have been completed to consider the impacts of uncertainty associated with input parameters and perception uncertainty on the assurance of model vulnerability. For example, Gilbert and Tang [71] performed geotechnical reliability analysis and proposed a model to update and incorporate the model's uncertainty mean for the offshore applications. Juang et al. [72] developed a methodology to isolate the uncertainties in the liquefaction assessment model from the parameters' uncertainties with the guide of a Bayesian mapping capacity. Zhang [73] proposed a Bayesian technique for updating the associate model's uncertainties for slope stability analysis. The concept of likelihood was introduced by Zhang [73] to develop a methodology to incorporate the uncertainties in the model's parameters. Ching et al. [74] utilized a Bayesian framework to develop a pile load capacity model using the associated uncertainties to calibrate the resistance factors for LRFD design of piles. The basic concept of all Bayesian statistics is based on Bayes' theorem and that is posterior function depends on the prior and likelihood information.

The prior information is a key piece of Bayesian derivation that deals with the data about an uncertain parameter that is joined with the likelihood of new information to yield the posterior information (prediction), which is utilized for future deductions and choices that include the uncertain parameter. Generally, the likelihood is anything but a probability, which is relative to the probability function. The likelihood function of a defined hypothesis (H) at the point, when given a few information or data (D), is the probability of getting D given that H is multiplied by a positive constant, K. Then the likelihood of H will be $L(H) = K \times P(D|H)$. As a rule, the hypothesis deals with the estimation of a parameter in a factual model, such as the mean of a normal distribution. Since the likelihood is different from a probability, most of the time it disregards the different rules of probability; such as in the case of likelihood, the distribution area does not need to be 1. When the information from the prior is legitimately joined with the likelihood of the data, it yields a satisfactory posterior information [75]. The distribution of the posterior information, in the Bayesian analysis, is the overhauled or revised probability of an occasion happening, when new information is considered. The updated knowledge (or posterior) can be obtained from the prior information and likelihood using the Bayesian theorem. Statistically, it can be inferred that the posterior distribution is mainly the probability of any event X occurring (given that) when another event Y has already occurred. The posterior distributions ought to be a superior impression of the basic truth of an information producing process than the probability of prior, since the posterior distribution included more data. The posterior distribution can afterward turn into a prior distribution for an updated posterior distribution, in which this information can be incorporated into the analysis.

Markov chain Monte Carlo Simulation (MCMC)

Many sophisticated approaches for building and sampling from arbitrary posterior distributions have been proposed. Markov chain simulation (also known as Markov chain Monte Carlo, or MCMC) is a general method that involves extracting values from approximate distributions and then correcting those draws to better approximate the target posterior distribution, $p(\theta \mid y)$. The draws create a Markov chain since the sampling is done sequentially and the distribution of the sampled draws is determined by the previous value drawn. The key to the method's effectiveness, however, is that the approximation distributions improve at each step of the simulation, i.e., they converge to the target distribution. The Markov property is useful in establishing the convergence.

Figure 13 presents a simple Markov chain simulation, which is a Metropolis algorithm in this case, in which θ is a two-component vector with a bivariate unit normal posterior distribution θ ~ N (0,I), and is a vector with only two components. Figure 13a depicts the simulation's initial stages. Each of the five jagged lines in the figure presents the early path of a random walk starting near the center or extremes of the target distribution and leaping through the distribution according to a suitable sequence of random iterations. Figure 13b shows the final step of the same Markov chain simulation, in which the simulated random walks have all traced a path through the space of θ with a shared stationary distribution equal to the goal distribution.

Bayesian Framework used to update the Prior Information

The application of Bayesian framework to update data usually consist of two levels of analyses. In level 1 of the Bayesian framework, Prior1 (i.e., weakly informative prior) statistical data is usually taken from previous nationwide (or statewide) testing database when available. In the absence of such data, the authors can propose rationale values of λ and σ based on their judgment of the region. The prior distribution is taken as the probability density function (PDF) of the available prior information or data (e.g., previous database or engineering experience and judgment). It measures probabilistically the earlier prior information in the deficiency or shortage of information. In the absence of dominant prior information or data, a comparatively uninformative prior knowledge can be functional ([76], [77]) that composed with standard ranges of parameters ([6], [70], [78]). As the prior knowledge improves with time, in the future or in the next level of data and analysis, an increasingly useful prior can be evaluated from earlier information [77]. The definition of the prior distribution using prior data and knowledge is thoroughly discussed in the literature (e.g., [79]).

Figure 13. A Markov chain simulation with five separate sequences (a) after 50 iterations, away from the convergence (b) the sequences are closer to convergence after 1000 iterations

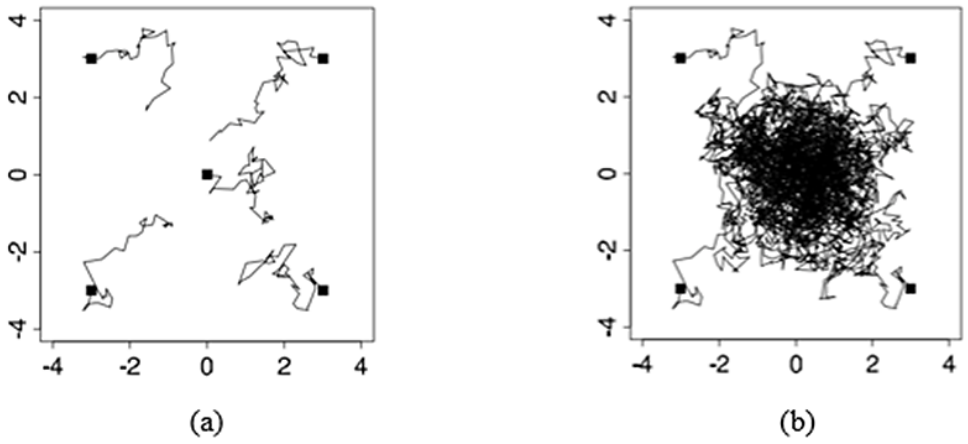

In this study, the Bayesian method was used to update the statistical data (mean, λ, and standard deviation, σ) of pile load test database in order to get the an updated information (i.e., posterior distribution) for the new tested site. The statewide observation data obtained from the pile load test database is expressed through a likelihood1 (likelihood function at level 1) function (logarithmic function). After deriving the prior and likelihood distribution for the level 1 using the Bayesian analysis, the posterior1 distribution (posterior function at level 1) that reflects the updated information (i.e., posterior knowledge) can be derived [80]. The posterior1 distribution data includes the combination of the prior information and the observation distribution (likelihood distribution) data. The posterior information generated in the preceding level of the Bayesian analysis can be considered as the prior information and utilized along with the extra site observation data to additionally update the information/data [81]. The Bayesian analysis deals with increasingly improving the existing information of the new project site conditions as the site observation data are gathered.

In level 2 of the Bayesian analysis, the posterior1 function obtained in the level 1 analysis can be taken as the prior2 knowledge or data. For example, data collected from pile load tests in the new site can be considered as the likelihood2 knowledge. After the prior2 and likelihood2 function are determined for the level 2 Bayesian analysis, posterior2 (updated knowledge) can be evaluated, which is associated with the prior knowledge/data and new observation data of the specific site.

The two levels of updating the mean bias (λ) and standard deviation of the bias values (σ) of data for any specific site are usually consist of three key elements, the prior

distribution, the likelihood function, and posterior distribution within the Bayesian framework. Figure 14 presents a flowchart of the Bayesian framework describing the two levels of updating the λ and σ for any new specific site. The distribution of posterior is proportional to the product of the prior and the likelihood, as will be described later in the Methodology section.

Figure 14. Bayesian framework for two levels of updating the mean bias (λ) and standard deviation of bias (σ) of data for any specific site

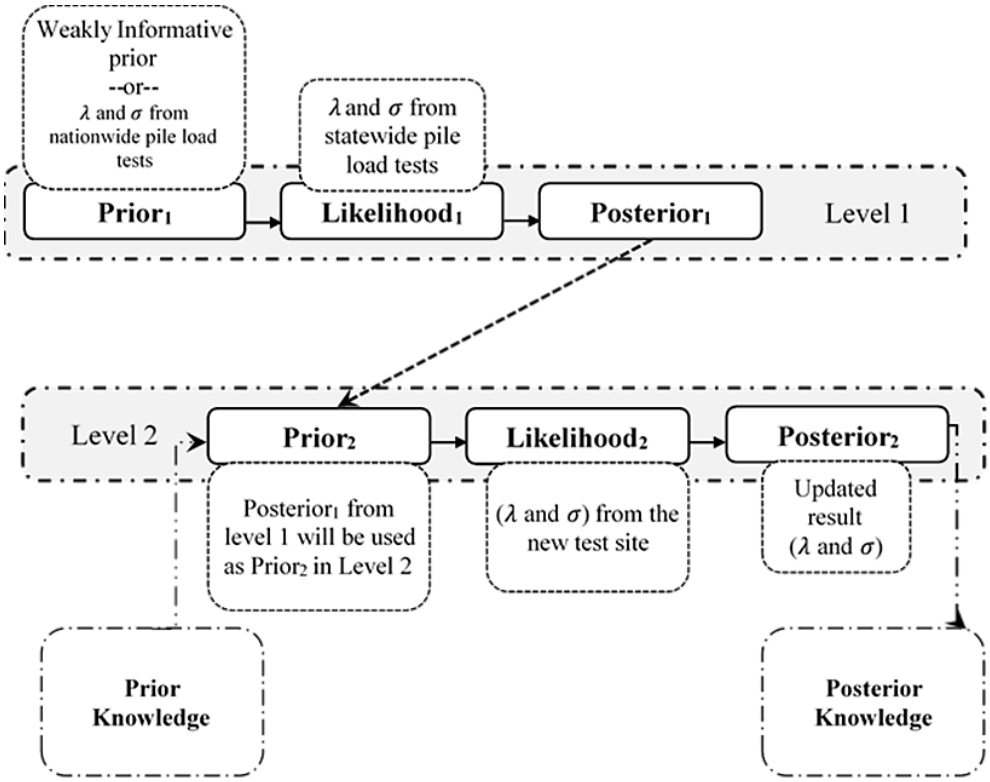

Probabilistic Analysis

Spatial interpolation techniques not only include simple mathematical or empirical methods such as inverse distance weighting and cubic spline interpolation but also include geostatistical methods. Whereas the former methods have limitations in processing all data in the target area owing to their irregular correlation, geostatistical-related techniques are effective for spatial interpolation across a wide area when considering the spatial tendency and influencing range of the raw data. The most

significant difference between them comes from considering or not considering the spatial variation (uncertainty) based on distance and direction.

Whereas the values of the inverse distance are weighed the same at a specific distance, those of an ordinary kriging, which is a representative method used in geostatistics, may vary even at the same distance [82]. The conventional two point based geostatistical methods adopt a variogram (semivariogram) or covariance to quantify the spatial variability. Accordingly, the prediction accuracy of a spatial interpolation is known to be equal to or higher than that of inverse distance weighing (e.g., [83], [84], [85]).

Since originating in the mining industry, geostatistics have been utilized in various fields such as meteorology, geology, and petroleum engineering (e.g., [82], [83], [84]). Recently, they have been used in geotechnical engineering and engineering geology for creating 3D geotechnical models of soil or rock properties (e.g., [85], [86], [87]) and for characterization of the subsurface strata (e.g., [88] , [89]). Recently, some studies have attempted to analyze geotechnical datasets with different characteristics using geo-statistics (e.g., [90]).

Kriging Method

It is believed that geostatistics have been derived from the research on the geology and mining done by Krige [91]. However, it was introduced before in the field of agronomy and meteorology [92]. Geostatistics includes various methods that use kriging formulas to estimate missing data.

Semivariance and Variogram: The first step in the kriging interpolation method is the computation of an experimental semivariogram. Generally, to examine the spatial distribution structure of the soil properties, the basic tool of semivariograms were used. The semivariance can be described by the following equation:

$$\gamma(h) = \frac{1}{2n}\sum_{i=1}^{n}(z(x_i) - z(x_i + h))^2 \quad [26]$$

where ‘n’ is the number of data points separated by distance ‘h,’ and γ(h) is the semivariogram (commonly referred to as variogram) [92].

The semivariogram has some important key properties (Figure 15). The first one is the ‘nugget.’ The nugget effect means when the variogram does not start from 0 and estimates the error caused by measurement and spatial variability. The ‘range’ is the distance value where ‘sill’ is reached. In general, if a nugget/sill ratio is less than 25%, it

indicates strong spatial dependency. When it is greater than 75%, it indicates weak spatial dependency; otherwise, the spatial dependency is called moderate [93]. The size of a search distance that will be used in the spatial interpolation methods is determined by the range [94].

Figure 15. Semivariogram terminology and properties [95]

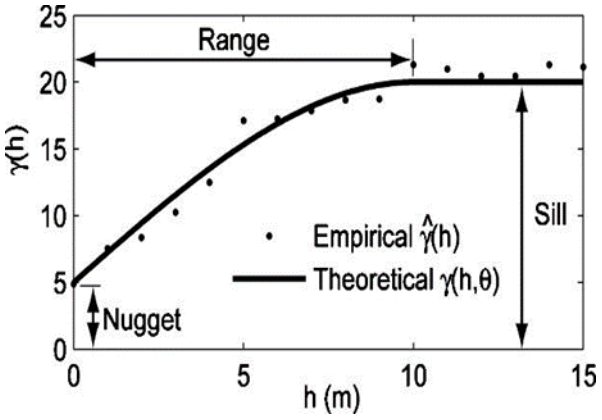

There are some simple variogram models, including: exponential, spherical, Gaussian, linear, and power model ([92], [94]). Generally, all types of spatial interpolation techniques can be represented as the weighted average of known data. They can be estimated from the general spatial interpolation equation, as follows:

$$Z(x_0) = \sum_{i=1}^{n} \lambda_i z(x_i) \quad [27]$$

where, 'Z' is the expected value at an unsampled location 'x_0,' 'z' is the measured value at sampled location 'x_i,' 'λ_i' is the kriging weight, and 'n' is the number of sampled points for the spatial interpolation [92]. However, all kind of kriging interpolation methods have a basic equation, which is slightly modified version of the above equation, as follows:

$$Z(x_0) - \mu = \sum_{i=1}^{n} \lambda_i [Z(x_i) - \mu(x_0)] \quad [28]$$

where, 'μ' is the stationary known mean, and '$\mu(x_0)$' is the mean of the sampled data. Step by step procedure of kriging interpolation methods were done by Clark and Harper [96].

To define the spatial continuity, the kriging approach uses the semivariogram, which is also used to measure the strength of statistical correlation as a function of distance.

The general formula of simple kriging (SK) depends on the above equation for its weight. After a slight modification, we can derive the following equation:

$$Z(x_0) = \sum_{i=1}^{n} \lambda_i Z(x_i) + [1 - \sum_{i=1}^{n} \lambda_i]\, \mu \quad [29]$$

Ordinary Kriging (OK): Statistical properties of sampled data can be incorporated using the ordinary kriging (OK) method, which is pretty similar to SK. The main difference is that OK considers the attribute value by replacing μ with a local mean $\mu(x_0)$ that is the mean of samples within the search window. The equation for ordinary kriging will then be given as follows:

$$Z(x_0) = \sum_{i=1}^{n} \lambda_i Z(x_i) + [1 - \sum_{i=1}^{n} \lambda_i]\, \mu(x_0) \quad [30]$$

For ordinary kriging, $[1 - \sum_{i=1}^{n} \lambda_i] = 0$, that is $\sum_{i=1}^{n} \lambda_i = 1$, which is achieved from equation 26. Therefore, ordinary kriging uses equations 26 and 30 to make the estimation and estimates local constant mean [96]. Figure 16 given by the Environmental Systems Research Institute (ESRI) [97] presents an example of one spatial dimension of ordinary kriging (where μ is an unknown constant).

Figure 16. Example of ordinary kriging with one spatial dimension [97]

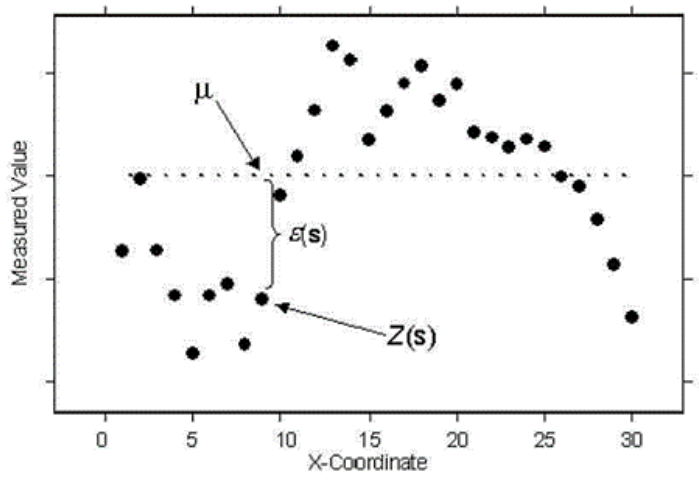

Conditional Simulations

A conditional simulation is a type of variable generation method used as an alternative to ordinary kriging, which has a smoothing effect. In addition to maintaining the distribution characteristics of dataset, it is possible to simulate its heterogeneity [98]. Uncertainty can also be assessed by generating the stochastic results multiple times [99]. As the principle of a conditional simulation, the prediction value of uninvestigated locations has a random function rather than a fixed value. Parametric or nonparametric methods are used to construct a random function. In this study, a three-dimensional interpolation of the

geotechnical property is performed using a sequential Gaussian simulation (SGS) as a parametric method and a sequential indicator simulation (SIS) as a non-parametric method.

In an SGS, the distribution of a point or grid to be simulated is assumed to have a normal distribution. Its mean and variance are the prediction value and error variance calculated through simple kriging, respectively. It is suitable for predicting the given dataset following a normal distribution. If the distribution of the experiment data is not normal, preprocessing such as a normal score or a log normal transform is required.

An SIS is a non-parametric method used to obtain the local cumulative distribution function of the predicted points or grids through indicator kriging, and can be applied to a dataset with any form of distribution [100]. It can be also employed even if the dataset has a highly skewed distribution or a large coefficient of variation without any specific preprocessing [101]. It uses the indicator variables instead of the given data to draw the local cumulative distribution function. The process of calculating the indicator variable is called the indicator transform, which is conducted using the indicator thresholds.

Sequential Gaussian simulation (SGS)

The values obtained by the kriging or cokriging system are predicted with minimized estimation variance and, therefore, show lower fluctuation than the actual, unknown values [102]. Hence, conditional simulation models are used to reproduce the actual statistics, maintain the texture of the variation, and take precedence over local accuracy. Unconditional simulation is simply the application of the general Monte Carlo technique whereby values are created with a particular covariance or semivariogram functions. However, in conditional simulation, in addition to creating possible values of random variables elsewhere, the generator must return the data values to known places.

The conditional simulation techniques can be categorized into indirect and direct approaches. Indirect approaches are based on unconditional simulation, which is transformed to the conditional ones [103]. These approaches are used when the mean and variance are known and constant over the region of interest. However, direct approaches, such as SGS, are used when the mean and variance are unknown or variable. In this study, it was assumed that the mean does not stabilize and the variance always increases over increasingly large domains, which opened up a wider field of application. Hence, the SGS method was implemented to perform conditional simulations.

The sequential Gaussian simulation is a straightforward algorithm for generating a realization of a multivariate Gaussian field. In this technique, each variable is simulated sequentially according to its normal conditional cumulative distribution function (CCDF) through a kriging or cokriging estimation system. The basic conditional sequential simulation steps are mentioned as follows [104]:

1. Define a random path which meets all nodes of the grid in each realization,
2. Define a search ellipsoid for each grid node to find the adjacent known data,
3. Use kriging/cokriging with a semivariogram model to determine the mean and variance of CCDF,
4. Draw a value from the CCDF of the random variable,
5. Add this new value to the initial conditioning dataset, and
6. Repeat until all nodes are simulated.

As is discussed by Dowd, the SGS method has several advantages including automatic handling of anisotropies, data conditioning, and fast computer implementation since an efficient kriging/cokriging algorithm with a moving neighborhood search capability is all that is required [105].

Variograms of transformed data are calculated and modeled. It is necessary to define a grid for simulation and a random path to asses' grids nodes. According to the kriging mean and variance, a Gaussian probability distribution is determined in each node. For estimating at each node it's necessary to choose a random path. A random value, which is drawn from Gaussian probability distribution, is known as a simulated value in each node. The basic steps in SGS algorithm are shown in Figure 17 [106].

Figure 17. The basic steps of SGS algorithm [106]

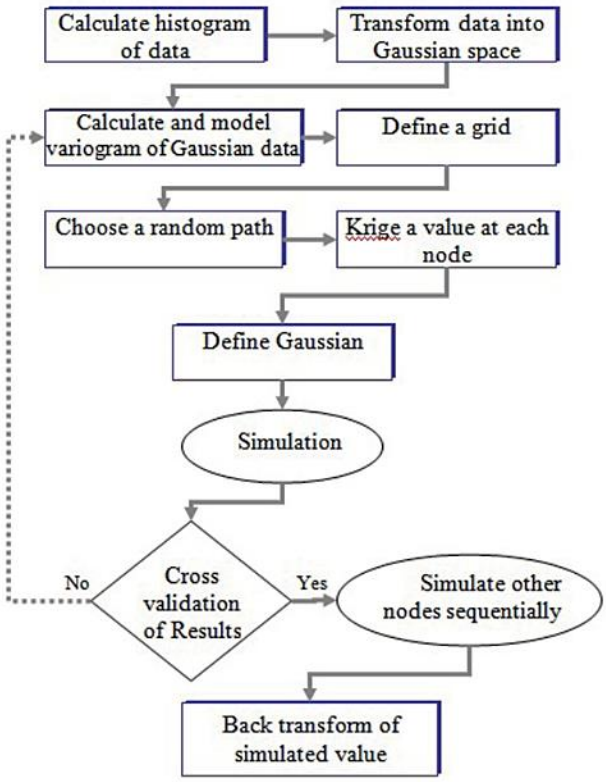

In many applications, the major objective has been to obtain the "best" estimate of the variable studied. To achieve this objective, estimation methods have progressed from geometric triangulation and polygonal approaches to a variety of kriging algorithms. All of these estimation approaches produce a map of locally averaged values and in the case of kriging, a map of the estimation variance at each estimated location. The result models produced by these estimation methods have several limitations. These limitations include:

- The spatial variability and histogram of the estimates is "smoothed" compared to that known from sample data,
- The assessment of uncertainty (by means of the kriging variance) is strongly controlled by the sampling configuration without reference to the magnitude of the sample grades that inform the estimated value.
- It is very difficult to obtain a quantification of the uncertainty of a collection of blocks because the uncertainty in each block is not independent of the uncertainty in the adjoining block.

In contrast to the estimation methods, geostatistical simulation provides maps of the variable that honor the sample data values, reproduce the histogram, and reproduce the spatial variability of the variable of interest. In addition, simulation is a probabilistic procedure that results in many different realizations of the same attribute. Each realization honors sample values, geological interpretation, data statistics and spatial continuity.

Unlike estimation, where a best map can be generated under some definition of quality (for kriging it is the minimization of the mean square error), realizations are accepted or rejected based on their capacity to honor the data, geology, histogram, variogram, and any secondary information. Therefore, there is no single best realization, since they are all considered equally likely to occur. The set of equally probable realizations allows us to obtain a distribution of the possible grade at that location. Similar procedures exist for categories such as the geological unit. This distribution of outcomes is interpreted as the uncertainty in the variable. This allows to report an uncertainty value that is conditioned by the surrounding sample values and geological attributes. The set of simulated values on a point scale allows us to consider the uncertainty of a collection of related points or joint uncertainty. This means a change of support can be performed, and simulations at block support are obtained. The set of block support realizations represents the uncertainty of the variable at that support.

In summary, the conditional simulation provides a quantification of the uncertainty surrounding an estimate. These values may account for the support and information effects, hence allowing quantification of uncertainty in any response variable. Response variables that depend upon several input variables can be correctly assessed with simulation and their uncertainty, quantified. This is the case of the response in mine planning, in geometallurgical studies or in geotechnical classification. A complete introduction to SGS method is available in [106] and [107]. The procedure of SGS algorithm used in this study is described in Figure 18.

In general, the SGS algorithm relies on the multi-Gaussian approach [106]. Therefore, prior to the application of SGS algorithm, the observations were checked by the Kolmogorov-Smirnov (K-S) test to verify whether they were normally distributed. After treating the outliers ([108], [109]) and creating a lognormal transformation, a lognormal distribution was obtained for the given soil layer. The semivariogram for the given soil layer were then calculated with the transformed data. After 100 realizations in different numbers of random seeds, the resulting data were back transformed into the original scale (e.g., [110], [111]).

Figure 18. Steps of SGS, based on Goovaerts [107]

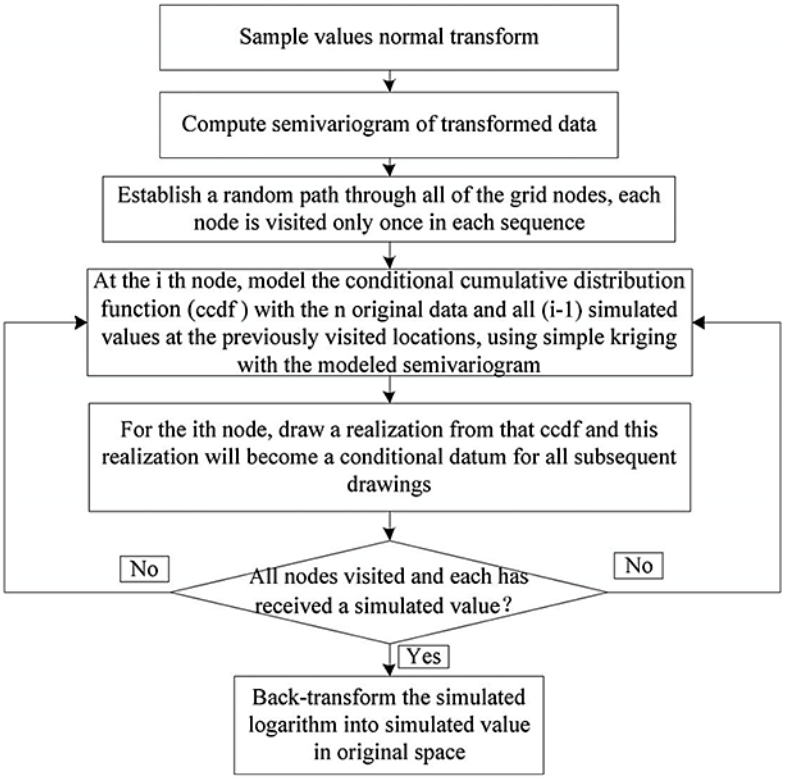

Application of Site Variability in Geotechnical Analysis

Application of Site Variability in Slope Stability Analysis

Slope stability analysis is a highly challenging task in geotechnical engineering as the influence of uncertainty involved in geotechnical properties on failure behavior of slopes is inevitable. Traditional slope stability methods, such as limit equilibrium method (LEM), ordinary method of slices, Bishop's simplified method, Janbu's simplified method and Spencer method, have been used for slope stability analysis. The traditional deterministic slope stability approaches that are based on a single factor of safety (FS) cannot explicitly encounter the uncertainties involved in geotechnical properties and failure mechanism, leading to erroneous results of slope stability. Hence, slope stability practice is highly persuadable to probabilistic treatment, which allows quantification of the uncertainty and rationally integrating the same into the analysis. Many researchers studied the effect of spatial variation of the soil properties on the probabilistic slope analysis (e.g., [19], [112], [113], [114]). A more advanced approach of probabilistic

analysis in geotechnical engineering for incorporating spatial variability of soil, referred as the ‘random finite element method’ (RFEM) (e.g., [112]), was developed in 1990s. The RFEM is a completely different approach for evaluating failure probability. In RFEM, the soil properties are considered random variables at any location within the soil domain. A typical two-dimensional random field with low and high correlation lengths is shown in Figure 19.

The random limit equilibrium method (RLEM), a random field that was first generated using the local average subdivision (LAS) method developed by Fenton and Vanmarcke [23] and then mapped into a grid of elements (mesh). Each mesh element in the random field has different values of soil properties, and cells close to one another have values that are closer in magnitude, based spatial correlation length. In each realization, a search is carried out to find the mesh elements intersected by the slip surface. The random soil property values are assigned to the slices whose base mid-point falls within that element. A limit equilibrium approach is then used to calculate factor of safety (FS) for each trial (simulation). The probability of failure is calculated as the ratio of the number of simulations resulting in FS < 1 to the total number of simulations.

Figure 19. Typical 2D random filed for slope with a) Small correlation length, and b) high correlation length [20]

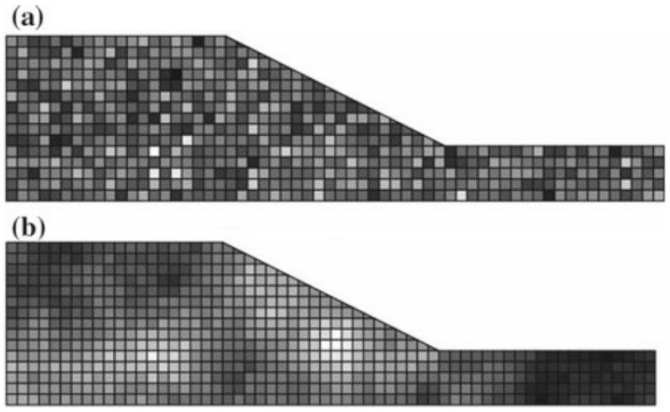

The spatial variability analysis using the random variable approach has been implemented in many geotechnical software such as GeoStudio, Soil Vision, and Rocscience Slide 2018. In this study, the Rocscience Slide 2018 software was used to evaluate the effect of site variability in slope stability analysis. The spatial variability analysis is a sub-option of the probabilistic analysis in Slide software, which allows the user to simulate the variability of soil properties, such as strength and unit weight, with location within the soil mass. A traditional probabilistic slope stability analysis does not

account for this type of variability. In a traditional probabilistic analysis, a statistical distribution is defined for a parameter (e.g., cohesion c, friction angle, ϕ), and for each simulation, the entire soil mass is assigned a single random value as shown in Figure 20a. With the spatial variability analysis, a statistical distribution will be defined for each parameter (e.g., c, ϕ). Correlation length between the parameters are defined in both x and y direction, and for each simulation, a random field of values is generated for soil mass as shown in Figure 20b. During the slope stability analysis, any slip surface that passes through the spatially variable material, will encounter variability of properties along the slip surface.

Since most of the geotechnical design parameters (e.g., c, ϕ, and unit weight) have certain degree of spatial variability, the slope stability analysis that incorporates the spatial variability is considered more realistic to define the factor of safety and probability of failure. The use of spatially variable analysis has been shown to affect the calculated probability of failure of slopes. For example, slope stability models that account for spatial variability of soil properties (e.g. c and unit weight) results in a lower probability of failure, as compared to the same analysis without including spatial variability [115]. A probabilistic analysis that does not consider spatial variability has been shown to result in unrealistic and overly conservative probabilities of failure [115].

Figure 20. (a) Single random sample value (cohesion) applied to entire soil region, (b) Random field of spatially variable cohesion

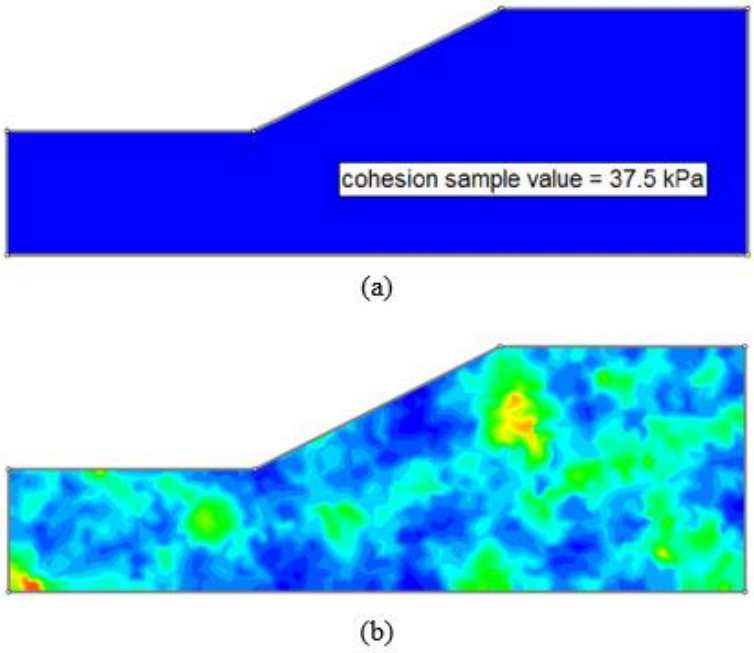

The conventional slope stability methods frequently fail to predict the progressive failure phenomenon. The finite element method (FEM) was proposed to solve this constraint, and two major applications for analyzing slope stability were created. The first application involves applying the soil's body force to the slope system in order to perform an elasto-plastic stress analysis. The stresses and the Mohr–Coulomb criterion can then be used to calculate the local safety factors (FS) after the stresses have been determined. The overall FS can also be defined using the actual driving force and the ultimate shear force. It's worth noting that the FS and critical failure surface position from FEM analysis are frequently close to those from a limit equilibrium analysis [116]. A number of scholars have used the FEM, including Shamekhi and Tannant [117], who used it to analyze slope stability, and Lu et al. [118], who used a numerical method based on the FEM to evaluate slope stability during seismic loading.

The primary aim for developing probabilistic techniques for slope stability analysis is to recognize the variations in soil properties. Although a sensitivity analysis can be used to determine these variables, it cannot estimate the likelihood of a slope failure. The chance or likelihood of a slope failure is computed using the stochastic character of the input components, which is based on the fundamental notions of a probabilistic technique.

When the chances of failure are greater than the safety considered, a slope collapse is more likely. This is a more realistic approach than categorizing a FS as stable or unstable. A quantitative explanation of the failure probability can also be used in a risk or decision analysis. Different researchers have used the probabilistic approaches for slope stability analysis. Shou and Wang [119] analyzed the Chiufengershan landslide's failure and proposed a Monte Carlo analysis to look into the residual slope. The probability analysis suggested that the residual slope was more important than the static slope analysis. Leynaud and Sultan [120] proposed a probabilistic approach to account for complicated geometry using a modified version of 3D slope stability software. Stankovic et al. [121] employed Monte Carlo simulation and the first order reliability method enforced with the response surface method at an open pit mine "Potrlica" in Pljevlja, Monte Negro, to conduct a probabilistic analysis of slope stability. Griffiths and Fenton [19] investigated the probability of failure of a clayey slope using several probabilistic analysis methods.

Application of Site Variability in Shallow Foundation

Many researchers investigated the effect of site variability on the bearing capacity of the sallow foundations (e.g., [17], [122]). Fenton and Griffiths [17] modeled shallow foundation loaded over soils using random field theory and elasto-plastic finite element to investigate the effect of site variability, and the cross correlation length on the bearing capacity of shallow foundations.

In the load and resistance factor design (LRFD) for shallow foundations, the design resistance factor can be affected by many factors including the distance between the sampling borehole and the foundation, the correlation length, the probability of failure, and the variation of soil parameters (e.g., cohesion c, and internal friction angle ϕ). The soil parameters can be interpreted from the in-situ field tests such as cone penetration tests (CPT), standard penetration (SPT) tests, or from the laboratory tests. The variation in the soil parameters depends on the inherited variability due to the original soil formation, the operator and machine error, and the model bias. The effect of the variation on soil parameters on the bearing capacity of shallow foundation was studied in detail by Fenton et al. [123]. Both the variations in ϕ and c were included in the analysis to define the resistance factor for shallow foundations. The statistical relationship between the two soil properties (c and ϕ) is referred as cross-correlation.

Bearing Capacity of Shallow Foundation

Terzaghi [124] provide a complete approach for determining the ultimate bearing capacity of shallow foundations. He proposed that the surface (failure) in soil at ultimate load for a continuous, or strip, foundation be considered to be comparable to that shown in Figure 21.The ultimate bearing capacity, q_u, of shallow foundations can be estimated using the following relationship [124]:

$$q_u = cN_c + qN_q + \frac{1}{2}\gamma BN_\gamma \qquad [31]$$

where, c is the cohesion, q is the overburden stress, γ is the unit soil weight, B is the footing width, and N_c, N_q, and N_γ are the bearing capacity factors. Tarzaghi [124] used an approximation method to determine q_u; that is when γ=0 (i.e., weightless soil) and q=0, then q_u = c.Nc, which will be used in this study for the analysis.

Figure 21. Tarzaghi bearing capacity analysis [124]

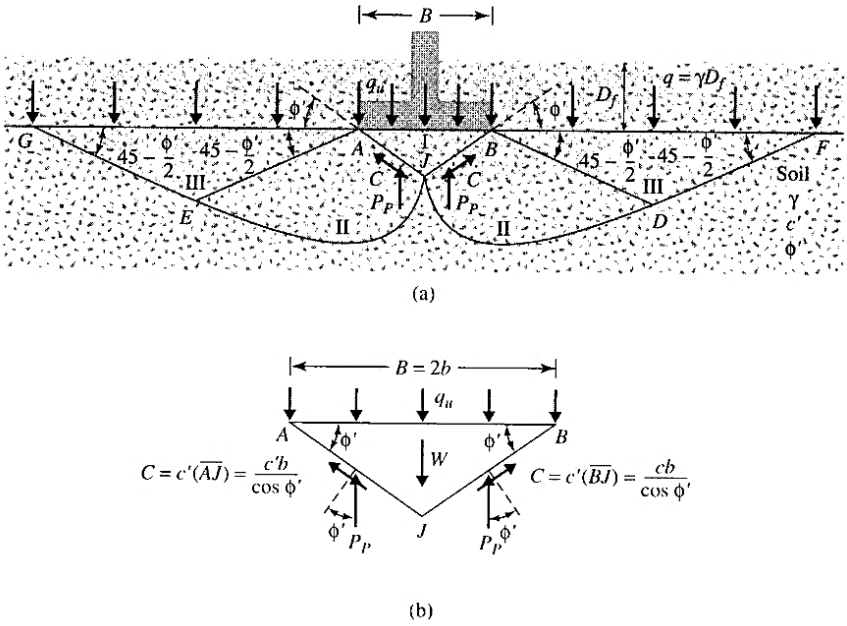

Incorporating site variability into shallow foundation resistance factor

The bearing capacity of shallow foundation depends on the soil properties, foundation dimensions and depth. Due to spatial variation in soil properties the failure surface under the footing will follow the weakest path through the soil, constrained by the stress field.

The resistance factor based on the soil properties is:

$$\Phi_{sf}\hat{R}_u \geq \mathrm{I}\sum_i \alpha_i \widehat{L_\iota} \quad [32]$$

where, $\hat{R}_u$= Resistance of the soil, Φ_{sf}= Geotechnical resistance factor for shallow foundation, and 'sf' = shallow foundation, I = importance factor, α_i = load factor, and $\widehat{L_\iota}$ = characteristic load. The soil properties used to calculate the resistance, $\hat{R}$ are:

$$\hat{c} = \prod_{i=1}^{m} c_i^o = \exp\left(\frac{1}{m}\sum_{i=1}^{m} \ln c_i^o\right) \quad [33]$$

$$\widehat{\Phi} = \left(\frac{1}{m}\sum_{i=1}^{m} \Phi_i^o\right) \quad [34]$$

For cohesion, the geometric average is used because of its lognormal distribution. The friction angle is computed as an arithmetic average. To determine the characteristic

ultimate geotechnical resistance, $\hat{R}_u$, it will first be assumed that the soil is weightless. This simplifies the calculation of the ultimate bearing capacity, q_u, to:

$$q_u = cN_c \quad [35]$$

The assumption of weightlessness is conservative since the soil weight contributes to the overall bearing capacity. This assumption also allows the analysis to explicitly focus on the role of cN_c on ultimate bearing capacity, since this is the only term that includes the effects of spatial variability relating to both shear strength parameters c and ϕ.

Most of the bearing capacities theories assume that the failure slip surface takes on a logarithmic spiral shape:

$$N_c = \frac{e^{\pi tan\phi}\, tan^2\left(\frac{\pi}{4}+\frac{\phi}{2}\right)-1}{\tan\phi} \quad [36]$$

The ultimate geotechnical resistance $\hat{R}_u$ as function in bearing capacity, $\hat{q}_u$ and foundation width, B, becomes as following:

$$\hat{R}_u = B\hat{q}_u \quad [37]$$

$$\hat{q}_u = \hat{c}\hat{N}_c \quad [38]$$

The characteristic of $\hat{N}_c$ factor is determined using the characteristic friction angle. For strip footing the LRFD equation as following:

$$\phi_{sf} B\hat{q}_u = I\left[\alpha_L \hat{L}_L + \alpha_D \hat{L}_D\right] \quad [39]$$

The width of the footing could be calculated as:

$$B = \frac{I[\alpha_L \hat{L}_L + \alpha_D \hat{L}_D]}{\phi_{sf}\hat{q}_u} \quad [40]$$

The random soil model

The cohesion, c, is assumed to be lognormally distributed with mean, μ_c, standard deviation, σ_c, and some spatial correlation structure, $\theta_{\ln c}$. The lognormal distribution is selected because it is commonly used to represent nonnegative soil properties and has a simple relationship with the normal. The lognormally distributed random field can be

obtained from a normally distributed random field, $G_{\ln c}(\underset{\sim}{x})$, having zero mean, unit variance, and spatial correlation length, $\theta_{\ln c}$, through the transformation

$$c(\underset{\sim}{x}) = \exp[\mu_{lnc} + \sigma_{lnc} G_{\ln c}(\underset{\sim}{x})] \qquad [41]$$

where, $(\underset{\sim}{x})$ is the spatial position at which c is desired, the mean and variance of ln*c* are obtained from the specified mean, and variance of cohesion using the transformations are $\mu_{lnc} = \ln(\mu_c) - \frac{1}{2}\sigma_{lnc}^2$ and $\sigma_{lnc}^2 = \ln(1 + v_c^2)$, respectively; where $v_c = \sigma_c/\mu_c$ is the coefficient of variation of the cohesion.

The correlation coefficient between the log cohesion at some point $\underset{\sim}{x}_1$ and a second point $\underset{\sim}{x}_2$, is specified by a correlation function, ρ. In this study, a simple exponentially decaying (Markovian) correlation function will be assumed, having the form:

$$\rho(t) = \exp\{-\frac{2|t|}{\theta}\} \qquad [42]$$

where, t = $\underset{\sim}{x}_1 - \underset{\sim}{x}_2$ is the distance between the two points.

It should be noted that the correlation function selected above acts between values of ln*c* because ln*c* is normally distributed, and a normally distributed random field is simply defined by its mean and covariance structure. In practice, the correlation length, $\theta_{\ln c}$, can be estimated by evaluating the spatial statistics of the log cohesion data directly [125].

The spatial correlation function, ρ(t), has a corresponding variance reduction factor, $\gamma_{lnc}(D)$, which specifies how the variance is reduced upon local averaging of ln*c* over some domain D. In the two-dimensional analysis considered here, $D = D_1 \times D_2$ is the area. The two-dimensional variance reduction factor is defined as:

$$\gamma_{\ln c}(D_1, D_2) = \frac{4}{(D_1 D_2)^2} \int_0^{D_1} \int_0^{D_2} (D_1 - t_1)(D_2 - t_2)\rho(t_1, t_2) dt_1 dt_2 \qquad [43]$$

which can be evaluated using Gaussian quadrature (see [17] and [126], for more details).

The soil friction angle, ϕ, is assumed to be lognormally distributed with mean, μ_ϕ, standard deviation, σ_ϕ, and some spatial correlation structure. The lognormal distribution is selected because it is commonly used to represent nonnegative soil properties and has a simple relationship with the normal; a lognormally distributed random field can be obtained from a normally distributed random field having zero mean, unit variance.

It seems reasonable to assume that if the spatial correlation structure of a soil is caused by changes in the constitutive nature of the soil over space, then both cohesion and friction angle would have similar correlation lengths. Since both fields have the same correlation function, $\rho(t)$. They will also have the same variance reduction function, i.e., $\gamma_{lnc}(D) = \gamma_{\phi}(D) = \gamma(D)$. A detailed description on the random soil model was given by Fenton et al. [123].

Analytical solution of the probability of failure

In this section, an analytical approximation to the probability of bearing capacity failure of a strip footing is summarized. Equation 38 was developed assuming an ideal soil whose shear strength is the same everywhere (i.e. a uniform soil). When soil properties are spatially variable, as they are in reality, then the hypothesis made in this study is that Equation 31 can be replaced by the following equation:

$$q_u = \bar{c}\bar{N}_c \qquad [44]$$

Where, $\bar{c}$ and $\bar{N}_c$ are the equivalent cohesion and equivalent N_c factor, defined as those uniform soil parameters which lead to the same bearing capacity as observed in the real, spatially varying soil. In other words, it is proposed that equivalent soil properties, $\bar{c}$ and $\bar{N}_c$, exist such that a uniform soil having these properties will have the same bearing capacity as the actual spatially variable soil. The value of $\bar{N}$ is obtained by using the equivalent friction angle, $\bar{\phi}$, in Equation 34,

$$\bar{N}_c = \frac{e^{\pi tan\bar{\Phi}}\, tan^2\left(\frac{\pi}{4}+\frac{\bar{\Phi}}{2}\right)-1}{\tan\bar{\Phi}} \qquad [45]$$

then the width of footing become

$$\mathrm{B} = \frac{\mathrm{I}[\alpha_L\hat{L}_L+\alpha_D\hat{L}_D]}{\Phi_{sf}\bar{c}\bar{N}_c} \qquad [46]$$

If the load L exceed the resistance load, q_u B, bearing failure will happen. The probability of failure could be calculated as:

$$p_f = P[L > q_u B] = P[L > \bar{c}\bar{N}_c B] \qquad [47]$$

The probability of failure should be less than the acceptable failure probability p_m. The probability of failure can be calculated as:

$$p_f = P\left[L\frac{\hat{c}\widehat{N}_c}{\bar{c}\bar{N}_c} > \left(\frac{I[\alpha_L\hat{L}_L+\alpha_D\hat{L}_D]}{\varphi_{sf}}\right)\right] \quad [48]$$

Letting

$$Y = L\frac{\hat{c}\widehat{N}_c}{\bar{c}\,\bar{N}\mathrm{c}} \quad [49]$$

means that

$$p_f = P\left[Y > \left(\frac{I[\alpha_L\hat{L}_L+\alpha_D\hat{L}_D]}{\varphi_{sf}}\right)\right] \quad [50]$$

and the task is to find the distribution of Y. Assuming that Y is lognormally distributed (an assumption found to be reasonable by Fenton et al. [127], and which is also supported to some extent by the central limit theorem), then:

$$lnY = lnL + ln\widehat{N}_c + ln\hat{c} - ln\overline{N}_c - ln\bar{c} \quad [51]$$

The mean of lnY is:

$$\mu_{lnY} = \mu_{lnL} + \mu_{ln\widehat{N}_c} + \mu_{ln\hat{c}} - \mu_{ln\overline{N}_c} - \mu_{ln\bar{c}} \quad [52]$$

The variance of lnY is:

$$\sigma^2_{lnY} = \sigma^2_{lnL} + \sigma^2_{ln\widehat{N}_c} + \sigma^2_{ln\hat{c}} + \sigma^2_{ln\overline{N}_c} + \sigma^2_{ln\bar{c}} - 2Cov(ln\bar{c}, ln\hat{c}) - 2Cov(ln\overline{N}_c, ln\widehat{N}_c) \quad [53]$$

where the load, L, and soil properties, c and ϕ have been assumed mutually independent.

To find the parameters in the mean and variance of lnY equations, the following two assumptions are made;

(1) The equivalent cohesion $\bar{c}$, is the geometric average of cohesion field over the influence zone D under the footing.

$$\bar{c} = \exp\left\{\frac{1}{D}\int_0^D \ln c\left(\underset{\sim}{x}\right) d\,\underset{\sim}{x}\right\} \quad [54]$$

(2) The equivalent friction angle, $\overline{\Phi}$, is the arithmetic average of the friction angle over the zone of influence, D,

$$\overline{\Phi} = \frac{1}{D}\int_0^D \Phi(\underset{\sim}{x})d\,\underset{\sim}{x} \quad [55]$$

Probably the greatest source of uncertainty in this analysis involves the choice of the domain, D, over which the equivalent soil properties are averaged under the footing. The averaging domain was found by trial andanalysis solution of error to be best approximated by $D = W \times W$, centered directly under the footing (see Figure 22). In this study, W is the influence depth taken as 80% of the average mean depth of the wedge zone directly beneath the footing, as given by the classical Prandtl failure mechanism,

$$W = \frac{0.8}{2}\widehat{\mu_B}\tan\left(\frac{\pi}{4} + \frac{\mu_\phi}{2}\right) \quad [56]$$

The friction angle in radians. The estimated footing width is μ_B

$$\widehat{\mu_B} = \frac{\mathrm{I}(\alpha_L\ \widehat{L_L} + \alpha_D\ \widehat{L_D})}{\phi_{sf}\mu_c\,\mu_{N_c}} \quad [57]$$

The footing shown on Figure 22 is just one possible realization since the footing width, B, is actually a random variable. Fenton and Griffiths [17] study assumed that the footing width was known, rather than designed, and recognized that the larger averaging region did not well represent the mean bearing capacity, which of course is the most important value in probability calculations. In the simulations performed to validate the theory presented here, the soil depth is taken to be H = 4.8 m and Δx = 0.15 m, where Δx is the width of the columns of finite elements used in the simulations (see Figure 22).

To first order, the mean of N_c is:

$$\mu_{N_c} = \frac{e^{\pi tan\mu_\phi}\ tan^2\left(\frac{\pi}{4} + \frac{\mu_\phi}{2}\right) - 1}{\tan\mu_\phi} \quad [58]$$

Using the above information and assumptions, the components of mean and variance of lnY equations can be computed as follows (given the basic statistical parameters of the loads, c, ϕ, number and locations of the soil samples, and the averaging domain size D);

(1) Assuming that the total load L is equal to the sum of the maximum live load, L_{Le}, acting over the lifetime of the structure and the static dead load, L_D (i.e. $L = L_{Le} + L_D$), both of which are random, then the specified mean and variance of total load using the transformations are $\mu_{ln\mathrm{L}} = \ln(\mu_\mathrm{L}) - \frac{1}{2}ln\,(1 + v_\mathrm{L}^2)$ and $\sigma_{ln\mathrm{L}}^2 = \ln(1 + v_\mathrm{L}^2)$, respectively. where $v_\mathrm{L} = \sigma_\mathrm{L}/\mu_\mathrm{L}$, is the coefficient of variation of total load.

(2) Calculating the mean and variance of $ln\hat{c}$:

$$\mu_{ln\hat{c}} = \mu_{lnc} \quad [59]$$

Figure 22. Typical sketch used to determine the shallow foundation bearing capacity failure

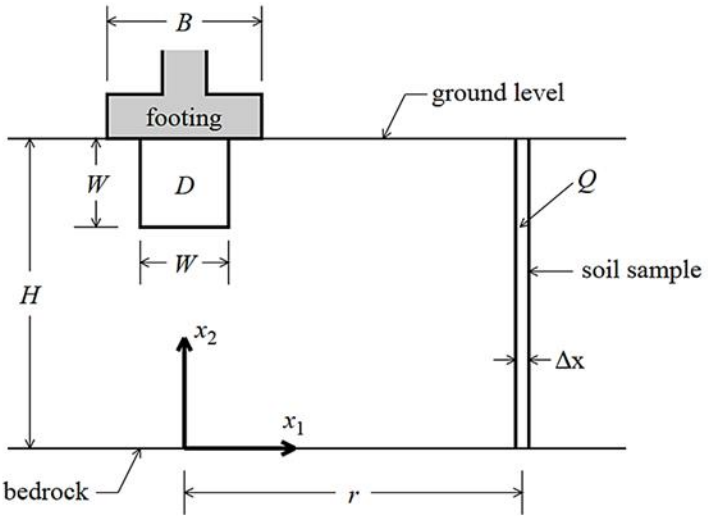

Assuming that $ln\hat{c}$ actually represents a local average of ln c over a domain of size Δx × H; where Δx is the horizontal dimension of the soil sample, which can be thought of as the horizontal zone of influence of a CPT or SPT sounding; and H is the depth over which the samples are taken, then $\sigma^2_{ln\hat{c}}$ is probably more accurately computed as:

$$\sigma^2_{ln\hat{c}} = \frac{\sigma^2_{lnc}}{m^2}\sum_{i=1}^{m}\sum_{j=1}^{m}\rho(\underset{\sim}{x}_i^0 - \underset{\sim}{x}_j^0) = \sigma^2_{lnc}\gamma(\Delta x, H) \quad [60]$$

(3) Calculating the mean and variance of $ln\bar{c}$:

$$\mu_{ln\bar{c}} = \mu_{lnc} \quad [61a]$$

$$\sigma^2_{ln\bar{c}} = \sigma^2_{lnc}\gamma(D) \quad [61b]$$

where γ(D) = γ(W, W), as discussed above.

(4) Calculating the mean and variance of $ln\widehat{N}_c$:

$$\mu_{ln\widehat{N}_c} = \mu_{lnN_c} = ln\frac{e^{л tan\mu_\Phi}\, tan^2\left(\frac{л}{4}+\frac{\mu_\Phi}{2}\right)-1}{\tan\mu_\Phi} \quad [62a]$$

$$\sigma^2_{ln\widehat{N}_c} = \sigma^2_{\widehat{\Phi}}\left[\frac{bd}{bd^2-1}[л(1+a^2)d+1+d^2\,] - \frac{1+a^2}{a}\right]^2 \quad [62b]$$

where, $a = \tan(\mu_\Phi)$, b = $e^{л a}$, $d = \tan(\frac{л}{4}+\frac{\mu_\Phi}{2})$. The variance of $\widehat{\Phi}$ can be obtained by

$$\sigma_{\bar{\Phi}}^2 = \frac{\sigma_{\Phi}^2}{m^2}\sum_{i=1}^{m}\sum_{j=1}^{m}\rho(\underset{\sim}{x}_i^0 - \underset{\sim}{x}_j^0) = \sigma_{\Phi}^2\gamma(\Delta x, H) \quad [62c]$$

(5) Calculating the mean and variance of $ln\bar{N}_c$:

$$\mu_{ln\bar{N}_c} = \mu_{ln\hat{N}_c} = \mu_{lnN_c} \quad [63a]$$

$$\sigma_{ln\bar{N}_c}^2 = \sigma_{\bar{\Phi}}^2\left[\frac{bd}{bd^2-1}[л(1+a^2)d + 1 + d^2\ ] - \frac{1+a^2}{a}\right]^2 \quad [63b]$$

where, $a = \tan(\mu_{\Phi})$, $\mathrm{b} = e^{лa}$, $d = \tan(\frac{л}{4} + \frac{\mu_{\Phi}}{2})$. The variance of $\hat{\Phi}$ can be obtained by

$$\sigma_{\bar{\Phi}}^2 = \sigma_{\Phi}^2\gamma(W, W) \quad [63c]$$

(6) The covariance between the observed cohesion values and the equivalent cohesion beneath the footing is obtained as follows for $D = W \times W$ and $Q = \Delta x \times H$;

$$Cov(ln\bar{c}, ln\hat{c}) = \frac{\sigma_{lnc}^2}{D^2Q^2}\int_0^D\int_0^Q \rho(\underset{\sim}{x}_1 - \underset{\sim}{x}_2)\, d\,\underset{\sim}{x}_1\, d\,\underset{\sim}{x}_2 = \sigma_{lnc}^2\gamma_{DQ} \quad [64]$$

where γ_{DQ} is the average correlation coefficient between the two areas D and Q [123]. The area D denotes the averaging region below the footing over which equivalent properties are defined and the area Q denotes the region over which soil samples are gathered. These areas are illustrated in Figure 22.

(7) Calculating the $Cov\ (ln\bar{N}_c, ln\hat{N}_c)$

$$Cov\left(ln\bar{N}_c, ln\hat{N}_c\right) = \sigma_{lnN_c}^2\gamma_{DQ} \quad [65]$$

Substituting these results into mean and variance equation of lnY gives

$$\mu_{lnY} = \mu_{lnL} \quad [66a]$$

$$\sigma_{lnY}^2 = \sigma_{lnL}^2 + \left[\sigma_{lnc}^2 + \sigma_{lnN_c}^2\right]\left[\gamma(\Delta x, H) + \gamma(W, W) - 2\gamma_{DQ}\right] \quad [66b]$$

Letting

$$\mathrm{q} = \mathrm{I}\left[\alpha_L\hat{L}_L + \alpha_D\hat{L}_D\right] \quad [67]$$

Allows the probability of failure to be expressed as:

$$p_f = P\left[Y > \frac{q}{\Phi_{sf}}\right] = P\left[ln\,Y > ln\left(\frac{q}{\Phi_{sf}}\right)\right] = 1 - \Phi\left(\frac{ln\left(\frac{q}{\Phi_{sf}}\right) - \mu_{lnY}}{\sigma_{lnY}}\right) \quad [68]$$

where Φ is the standard normal cumulative distribution function. The resistance factor could be calculated as:

$$\Phi_{sf} = \frac{\mathrm{I}(\alpha_L\ \widehat{L_L} + \alpha_D\ \widehat{L_D})}{\exp(\mu_{\ln Y} + \sigma_{\ln Y}\beta)} \quad [69]$$

Incorporating variability into reliability analysis

The reliability index is used to offer a reliability-based study of a shallow foundation with a vertical load (central). The limit state function used in this research is g(x) = C – D; where, C is the foundation capacity and D is the demand. g(x)>0 represents safe condition while g(x)<0 represents unsafe condition. The Hasofer-Lind reliability index (β_{HL}) is widely used method, and the equation of this method is given as follows [128]:

$$\beta_{HL} = \min(\sqrt{(X-\mu)^T C^{-1}(X-\mu)}) \quad [70]$$

Where, the vector of random parameters (n) is denoted as X, μ is the mean values (in vector format) and their covariance matrix is denoted as C. Figure 23 shows the Hasofer-Lind reliability index and the corresponding design point.

Figure 23. Hasofer- Lind reliability index and the design point [129]

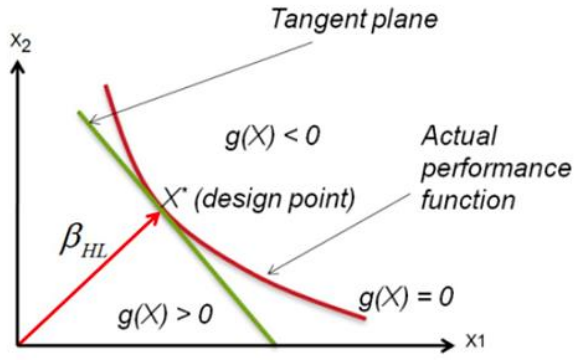

Application of Site Variability in Deep Foundation

A punching shear failure occurs when the force applied to the pile (deep foundation) surpasses the shear strength of the surrounding ground [130]. The pile is supported by the soil through friction, end bearing, and cohesion between the pile sides and the soil. Naghibi [131] and Naghibi and Fenton [18] proposed a methodology to implement site variability for deep foundations where only cohesive resistance was addressed, as it would be in a soil under the total stress condition (entirely cohesive), i.e., ignoring the end-bearing. They also applied similar analysis to examine the effective stress resistance of piles for cohesionless soil when the end bearing was ignored. The method proposed by Naghibi [125] and Naghibi and Fenton [18] will be described below for cohesive and cohesionless soils.

For Cohesive Soil Condition

The ultimate pile resistance due to soil cohesion (c) between the surrounding soil and the pile foundation surface is given by:

$$R_u = \int_0^H p\tau(z)dz \qquad [71]$$

where, p is the perimeter of the pile, τ(z) is the pile's ultimate shear stress (at depth z), and the length of the pile is H.

α-Tomlinson Method

Several approaches can be used to determine the ultimate shear stress occurring between the soil and the pile under total stress circumstances. The most widely method used for cohesive soils is the α-Tomlinson method. Total stress analysis is a critical component of the α method. For any specific soil with friction angle, ϕ = 0, based on the α method, the following equation can be used to represent the surface shear resistance (unit) in soils under the total stress conditions:

$$\tau(z) = \alpha c(z) \qquad [72]$$

where, c(z) is the cohesion of the soil (average) around the pile (at depth z), and α is the empirical adhesion factor, as suggested by the Federal Highway Administration (FHWA). Figure 24 shows the α factors for driven piles in clay according to FHWA.

Figure 24. α factors for driven piles in clay according to FHWA [132]

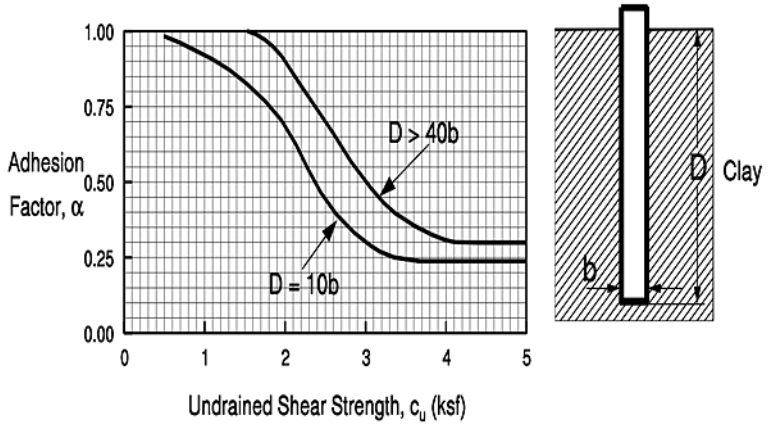

Substituting Equation 72 into Equation 71, the ultimate cohesive resistance becomes

$$R_u = \int_0^H p\alpha c(z)dz \qquad [73]$$

It is assumed in analysis that the type of the pile is chosen, so the perimeter (p) is known and the design entails determining H. The p seems to have no impact on the resistance factors (required), as will be proven later. Because these data are typically acquired through an investigation aimed at describing the site, the term characteristic is preferred in this study. Just the ultimate limit state is taken into account in this design, and the factored load must not exceed the factored resistance,

$$\Phi_{df}\hat{R}_u \geq \sum_i I_i\alpha_i\hat{F}_i \qquad [74]$$

where, ϕ_{df} is the ultimate geotechnical resistance factor for deep foundation, $\hat{R}_u$is the geotechnical resistance (ultimate) based on the nominal soil properties (characteristic), I_i is the importance factor, $\alpha_i\hat{F}_i$is the load factor.

In this study, the combination of dead load plus live load will be studied,

$$\hat{F} = \alpha_L\hat{F}_L + \alpha_D\hat{F}_D \qquad [75]$$

where $\hat{F}_L$ is the live load (characteristic), $\hat{F}_L$ is the dead load (characteristic), α_L and α_D are the live load factors and dead load factors, respectively, α_T is the total load factor (equivalent). The FHWA-specified load factors will be employed in this study (where α_L = 1.75 and α_D =1.25). However, the idea described here can simply be applied to different load combinations and circumstances.

In some circumstances, the means of the load (characteristic) values utilized in any design are defined, however, they can be defined more broadly as means as

$$\hat{F}_L = k_L \mu_L \quad [76a]$$

$$\hat{F}_D = k_D \mu_D \quad [76b]$$

where, μ_L is the means of the live load, μ_D is the means of the dead loads, k_L is the live load bias factors, and k_D is the dead load bias factors [133]. The values of k_L and k_D were estimated to be 1.41 and 1.18, respectively.

The soil cohesion (characteristic) $\hat{c}$, is the weighted average of the $\hat{c}_i$ (sampled observations),

$$\hat{c} = \frac{1}{m}\sum_{i=1}^{m} \hat{c}_i \quad [77]$$

The ultimate geotechnical resistance, $\hat{R}_u$, can be derived from the Equation 73 by assuming $\mathrm{c(z)} = \hat{c}$,

$$\hat{R}_u = pH\alpha\hat{c} \quad [78]$$

According to The Federal Highway Administration (FHWA) two reliability indexes, 2.33 and 3.0, were considered in this study.

Random soil model

In this study, we assumed cohesion of soil (c) is distributed lognormally with μ_c (mean), σ_c (standard deviation), and $\theta_{\ln c}$ (spatial correlation structure). Because it is often used to illustrate nonnegative soil attributes and has a relationship with the normal distribution, the lognormal distribution was chosen; Out of a normally distributed (random field) function [$G_{lnc}(z)$, with mean (=0), unit variance, and $\theta_{\ln c}$ (spatial correlation length)], a lognormally distributed (random field) function can be created, by following transformation:

$$c(z) = \exp[\mu_{lnc} + \sigma_{lnc} G_{lnc}(z)] \quad [79]$$

where,

$$\mu_{lnc} = \ln(\mu_c) - \frac{1}{2}\sigma_{lnc}^2 \quad [80a]$$

$$\sigma_{lnc}^2 = \ln(1 + v_c^2) \quad [80b]$$

The coefficient of variation of the cohesion, $v_c = \sigma_c/\mu_c$ and (z) is the spatial position. A Markovian correlation (simple exponentially decaying) function is assumed in this study, where, ρ is the correlation function, in the form of

$$\rho(t) = \exp\{-\frac{2|t|}{\theta}\} \quad [81]$$

where $t = z_1 - z_2$ is the inter point distance.

In the above equation, θ (spatial correlation length) is generally described as the separation distance between two lnc values that are significantly associated. The $\rho(t)$ (spatial correlation function) has a variance reduction function, γ(H), which is defined by:

$$\gamma(H) = \frac{1}{H^2}\int_0^H \int_0^H \rho(z_1 - z_2)dz_1 dz_2 \quad [82]$$

Both μ_c and α will cancel out of the probability (failure) prediction equations, as will be shown later, so their values are completely arbitrary and have no impact on the geotechnical resistance factor utilized in the design process.

Random load model

The dead loads (mostly static) and live loads (mostly dynamic) make up the load acting on a foundation. The dead load can be calculated, and therefore, the mean and the variance of dead loads are quite well understood. The live loads, on the other hand, are more challenging to probabilistically characterize. The total load, F will be:

$$F = F_L + F_D \quad [83]$$

The mean and the variance of the load, F, are given by:

$$\mu_F = \mu_L + \mu_D \quad [84a]$$

$$\sigma_F^2 = \sigma_L^2 + \sigma_D^2 \quad [84b]$$

The dead loads and the live loads are considered to be distributed lognormally. So, the total load is also distributed lognormally, which is also supported by Fenton et al. [123]. So,

$$\mu_{lnF} = \ln(\mu_F) - \frac{1}{2}\sigma_{lnF}^2 \quad [85a]$$

$$\sigma_{lnF}^2 = \ln(1 + \frac{\sigma_F^2}{\mu_F^2}) \quad [85b]$$

Theoretical approach to estimate probability of failure of cohesive soil

The soil is first represented as a spatially variable random field to assess the probability of a pile failure. In general, cohesion varies in all the three dimensions, however, considering the third dimension has minimal effect since piles are one dimensional, a 2D random field analysis is used, where the pile is positioned vertically about the soil samples, as the soil boring, CPT test or SPT sounding, are performed vertically in a distinct, perhaps different locations, as depicted in Figure 25. The following is a hypothetical estimate to the pile failure probability in soils at total stress circumstances. When soil parameters are spatially varied, as they are in practice, the value of R_u becomes:

$$R_u = pH\alpha\bar{c} \quad [86]$$

where $\bar{c}$ is the cohesion (equivalent). The average of the spatially variable cohesion ($\bar{c}$) across the pile length H is hypothesized given as:

$$\bar{c} = \frac{1}{H}\int_0^H c(z)dz \cong \frac{1}{n}\sum_{i=1}^n \bar{c}_i \quad [87]$$

Figure 25. Location of pile and soil sample

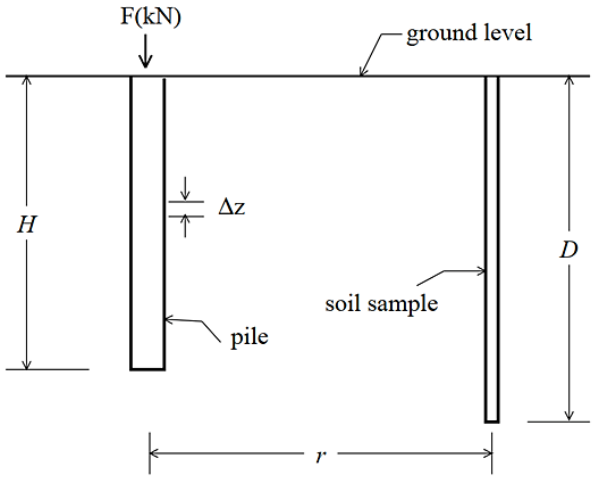

By replacing Equation 87 into Equation 74 yields the requisite design pile length, H as:

$$\phi_{df} pH\alpha\hat{c} = \alpha_L\hat{F}_L + \alpha_D\hat{F}_D \rightarrow H = \frac{\alpha_L\hat{F}_L + \alpha_D\hat{F}_D}{\phi_{df} p\alpha\hat{c}} \quad [88]$$

By further replacing Equation 88 into Equation 86, the ultimate resistance, R_u, can be estimated as:

$$R_u = \left(\frac{\alpha_L \hat{F}_L + \alpha_D \hat{F}_D}{\Phi_{df}}\right)\left(\frac{\bar{c}}{\hat{c}}\right) \quad [89]$$

The probability of failure, p_f, will be given as:

$$p_f = P[F > R_u] \quad [90]$$

and a successful design methodology will have $p_f \leq p_m$. Substituting Equation 89 into Equation 90 leads to

$$p_f = P\left[F > \left(\frac{\alpha_L \hat{F}_L + \alpha_D \hat{F}_D}{\Phi_{df}}\right)\left(\frac{\bar{c}}{\hat{c}}\right)\right] \quad [91]$$

$$= P\left[\frac{F\hat{c}}{\bar{c}} > \left(\frac{\alpha_L \hat{F}_L + \alpha_D \hat{F}_D}{\Phi_{df}}\right)\right]$$

It is noteworthy that the α (adhesion factor) and p (perimeter length) have both been cancelled out of the failure probability calculations. This indicates that these parameters have no effect on the resistance factors needed for this investigation. Rearranging the above equation leads to

$$p_f = P\left[\frac{F}{\alpha_L \hat{F}_L + \alpha_D \hat{F}_D} > \frac{1}{\Phi_{df}}\left(\frac{\bar{c}}{\hat{c}}\right)\right] \quad [92]$$

Returning to Equation 91 for p_f calculation, the next two components are defined as follows:

$$W = \frac{F\hat{c}}{\bar{c}} \quad [93a]$$

$$\hat{Q} = \alpha_L \hat{F}_L + \alpha_D \hat{F}_D \quad [93b]$$

So that Equation 92 can be written as:

$$p_f = P\left[W > \frac{\hat{Q}}{\Phi_{df}}\right] \quad [94]$$

W (distribution) must be determined in order to solve Equation 94. If all of the F (random load), and $\hat{c}$ and $\bar{c}$ (cohesion values) are considered to be lognormally distributed [123], W

will therefore be lognormally distributed as well, and its values can be found by looking at the individual F, $ln\hat{c}$, and $ln\bar{c}$ distributions. If W is distributed in a lognormal way,

$$lnW = lnF + ln\hat{c} - ln\bar{c} \quad [95]$$

p_f can be derived from the following:

$$p_f = P\left[W > \frac{\hat{Q}}{\Phi_{df}}\right] = P\left[lnW > \ln\left(\frac{\hat{Q}}{\Phi_{df}}\right)\right] = 1 - \Phi\left[\frac{\ln\left(\frac{\hat{Q}}{\Phi_{df}}\right) - \mu_{lnW}}{\sigma_{lnW}}\right] \quad [96]$$

where, Φ is the cumulative distribution function (standard normal).

To find p_f, we have to determine lnW's mean and the variance. lnW's mean and the variance as:

$$\mu_{lnW} = \mu_{lnF} + \mu_{ln\hat{c}} - \mu_{ln\bar{c}} \quad [97a]$$

$$\sigma^2_{lnW} = \sigma^2_{lnF} + \sigma^2_{ln\hat{c}} + \sigma^2_{ln\bar{c}} - 2Cov(ln\hat{c}, ln\bar{c}) \quad [97b]$$

The components of 97 were given by Naghibi [131]:

$$\mu_{ln\hat{c}} = E[ln\hat{c}] = E\left[ln\left(\frac{1}{m}\sum_{i=1}^{m}\hat{c}_i\right)\right] \cong \ln(\mu_c) \quad [98a]$$

$$\sigma^2_{ln\hat{c}} \cong \frac{\sigma^2_{lnc}}{m^2}\sum_{i=1}^{m}\sum_{j=1}^{m}\rho\left(z_i^0 - z_j^0\right) \quad [98b]$$

$$\sigma^2_{ln\hat{c}} = \sigma^2_{lnc}\gamma(D) \quad [98c]$$

where, $\gamma(D)$ is the variance reduction function, given by Equation 82.

$$\mu_{ln\bar{c}} = E\left[ln\left(\frac{1}{H}\int_0^H c(z)dz\right)\right] \cong \ln(\mu_c) \quad [99a]$$

$$\sigma^2_{ln\bar{c}} = \sigma^2_{lnc}\gamma(H) \quad [99b]$$

where, $\gamma(H)$ is defined by Equation 82.

$$Cov(ln\hat{c}, ln\bar{c}) \cong \frac{\sigma^2_{lnc}}{mH}\sum_{i=1}^{m}\int_0^H \rho\left[\sqrt{r^2 + (z - z_i^0)^2}\right]dz \cong \sigma^2_{lnc}\gamma_{HD} \quad [100]$$

where, γ_{HD} is the correlation coefficient (average) between cohesion across domain D and cohesion along H. γ_{HD} can be defined as:

$$\gamma_{HD} \cong \frac{1}{mH}\sum_{i=1}^{m}\int_0^H \rho\left[\sqrt{r^2+(z-z_i^0)^2}\right]dz \qquad [101]$$

As indicated in Figure 25, r is the distance (horizontal) between the centerline of the pile and the soil sample (centerline).

Substituting Equation 98 into Equation 101 leads to

$$\mu_{lnW} = \mu_{lnF} \qquad [102a]$$

$$\sigma_{lnW}^2 = \sigma_{lnF}^2 + \sigma_{lnc}^2[\gamma(D)+\gamma(H)-2\gamma_{HD}] \qquad [102b]$$

The reliability index, β will be given as:

$$\beta = \frac{\ln\left(\frac{q}{\Phi_{df}}\right)-\mu_{lnW}}{\sigma_{lnW}} \qquad [103]$$

The geotechnical resistance factor (Φ_{df}) can then be calculated as:

$$\Phi_{df} = \exp(lnq - \mu_{lnW} - \beta\sigma_{lnW}) \qquad [104]$$

Cohesionless soil

The friction angle of sand (ϕ) is assumed to be lognormally distributed with μ_ϕ (mean), σ_ϕ (standard deviation), and $\theta_{\ln\phi}$ (spatial correlation structure). Out of a normally distributed (random field) function [$G_{ln\phi}(z)$, with mean (=0), unit variance, and $\theta_{\ln\phi}$ (spatial correlation length)], a lognormally distributed (random field) function can be created, by following transformation:

$$\phi(z) = \exp[\mu_{ln\phi} + \sigma_{ln\phi}G_{ln\phi}(z)] \qquad [105]$$

where,

$$\sigma_{ln\phi}^2 = \ln(1+v_\phi^2) \qquad [106a]$$

$$\mu_{ln\phi} = \ln(\mu_\phi) - \frac{1}{2}\sigma^2_{ln\phi} \quad [106b]$$

The coefficient of variation of ϕ, $v_\phi = \sigma_\phi/\mu_\phi$ and (z) is the spatial position. A Markovian correlation (simple exponentially decaying) function is assumed in this study, where, ρ is the correlation function, in the form of

$$\rho(t) = \exp\{-\frac{2|t|}{\theta}\} \quad [107]$$

where, $t = z_1 – z_2$ is the inter point distance.

In the above Equation, the θ (spatial correlation length) is generally described as the separation distance between two lnc values that are significantly associated. The $\rho(t)$ (spatial correlation function) has a variance reduction function, $\gamma(H)$, which is defined by:

$$\gamma(H) = \frac{1}{H^2}\int_0^H \int_0^H \rho(z_1 - z_2)dz_1 dz_2 \quad [108]$$

In this study, the random load model was considered similar as the cohesive soil.

Theoretical approach to estimating probability of failure of cohesionless soil

The soil is first represented as a spatially variable random field to assess the probability of a pile failing. This research investigates a 2D random field where the pile is positioned vertically about the soil samples, as the soil boring, CPT test or SPT sounding, are performed vertically in a distinct, perhaps different locations. When soil parameters are spatially varied, as they are in practice, the ultimate resistance, R_u, can then be estimated using the following equations:

$$R_u = \frac{1}{2}pa\gamma H^2(1 - sin\,\bar{\phi})\,tan\,(b\bar{\phi}) \quad [109]$$

where $\bar{\phi}$ is the cohesion (equivalent). The average of the spatially variable cohesion ($\bar{\phi}$) across the pile length H is hypothesized here,

$$\bar{\phi} = \frac{1}{H}\int_0^H \phi(z)dz \cong \frac{1}{n}\sum_{i=1}^n \bar{\phi}_i \quad [110]$$

The required minimum design pile length, H, can be obtained by

$$\Phi_{df}\left(\frac{1}{2}pa\gamma H^2\left(1 - sin\,\hat{\phi}\right)tan\,(b\hat{\phi})\right) = \alpha_L\hat{F}_L + \alpha_D\hat{F}_D \rightarrow H = \sqrt{\frac{2(\alpha_L\hat{F}_L + \alpha_D\hat{F}_D)}{\Phi_{df}pa\gamma(1 - sin\,\hat{\phi})\,tan\,(b\hat{\phi})}}$$

[111]

The ultimate geotechnical resistance, R_u, can be written as,

$$R_u = \left(\frac{\alpha_L \hat{F}_L + \alpha_D \hat{F}_D}{\Phi_{df}}\right)\left(\frac{(1-sin\,\bar{\phi})\,tan\,(b\bar{\phi})}{(1-sin\,\hat{\phi})\,tan\,(b\hat{\phi})}\right) \quad [112]$$

The probability of failure, ρ_f, will be:

$$p_f = P[F > R_u] \quad [113]$$

and a successful design methodology will have $\rho_f \leq \rho_m$. Substituting Equation 89 into Equation 113 leads to:

$$p_f = P\left[F > \left(\frac{\alpha_L \hat{F}_L + \alpha_D \hat{F}_D}{\Phi_{df}}\right)\left(\frac{(1-sin\,\bar{\phi})\,tan\,(b\bar{\phi})}{(1-sin\,\hat{\phi})\,tan\,(b\hat{\phi})}\right)\right]$$

$$= P\left[\left(\frac{F(1-sin\,\hat{\phi})\,tan\,(b\hat{\phi})}{(1-sin\,\bar{\phi})\,tan\,(b\bar{\phi})}\right) > \left(\frac{\alpha_L \hat{F}_L + \alpha_D \hat{F}_D}{\Phi_{df}}\right)\right] \quad [114]$$

Assuming that,

$\hat{X} = (1 - sin\,\hat{\phi})\,tan\,(b\hat{\phi})$, $\bar{X} = (1 - sin\,\bar{\phi})\,tan\,(b\bar{\phi})$, $q = \alpha_L \hat{F}_L + \alpha_D \hat{F}_D$ then, $Y = \frac{F\,\hat{X}}{\bar{X}}$

So that Equation 114 can be written as

$$p_f = P\left[Y > \frac{q}{\Phi_{df}}\right] \quad [115]$$

If Y is lognormally distributed, then:

$$lnY = lnF + ln\hat{X} - ln\bar{X} \quad [116]$$

The probability of failure, p_f, can be derived from the following:

$$p_f = P\left[Y > \frac{q}{\Phi_{df}}\right] = P\left[lnY > \ln\left(\frac{q}{\Phi_{df}}\right)\right] = 1 - \Phi\left[\frac{\ln\left(\frac{q}{\Phi_{df}}\right) - \mu_{lnY}}{\sigma_{lnY}}\right] \quad [117]$$

where, Φ is the cumulative distribution function (standard normal).

The probability of failure (p_f) in the above equation can be determined by $\mu_{lnY} = \mu_{lnF} + \mu_{ln\hat{X}} - \mu_{ln\bar{X}}$ and $\sigma^2_{lnY} = \sigma^2_{lnF} + \sigma^2_{ln\hat{X}} + \sigma^2_{ln\bar{X}} - 2Cov(ln\hat{X}, ln\bar{X})$ and solving the equations [131].

The reliability index, β, can be expressed as,

$$\beta = \frac{\ln\left(\frac{q}{\Phi_{df}}\right) - \mu_{lnY}}{\sigma_{lnY}} \quad [118]$$

The geotechnical resistance factor, Φ_{df}, can then be calculated as:

$$\Phi_{df} = \exp(lnq - \mu_{lnY} - \beta\sigma_{lnY}) \quad [119]$$

Research Objectives

The main objective of this research was to evaluate the different sources of geotechnical variability and quantify the special variability of soil properties for incorporation into analysis and design of different geotechnical engineering applications. This included:

a) Evaluating the operator-induced and equipment-induced variations on the design soil properties
b) Evaluating site spatial variations of design soil properties
c) Evaluating the best spatial interpolation method to generate synthetic CPT profiles and soil boring data (Standard Penetration Test, SPT, values and undrained shear strength, Su) from the existing CPT and soil boring data of the specific site
d) Incorporating the special site variability into LRFD design of pile foundations,
e) Incorporating the special site variability into different geotechnical engineering applications

Scope

This objective of this research study were achieved through conducting extensive in-box, laboratory and field tests to evaluate variability of the measured strength/stiffness parameters from different devices and the variability of the different soil properties; in addition to evaluating the spatial site variability from soil borings and/or in-situ tests for many geotechnical engineering analysis and design.

The in-box tests included constructing several geomaterial sections (5 ft. long × 3 ft. wide) of different types of soils and aggregate stones that were compacted and tested using different devices including DCP, LFWD, Geogauge, plate load, Dirt Seismic Properties Analyzer (D-SPA), Nuclear Density Gauge (NDG) and E-Gauge. The tests were conducted by different operators, in which each operator tested each section several times at different locations. The field tests were conducted using Geogauge, LFWD and DCP on 14 constructed sections at ALF site and 3 under-construction sections from different projects. In each field test, measurements were taken by several operators at different locations. The operator-related and location-related variabilities in terms of COV was evaluated for each device measurement using the X/Bar-R, ANOVA, and second moment methods.

Typical laboratory tests that included Atterberg limits tests, unconsolidated undrained (UU) triaxial tests, small direct shear tests, consolidation tests, and California bearing ratio (CBR) tests were conducted on different specimens of various soil types using different operators to evaluate specimen-related and operator-related variability of the different soil properties in terms of COV. The tests were performed by several operators on three specimen of the same soil type.

Several geostatistical methods and techniques, such as semivariogram and probabilistic approach, were used to evaluate the spatial site variability from soil borings with laboratory data and/or in-situ CPT data for incorporating the effect of specific site variability into many geotechniocal engineering applications such shallow foundation, deep foundations settlement and slope stability analysis.

The Bayesian analysis technique was used to update the mean bias, standard deviation, and COV, of the measured/predicted pile capacity of specific site from national and state variables and using the pile load test data of the new site. The updated variables were

used to calibrate the resistance factors for LRFD design of pile foundations of the specific site.

The method proposed by Fenton and Griffiths [17] was used to incorporate the variability in soil properties and the distance from soil boring(s) for analysis and design of shallow foundations.

The method proposed by Naghibi and Fenton [18] was used to incorporate the variability in soil properties and distance from soil boring(s) for analysis and design of deep foundations.

.

Methodology

This section will present the different approaches used to evaluate the variability of soil properties and the different sources of geotechnical variability, and quantify the variability of soil properties for inclusion in analysis and design of different geotechnical engineering applications. This includes conducting: (1) in-box laboratory tests using different devices such as Geogauge, Light Falling Weight Deflectometer (LFWD), and Dynamic Cone Penetrometer (DCP); (2) field tests using Geogauge, LFWD, and DCP on constructed sections at ALF sites and under-construction sections from different projects; (3) typical laboratory tests such as unconsolidated undrained (UU), direct shear tests, and consolidation tests; and (4) evaluations of site variability from soil borings and in-situ Cone Penetration Test (CPT). This section will also include different geostatistic methods and techniques used for incorporating site variability in different geotechnical engineering applications, such as bearing capacity of shallow foundations, ultimate capacity of pile foundations, and slope stability analysis. The incorporated techniques include spatial correlation and semivariogram modeling, Bayesian technique, probabilistic approach Fenton and Griffiths method, and Naghibi and Fenton method.

In-box Laboratory Tests

This study included conducting extensive in-box laboratory tests on several geomaterials including different types of soils and aggregate stone sections that were compacted and tested in the geotechnical lab at the Louisiana Transportation Research Center (LTRC). Twelve test sections were prepared, compacted and tested inside a box with dimensions of 5 ft. L × 3 ft. W × 4 ft. D. The sections were tested using different devices including Geogauge, Light Falling Weight Deflectometer (LFWD), Dynamic Cone Penetrometer (DCP), Plate Load, Dirt Seismic Properties Analyzer (D-SPA), Nuclear Density Gauge (NDG) and E-Gauge. Detailed descriptions of these devices, their measurements and corresponding equations are presented in Appendix A. Summary of these devices and their measurements are presented in Table 4.

The Geogauge, LFWD and D-SPA devices were conducted with five operators and each operator tested three times in the front, middle and back locations of the blue box, respectively. The DCP test was run by three operators and each operator conducted the test one time in the front, middle, and back location of the box. The plate load test (PLT)

was performed in the middle location of the box, in which only one operator did the test. The NDG and E-Gauge tests were performed in the front, middle and back locations and one operator performed the test.

Table 4. Devices used to measure soil variability

Different Devices to Measure Variability			
SL	Device	Measure	Units
1	Geogauge	Stiffness Modulus	MPa
2	Light Falling Weight Deflectometer (LFWD)	Deformation Modulus	MPa
3	Dynamic Cone Penetrometer	Dynamic Cone Penetration Index (DCPI)	mm/ blow
4	Dirt Seismic Properties Analyzer (D-SPA)	Shear Modulus	ksi
5	Nuclear Density Gauge (NDG)	Dry Density	pcf
		Moisture Content	%
6	Low Nuclear Density Gauge (E-Gauge)	Dry Density	pcf
		Moisture Content	%
7	Plate Load	Deformation Modulus	MPa

The reason for taking measurements in the same section with different operators is to evaluate variability of soil properties among the operators. Besides, the location-related variability can also be evaluated by taking measurements in different locations. The collected testing data were used to perform statistical analyses using the X-Bar/R and ANOVA method to assess the mean value and the coefficient of variation of testing devices' measurements.

Materials Used in the In-Box Tests

Twelve different geomaterials were used for conducting the in-box laboratory tests. These materials are: low PI (PI=11) clay soil, medium PI 1 (PI=21) clay soil, medium PI 2 (PI=31) clay soil, medium PI 3 (PI=38) clay soil, high PI (PI=53) clay soil, sand, Kentucky limestone, and Mexican limestone. In addition, three stabilized sections were also tested including medium PI 3 (PI=38) mixed with 5% lime and 4% cement by volume; high PI (PI=53) mixed with 5% lime and 4% cement by volume and low PI (PI=11) mixed with 3% cement by volume.

Layout of the In-Box Tests

The experimental testing program in this study was conducted inside a box with dimensions of 5 ft. L × 3 ft. W × 4 ft. D to evaluate the variability of compacted soil layers using different devices and different operators. For each test, four layers were compacted with the same type of geomaterial up to 24 in. thickness maintaining the 95% of the maximum dry density and optimum moisture content. Each layer was compacted inside the box to 6 in. thickness, as is illustrated in Figure 26. The in-box constructed sections were tested using different devices (i.e., Geogauge, LFWD, DCP, Plate Load, D-SPA, NDG and E-Gauge) using different operators as shown in Figure 27.

Figure 26. Cross-section layout of compacted layers inside the box

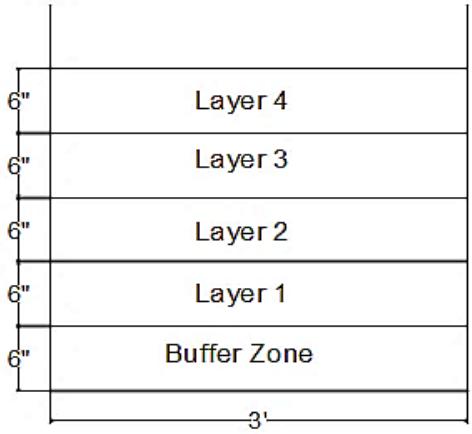

After compacting the layers, five operators ran the tests using the same device to check the variability of the measurements with respect to Geogauge, LFWD and D-SPA. Each operator took three measurements in different locations of the box for the same compacted geomaterial layers. The same procedure was applied for the different geo materials. Three operators ran the DCP tests in different locations of the box, following the same procedure for all geomaterials. The PLT was conducted by one operator in the middle location of the box. Tests were conducted by NDG and E-Gauge maintaining one operator in three different locations of the box. Figure 28a presents the layout for the Geogauge, D-SPA and plate load tests. Figure 28b presents the layout for the LFWD tests. Figure 28c presents the layout for DCP tests. The layout for the NDG and E-Gauge tests are similar to Figure 28a.

Figure 27. In-box testing: (a) Geogauge test, (b) LFWD test, (c) DCP test, (d) Plate load test, (e) D-SPA test, (f) NDG, and (g) E-Gauge test

(a) Geogauge test

(b) LFWD Test

(c) DCP Test

(d) Plate load test

(e): D-SPA test

(f) NDG test

(g) E-Gauge Test

Figure 28. Layout of test setup in different location of the box

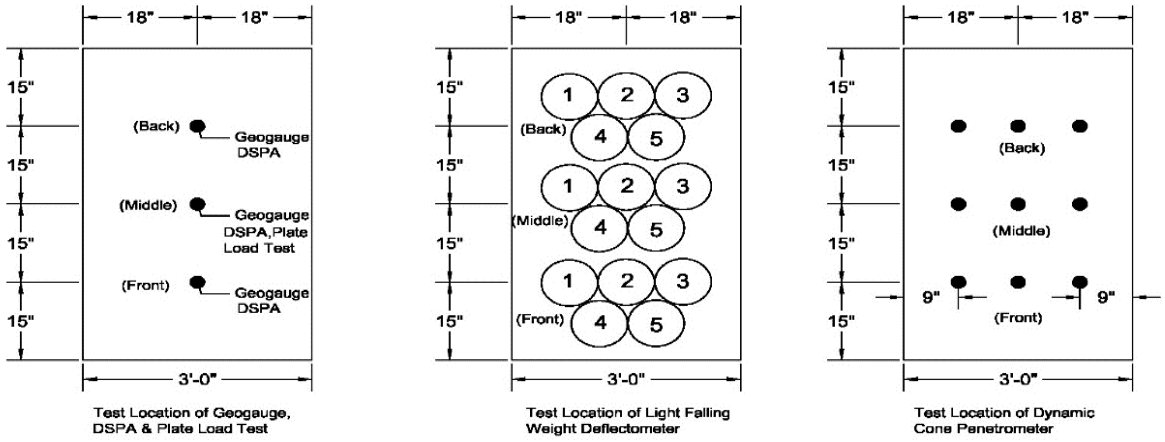

(a) Geogauge, DSPA and plate load tests (b) LFWD tests (c) DCP tests

Field Tests on Constructed Sections

This study included conducting field tests on several constructed and under-constructed sections in different projects within Louisiana. In addition, 14 test sections were tested at the accelerated load facility (ALF) site of DOTD. Three under-constructed test sections were also tested at the LA 98 and LA 417. In each field test, the Geogauge, LFWD and DCP measurements were taken to evaluate the soil's site variability among locations and operators. In addition, the dry unit weight and moisture content were obtained using the Nuclear Density Gauge and E-Gauge devices.

Constructed Sections at ALF site

Eight sections were constructed at the ALF site. Among these, four sections were constructed with 5 ft. × 5 ft. dimensions at the lower level location of ALF site, and the another four sections were constructed with 4 ft. × 4 ft. dimensions at the upper level location of ALF site. Each section was constructed with 12-in. thickness. All sections were constructed with cementitious materials including either low PI (PI=11) or high PI (PI=53) soils. Figure 29 presents the layout of the lower level sections constructed at ALF; while Figure 30 illustrates the test setup layout for all the lower level test sections at ALF. The layout of the upper level sections constructed at ALF is presented in Figure 31, and the layout of test setup for all the upper lever sections is illustrated in Figure 32.

Figure 29. Layout of the lower level constructed sections at ALF

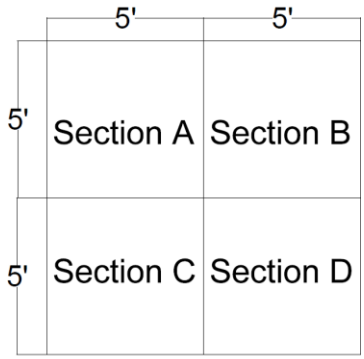

Figure 30. Layout of test setup for the lower level sections at ALF

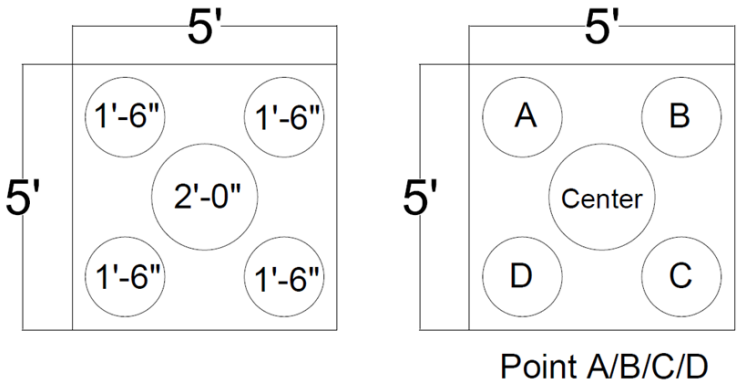

Measurements were taken using Geogauge and LFWD at each point (A, B, C, and D, or 1, 2, 3, and 4) including the center in every section. Five operators took the measurements using Geogauge and LFWD devices at every section. DCP, NDG and E-Gauge measurements were taken at every point except the center. The DCP was conducted by three operators in each section whereas NDG and E-Gauge were operated by one operator.

In addition, six sections (I to VI) with dimensions of 70 ft. × 13 ft. that were constructed at the upper location of ALF under another research project to study micro cracks of cement stabilized sections were also tested. The cement soil sections were designed with a minimum 7-day UCS of 150 and 300. Section I was the control section. The stabilized sections II, III, and IV were constructed using 8% cement, and maintaining an 8.5-in. thickness for each section. The stabilized sections V and VI were constructed using 6% cement, and maintaining a 12-in. thickness each. The A-2-7 (AASHTO) geomaterials was

used in the construction of all the six sections. Figure 33 depicts the layout of the constructed soil cement sections with no micro-cracking (MC), low MC, medium MC and high MC. Figure 34 illustrates the five points where tests were performed.

Figure 31. Layout of the upper level sections constructed at ALF

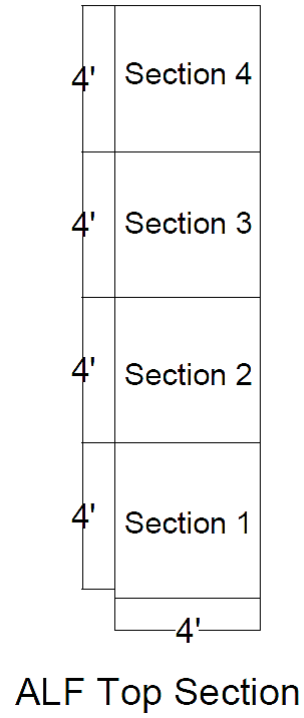

Figure 32. Layout of test setup for the upper level sections at ALF

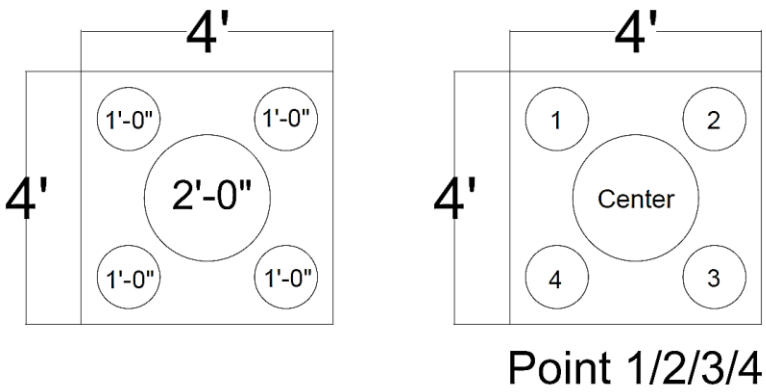

Figure 33. Layout of soil cement sections at ALF

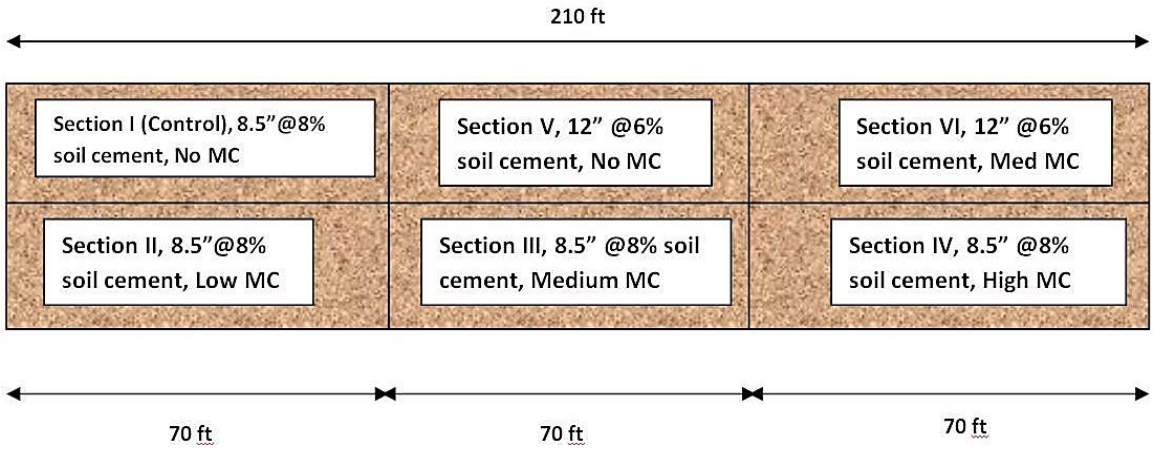

Figure 34. Test setup layout of the soil cement sections at ALF

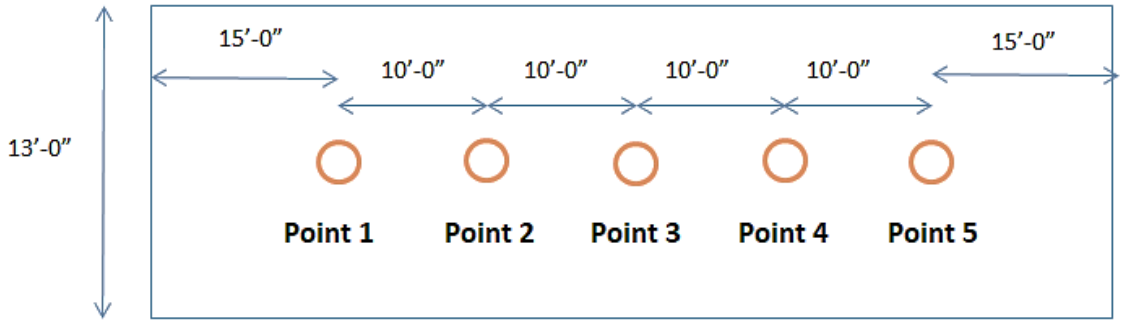

All the constructed sections at ALF site were tested using the Geogauge, LFWD and DCP devices taken at each point. The Geogauge and LFWD tests were run by five operators; whereas, the DCP tests were conducted with three operators. The NDG and E-Gauge tests were performed by one operator at each point.

Under-Constructed Sections at LA 98 and LA 417

The field testing program also included testing three under-constructed sections at LA 98 and LA 417 highway sites. The sections were tested with different devices to determine compacted soil site variability among operator and locations. Five testing devices (i.e., Geogauge, LFWD, DCP, NDG and E-Gauge) were engaged and run by different operators for evaluating the site variability. The Geogauge and LFWD tests were performed by five operators; whereas, one operator was involved in taking measurements for the DCP, NDG and E-Gauge tests.

Tests were conducted on the cement stabilized base layer at two different stations (266+00 and 267+00) within the LA 98 site, which are located in Lafayette, LA. The base section was constructed using 10 in. thick stabilized with 7% cement. Tests were also performed on a another cement stabilized base layer at station (101+25) of the LA 417, which is located near False River of Louisiana. The thickness of the base layer was 24 in., which was stabilized with 10% cement. The layout of the test sections and test setup layout of the devices were the same for all sections. Figure 35 presents the layout and testing setup for the under-constructed field base sections.

Figure 35. Layout and testing setup of the under-constructed field base sections

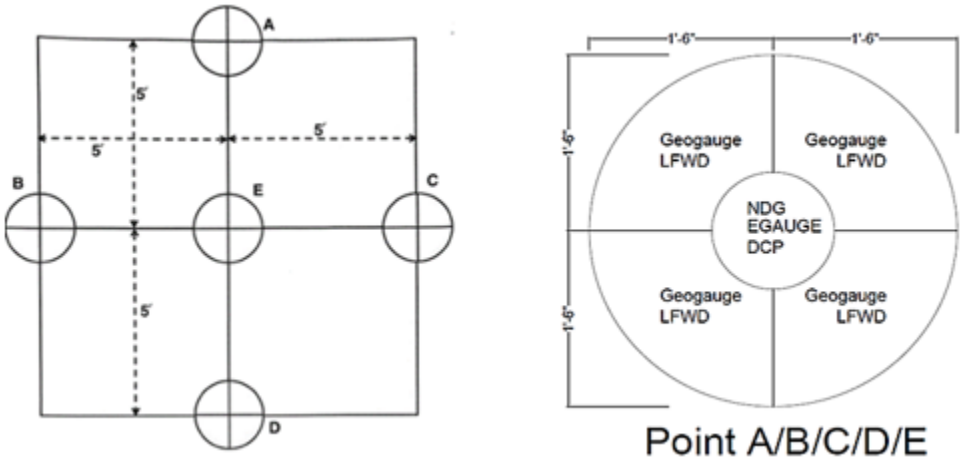

Laboratory Testing Program

The laboratory testing program involved conducting several laboratory tests on various types of soil in order to evaluate the laboratory variation of soil properties. The laboratory tests included the unconsolidated undrained (UU) test, Atterberg Limit test, small direct shear test, one dimensional consolidation test, and the California Bearing Ratio (CBR) test. All the laboratory tests were performed in accordance with the ASTM procedure methods.

The soils used in the laboratory tests were collected from the ALF site. The soil samples were put inside the oven to dry out for three days at a 60º C temperature. The soil samples were then remolded at the optimum moisture contents for all the lab tests.

Unconsolidated Undrained (UU) Test

The UU tests were conducted using the triaxial machine in the soil lab at LTRC. The soil samples used for the UU tests are: Low PI (PI=11), Medium PI 1 (PI=21), Medium PI 2 (PI=31), Medium PI 3 (PI=38) and High PI (PI=53) clay soils. The tests are performed according to ASTM D2850 - 15 for all soil samples. In order to determine the laboratory variability of soil properties, the UU tests were run by five operators for each soil type. Each operator prepared 3 samples of the same soil type maintaining optimum moisture content. Figure 36 shows the soil samples prepared for the UU test of one operator. The soil samples in UU tests were loaded up to 15% strain for all soil types. Figure 37 presents an example of the stress-strain curve obtained of Low PI (PI=11) soil that was performed by one operator, and Figure 38 shows the Mohr's circle for the same tests.

The strength of this test is performed under undrained conditions and is applicable to field conditions where soils are subjected to a change in stress without time for consolidation to take place. Also, the field stress conditions are applied to those in the tests. The shear strength measured from the UU tests expressed in terms of total stresses is commonly used in the short-term embankment stability analyses, earth pressure calculations, and foundation design.

Figure 36. Samples prepared for UU test.

Figure 37. Stress-strain curve of Low PI (PI=11) soil

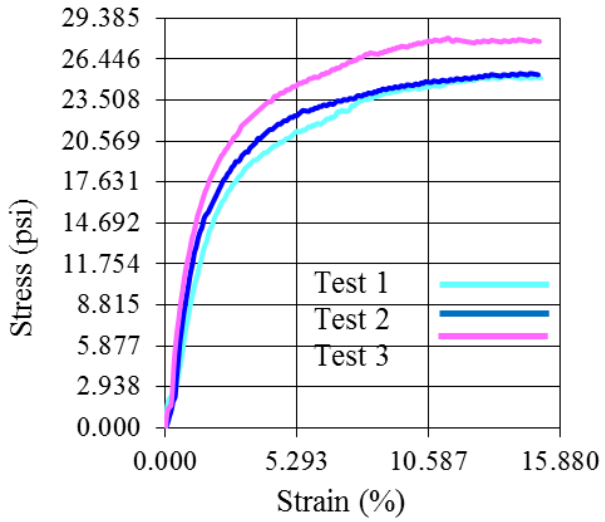

Figure 38. Mohr's circles for the UU tests

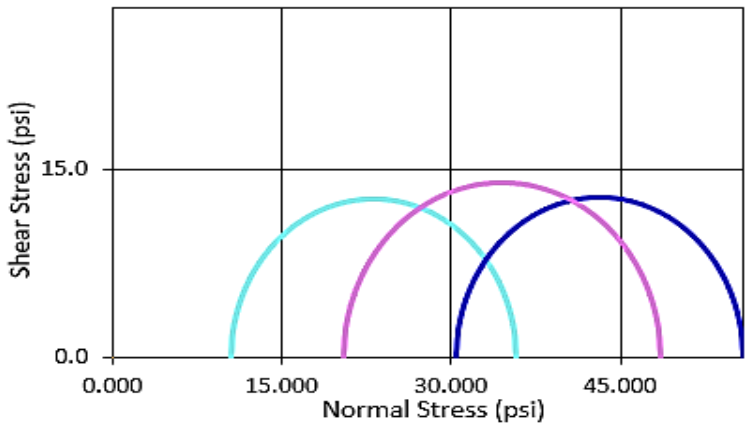

Atterberg Limit Tests

The Atterberg limits are critical water contents of fine-grained soils that define the transitional boundaries between the different consistency states of the soil (solid, semi-solid, plastic and liquid) to another consistency state. They are also known as consistency limits. These Atterberg limits are: shrinkage limit (SL), plastic limit (PL), and liquid limit (LL), which are outlined in ASTM D4943 testing procedure. The behavior and consistency of the soil, as well as engineering properties, are different at varying degrees of moisture content. Thus, the boundary between each state can be established based on the change in water content and hence the soil's behavior. The Atterberg limits are usually

used for classification of cohesive soils, distinguish between silt and clay soils, and to distinguish between different compositions of silts and clays. Several correlations have been developed to relate the indices obtained from Atterberg limits (e.g., plasticity index, PI = LL - PL) to different soil properties and behavior.

For the laboratory tests, remolded soils were used to determine the liquid limit and plastic limit of the different soil samples. Samples were prepared using different moisture contents by five different operators. Each operator prepared 3 samples with similar moisture content for the same soil type and the process was followed for all other soil types. Figure 39 shows some soil samples prepared to determine the liquid limit and plastic limit of one soil.

Figure 39. Samples prepared for the Atterberg limit tests

Small Direct Shear Test

The small direct shear test was performed in this study to measure the laboratory variation in the consolidated-drained shear strength of sandy and clayey soils. The shear strength is one of the most significant engineering parameter of geotechnical engineering analysis and design since it is necessary whenever a structure relies on the soil's shearing resistance. The shear strength is required for engineering situations such as evaluating the stability of slopes or cuts, determining the bearing capacity for foundations, and measuring the pressure exerted by a soil on a retaining wall. The direct shear test was performed following the ASTM D3080-72 procedure. Figure 40 presents a soil sample ready to undergo shear test.

Dry sandy soil and clay soils with different consistencies were tested in the direct shear test devise to measure the corresponding shear strength parameters (i.e., friction angle, ϕ, and cohesion, c). The clay soils included in the tests are: Low PI (PI=11), Medium PI 1 (PI=21), Medium PI 2 (PI=31), Medium PI 3 (PI=38) and High PI (PI=53) soils. The direct shear tests were conducted by five operators, in which every operator prepared nine samples for each type of soil material. For all the tests, shearing was maintained up to 10% strain.

Figure 40. Small direct shear test

One Dimensional Consolidation Test

This one dimensional consolidation test is usually performed on fine-grained soils, which are undisturbed and naturally sediment in water, in order to evaluate the consolidation parameters. In this study, the consolidation tests were performed to evaluate the variation in laboratory measured consolidation parameters (i.e., compression index, C_c, and coefficient of consolidation, c_v). The testing procedure and the evaluation techniques are specified in the ASTM D2435-04 reference. The basic test procedure is applicable to specimens of compacted soils and undisturbed samples of soils formed by other processes such as chemical alteration, weathering, and stress distribution.

The consolidation parameters of the soil determined from the consolidation test are used to calculate the magnitude and time rate of both primary and secondary consolidation settlements of a structure or an earth fill. The properties determined from this test are of key significance in the evaluation and design of structural performance. Figure 41 shows the one-dimensional consolidation test devises.

The one dimensional consolidation tests were conducted on clays soils with the following different consistencies: Low PI (PI=11), Medium PI 1 (PI=21), Medium PI 2 (PI=31), Medium PI 3 (PI=38) and High PI (PI=53) soils. To evaluate the laboratory variability of consolidation parameters, the consolidation tests were performed by three operators, in which each prepared and tested three specimens of the same soil prepared at the optimum moisture content.

Figure 41.One-dimensional consolidation test

The results of consolidation tests can be used to evaluate the pre-consolidation pressure (P_c), compression index (C_c), and recompression index (C_r) from the measured void ratio vs log (pressure) curve. The coefficient of consolidation, c_v, can be evaluated from the settlement versus time curve for each load increment using either Casagrande or Taylor methods. The following equation can be used to calculate c_v using:

$$c_v = \frac{T_{50} * H_{dr}^2}{t_{50}} \quad (Casagrande) \quad or \quad c_v = \frac{T_{90} * H_{dr}^2}{t_{90}} \quad (Taylor) \qquad [120]$$

where, T_{50} = dimensionless time factor for 50% consolidation, equals 0.197; T_{90} = dimensionless time factor for 90% consolidation, equals 0.848; t_{50} = time corresponding to 50% degree of consolidation; t_{90} = time corresponding to 90% degree of consolidation; and H_{dr} = length of the drainage path at 50% consolidation. For double-sided drainage, H_{dr} = half the specimen height at the specific load increment; and for one-sided drainage, H_{dr} = full-specimen height at the specific load increment.

California Bearing Ratio (CBR) Test

The California Bearing Ratio (CBR) test is a comparative test that is usually designed as an indicator of the strength of subbase and base course materials in highways and airfield pavement systems. The testing procedure is explained in ASTM D1883-99. The CBR test is generally performed on remolded (compacted) specimens, although it can be conducted on undisturbed soils. Remolded specimens can be compacted to their maximum unit weights at their optimum moisture contents if the CBR is desired these values. However, the CBR tests can also be performed at the desired unit weights and moisture contents. Soil samples are tested after being placed in water for 96 hours in order to simulate the very poor soil conditions. Figure 42 shows the CBR test in the universal testing machine.

Figure 42. California bearing ration (CBR) test

The CBR is defined as the ratio of the bearing load that penetrates a geomaterial to a specific depth as compared with the load that penetrates a well-graded crushed stone to the same depth. It is expressed as a percentage. A load is applied by a piston with a diameter of 1.95 in. to penetrate it into the soil. The penetrations versus load values are plotted on a graph and corrected following the procedure specified in the test standard. The corrected stress values corresponding to penetration depths of 0.10 in. and 0.20 in. are divided by the standard stresses of 1,000 psi and 1,500 psi, and then multiplied by 100. The CBR can be expressed as follows:

$$CBR = \frac{\text{penetration stress (psi) required to penetrate 0.10 in.or 0.20 in.}}{\text{standard stresses (1,000 psi and 1,500 psi)}} \quad [121]$$

If the bearing ratio based on a penetration stress required to penetrate 0.20 in. with a corresponding standard penetration stress of 1,500 psi is greater than the one for a 0.10 in., the test should be repeated, and if the result is still similar, the ratio based on the 0.20 in. penetration should be reported as the CBR value.

The materials used for the CBR tests are: sand, recycled asphalt pavement (RAP), Kentucky limestone and Mexican limestone. In order to evaluate the laboratory variations of CBR values, five operators were involved in performing the CBR tests for all materials, and each operator prepared and tested three specimens for the same material.

Evaluation of Site Variability using Semivariogram

In this study, the site variability from different project sites were evaluated using the semivariobram approach, and the results were implemented into LRFD design of pile foundations. Field data from six project sites with multi CPT tests performed at different locations within each site, and four project sites with multi soil borings conducted at different locations within each site were collected. These include: Metairie, ALF, Bayou Lacassine, US 90, LA 85, Hammond, and LA 1 CPT project sites; and Metairie, Bayou Lacassine, Red River, and Williams Boulevard soil boring sites. The spatial variability of CPT data (corrected tip resistance, q_t) and the spatial variability from soil boring data (either SPT-N or undrained shear strength, S_u) for each site were evaluated using the semivariogram approach. The coefficient of variation due to spatial variability ($COVR_{spatial}$) was determined for each site for use to calibrate the specific site resistance factor.

Description of CPT Sites

Six different project sites in Louisiana with several CPT tests performed at each site were used to evaluate the effect of site variability on the LRFD design of driven piles. The profiles of the different CPT data with depth were obtained for each site. The first project site is in Metairie, which covers 5,382,000 ft^2 (500,000 m^2), located at 29°59′52″N and 90°10′39″W, and is situated at 3 ft. above the mean sea level. The project consists of constructing five dedicated ramps at the Interstate 10/Causeway Boulevard interchange located in Metairie in Jefferson Parish of Louisiana. Fourteen CPT tests were performed at different locations to a depth of 120 ft. as shown in Figure 43a. The second site is the Accelerated Loading Facility (ALF) site of the Louisiana Transportation Research Center (LTRC), which covers an area about 21,528 ft^2 (2000 m^2), which is located at

30°26′12.37″N and 91°14′39″W. Ten CPT tests were performed at different locations down to 50 ft. depth as shown in Figure 43b. For the third site at Bayou Lacassine, the area is about 107,640 ft^2 (10000 m^2), located at 30°04′13″N and 92°52′52″W, in which 10 CPT tests were performed at different locations down to 75 ft. as shown in Figure 43c. For the fourth site at US 90 and LA 85, the area is about 1,345,500 ft^2 (125,000 m^2), and is located at 29°55′17″N and 91°43′34″W. Twenty-two CPT tests were performed at different locations to a depth of 90 ft. as shown in Figure 43d. The area of the fifth site at Hammond is about 5,812,500 ft^2 (540,000 m^2), located at 30°28′50″N and 90°29′29″W, in which seven CPT tests were performed at different locations as shown in Figure 43e. For the sixth LA 1 site, the area is about 21,530 ft^2 (2,000 m^2), located at 30°26′00″N and 91°12′37.45″W, in which 13 CPT tests (75 ft. deep) were performed at different locations as shown in Figure 43f.

Figure 43. Plan view of the CPT locations for the different sites

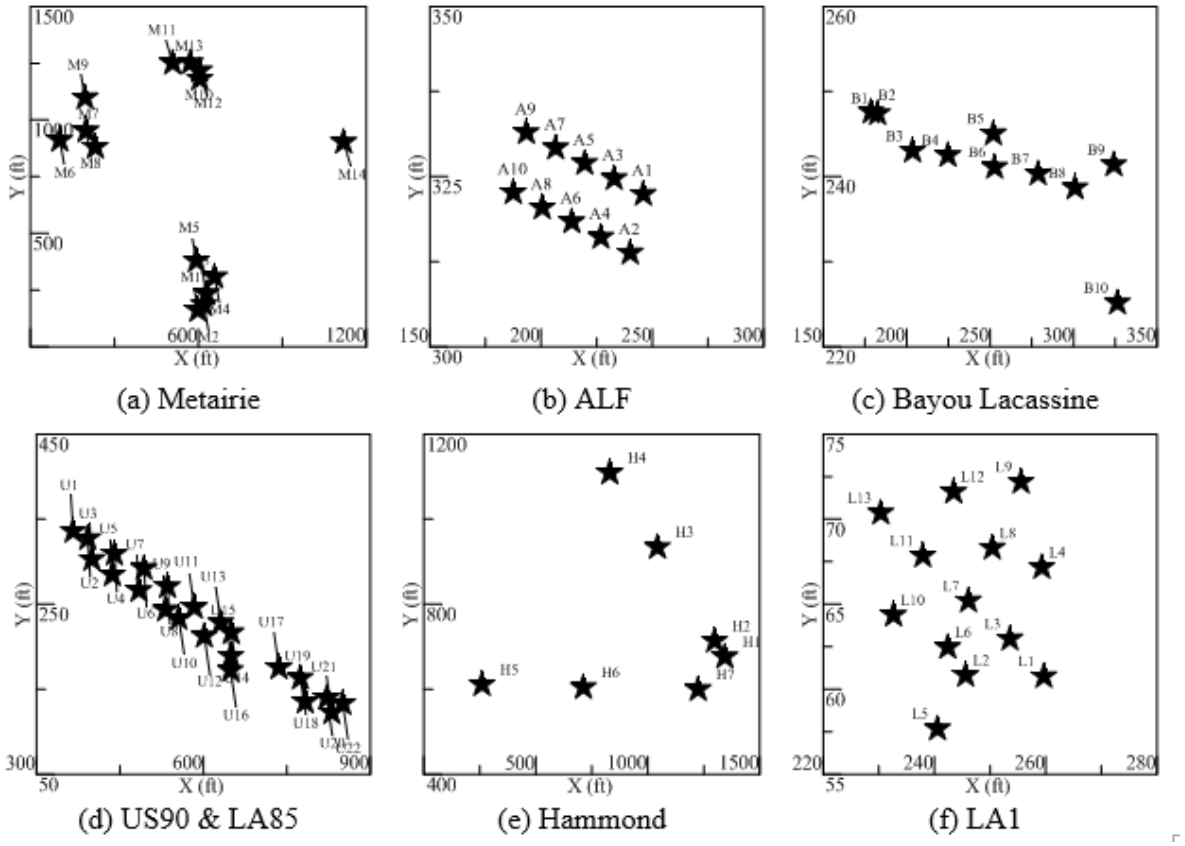

Description of Soil Boring Sites

Four different project sites in Louisiana with several soil borings performed in each site were considered in this study to evaluate the effect of site variability on LRFD design of driven piles. The profiles of soil boring data (undrained shear strength, S_u, and SPT-N) with depth were obtained for each site. Two of the project sites (Metairie and Bayou Lacassine) are the same sites used for CPT test data. Fifteen soil borings were performed at different locations in Metairie site down to 105 ft. depth as shown in Figure 44a. For the Bayou Lacassine site, 12 soil borings (75 ft. deep) were performed in this project as described in Figure 44. The third site is the Red River project site at Alexandria, Louisiana. The area in this site is about 6,460 ft^2 (600 m^2), located at 31°19′36″N and 92°26′55″W, in which eight soil borings were performed to 105 ft. depth at different locations as shown in Figure 44c. The fourth site is the Williams Boulevard project site with an area of about 1,722,200 ft^2 (160,000 m^2), which is located at 30°0′34″N and 90°14′17″W. In this site, eight soil borings (120 ft. deep) were performed at different locations as shown in Figure 44d.

Subsurface Soil Characterization

The subsurface soil conditions for the different project sites were characterized using the results of CPT tests and/or the soil borings and the associated laboratory test results. In this study, the site variability of six project sites with CPT data and four sites with soil borings and laboratory tests were evaluated, in which the Metairie and Bayou Lacassine sites have both data. The profile soil type, profile of corrected tip resistance ($q_t = q_c + (1 - a) \times u_2$) from CPT data and/or profiles of SPT-N values and undrained shear strength, S_u, from soil borings were determined for all sites. Here, (a) is the ratio of the effective area of the cone ($a = A_n/A_c$), where A_n and A_c are the area of cross-section and the projected area of the load cell and the cone, respectively. Additionally, (u_2) is the pore water pressure measured behind cone base. For example, the profile of soil type for Metairie site, the results of SPT tests, S_u values, and the profiles of average q_t values per ft. for all the CPTs obtained from the site are presented in Figure 45. The site consists of silty clay soils down to about 30 ft. deep, followed by a sandy soil layer to about 45 ft. deep, then clay soils to about 85 ft. deep. Below that lie another sandy layer down to 120 ft. The profile of CPT tests was used to classify the subsurface soil using the probabilistic region “soil behavior” estimation method introduced by Zhamg and Tumay [134], in addition to the CPT soil classification proposed by Robertson [110] as shown in the Figure 45 for Metairie site. The profiles of CPT data and CPT soil classifications, and the profiles of SPT-N values and S_u for the other CPT and soil boring sites are presented in Appendix B.

Figure 44. Plan view of the Soil Boring locations for the different sites

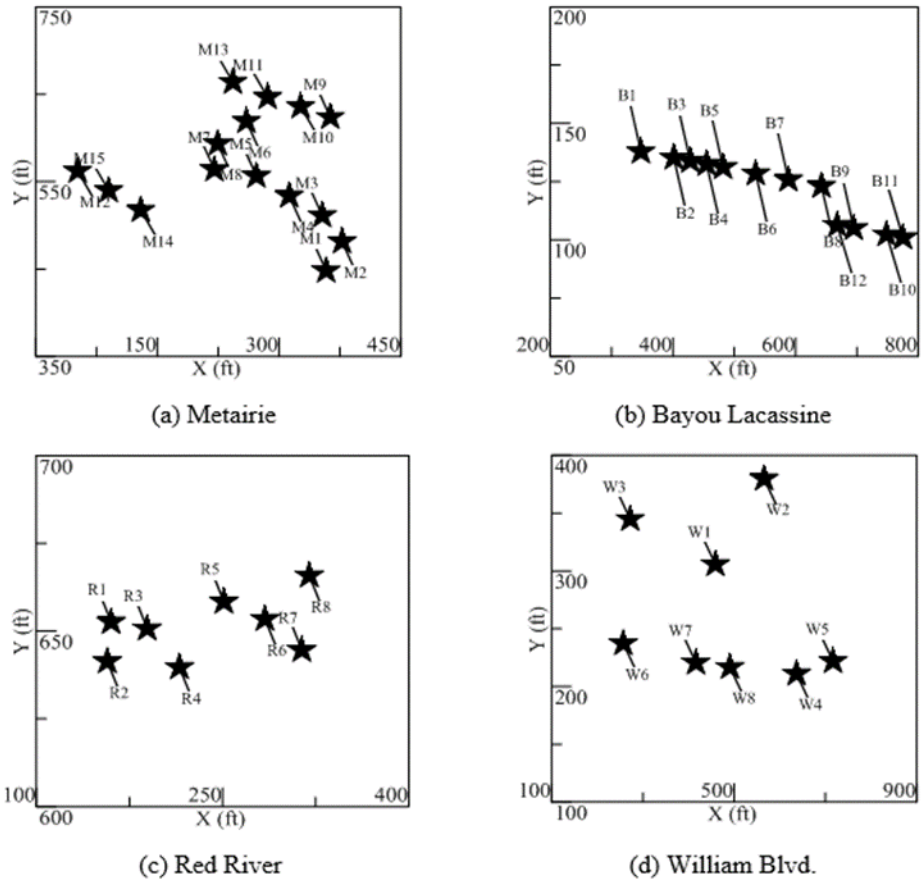

For the CPT sites, the coefficient of variation (COV) of the corrected cone tip resistance (q_t) data were calculated for each site. For Metairie site, the maximum, minimum and average COV of q_t values are 2.46, 0.00 and 0.74 tsf, respectively. The maximum, minimum, and average COV of q_t values for the Bayou Lacassine site are 2.63, 0.09, and 0.46 tsf, respectively. For ALF site, the maximum, minimum, and average COV of q_t values are 1.48, 0.09, and 0.39 tsf, respectively. The maximum, minimum, and average COV of q_t values for US 90 and LA 85 site, are 3.26, 0.07, and 0.48 tsf, respectively. For Hammond site, the maximum, minimum and average COV of q_t values are 2.01, 0.25 and 0.98 tsf, respectively. Finally, for LA 1 site, the maximum, minimum, and average COV of q_t values are 1.67, 0.15, and 0.55 tsf, respectively.

For the soil boring sites, the COV of S_u and SPT-N values were calculated for each site. The maximum, minimum, and average COV of S_u from soil borings for the Metairie site are 0.67, 0.17, and 0.27, respectively. The maximum, minimum, and average COV of SPT-N from soil borings are 0.70, 0.13, and 0.31, respectively. For Bayou Lacassine, the

maximum, minimum, and average COV of S_u from soil borings are 0.80, 0.29, and 0.51, respectively. The maximum, minimum, and average COV of S_u for the Red River site are 0.91, 0.11, and 0.35, respectively. For the Williams Boulevard site, the maximum, minimum, and average COV of S_u are 0.39, 0.13, and 0.26, respectively.

Figure 45. Profiles of soil boring data, CPT Data, and CPT soil classification at Metairie site

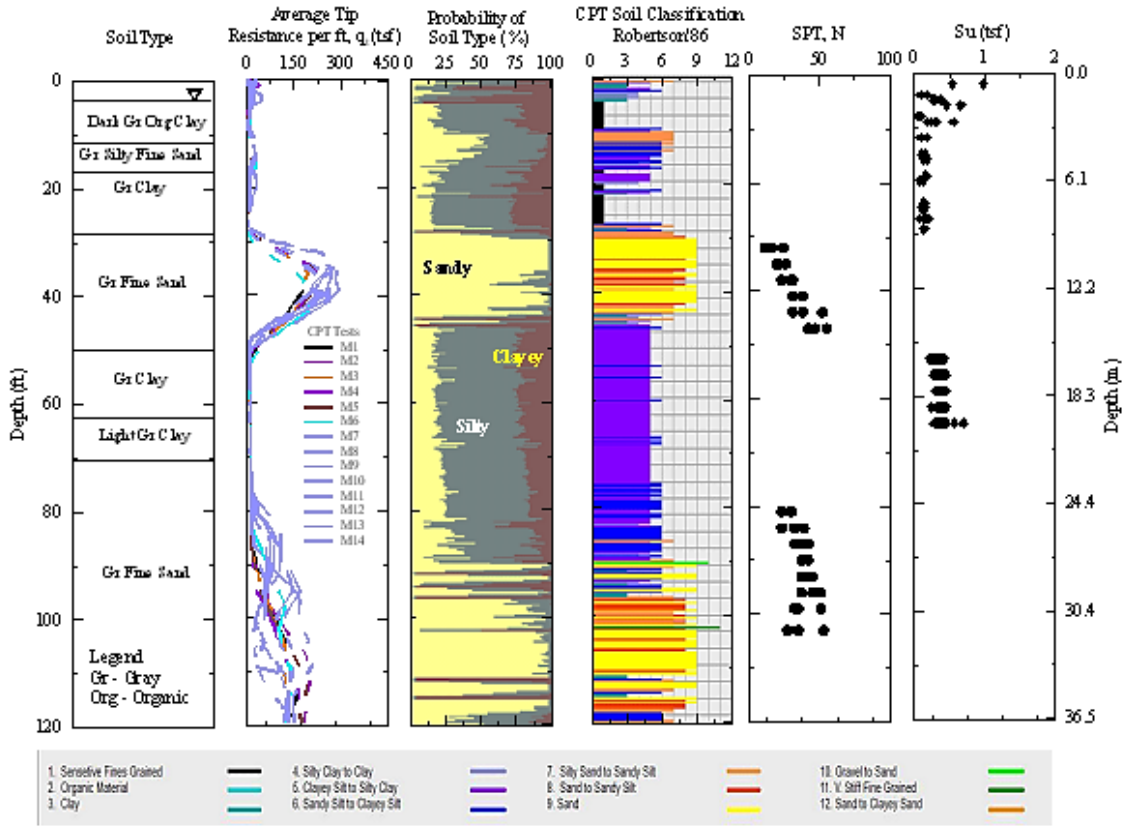

For the purpose of evaluating spatial site variability using the semivariogram analysis, the soil profile for each of the CPT and soil boring sites were divided into soil layers. In Metairie site, six soil layers were identified for analysis: 0-28 ft., 28-40 ft., 40-50 ft., 50-78 ft., 78-111 ft. and 111-120 ft. The subsurface condition for ALF site reveals four soil layers: 0-4 ft., 4-24 ft., 24-38 ft. and 38-50 ft. For Bayou Lacassine site, there were five soil layers identified for analysis: 0-5 ft., 5-20 ft., 20-30 ft., 30-52 ft. and 52-75 ft. Six soil layers were identified for the US 90 and LA 85 site: 0-10 ft., 10-25 ft., 25-38 ft., 38-49 ft., 49-64 ft. and 64-90 ft. For Hammond site, there have been three soil layers identified for analysis: 0-9 ft., 9-19 ft. and 19-24ft. The subsurface condition for LA 1 site shows four soil layers: 0-10 ft., 10-34 ft., 34-46 ft. and 46-75 ft. For the Red River site, there have been four soil layers identified for analysis: 0-20 ft., and 20-50 ft., 50-70 ft.,

and 70-115 ft. Finally, the subsurface soil condition for Williams Boulevard site reveals four soil layers: 0-30 ft., 30-60 ft., 60 ft.-90 ft., and 90-120 ft.

Evaluation of Site Variability using Bayesian Analysis

In this study, the Bayesian updating technique that follows the Baye's rule was used to probabilistically analyze and update the results of pile load tests that were collected in a previous study by Amirmojahedi and Abu-Farsakh [57] in order to get an updated data information (i.e., posterior distribution). The Bayesian technique was coded using MATLAB. Herein, the Bayesian technique is used to model the mean bias (λ = measured/ predicted ultimate pile capacity) and standard deviation of the bias (σ) obtained from the pile load test database collected from different previous project sites (34 sites) in order to update λ and σ for the new specific site. The updated values of λ and σ can be used in the design of pile foundation for the new site, taking into consideration the specific site variability.

Pile Load Test Database

The database used in this study consists of 80 precast prestressed concrete (PPC) test piles of different sizes and lengths that were collected from 34 different project sites across Louisiana. Figure 46 depicts the locations of the collected PPC test piles. All the piles in the database were square precast prestressed concrete (PPC) piles that were loaded to failure under static load tests. The pile lengths range from 36 ft. (11 m) to 200 ft. (61 m), and the pile widths range from 14 in. (356 mm) to 36 on. (914 mm). In each site, several CPT tests and soil borings were conducted, which were used for soil classification and evaluation of soil properties for different soil layers along the piles' lengths.

The pile load tests were performed based on quick load test as described by ASTM D1143 testing procedure [136]. The tests were performed 14 days after pile driving, partially accounted for pile setup. The load was increased from 10% to 15% of the design load up to 3 times the design load (or unless a failure occurs first), and settlement was measured for each load increment. In this study, only the piles that failed before reaching the maximum load were considered. The load-settlement curve for each pile load test was interpreted to evaluate the measured ultimate pile capacity, Q_m, using the Davisson interpretation method [113]. This method is defined as the load causes the pile top

deflection to be equal to the elastic compression of the pile plus 0.15 in. (3.81 mm) plus 1/120 of the pile's width/diameter. In this study, the CPT data for the tests conducted close to piles were used to estimate the ultimate pile capacity, Q_p, using the LCPC Pile design method [56]. The model bias factor, $\lambda = Q_m/Q_p$, and the corresponding standard deviation, σ, were calculated for the collected database.

Figure 46. Locations of PPC test piles [57]

Geotechnical Characterization of Database Sites

As stated earlier, the pile load test database was collected from 34 different project sites in Louisiana obtained from a previous study ([57], [138]). CPT tests and soil borings were conducted close to each pile load test. Soil data consist of information on the CPT or soil boring locations; soil type and stratigraphy; profiles of CPT data; and results of SPT-N values and laboratory testing (shear strength, physical properties, etc.), which were collected for each pile load test location. Detailed information on the subsurface soil conditions of the 80 pile load test locations can be found in Amirmojahedi [138]. Piles were driven into different sandy, clayey, and layered soils. However, the predominant soil type in most piles is silty clay soil. Figure 47 presents an example of the soil type and layering, soil properties (e.g., S_u), profile of corrected cone tip resistance (q_t), and the CPT classification using probabilistic region estimation method [134] for a test pile located at Houma Intracoastal Waterway (I.C.W.W.) Bridges project site.

The evaluation of pile capacities using the static analysis methods and CPT methods reveals that more than 70% of the pile capacity for 69 piles out of 80 piles comes from the side resistance. This means that most of the piles in this study can be considered as friction piles.

Figure 47 Subsurface soil condition at Houma I.C.W.W. Bridges project site [138]

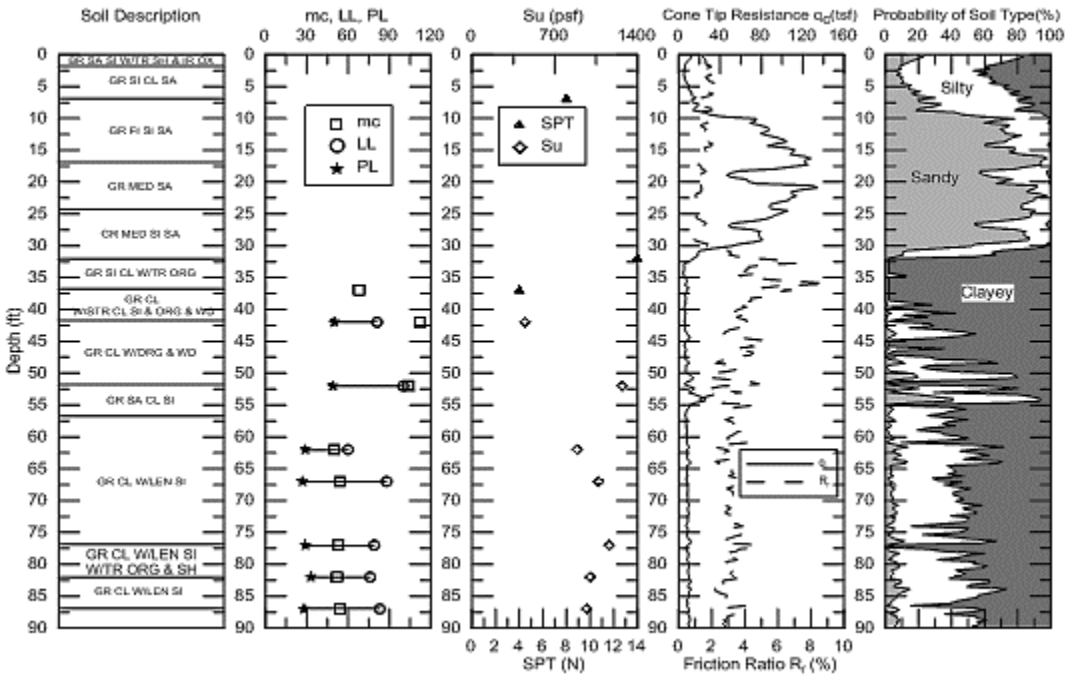

Updating Data Information

The Bayesian technique was used in this study to update the mean bias (λ) and standard deviation of the bias (σ) values obtained from previous pile load test database for the new specific site. The updated values of λ (or σ) are collectively represented as b in the vector form; and the bias values of pile load test data (previous) is represented by D. For a given a dataset, D, the posterior probability density of the parameters b, p(b | D) can be evaluated as follows:

$$p(b|D) = \frac{p(D|b)p(b)}{p(D)} \propto p(D|b)p(b) \quad [122]$$

In the above equation, p(b) is the unconditional joint probability distribution of the parameters in b (λ or σ). p(b) is typically referred to as the prior distribution, which is updated when new data, D, becomes available. p(D | b) is the likelihood (for level 1 of the

analysis, using 33 sites) of the data for given parameters b. p(D) is the probability of the observed data D. Since p(D) does not vary for a given dataset, the posterior distribution of b is proportional to the product of the prior and the likelihood, as described in the above equation.

Initially, when the first dataset D is used (in level 1), the prior p(b) can be based on existing data/knowledge and engineering judgement. In order to obtain the likelihood, $p(D|b)$, a probability distribution for the bias values, such as lognormal, needs to be assumed. For example, assuming that the data points in D follow a lognormal distribution, the value of $p(D|b)$ can be evaluated the following equation:

$$p(D|b) = \prod_i^{n_{tot}} LN(D_i, b) \quad [123]$$

where, n_{tot} is the number of data points in the dataset D, D_i is an individual data point, and $LN(D_i,b)$ represents the probability density value of the lognormal distribution with parameters b at a value of D_i. The above equation treats each data point, D_i, equally. However, data points can also be given a weight to indicate higher confidence or importance to the data point (i.e., confidence bias site parameter for level 2). For this purpose, the non-negative weights for each data point, w_i, can be used as followed:

$$p(D|b) = \prod_i^{n_{tot}} \big(LN(D_i, b)\big)^{w_i} \quad [124]$$

With the prior distribution and the likelihood values, the posterior distribution of b, which is proportional to $p(D|b)p(b)$ can be sampled using the Markov Chain Monte Carlo (MCMC) methods, which is based on the principle of random walks. The MCMC simulation is the technique to draw samples from the target PDF (in case of this research it is posterior PDF) with a Markov Chain, which converges with the target distribution. When the Markov Chain reaches convergence, the samples drawn from the Markov Chain are the same as those in the target distribution, so the samples in the Markov Chain can be used to study the properties of the target distribution. The validity of this method does not rely on the large sample assumption. Herein, an affine invariant MCMC algorithm by Goodman and Weare [139] that was implemented by Grinsted [140] is used.

For the next dataset (i.e., level 2 of the analysis), the above mentioned updating process can be used to determine the posterior2 by using the previous posterior1 distribution as the new prior2 distribution. Herein, the posterior distribution of b is modeled as a non-parametric joint multivariate density function using a multivariate kernel smoothing function that was implemented in MATLAB.

Evaluation of Site Variability using Probabilistic Analysis

Probabilistic analysis were used in this study to analyze the CPT data obtained from LA 1 site in Louisiana. Thirteen CPT tests were performed at LA 1 site. Analysis was performed through employing the program SGeMS. A characteristic of geostatistics and other stochastic methods is the ability to assign confidence intervals to the estimates. The confidence intervals are derived from cumulative distributions of random functions. Once a cumulative distribution is known, the options in terms of what confidence limits to employ are up to the user and can be any number in the domain extending from 0 to 100%.

Description and Subsurface Condition at LA 1 Site

In this study, the LA 1 site in Louisiana with several performed CPT was used to evaluate the probabilistic analysis. For the LA 1 site, the area is about 21,530 ft^2 (2,000 m^2), located at 30°26′00″N and 91°12′37.45″W, in which 13 CPT tests (75 ft. deep) were performed at different locations as shown in Figure 48.

Figure 48. Locations of the CPT points at LA 1 site

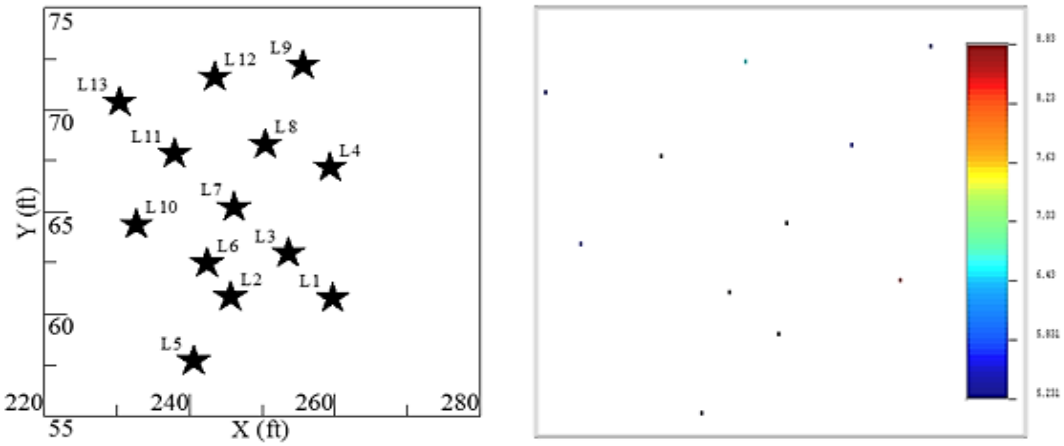

(a) Location of the CPT points

(b) Location of CPT points in SGeMS

The subsurface soil conditions for the LA 1 site was characterized using the results of CPT tests, as well as, the associated laboratory test results. The profiles of 13 CPT tests, the corresponding CPT soil classifications using the probabilistic region estimation method [134], and the CPT soil classification proposed by Robertson [135] are presented in Figure 141 of Appendix B. The maximum, minimum, and average COV of corrected

tip resistance (q_t) values for LA 1 site, are 1.67, 0.15, and 0.55 tsf, respectively. The site consists of alternating clayey and sandy layers. For the purpose of analysis, the subsurface soil condition at LA 1 site was divided into four soil layers: 0-10 ft., 10-34 ft., 34-46 ft. and 46-75 ft.

SGeMS Probabilistic Analysis

The SGeMS can read data from files in its own format and can also read files in GSLIB format, which is pretty much the standard format for geostatistical data. We have 13 CPT points in the LA 1 site. For each soil layer, the average for each CPT was calculated and then incorporated into the SGeMS data format. We have to give three inputs in the data, like X, Y, and Z (data). Here, in our analysis, X, Y, and Z are latitude, longitude and data (average CPT) for each CPT location. Then we plotted the data in the SGeMs platform.

After plotting the data, the variogram analysis was conducted. From the variogram analysis results, kriging can be done. In this study, we followed the ordinary kriging. To do the kriging in SGeMs, we need to expand the estimation entry on the algorithms panel and select the entry kriging. The middle part of the algorithms panel should then display two tabs, (General and Data and Variogram) for specifying the parameter controlling the kriging process. Next, 50 realizations of CPT using sequential Gaussian simulation were generated so that we can do the probabilistic analysis.

What the SGS algorithm really needs is the variogram of the normal-score transformed data, which was not computed. We can take a short-cut by assuming that the variogram of the normal score transformed data would look very much like the variogram of the raw data scaled to a unit sill. This is the case for these data, since the shape of the univariate porosity distribution is in fact reasonably normal.

If the probability distribution for the true value is N [$z^*(x_0)$, $\sigma^2(x_0)$], then its cumulative distribution is given as follows:

$$Prob\,[z \leq t]_{x_0} = F(t)_{x_0} = \int_{-\infty}^{t} \frac{1}{\sqrt{2\pi}} e^{-\frac{(t-\hat{z}(x_0))^2}{2\sigma^2(x_0)}} dz \qquad [125]$$

The probability estimate and its estimation variance completely determine the distribution of the variate (here CPT data) from which one can calculate the probability associated to any threshold or interval.

Suppose, we need to get the probability values when the data is between $q_{(t,avg)}$ - st.dev and $q_{(t,avg)}$ + st.dev. Then, the corresponding equation will be:

$$Prob\,[q_{t,avg} - st.dev \leq q_t \leq q_{t,avg} + st.dev\,]_{x_0} = Prob\,[z \leq q_{t,avg} + st.dev\,]_{x_0} - Prob\,[z \leq q_{t,avg} - st.dev\,]_{x_0} \quad [126]$$

Application of Site Variability in the Slope Stability Analysis

In order to study the effect of the spatial variability on the slope stability analysis, model of two soil layer and embankment was modeled and run for different scenarios. The model represents a typical subsurface soil condition. The clay soil layer on top and sand layer under it. The model details are shown in Figure 49. The soil properties used in the model for slope stability analysis (for drained and undrained conditions) are shown in Table 5.

Different scenarios were modeled to study the effect of variability of the soil layers and embankment properties variability on the embankment stability at drained condition. Bishop simplified, Janbu simplified and Spencer slice methods were used in the analyses. Brief description of the typical slice methods can be found in Appendix C. In this study 126 scenarios were run to investigate the effect of site variability (by increasing COV of friction angle, ϕ, cohesion, c, unit weight, γ, and changing the vertical and horizontal correlation lengths) on the coefficient variation of the factor of safety.

Figure 49. Case study model for slope stability analysis

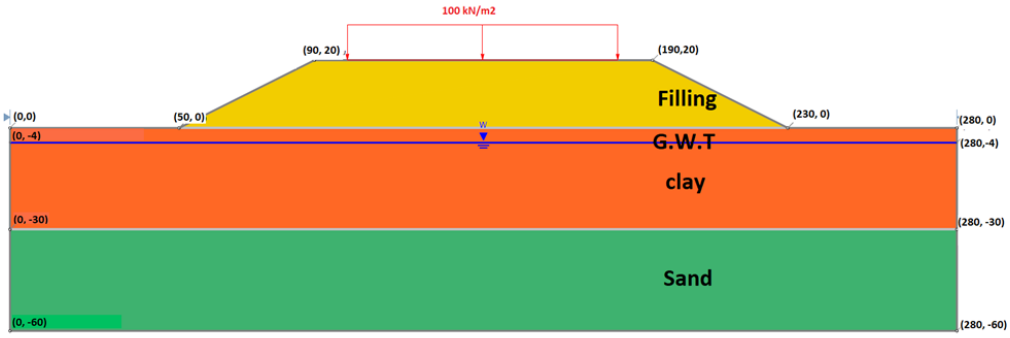

Table 5. Geotechnical Properties of soil layers for drained and undrained conditions

Layer	Properties	Symbol	Drained Values	Undrained Values
Filling	Cohesion	c	1 kPa	1 kPa
	Friction Angle	ϕ	35^o	35^o
	Unit Weight	γ	20 kN/m^3	20 kN/m^3
clay	Cohesion	c (or S_u)	20 kPa	40 kPa
	Friction Angle	ϕ	25^o	0
	Unit Weight	γ	20 kN/m^3	20 kN/m^3
sand	Cohesion	c	1 kPa	1 kPa
	Friction Angle	ϕ	35^o	35^o
	Unit Weight	γ	18 kN/m^3	18 kN/m^3

In this study, we considered the range of different soil parameters according to the variations reported in literature, as summarized in Table 6. For example, for the friction angle, ϕ, for sandy/clayey soil, we considered the range of COV of ϕ as 0-25% . In case of cohesion, c, we considered the range of COV of c to be 0-50%. When we are considering unit weight, γ, we considered the range of COV of γ as 0-10%. For the horizontal correlation length, we assumed low, mid and high horizontal correlation lengths as 65.6 ft. (20 m), 131.2 ft. (40 m), and 196.8 ft. (60 m), respectively according to the literature. However, for the vertical correlation length, we assumed low, mid and high vertical correlation length as 16.4 ft. (5 m), 6.6 ft. (2 m), and 0.98 ft. (0.3 m), respectively, according to the literature.

Table 6. Summary of variability of different soil parameters

Soil Type	Parameter	Parameter Range
Sandy and Clayey	Friction angle ([7], [78])	COV ranges from 0-25%
Clayey	Cohesion ([7], [141], (Shahin & Cheung, 2011)	COV ranges from 0-50%
Sandy and Clayey	Unit weight ([7], [55])	COV ranges from 0-10%
Sandy and Clayey	Correlation length ([7])	Horizontal - 20, 40, 60m
		Vertical – 0.3, 2, 5m

In the case of the spatial variability analyses, the statistics tool in the Slide 2018 2D software was activated. The coefficient variation of the material properties was put as value of the standard deviation for each single soil property. Latin-Hypercube probabilistic analysis sampling method was used to accomplish probabilistic analysis. A total of 1000 samples were generated and used in the analyses for each scenario. Log normal sample distribution was used.

For each iteration, the software used random properties as shown in Figure 50, and Figure 51 shows the different random generation of the friction angle at iterations numbers 2 and 1, respectively.

Figure 52, Figure 53, and Figure 54 show the factor of safety (FS) after the completion of slope stability analysis for scenario 11, 13 and 4, respectively. In case of the undrained condition, for clayey layers friction angle, $\phi = 0$, was considered.

Figure 50. Property contour value of friction angle of sample 2 of scenario 6

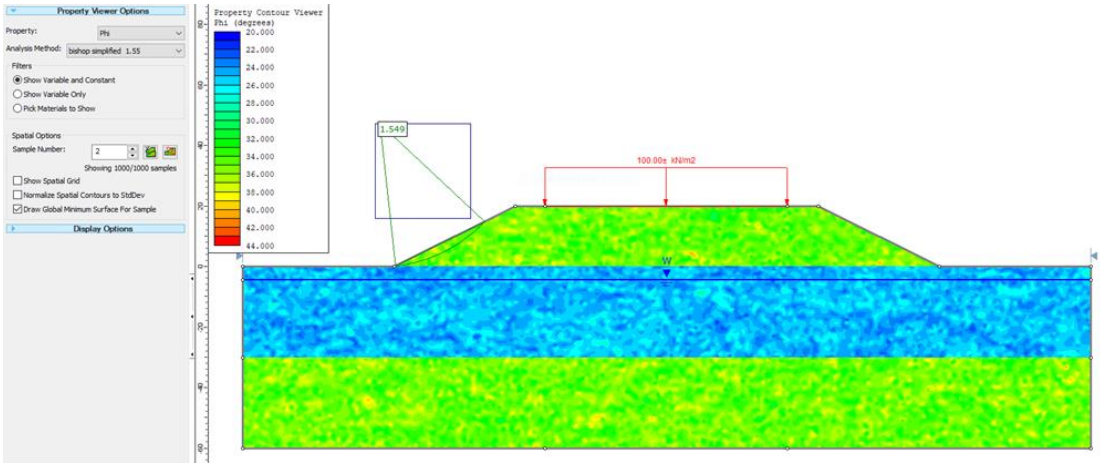

Figure 51. Property contour value of friction angle of sample 1 of scenario 34

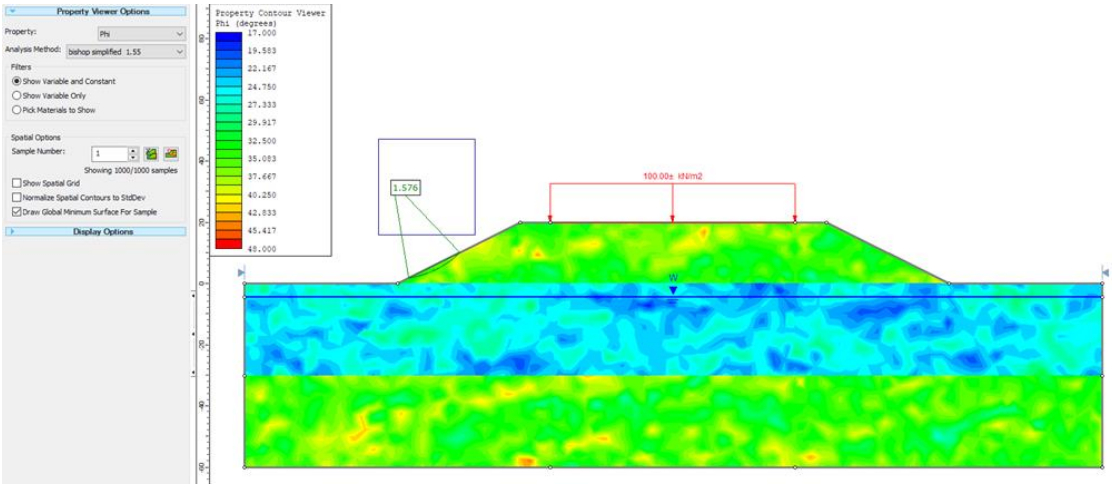

Figure 52. Factor of safety and critical slip circle of scenario 11

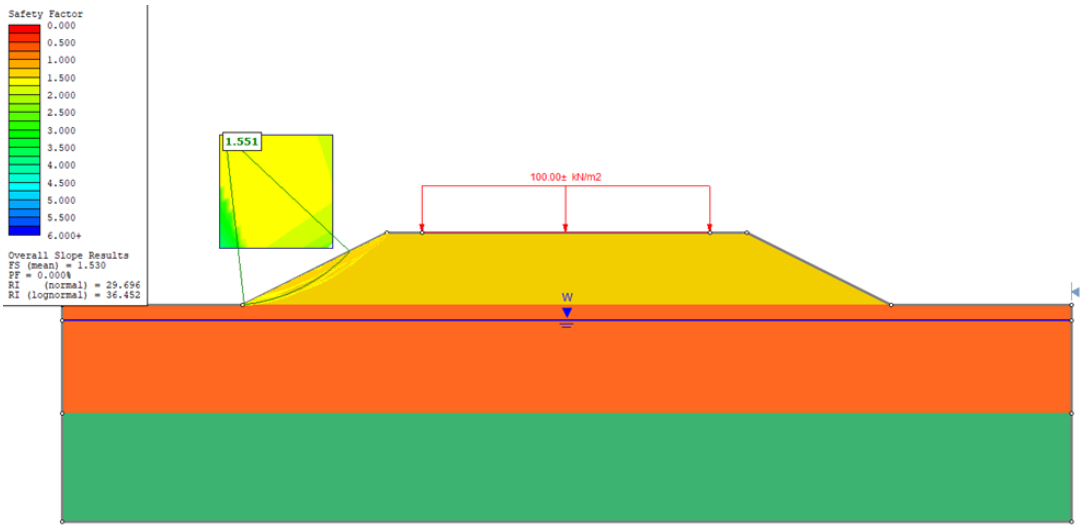

Figure 53. Factor of safety and critical slip circle of scenario 13

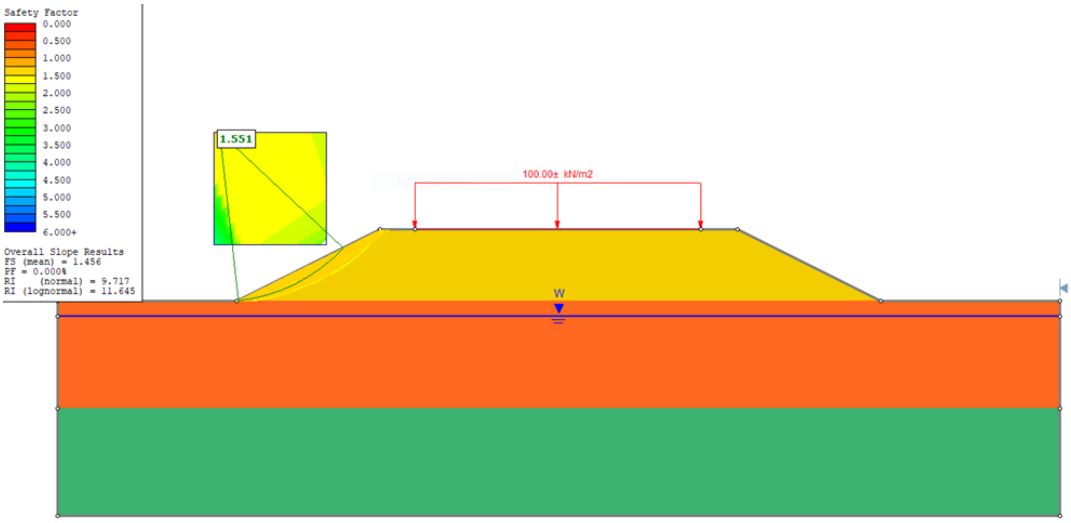

Figure 54. Factor of safety and critical slip circle of scenario 4

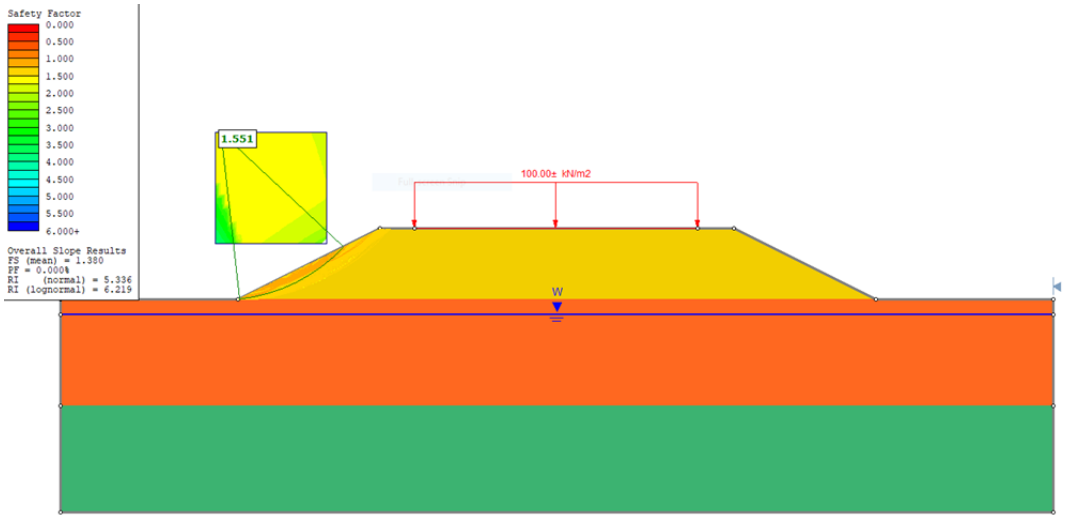

Application of Site Variability in Shallow Foundation Analysis

Effect of Site Variability on Bearing Capacity

Many researchers investigated the effect of site variability on the bearing capacity of the sallow foundations. In this study, different approaches will be used to study the effect of site variability on the bearing capacity of shallow foundation. These methods include the

second moment statistical analysis using the semivariogram ([54], [55]), and the Fenton and Griffiths [17] method.

To implement the spatial variability in shallow foundation design using the second moment statistical analysis using Vesper 6 software, a 6’ x 6’ foundation example is planned for design with a factor of safety (FS) of 3. In this analysis, lab data from unconsolidated undrained (UU) tests are considered as input parameter. The geotechnical design parameter that includes the undrained shear strength (S_u) is presented in Table 7; while the schematic diagram of the foundation example is described in Figure 55.

The first step in implementing spatial variability using the second moment statistical analysis is to plot the semivariogram for the S_u data and evaluate the range of influence (a) and the scale of fluctuation (θ), as will be described in the Results and Analysis section.

Table 7. S_u (psf) data assumed for analysis

Depth (ft.)	S_u (psf)
5	2475
6	2616
7	2518
8	2664
9	2359
10	2541
11	2706
12	3100
13	3072

Figure 55. Schematic diagram of shallow foundation for analysis

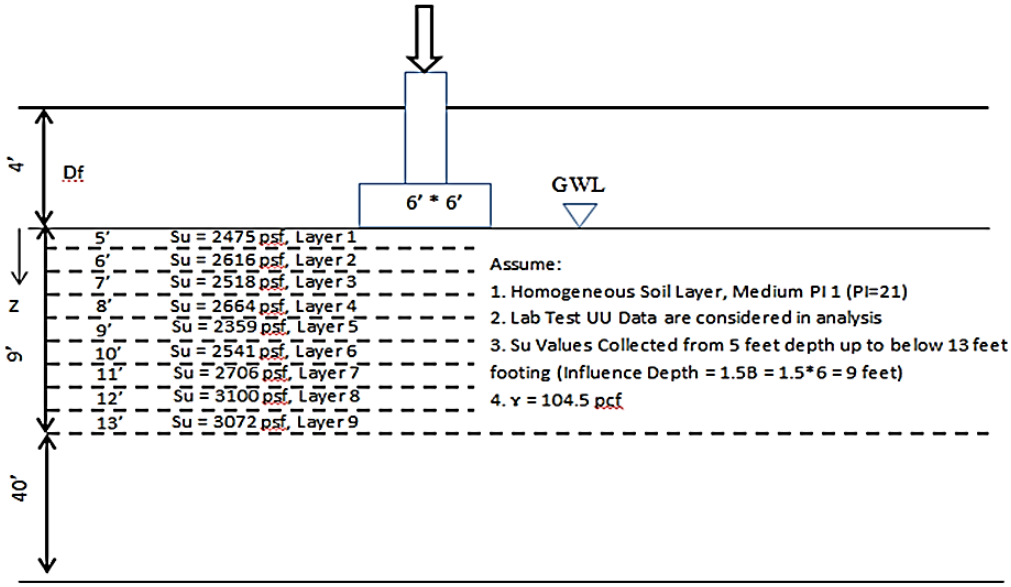

The Fenton and Griffiths [17] model is also used in this study to implement the spatial variability in evaluating the bearing capacity of shallow foundations. An open source software Rbear2D (http://random.engmath.dal.ca/rfem/) developed by Grifftith was used to compute the bearing capacity of shallow foundation considering site variability. The main software panel is presented in Figure 56. The software was used to analyze a 2D shallow foundation of 6 ft. width and element size of 0.5 ft. × 0.2 ft. Total of 1000 simulations were performed in this study.

Figure 56. User interface of Rbear2D software

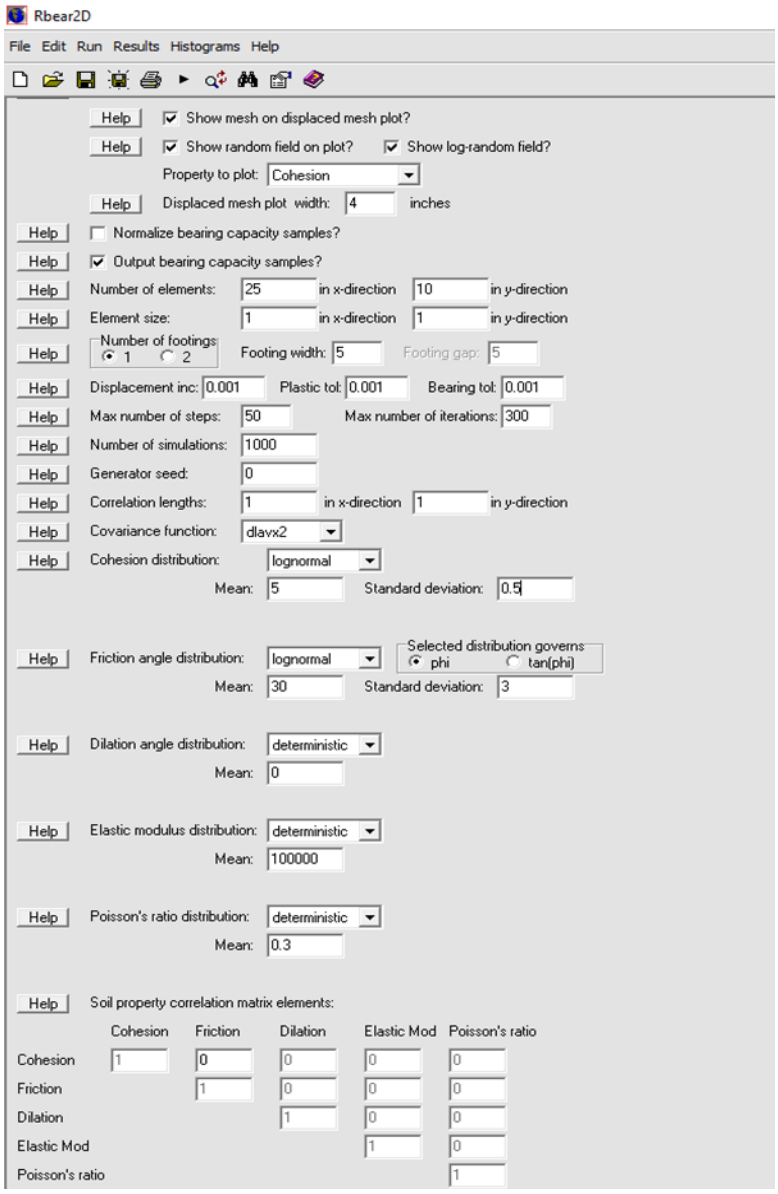

The vertical and horizontal correlation length were assumed to be 1 ft. (high vertical variability) and 60 ft. (high horizontal variability), respectively. The number of elements is 25 in the x-direction and 10 in the y-direction. The random distribution of soil properties is shown in Figure 57. In the case of soil without variation, the deformed soil mesh and the stress vectors under the foundation are similar to Therzaghi′s theory as shown in Figure 58 and Figure 59, respectively. The effect of the soil variability is investigated for different COV of cohesion and friction angle. The stress vector and mesh deformation are not symmetrical as shown in Figure 60. The deformed mesh usually follows the weakest soil path. At the end of every run, the bearing capacity and

corresponding standard deviation values were defined. As the soil variation increases, the bearing capacity decreases.

Figure 57. Random distribution soil properties

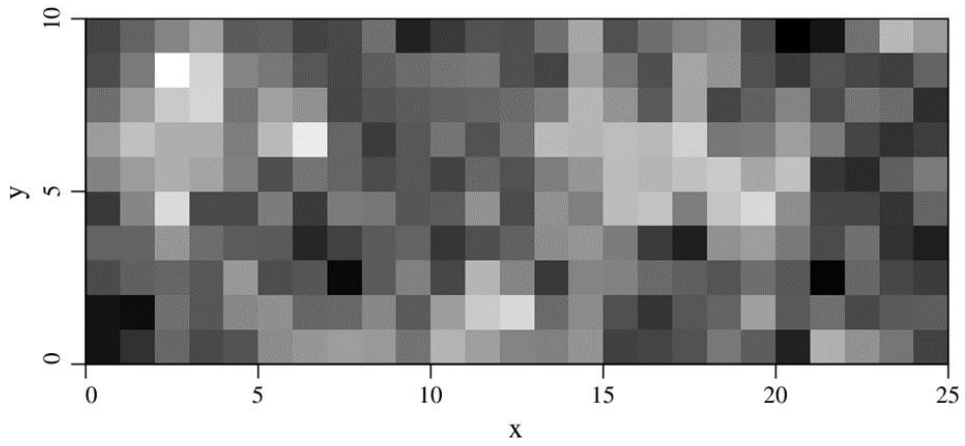

Figure 58. Typical deformed mesh at failure for soil without variation

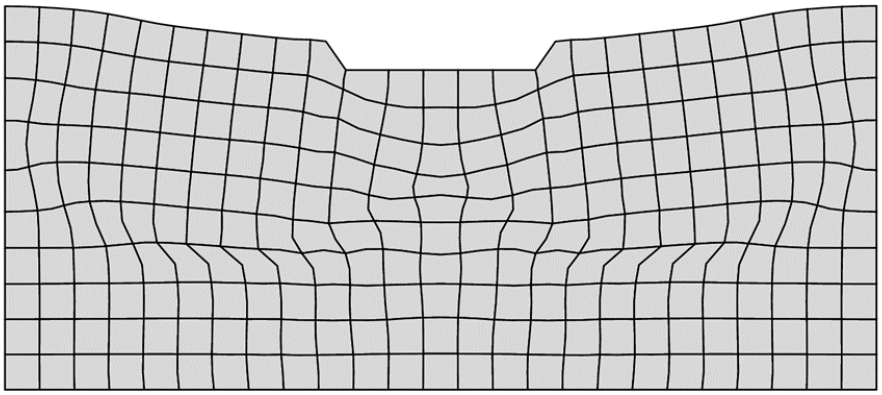

Figure 59. Typical soil stress vectors for soil without variation

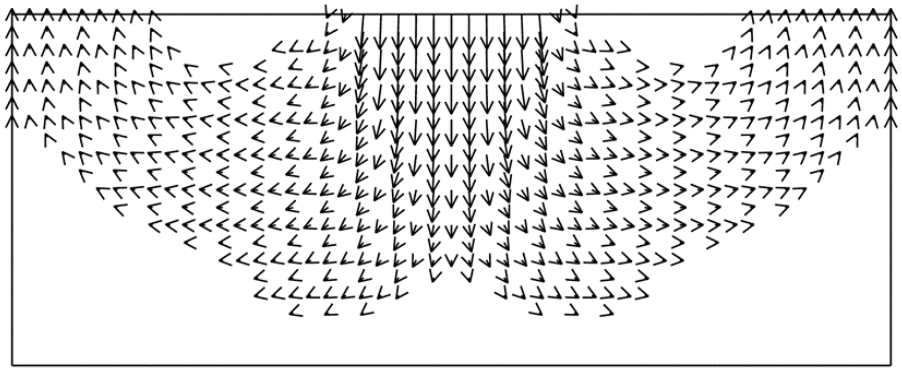

Figure 60. Typical distorted mesh deformation for soil with COV = 50%

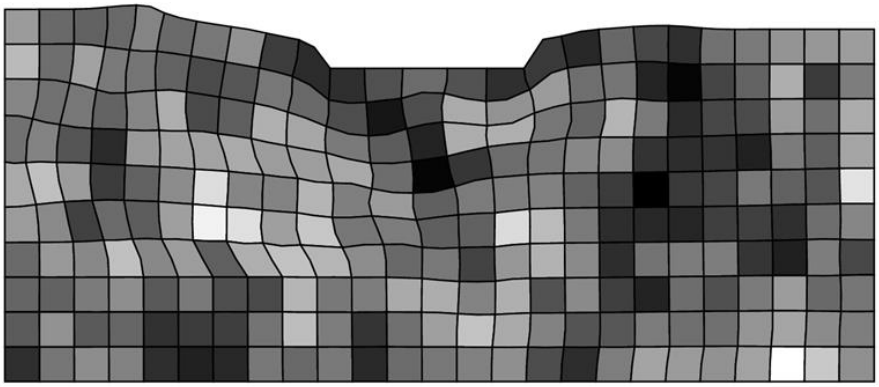

Variation of Soil Parameters

In this study, sandy soils with friction angles of 42º, 38º, 32º, respectively represent dense, medium dense, and loose sands (within range in literature) were selected to investigate the effect of soil variability on the bearing capacity of shallow foundations. In addition, clayey soils with cohesion and friction angle of 33º, 7 kPa; 30º, 4 kPa; and 20º, 2 kPa were selected to represent stiff, medium stiff, and soft clays, respectively, for the drained analysis condition. However, for the undrained condition, clay soils with undrained cohesion of 72, 36, 14.5 kPa were selected to represent stiff, medium stiff, and soft clays, respectively.

In this study, the range of COV for friction angle we considered to be from 0 to 25% (within range in literature), with an increase of 5% to investigate the effect of site variability. For cohesion, we considered the range of COV of cohesion from 0 to 50% (within range in literature), in which we increased COV by 10% to study the effect of site variability. For the horizontal variation, we assumed high horizontal correlation length of 60 ft.; while for the vertical variation, we also assumed high vertical correlation length of

1 ft., according to the literature. Table 8, Table 9, and Table 10 present the summary of variation of soil parameters for sand, drained condition clay and undrained condition clay, respectively.

Table 8. Parameters for different types of sandy soil

Soil Type		Cohesion, c (kPa)	Friction angle, ϕ (Degrees)	COVϕ (%)
Sand	Dense Sand	0	42	0-25%
	Medium dense sand	0	38	
	Loose sand	0	32	

Table 9. Parameters for different clayey soils for drained condition

Soil Type		Cohesion, c (kPa)	Friction angle, ϕ (Degrees)	COVc (%)	COVϕ (%)
Clay	Stiff clay	7	33	0-50%	0-25%
	Medium stiff clay	4	30		
	Soft clay	2	20		

Table 10. Parameters for different clayey soils for undrained condition

Soil Type		Cohesion, c (kPa)	Friction angle, ϕ (Degrees)	COVc (%)
Clay	Stiff clay	72	0	0-50%
	Medium stiff clay	36	0	
	Soft clay	14.5	0	

Reliability Analysis

Meyerhof gave the following equation to calculate the ultimate bearing capacity (q_u) for shallow foundation with footing width (B) and depth of footing (D_f):

$$q_u = cN_c s_c d_c + \gamma D_f N_q s_q d_q + 0.5\gamma B N_\gamma s_\gamma d_\gamma \quad [127]$$

where, N_c, N_q, and N_γ, are the bearing capacity factors; s_c, s_q, and s_γ are the shape factors; and d_c, d_q , and d_γ are the depth factors. The following is how the performance function is calculated in relation to the soil's ultimate bearing capacity:

$$g = q_u - P_S \quad [128]$$

where P_S is the vertical load. In this study, B and D_f were selected as 6 ft. and 3 ft., respectively. Three vertical loads of 27.4, 34.2, and 41.1 kips/ft. (400, 500 and 600 kN/m) were considered. The unit weight, cohesion and friction angle were selected as 127.5 pcf (20 kN/m^3), 209 psf (10 kPa) and 30^o, respectively. A Matlab code was developed for this part of analysis.

Application of Site Variability in Deep Foundation Analysis

In this study, we adopted the Naghibi [131] and Naghibi and Fenton [18] methodology for both the cohesive and cohesionless soils to evaluate the effect of soil variability on deep foundation design. We also expanded the applicability of Naghibi's [131] approach for the analysis of mixed soils. For the analysis of clayey (cohesive) soil, we did our analysis on the Red River site, which is located at Alexandria, Louisiana. Eight soil borings were performed to 95 ft. depth at different locations of the Red River site (Figure 142). For the analysis of mixed soil, we did our analysis on the Metairie site in which 15 soil borings were performed at different locations down to 105 ft. depth (Figure 45). A detailed discussion on the cohesive and cohesionless soil sites will be given later. An analysis was first performed for the cohesionless soil (using friction angle of 30^o) without considering the end bearing. Soil friction angle, ϕ, was considered with different COVϕ values of 0%, 10%, 20%, 30%, 40% and 50%. Different sampling location distances of 16.4 ft. (5 m), 32.8 ft. (10 m), 49.2 ft. (15 m), 65.6 ft. (20 m), and 82 ft. (25 m) were considered in this part of analysis.

In this study, we also updated the Naghibi's method (for both cohesive, cohesionless and mixed soils) in order to incorporate the end-bearing capacity in the design of deep foundations.

Incorporating End Bearing into Cohesive Soils

The unit end bearing capacity of piles tip on clay is given as follows [142]:

$$R_{EB} = N_c S_u \quad [129]$$

where, R_{EB} = unit end bearing of the pile, and N_c = bearing capacity factor = 9.0. According to Skempton [137], S_u = average undrained shear strength of clay for 1D below the tip.

Recalling the ultimate side resistance of a pile due to cohesion (c) is given as follows:

$$\hat{R}_u = pH\alpha\hat{c} \quad [130]$$

Adding the above two equations, the ultimate resistance of a pile becomes:

$$\hat{R}_u = pH\alpha\hat{c} + R_{EB} \quad [131]$$

Including $R_{EB} = 9c$, the above equation becomes:

$$R_u = \left(\frac{\alpha_L\hat{F}_L+\alpha_D\hat{F}_D}{\Phi_{df}}\right)\left(\frac{\bar{c}}{\hat{c}}\right) + R_{EB} \quad [132]$$

then, $R_u = \left(\frac{\alpha_L\hat{F}_L+\alpha_D\hat{F}_D+R_{EB}}{\Phi_{df}}\right)\left(\frac{\bar{c}}{\hat{c}}\right)$ [133]

Assuming $p_f = P[F > R_u]$, the above equation becomes:

$$p_f = P\left[F > \left(\frac{\alpha_L\hat{F}_L+\alpha_D\hat{F}_D+R_{EB}}{\Phi_{df}}\right)\left(\frac{\bar{c}}{\hat{c}}\right)\right] \quad [134]$$

then, $p_f = P\left[\frac{F\hat{c}}{\bar{c}} > \left(\frac{\alpha_L\hat{F}_L+\alpha_D\hat{F}_D+R_{EB}}{\Phi_{df}}\right)\right]$ [135]

Refereeing to the above equation for the failure probability calculation, the next two components are defined as follows:

$$W = \frac{F\hat{c}}{\bar{c}} \quad [136a]$$

$$q = \alpha_L\hat{F}_L + \alpha_D\hat{F}_D + R_{EB} \quad [136b]$$

By solving these equations, we will get:

$$p_f = P\left[W > \frac{q}{\Phi_{df}}\right] = P\left[lnW > \ln\left(\frac{q}{\Phi_{df}}\right)\right] = 1 - \Phi\left[\frac{\ln\left(\frac{q}{\Phi_{df}}\right)-\mu_{lnW}}{\sigma_{lnW}}\right] \quad [137]$$

then the geotechnical resistance factor, ϕ_{df}, can be determined as:

$$\Phi_{df} = \exp(lnq - \mu_{lnW} - \beta\sigma_{lnW}) \quad [138]$$

Incorporating End Bearing into Cohesionless Soil

The toe resistance of piles tip on cohesionless soil is calculated using the Nordlund method as follows:

$$R_{EB} = \alpha_t N'_q A_t q_t \quad [139]$$

where, α_t is the dimensionless factor (dependent on friction angle) (see Figure 61); N'_q is the bearing capacity factor (see Figure 62); q_t is the effective overburden pressure (at the

pile toe); and A_t is the cross-sectional area of the pile (at the pile toe). The average ϕ value within the toe influence zone [from 3D (diameter of the pile) above the toe to 3D below the toe], is selected as the ϕ value.

Figure 61. Relationship between α_t coefficient and friction angle for cohesionless soils

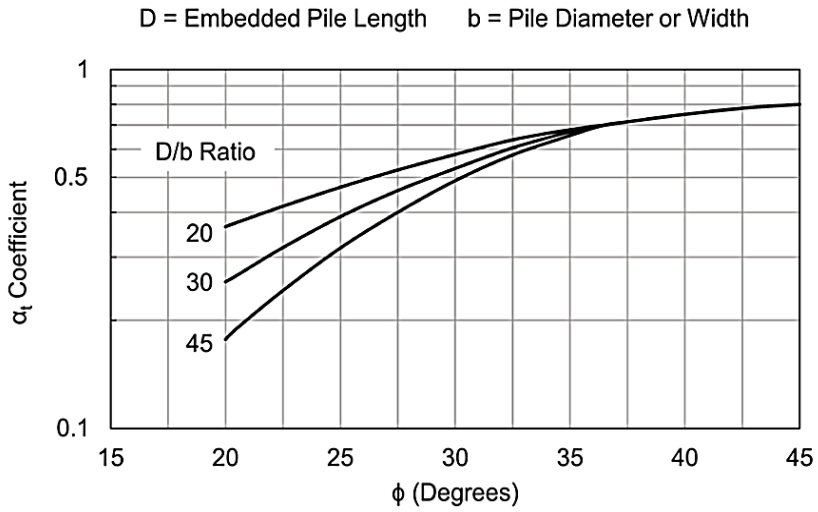

Figure 62. Relationship between N'_q and friction angle for cohesionless soils

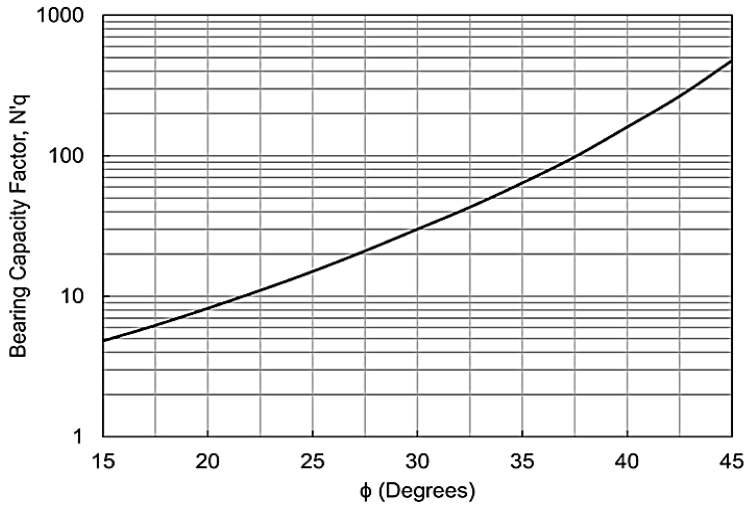

The characteristic ultimate geotechnical resistance, $\hat{R}_u$, is obtained as:

$$\hat{R}_u = \frac{1}{2} pa\gamma H^2 \left(1 - sin\,\hat{\phi}\right) tan\left(b\hat{\phi}\right) + R_{EB}; \text{ where, } R_{EB} = \alpha_t N'_q A_t q_t \quad [140]$$

The failure probability (actual), ρ_f, will be given as:

$$p_f = P[F > R_u] \quad [141]$$

And a successful design methodology will have $p_f \leq p_m$. By including the end bearing R_{EB}, the p_f becomes:

$$p_f = P\left[F > \left(\frac{\alpha_L \hat{F}_L + \alpha_D \hat{F}_D + R_{EB}}{\Phi_{df}}\right)\left(\frac{(1-sin\,\bar{\phi})\,tan\,(b\bar{\phi})}{(1-sin\,\hat{\phi})\,tan\,(b\hat{\phi})}\right)\right] = P\left[\left(\frac{F(1-sin\,\hat{\phi})\,tan\,(b\hat{\phi})}{(1-sin\,\bar{\phi})\,tan\,(b\bar{\phi})}\right) > \left(\frac{\alpha_L \hat{F}_L + \alpha_D \hat{F}_D + R_{EB}}{\Phi_{df}}\right)\right] \quad [142]$$

letting,

$\hat{X} = (1 - sin\,\hat{\phi})\,tan\,(b\hat{\phi})$; $\bar{X} = (1 - sin\,\bar{\phi})\,tan\,(b\bar{\phi})$; $q = \alpha_L \hat{F}_L + \alpha_D \hat{F}_D + R_{EB}$; and $Y = \frac{F\,\hat{X}}{\bar{X}}$

So the above equation can be written as:

$$p_f = P\left[Y > \frac{q}{\Phi_{df}}\right] \quad [143]$$

The p_f can be derived from the following:

$$p_f = 1 - \Phi\left[\frac{\ln\left(\frac{\hat{Q}}{\Phi_{df}}\right) - \mu_{lnY}}{\sigma_{lnY}}\right] \quad [144]$$

The reliability index, β, can be expressed as:

$$\beta = \frac{\ln\left(\frac{q}{\Phi_{df}}\right) - \mu_{lnY}}{\sigma_{lnY}} \quad [145]$$

The geotechnical resistance factor (Φ_{df}) is then calculated as follows:

$$\Phi_{df} = \exp(lnq - \mu_{lnY} - \beta\sigma_{lnY}) \quad [146]$$

In case of mixed soil layers, according to FHWA, for the piles terminated into a cohesive layer, use the R_{EB} (unit end bearing) for cohesive soil. For piles terminated into a cohesionless layer, use the R_{EB} (unit end bearing) for cohesionless soil.

Studied Case Sites

Cohesive Soil Site

The Red River site was selected here to analyze the effect of site variability on deep foundations for cohesive soil condition. Eight soil borings were performed in this site down to 105 ft. depth. The locations of soil borings for the Red River site were presented earlier in Figure 44c, and the subsurface soil profile with soil classification and undrained shear strength are presented in Figure 142 of Appendix B. For the Red River site, four soil layers were identified for analysis: 0-20 ft., and 20-50 ft., 50-70 ft., and 70-115 ft.

For the analysis purpose, we assumed our pile is located at the black (round) point. The corresponding distances of soil borings R1, R2, …, and R8 from the pile location are 40.5 ft. (12.33 m), 46.8 ft. (14.27 m), …, and 120.0 ft. (36.57 m), respectively as described in Figure 63(a-c). The weighted average of undrained shear strength (S_u), coefficient of variation of S_u (COV_{Su}), and standard deviation of S_u (σ_{Su}) for R1 are 2201 psf (105.39 kPa), 0.31 and 44, respectively. The weighted average of S_u, COV_{Su}, and σ_{Su} for R2 are 1773.6 psf (84.92 kPa), 0.25 and 47, respectively. Finally, the weighted average of S_u, COV_{Su}, and σ_{Su} for R8 are 1957.8 psf (93.74 kPa), 0.47 and 44, respectively.

Cohensionless Soil Site

Since we do not have any site in this study with only cohesionless soil, we considered a site with an average value of friction angle, $\phi = 30^o$, and different coefficients of variations, COV_ϕ, that ranged from 0% to 50%. In addition, we considered different boreholes with different sampling distances that ranged between 16.4 ft. (5 m) and 82 ft. (25 m).

Mixed Soil Site

The Metairie site was selected for analyzing the effect of soil variability on deep foundations for mixed soil condition. Fifteen soil borings were performed at different locations in Metairie site down to 105 ft. depth. The locations of these soil borings were presented earlier in Figure 44a. The subsurface soil profile with soil classification and undrained shear strength for Metairie site are presented in Figure 45. Four different soil layers were identified in Metairie site for use in analysis: two clayey layers (I: 0 to 29 ft. and III: 48 to 78 ft.), with total of 59 ft.; and two sandy layers (II: 29 to 48 ft. and IV: 78 to 105 ft.), with total of 46 ft.

Figure 63. Distance from the pile and soil classification of different point at Red River site

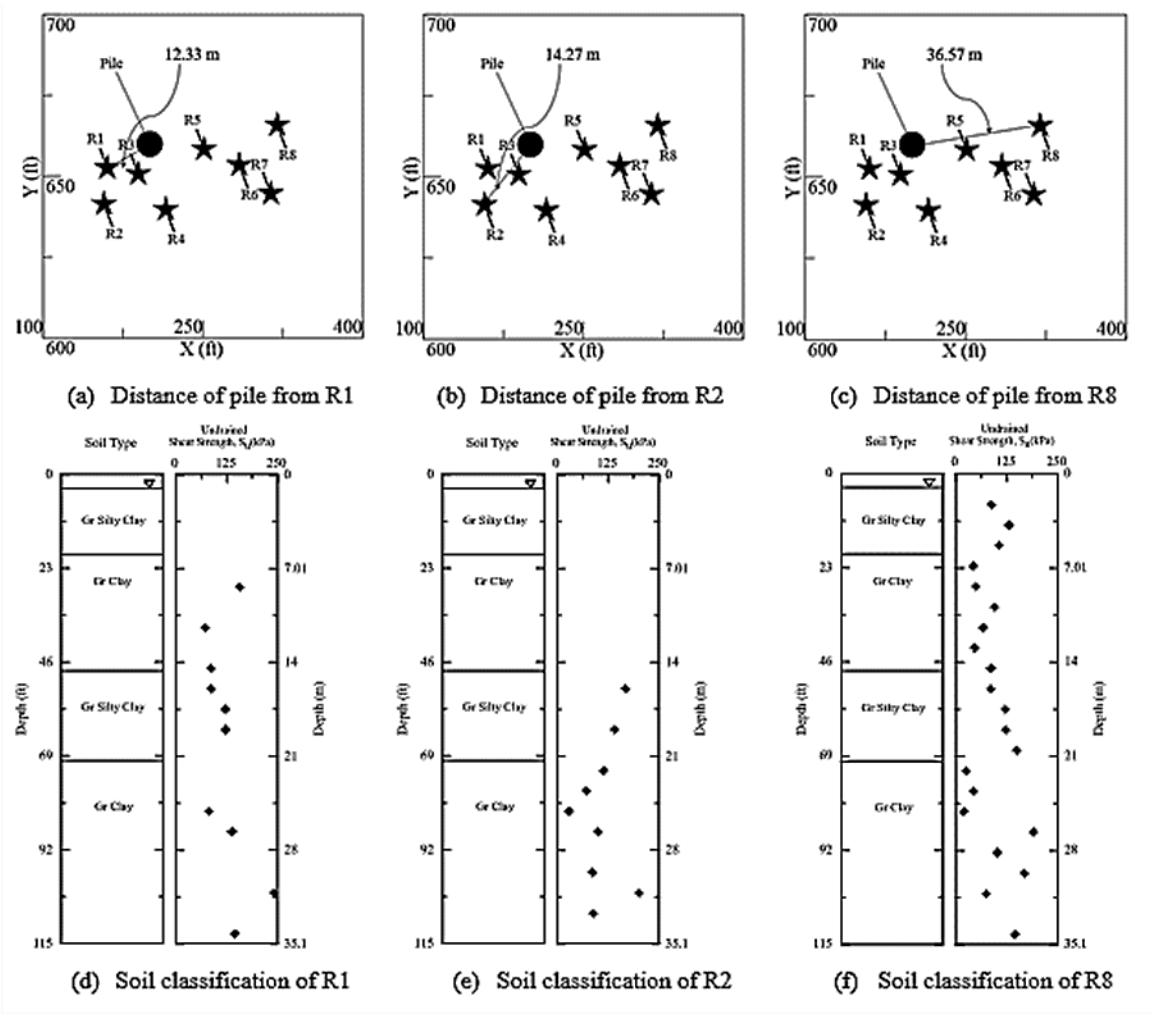

The mean of S_u, COV_{Su}, and σ_{Su} for the layer I are 229.8 psf (11.00 kPa), 0.31 and 3.4, respectively. For layer III, the mean of S_u, COV_{Su}, and σ_{Su} are 647.5 psf (31.00 kPa), 0.24 and 8.3, respectively. For layer II, the mean of friction angle, ϕ, COV_{ϕ}, and σ_{ϕ} are 42°, 0.36 and 15.12, respectively. For layer IV, the mean of ϕ, COV_{ϕ}, and σ_{ϕ} are 36°, 0.32 and 11.73, respectively. Therefore, the overall weighted averages for the two clay layers (I: 0 to 29 ft. and III: 48 to 78 ft.) are the mean of S_u, COV_{Su}, and σ_{Su} are 480.4 psf (23.00 kPa, 0.27. and 5.85, respectively. The overall weighted averages for the sandy soil layers (II: 29 to 48 ft. and IV: 78 to 105 ft.) are the mean of ϕ, COV_{ϕ}, and $\sigma\phi$ are 39°, 0.35, and 13.06, respectively.

For the analysis purpose, we assumed our pile is located at the black (round) point. The corresponding distances of soil borings M1, M2, and M11 from the pile location are 188

ft. (57.31 m), 190.5 ft. (58.07 m), and 129.2 ft. (39.37 m), respectively, as shown in Figure 64(a-c). Meanwhile, Figure 64 (d-f) shows the values of undrained shear strength and friction angle for the soil borings M1, M2, and M11.

Figure 64. Distance from the pile and soil classification of different point at Metairie site

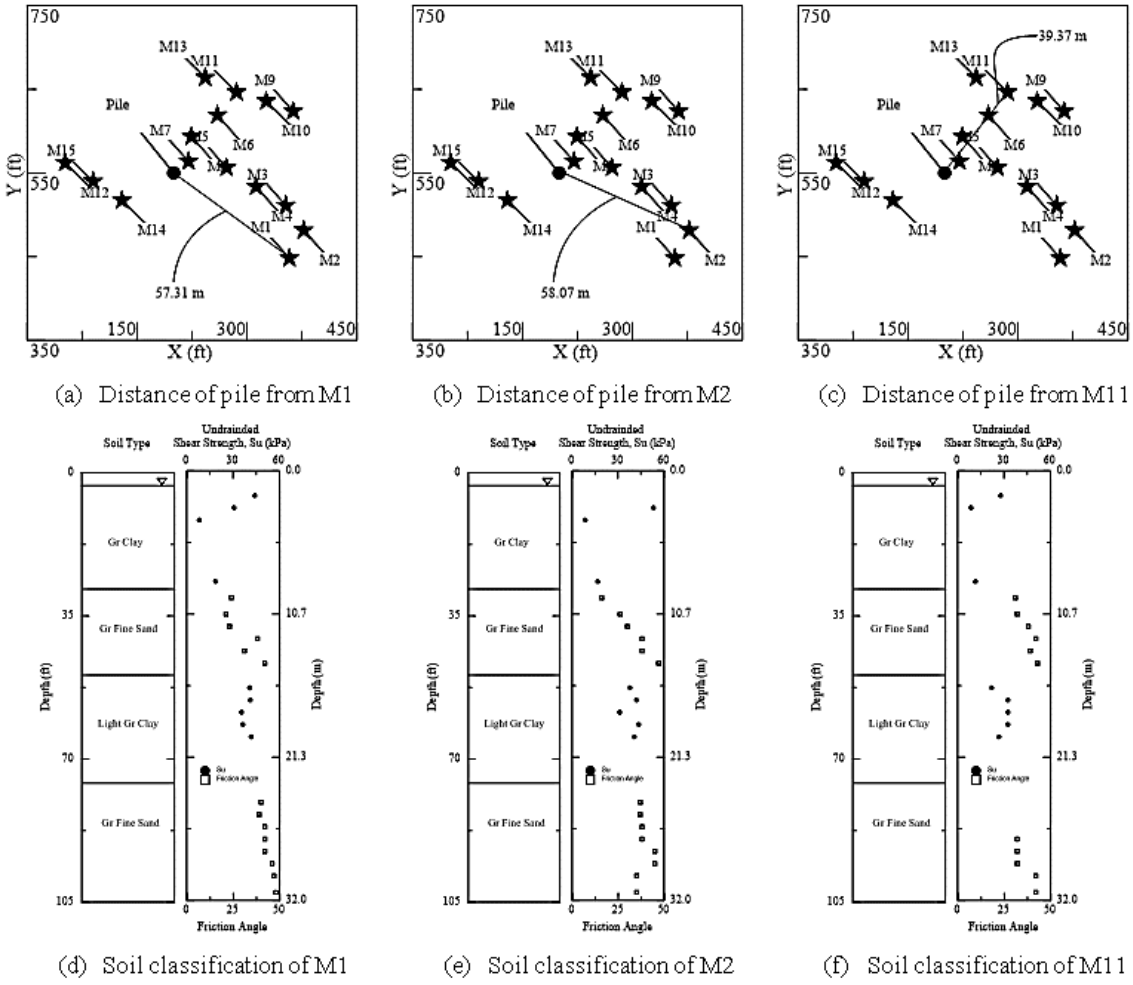

(a) Distance of pile from M1 (b) Distance of pile from M2 (c) Distance of pile from M11

(d) Soil classification of M1 (e) Soil classification of M2 (f) Soil classification of M11

Analysis and Results

Laboratory and Field Tests

This section includes the results and analysis of all experimental data, which include in-box, field and laboratory tests. Analyses are performed based on the Gauge R & R method, which includes the X-Bar/R method and the ANOVA (Analysis of Variance). Besides, the second moment (SM) statistics is also used where Gauge R & R method could not apply. The X-Bar/R and the ANOVA methods are followed from Measurement System Analysis (MSA) manual (4th Edition) (page 118-121, 195-198).

Results and Analysis of In-Box Tests

Tests were performed in the front, middle, and the back locations of the box. In order to apply the X-Bar/R and the ANOVA methods, the front, middle, and back locations are considered as specimen 1, 2, and 3, respectively. Data are then corrected with typical Poison's ratio if necessary. Figure 65 illustrates the specimen determination for analysis.

Figure 65. Specimen determination for analysis

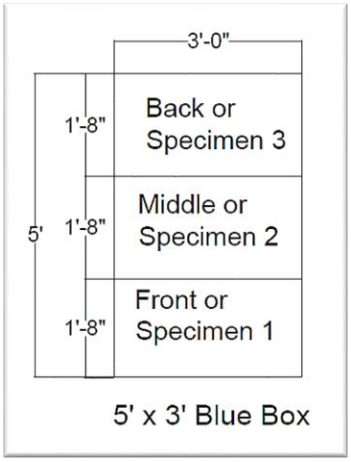

The Gauge R & R method can be applied for the Geogauge, Light Falling Weight Deflectometer (LFWD) and Dirt Portable Seismic Analyzer (D-SPA) whereas only the FOSM can be applied for the DCP, NDG, and the E-Gauge. The Gauge R & R method

can’t be applied for the DCP as repeatability can’t be measured, and for the NDG and the E-Gauge, reproducibility can’t be determined.

Analysis of Geogauge, LFWD and D-SPA Data according to X-Bar/R Method

To assess the variability within the device, operator and specimen; the repeatability and reproducibility; and specimen variability have to be considered. The Geogauge, LFWD, and D-SPA data can be evaluated using the X-Bar/R method as this method allows repeatability (repetition), reproducibility (operator variation), and specimen variability. Table 11 illustrates the calculation of averages, total averages, ranges, and average ranges of data for different operators according to the X-Bar/R method for the five different operators for sand soil and Geoguge device.

Table 11. Analysis of data according to X-Bar/R method for sand soil using Geogauge

Material	Location	Operator 1				
		Data	Average	Total Average	Range	Average Range
		MPa	MPa	MPa	MPa	MPa
Sand	Front or Specimen 1	59.16	60.03	58.78	2.00	1.82
		59.77				
		61.16				
	Middle or Specimen 2	60.55	60.84		0.43	
		60.98				
		60.98				
	Back or Specimen 3	56.65	55.46		3.04	
		53.61				
		56.13				

Material	Location	Operator 2				
		Data	Average	Total Average	Range	Average Range
		MPa	MPa	MPa	MPa	MPa
Sand	Front or Specimen 1	54.04	50.49	49.73	6.51	2.86
		47.54				
		49.88				
	Middle or Specimen 2	50.05	49.24		1.47	
		48.58				
		49.10				
	Back or Specimen 3	49.36	49.45		0.61	
		49.79				
		49.19				

Material	Location	Operator 3				
		Data	Average	Total Average	Range	Average Range
		MPa	MPa	MPa	MPa	MPa
Sand	Front or Specimen 1	59.34	58.53	57.75	1.65	2.46
		58.55				
		57.69				
	Middle or Specimen 2	55.78	55.43		3.47	
		53.52				
		56.99				
	Back or Specimen 3	58.29	59.31		2.26	
		59.08				
		60.55				

Material	Location	Operator 4				
		Data	Average	Total Average	Range	Average Range
		MPa	MPa	MPa	MPa	MPa
Sand	Front or Specimen 1	56.04	55.61	54.81	0.78	2.05
		55.52				
		55.26				
	Middle or Specimen 2	50.75	51.99		3.64	
		50.83				
		54.39				
	Back or Specimen 3	55.87	56.82		1.73	
		57.60				
		56.99				

Material	Location	Operator 5				
		Data	Average	Total Average	Range	Average Range
		MPa	MPa	MPa	MPa	MPa
Sand	Front or Specimen 1	49.79	51.12	51.02	3.73	2.89
		50.05				
		53.52				
	Middle or Specimen 2	51.61	51.76		2.69	
		50.49				
		53.18				
	Back or Specimen 3	50.92	50.17		2.26	
		50.92				
		48.67				

At first, the total average and average range need to be calculated for each operator to determine the repeatability and reproducibility. The bias correction factors can be determined from Table 3. After calculating the specimen variability, the total variability can be evaluated. Using the total variability and data average, the coefficient of variations can be determined. All equations required to calculate total variability are described earlier in Table 1. Table 12, Table 13, Table 14, and Table 15 show calculations of repeatability, reproducibility, specimen variability and the coefficient of total variability, respectively.

Table 12. Repeatability analysis according to X-Bar/R method

Analysis - Repeatability (EV)		
Average Range (R-Bar)	Bias Correction Factor (d2)	Repeatability or Equipment Variation, σ repeatability (R-bar/d2)
MPa		MPa
2.89	1.693	1.7

Table 13. Reproducibility analysis according to X-Bar/R method

Analysis - Reproducibility (AV)					
Range of average of operators (Ro)	Bias Correction Factor (d2*)	Number of specimens, (n)	Number of measurements repetition, (r)	EV^2 (Equipment Variation, σ repeatability)	Reproducibility σ reproducibility
MPa					MPa
9.05	1.74	3.00	3.00	1.43	5.18

Table 14. Specimen variability analysis according to X-Bar/R method

Material	Specimen 1	Specimen 2	Specimen 3	Specimen Variability (SV)		
	Data Avg.	Data Avg.	Data Avg.	Range of the specimen average (Rs)	Bias Correction Factor (d2*)	Specimen Variability, σ specimen (Rs/d2*)
	MPa	MPa	MPa	MPa		MPa
Sand	55.15	53.85	54.24	1.3	3.5	0.37

Table 15. The coefficient of variation (COV) analysis according to X-Bar/R method

Combined Device Variability	Specimen Variability (SV)	Total Variability (TV)	Average of Modulus Measurements	COV of Total Variability
GRR (GAUGE R&R), $\sqrt{(EV^2+AV^2)}$	Specimen Variability, σspecimen (Rs/d2*)	Total Variability, $\sqrt{(EV^2+AV^2+SV^2)}$	Total Average	The coefficient of variations
MPa	MPa	MPa	MPa	%
5.4	0.4	5.5	54.4	10.0

Analysis of Geogauge, LFWD and D-SPA data according to ANOVA Method

Another statistical technique to evaluate the total variability is analysis of variance (ANOVA). This technique is superior to the X-Bar/R method as it incorporates operator – specimen interaction. Equations required to calculate the total variability are taken from Table 2. ANOVA analysis is performed via the Statistical Analysis System (SAS) program where the probability is taken for the 95 percent confidence interval. Table 16 describes the process to calculate the total variability.

Table 16. The coefficient of variation (COV) analysis of Geogauge according to ANOVA method

Geogauge - ANOVA									
Material Type	Avg.	EV^2	$AV^2 = \theta^2 + \alpha^2$			SV^2	Gauge R & R	TV (Total Variability)	COV
		MSSE	θ^2	α^2	$\theta^2 + \alpha^2$	υ^2	$\sqrt{(EV^2 + AV^2)}$		
	MPa						MPa	MPa	%
Sand	54.4	2.2	14.5	3.7	18.2	0.4	4.5	4.6	8.4

Here, EV = Equipment Variability, AV = Appraiser (Operator) Variability, SV = Specimen Variability, MSSE = Mean Sum of Square Error.

Summary of the COV for the Geogauge, LFWD, and D-SPA is presented in Table 17. The table shows that the COV for Geogauge ranges from 5.1% to 15.3% for the X-Bar/R method; while it varies from 7.4% to 18.1% for the ANOVA method. For LFWD, the COV ranges from 7.4% to 14.3% and 8.2% to 24.4% for the X-Bar/R method and the ANOVA method, respectively. For D-SPA, the COV ranges from 4.2% to 9.6% for the X-Bar/R method; while it varies from 6.7% to 15.4% for the ANOVA method. In addition, the COV was also calculated using the second moment statistics and is also presented in Table 17. The ranges of COV of Geogauge, LFWD, and D-SPA data ranges from 6.7% to 15.6%, 10.9% to 20.8% and 5.9% to 13.4%, respectively. Moreover, the COV for the high PI (PI=53) with 5% lime and 4% cement, medium PI 2 (PI=31) and high PI (PI=53) are the greatest for Geogauge, LFWD and D-SPA, respectively.

While comparing the variability among the materials tested in the box with the Geogauge and LFWD devices, the medium PI 2 (PI=31) soil shows the higher COV. Among all statistical techniques, the maximum COVs were obtained from ANOVA and second moment methods for LFWD, which are 24.4% and 20.8%, respectively. In the case of the

D-SPA, the maximum COV was evaluated using the ANOVA method for medium PI 3 (PI=35) soil.

Table 17. Summary of COVs of Geogauge, LFWD, and D-SPA data according to the X-Bar/R and ANOVA methods

Material	Geogauge			LFWD			DSPA		
	Second Moment	X-Bar/R	ANOVA	Second Moment	X-Bar/R	ANOVA	Second Moment	X-Bar / R	ANOVA
	COV	COV	COV	COV	COV	COV	COV	COV	COV
	%	%	%	%	%	%	%	%	%
Sand	7.6	9.9	8.3	10.9	7.4	13.1	6.5	5.5	6.7
RAP	7.1	7.2	7.4	11.4	12.9	12.4	5.9	4.2	6.8
Low PI (PI=11)	11.4	8.8	12.2	14.2	11.6	19.1	-	-	-
High PI (PI=53)	7.2	5.1	8.3	11.3	10.6	11.8	10.0	5.4	10.2
High PI (PI=53) +5% lime + 4% Cement	14.9	12.5	16.5	15.9	10.3	18.4	-	-	-
Medium PI 3 (PI=35) + 5% lime + 4% Cement	11.0	10.8	11.8	15.6	12.4	18.7	-	-	-
Kentucky Limestone	11.7	8.7	13.7	11.9	13.1	13.4	- -	- -	- -
Mexican Limestone	8.2	8.4	8.6	7.8	8.8	8.2	-	-	-
Medium PI 1 (PI=21)	6.7	7.2	6.9	16.3	11.7	19.4	-	-	-
Medium PI 2 (PI=31)	15.6	13	18.1	20.8	14.3	24.4	9.2	7.8	10.2
Medium PI 3 (PI=35)	14	10.1	15.8	16.8	11.3	18.3	13.4	9.6	15.4
Low PI (PI=11) with 3% Cement	15.2	15.3	17	16.9	9.5	20.4	-	-	-

Analysis of Dynamic Cone Penetrometer (DCP) Data

The DCP tests were conducted on 12 different geomaterials inside the box. The profile of DCP index (DCPI) in (mm/blow) was calculated for each test. The DCPI is an indication of the strength of material with depth. The lower the DCPI, the higher the strength of geomaterial. For the compacted materials with high maximum dry density and optimum moisture content, the DCPI values were low. Figure 66 presents examples of DCPI profile for sand, which shows the DCPI values decrease along the depths.

Figure 66. Examples of DCPI profiles for sand

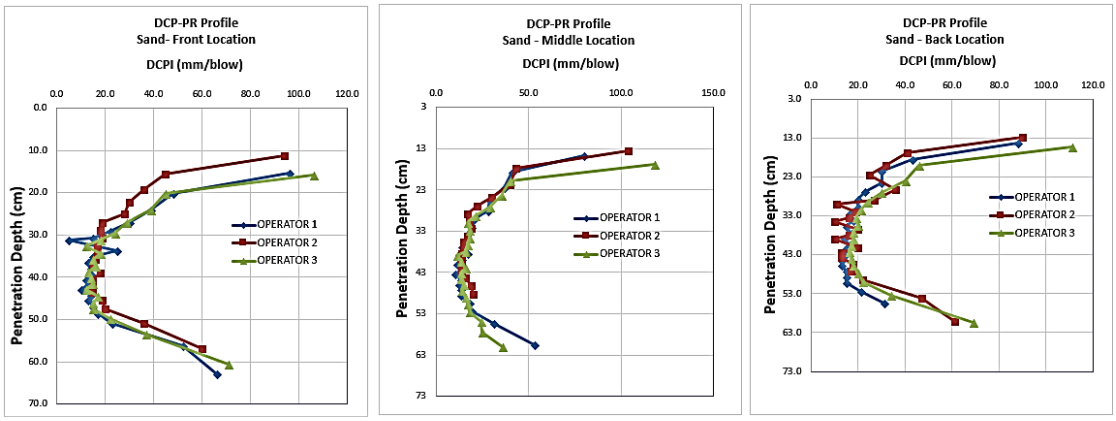

As the DCP tests were performed by three operators, the operator-related variabilities are grouped into three segments. Therefore, the COV can be found for operator 1, operator 2, and operator 3, which is shown in Table 18. From the summary of the operator-related variability, the COV range from 1.6% to 16.4%. The value of COV was the lowest for Kentucky limestone and the highest for High PI (PI=53) soil.

Summary of the location-related variability of the DCPI average (mm/blow) is presented in Table 19, in which the COV range from 0.4% to 18.1%.

Table 18. Summary of operator-related variability of DCPI avg. (mm/blow)

Material	Operator 1			Operator 2			Operator 3		
	DCPI Avg.	SD	COV	DCPI Avg.	SD	COV	DCPI Avg.	SD	COV
	mm/ blow	mm/ blow	%	mm/ blow	mm/ blow	%	mm/ blow	mm/ blow	%
Low PI (PI=11)	15.8	1.5	9.5	15.9	0.7	4.5	15.3	0.5	3.0
Mexican Limestone	2.7	0.1	2.1	3.1	0.3	10.0	2.3	0.1	2.5
High PI (PI=53)	52.5	8.6	16.4	48.5	5.0	10.4	50.7	5.5	10.8
Medium PI 1 (PI=21)	27.9	1.0	3.5	27.1	0.9	3.2	31.7	3.8	12.0
Medium PI 2 (PI=31)	28.3	0.8	2.7	31.4	2.0	6.3	34.6	1.8	5.2
Medium PI 3 (PI=38)	36.8	4.7	12.8	35.3	5.4	15.2	37.0	5.9	16.0
Sand	24.7	1.3	5.3	26.9	0.7	2.4	27.7	3.4	12.3
RAP	9.0	0.4	4.0	8.0	0.3	3.8	6.8	0.4	5.3
Kentucky Limestone	3.3	0.1	1.8	3.6	0.1	1.6	3.0	0.1	3.9
Medium PI 3 (PI=38) with 5% Lime & 4% Cement	17.8	0.8	4.7	17.9	2.0	11.0	17.8	0.7	4.2
Low PI (PI=11) with 3% Cement	14.7	1.1	7.4	13.1	0.9	7.0	15.0	0.7	4.4
High PI (PI=53) with 5% Lime & 4% Cement	20.2	2.1	10.2	20.2	2.0	9.7	20.7	1.3	6.3

Table 19. Summary of location-related variability of DCPI avg. (mm/blow)

Material	Location 1			Location 2			Location 3		
	DCPI Avg.	SD	COV	DCPI Avg.	SD	COV	DCPI Avg.	SD	COV
	mm/ blow	mm/ blow	%	mm/ blow	mm/ blow	%	mm/ blow	mm/ blow	%
Low PI (PI=11)	15.0	0.1	0.4	16.6	0.9	5.2	15.4	0.8	5.3
Mexican Limestone	2.7	0.4	13.2	2.8	0.5	18.1	2.6	0.3	11.0
High PI (PI=53)	58.2	5.8	10.0	50.1	2.9	5.7	44.0	2.9	6.6
Medium PI 1 (PI=21)	31.6	4.0	12.7	32.9	4.4	13.3	29.5	4.6	15.7
Medium PI 2 (PI=31)	32.8	3.7	11.3	31.4	3.5	11.1	30.0	2.5	8.4
Medium PI 3 (PI=38)	38.3	1.1	2.9	40.4	1.0	2.5	30.3	1.2	3.8
Sand	27.1	1.0	3.5	24.7	1.5	6.0	27.5	3.3	12.0
RAP	7.9	1.3	16.6	7.8	0.9	11.6	8.2	1.2	14.1
Kentucky Limestone	3.3	0.4	10.8	3.3	0.3	9.6	3.3	0.4	10.8
Medium PI 3 (PI=38) with 5% Lime & 4% Cement	18.4	1.6	8.9	18.1	0.8	4.3	17.0	0.6	3.8
Low PI (PI=11) with 3% Cement	14.4	0.6	3.9	14.8	1.3	9.0	13.6	1.6	11.4
High PI (PI=53) with 5% Lime & 4% Cement	20.2	2.1	10.2	20.2	2.0	9.7	20.7	1.3	6.3

Analysis of Nuclear Density Gauge (NDG) Data

The NDG tests were performed in three different locations of the box by one operator. Therefore, only the location-related variability analysis was performed for the NDG. The location-related variability can be analyzed for dry density and moisture content. Table 20 and Table 21 present the location-related variabilities for dry density and moisture content of the materials, respectively.

It can be seen from the tables that the COVs range from 0.5% to 6.1% for dry density and from 2.4% to 25.1% for moisture content. For dry density, the High PI (PI=53) with 5% lime, 4% cement, and Mexican limestone show the maximum and minimum COVs, respectively. For the moisture content, maximum and minimum COV were observed for the high PI (PI=53) with 5% lime & 4% cement and the low PI (PI=11) with 3% cement, respectively.

Table 20. Summary of location-related variability of COV of NDG (dry density)

Material	Front Location			Middle Location			Back Location		
	Data Avg.	SD	COV	Data Avg.	SD	COV	Data Avg.	SD	COV
	pcf	pcf	%	pcf	pcf	%	pcf	pcf	%
Low PI (PI=11)	104.6	1.3	1.3	105.7	1.7	1.6	104.6	1.8	1.7
Mexican Limestone	125.4	0.8	0.6	124.2	0.6	0.5	125.3	1.8	1.5
High PI (PI=53)	77.7	2.4	3.1	78.0	1.3	1.6	76.9	2.1	2.7
Medium PI 1 (PI=21)	103.1	2.9	2.8	102.1	0.7	0.7	101.2	1.0	0.9
Medium PI 2 (PI=31)	93.6	2.7	2.8	95.4	2.9	3.1	94.7	1.8	1.9
Medium PI 3 (PI=38)	91.5	2.4	2.6	90.8	1.9	2.1	88.6	2.1	2.3
Sand	101.3	1.7	1.7	101.0	1.9	1.9	100.4	1.1	1.1
RAP	122.4	5.1	4.2	123.5	5.1	4.1	122.7	5.2	4.2
Kentucky Limestone	139.3	1.6	1.1	138.4	2.1	1.5	138.5	1.2	0.9
Medium PI 3 (PI=38) with 5% Lime & 4% Cement	93.4	1.3	1.4	91.6	0.8	0.8	92.3	0.7	0.7
Low PI (PI=11) with 3% Cement	100.3	3.1	3.1	97.3	0.6	0.6	99.6	0.9	0.9
High PI (PI=53) with 5% Lime & 4% Cement	100.7	6.2	6.1	88.5	1.7	2.0	93.7	1.6	1.7

Table 21. Summary of location-related variability of COV of NDG (moisture content)

Summary of NDG (Moisture Content) Based on Locations									
Material	Front Location			Middle Location			Back Location		
	Data Avg.	SD	COV	Data Avg.	SD	COV	Data Avg.	SD	COV
	%	%	%	%	%	%	%	%	%
Low PI (PI=11)	16.8	0.7	4.1	16.6	0.8	4.5	16.4	0.7	4.5
Mexican Limestone	10.1	1.0	10.2	10.1	1.2	12.2	9.6	1.4	14.6
High PI (PI=53)	36.9	1.7	4.7	37.0	1.5	4.1	36.1	1.5	4.2
Medium PI 1 (PI=21)	18.9	0.7	3.6	19.3	0.8	4.4	19.3	0.8	3.9
Medium PI 2 (PI=31)	22.3	1.1	5.0	21.1	0.9	4.0	20.8	0.7	3.3
Medium PI 3 (PI=38)	23.5	0.7	2.9	23.5	1.4	5.9	23.9	1.5	6.4
Sand	9.3	1	10.7	9.1	1.1	12.3	9.4	0.9	9.9
RAP	5.4	1.1	19.8	5.4	1.1	19.5	5.6	1	18.5
Low PI (PI=11)	16.8	0.7	4.1	16.6	0.8	4.5	16.4	0.7	4.5
Kentucky Limestone	6.6	0.5	7.3	6.6	0.5	6.9	6.7	0.4	6.5
Medium PI 3 (PI=38) with 5% Lime & 4% Cement	23.4	1.1	4.8	24.4	1	4	24	0.6	2.6
Low PI (PI=11) with 3% Cement	16.3	1.1	6.8	17	0.7	4.2	16.9	0.4	2.4
High PI (PI=53) with 5% Lime & 4% Cement	17.7	3.4	25.1	20	0.6	2.8	17.3	1.6	9.1

Analysis of E-Gauge Data

Like the Nuclear Density Gauge, the E-Gauge test was also performed in three different locations inside the box. The E-Gauge test was also performed by a single operator. This test can measure both the dry density and moisture content. While performing the test, the moisture probe sometimes did not work due to internal problems with the device. In that case, only the wet density of the tested material could be measured. Table 22 and Table 23 summarize the COVs induced by dry/wet density and moisture content, respectively.

Table 22 shows that the COVs range from 0.37% to 8.19% and from 0.41% to 4.02% for dry density and wet density, respectively. The COV of moisture content varies from 1.76% to 18.8% (Table 23). The maximum and minimum COV for dry density were

noticed for high PI (PI=53) and high PI (PI=53) with 5% lime and 4% cement, respectively. For the case of moisture content, the maximum and minimum COV were observed for high PI and high PI with 5% lime and 4% cement, respectively.

Table 22. Summary of location-related variability of COV of E-Gauge (dry/wet density)

Material	Front Location			Middle Location			Back Location		
	Data Avg.	SD	COV	Data Avg.	SD	COV	Data Avg.	SD	COV
	pcf	pcf	%	pcf	pcf	%	pcf	pcf	%
High PI (PI=53) (Dry Density)	88.65	6.92	7.81	88.06	6.94	7.88	87.07	7.13	8.19
Medium PI 1 (PI=21) (Wet Density)	114.85	1.05	0.92	115.97	2.71	2.33	116.11	2.68	2.31
Medium PI 3 (PI=38) (Wet Density)	116.74	0.60	0.52	116.24	0.93	0.80	115.91	0.96	0.83
Sand (Wet Density)	106.36	3.46	3.25	106.93	3.74	3.49	106.41	4.28	4.02
RAP (Wet Density)	120.94	2.88	2.38	120.94	3.25	2.69	121.40	2.92	2.41
Kentucky Limestone (Wet Density)	158.01	0.64	0.41	157.82	0.82	0.52	158.23	0.84	0.53
Medium PI 3 (PI=38) with 5% Lime & 4% Cement (Dry Density)	95.98	0.53	0.55	96.77	0.50	0.52	97.40	0.42	0.43
Low PI (PI=11) with 3% Cement (Dry Density)	105.27	0.55	0.52	106.33	0.81	0.77	107.30	0.50	0.47
High PI (PI=53) with 5% Lime & 4% Cement (Dry Density)	92.93	1.16	1.25	87.00	0.70	0.80	81.70	0.30	0.37

Table 23. Summary of location-related variability of COV of E-Gauge (moisture content)

Material	Front Location			Middle Location			Back Location		
	Data Avg.	SD	COV	Data Avg.	SD	COV	Data Avg.	SD	COV
	%	%	%	%	%	%	%	%	%
High PI (PI=53)	25.11	4.54	18.10	24.26	4.19	17.26	25.44	4.78	18.80
Medium PI 3 (PI=38) with 5% Lime & 4% Cement	21.07	0.42	1.98	20.20	0.36	1.78	20.50	0.60	2.93
Low PI (PI=11) with 3% Cement	14.20	0.46	3.23	13.87	0.60	4.35	13.87	0.35	2.53
High PI (PI=53) with 5% Lime & 4% Cement	24.17	0.72	2.99	24.97	2.05	8.21	26.23	0.46	1.76

Analysis of Plate Load Test Data

In plate load tests (PLT), the determination of amounts of plastic and elastic deformations are desirable. Besides, the initial modulus and reloading modulus are evaluated with the help of normal stress vs settlement plot. The initial modulus [EPLT(i)] and the reloading modului can be evaluated from the test results (Figure 67) using the following equation:

$$E_{PLT} = \frac{1.18\ P.R}{\delta} \qquad [147]$$

where: P = applied load on plate, δ = deflection of the plate, and R = radius of plate.

The PLTs were performed in the middle location of the box. The tests may not be included to analyze for variability as this test was performed by a single operator with one repetition. The PLTs were conducted on 12 geomaterials to determine the initial modulus [EPLT(i)] and the first reloading modulus [EPLT(R1)].

Figure 67. Plate load test of low PI (PI=11) soil

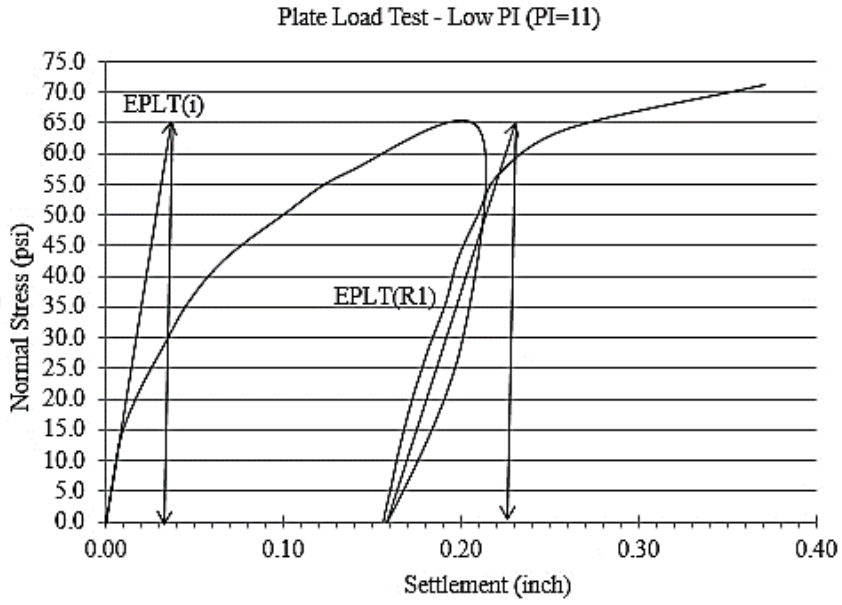

Referring to Figure 67, the initial modulus can be evaluated from the initial portion of the stress-settlement curve, where the slope of the initial modulus extends to the increase of the initial loading; and, the first reloading modulus can be evaluated from the reloading part of the curve. The first reloading modulus is the average value between the unloading

curve of the first cycle and reloading curve of the second cycle. The calculated initial and reloading moduli are presented in Table 24.

Table 24. Calculation of initial and reloading modulus of low PI (PI=11) soil

Type	Stress	Load	Poison's Ratio	Radius of Plate	Deflection	Modulus Value	Modulus Value
	psi	lb		inch	inch	psi	MPa
Initial Modulus (EPLT(i))	65	2872	0.4	3.75	0.035	11700	80.7
Reloading Modulus (EPLT(R1))	65	2872	0.4	3.75	0.067	6112	42.1

Summary of initial and reloading modules of all materials is shown in Table 25. The maximum EPLT(i) was observed for Kentucky limestone (344.9 MPa) and the minimum was obtained for high PI (PI=53) soil (23.5 MPa). However, the maximum and minimum EPLT(R1) was obtained for Kentucky limestone (222.5 MPa) and high PI (PI=53) (11.7 MPa), respectively.

Table 25. Summary of plate load test of all materials

Summary of Plate Load Test		
Material	Initial Modulus	Reloading Modulus
	MPa	MPa
Low PI (PI=11)	80.7	42.1
Mexican Limestone	311.2	163.5
High PI (PI=53)	23.5	11.7
Medium PI 1 (PI=21)	44.5	24.3
Medium PI 2 (PI=31)	38.9	19.4
Medium PI 3 (PI=38)	32.0	12.4
Sand	23.6	42.1
RAP	68.1	54.5
Kentucky Limestone	344.9	222.5
Medium PI 3 (PI=38) with 5% Lime & 4% Cement	114.6	43.5
Low PI (PI=11) with 3% Cement	150.8	41.8
High PI (PI=53) with 5% Lime & 4% Cement	110.3	33.2

Results and Analysis of Constructed Field Tests

Analyses of the constructed field test data were performed the same way as the in-box test data. The X-Bar/R and ANOVA methods can also be applied to Geogauge and LFWD tests in the field. There were 14 sections constructed at the Accelerated Loading Facility (ALF). Four sections were construed on embankment location and another four sections were constructed at lower level over natural soil. There were also six more sections that were constructed on embankment location as part of micro-cracking research project. In the case of dynamic cone penetrometer, the operator and location-related variability were analyzed using the second moment statistics. In the case of the Nuclear Density Gauge (NDG) and E-Gauge, only the location-related variability can be evaluated since these devices were conducted by a single operator. Table 26 shows the properties of the 14 constructed sections that will be analyzed for the variability assessment.

Table 26. Properties of the 14 constructed sections at ALF

Section Type	Properties of the sections
Section 1	Low PI (PI = 11) with 7% Lime + 15% Fly Ash
Section 2	Heavy Clay (PI = 38) with 7% Lime + 6% Cement
Section 3	Low PI (PI = 11) with 8% Cement
Section 4	Heavy Clay (PI = 38) with 3%Lime + 2% Cement
Section A	Low PI (PI = 11) with 5% Lime + 11% Fly Ash
Section B	Heavy Clay (PI = 38) with 2.5% Lime + 2% Cement
Section C	Heavy Clay (PI = 38) with 6.0% Lime + 4% Cement
Section D	Low PI (PI = 11), 5% Cement
Soil Cement Section 1	8% Soil Cement, No Micro-Cracking
Soil Cement Section 2	8% Soil Cement, Low Micro-Cracking
Soil Cement Section 3	8% Soil Cement, Medium Micro-Cracking
Soil Cement Section 4	8% Soil Cement, High Micro-Cracking
Soil Cement Section 5	6% Soil Cement, No Micro-Cracking
Soil Cement Section 6	6% Soil Cement, Medium Micro-Cracking

Analysis of Geogauge and LFWD Test Data

Analyses of the Geogauge and the LFWD include the X/Bar-R, ANOVA, and second moment methods. The results of analyses are presented in terms of the coefficient of variations (COV). The COV for both the Geogauge and the LFWD data were determined for total variability, where the total variability is grouped into repeatability, reproducibility and specimen variability. Table 27 shows a summary of the COVs of the Geogauge and the LFWD according to the X-Bar/R, ANOVA, and second moment methods. The table shows that the COV for the Geogauge ranges from 7.7% to 21.0%;

the X-Bar/R method, from 11.4% to 23.6%; the ANOVA method from 11.1% to 20.2%; and for the second moment method. Meanwhile, for LFWD, the COV ranges from 7.3% to 20.3% for the X-Bar/R method, 7.9% to 18.9% for the ANOVA method, and 7.0% to 16.7% for the second moment method.

Table 27. Summary of COV of Geogauge and LFWD according to X-Bar/R and ANOVA method

Soil Type	Geogauge			LFWD		
	Second Moment	X-Bar	ANOVA	Second Moment	X-Bar	ANOVA
	COV	COV	COV	COV	COV	COV
	%	%	%	%	%	%
Section 1	13.2	17.5	14.3	7.1	9.1	7.9
Section 2	15.5	7.7	16.3	10.9	13.9	8.2
Section 3	12.5	15.7	15.3	9.3	19.8	10.0
Section 4	14.4	10.3	16.1	14.2	18.0	13.2
Section A	20.2	16.4	23.6	7.0	7.3	8.1
Section B	11.1	12.3	11.8	7.5	7.4	13.0
Section C	18.6	14.7	21.6	13.9	9.4	14.9
Section D	11.6	18.9	11.4	12.5	13.6	14.3
Soil Cement Section 1	12.1	17.0	14.0	8.5	8.0	9.8
Soil Cement Section 2	13.2	21.0	16.3	14.7	15.1	15.8
Soil Cement Section 3	12.9	18.1	14.9	16.5	18.3	18.9
Soil Cement Section 4	11.6	9.2	13.6	16.7	20.3	18.6
Soil Cement Section 5	11.9	10.2	14.2	12.1	10.3	13.1
Soil Cement Section 6	11.6	17.2	13.9	8.9	9.0	9.2

Analysis of Dynamic Cone Penetrometer (DCP) Data

The DCP tests were conducted in each of the constructed sections at ALF. The thickness of each section is 12 in. or 30.5 cm. Figure 68 shows the DCP test results for two sections—Section 4 and Section C. The DCP tests were conducted by three operators, and as there were four locations of each constructed section, every operator conducted DCP tests four times. From the summary of DCPI (mm/blow), the COV for operator-related variability ranges from 3.2% to 20.3%; while the COV for location-related variability varies from 2.6% to 29.4%, which are presented in Table 28 and Table 29, respectively. For the micro-cracking sections, the COV of DCPI fluctuates from 14.90% to 20.1%, which is presented in Table 30.

Figure 68. DCPI profiles of section 4 and section C at ALF site

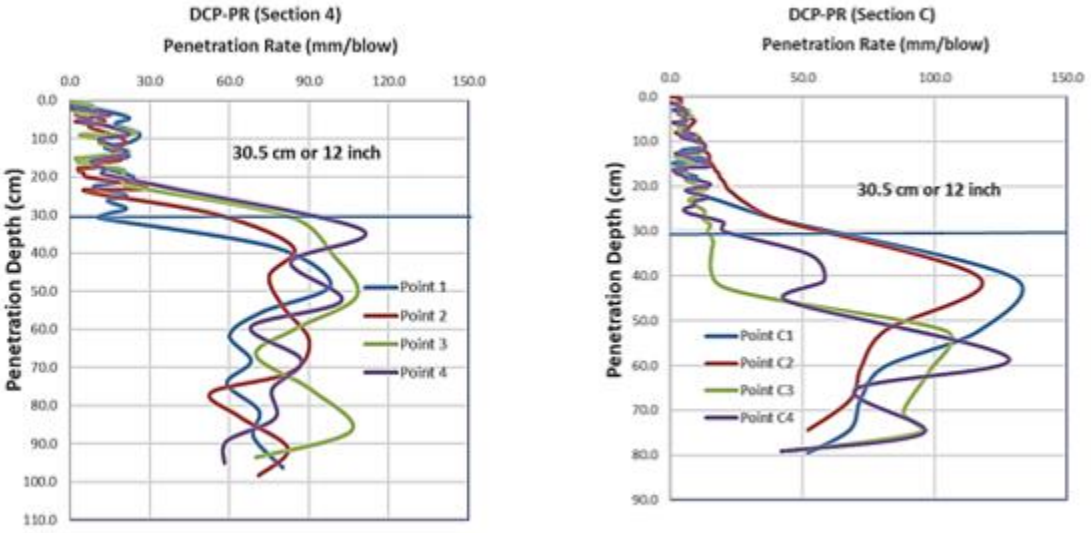

Table 28. Summary of operator-related variability of COV of DCPI

Material	Operator 1			Operator 2			Operator 3		
	DCPI Avg.	SD	COV	DCPI Avg.	SD	COV	DCPI Avg.	SD	COV
	mm/ blow	mm/ blow	%	mm/ blow	mm/ blow	%	mm/ blow	mm/ blow	%
Section 1	26.4	1.5	5.6	27.2	0.9	3.2	27.7	1.0	3.7
Section 2	12.9	2.3	17.7	19.0	3.3	17.1	17.8	1.9	10.4
Section 3	6.8	0.4	6.3	6.8	0.4	6.6	9.3	1.0	10.8
Section 4	15.2	1.3	8.4	18.6	2.8	14.9	16.0	0.8	5.1
Section A	26.3	1.7	6.3	26.3	2.3	8.6	26.9	1.8	6.9
Section B	33.2	5.6	16.7	32.3	6.5	20.1	32.2	4.4	13.6
Section C	13.3	2.1	15.8	11.6	1.7	15.0	11.2	0.9	8.2
Section D	11.3	2.3	20.3	12.9	2.1	16.5	11.2	0.9	8.2

Table 29. Summary of location-related variability of COV of DCPI

Material	Location 1		Location 2		Location 3		Location 4	
	DCPI Avg.	COV	DCPI Avg.	COV	DCPI Avg.	COV	DCPI Avg.	COV
	mm/ blow	%	mm/ blow	%	mm/ blow	%	mm/ blow	%
Section 1	27.0	4.9	26.6	2.6	27.0	7.6	27.8	2.7
Section 2	18.1	20.1	16.2	29.4	14.4	21.8	17.5	20.5
Section 3	7.4	13.6	7.4	16.3	7.6	19.9	7.6	19.2
Section 4	17.1	18.4	16.5	3.9	15.6	8.4	17.1	21.2
Section A	24.7	7.8	26.5	7.2	27.0	4.8	27.8	2.9
Section B	31.2	5.0	32.7	3.6	26.7	7.8	39.7	2.9
Section C	11.3	16.8	10.8	5.1	13.4	8.8	12.6	19.0
Section D	10.6	4.3	12.3	20.8	13.4	8.6	10.8	17.2

Table 30. Summary of whole section variability of COV of micro-cracking sections

Materials	DCPI Avg.	SD	COV
	mm/blow	mm/blow	%
Soil Cement Section 1	10.7	1.9	17.5
Soil Cement Section 2	12.3	2.5	20.1
Soil Cement Section 3	10.3	1.6	15.5
Soil Cement Section 4	11.2	2.1	18.8
Soil Cement Section 5	9.4	1.4	14.9
Soil Cement Section 6	9.8	1.7	16.9

From Table 28 and Table 29, it can be seen that section D (low PI (PI = 11), with 5% cement) showed the maximum COV for operator-related variability; whereas, Section 2 (Heavy Clay (PI = 38) with 7% lime and 6% cement) showed the maximum COV for location-related variability. The minimum COVs are found for Section 1 (low PI (PI = 11) with 7% lime and 15% Fly Ash). From Table 30, the maximum and minimum COVs are observed for Soil Cement Section 2 (8% soil cement, low MC) and Soil Cement Section 5 (6% soil cement, no MC), respectively.

Analysis of Nuclear Density Gauge (NDG) Data

The Nuclear Density Gauge (NDG) tests were conducted on four (or five) different locations of each section, and it was run by a single operator. The NDG tests were performed on four locations at the eight constructed sections (Sections 1-4 and Sections A-D). However for micro-cracking cement sections (Soil Cement Section 1 to Soil Cement Section 6), the NDG tests were performed on five locations at three sections (Sections 1, 4 and 6); while the tests couldn't be run on Section 2, 3 and 5 as the device didn't work at that time. Table 31 and Table 32 present the location-related variabilities for dry density of the eight sections and three micro-cracking sections, respectively.

Table 31. Summary of location-related variability of NDG (dry density) at the eight sections

Material	Location 1		Location 2		Location 3		Location 4	
	Avg. Dry Density	COV	Avg. Dry Density	COV	Avg. Dry Density	COV	Avg. Dry Density	COV
	pcf	%	pcf	%	pcf	%	pcf	%
Section 1	83.9	0.8	80.2	3.9	76.6	1.7	78.7	0.9
Section 2	97.3	0.6	99.9	3.2	99.3	1.1	84.5	2.1
Section 3	97.5	0.6	96.3	1.0	100.6	0.6	98.9	0.9
Section 4	72.7	2.1	75.5	0.7	70.7	1.4	71.2	2.0
Section A	76.6	1.5	76.8	1.2	75.1	0.2	78.2	2.0
Section B	74.2	1.3	72.8	2.9	70.9	1.3	71.0	1.9
Section C	95.4	0.7	96.2	0.2	92.9	1.2	89.4	0.4
Section D	93.1	2.6	92.2	4.2	96.8	1.7	90.9	2.0

Table 32. Summary of location-related variability of NDG (dry density) at the three micro-cracking sections

Material	Location 1		Location 2		Location 3		Location 4		Location 5	
	Avg. Dry Density	COV	Avg. Dry Density	COV	Avg. Dry Density	COV	Avg. Dry Density	COV	Avg. Dry Density	COV
	pcf	%	pcf	%	pcf	%	pcf	%	pcf	%
Soil Cement Section 1	140.6	2.9	146.5	1.1	140.4	1.8	126.7	2.4	138.6	1.4
Soil Cement Section 4	135.3	2.3	146.6	1.6	140.5	1.8	127.4	2.0	127.9	2.0
Soil Cement Section 6	127.7	2.0	137.2	1.9	137.0	1.5	119.7	1.4	131.7	1.4

It can be seen from Table 31 that the location-related COV of the dry density for the eight sections range from 0.2% to 4.2%. It is also noticed from Table 32 that the location-related COV of the dry density for the Micro-cracking cement sections range from 1.4% to 2.9%.

The calculations of location-related variabilities for moisture content is similar to the dry density calculation, which are presented in Table 33 and Table 34 for the eight sections and the three micro-cracking cement sections, respectively.

Table 33. Summary of location-related variability of NDG (moisture content) for the eight sections

Material	Location 1		Location 2		Location 3		Location 4	
	Moisture Content, m.c.	COV	Avg. m.c.	COV	Avg. m.c.	COV	Avg. m.c.	COV
	%	%	%	%	%	%	%	%
Section 1	28.0	4.0	24.2	3.8	30.3	2.2	30.6	4.1
Section 2	20.2	2.3	19.0	5.3	15.8	1.7	24.7	6.9
Section 3	17.8	4.4	18.4	3.7	17.7	2.0	19.3	3.2
Section 4	38.2	1.4	34.7	2.0	39.4	0.7	39.0	3.9
Section A	30.9	4.4	31.7	2.4	32.0	3.8	28.8	2.6
Section B	38.0	4.6	34.5	13.3	37.4	5.4	33.1	1.8
Section C	19.8	1.3	18.2	2.2	17.9	1.5	19.2	1.9
Section D	25.4	5.6	19.4	9.8	21.4	17.5	23.1	9.6

Table 34. Summary of location-related variability of NDG (moisture content) of the micro-cracking three sections

Material	Location 1		Location 2		Location 3		Location 4		Location 5	
	Avg. m.c.	COV	Avg. m.c.	COV	Avg. m.c.	COV	Avg. m.c.	COV	Avg. m.c.	COV
	%	%	%	%	%	%	%	%	%	%
Soil Cement Section 1	12.5	9.2	13.6	7.0	15.1	5.4	13.9	5.8	13.7	1.4
Soil Cement Section 4	12.4	8.7	13.2	9.0	16.1	7.2	14.5	7.8	14.8	8.8
Soil Cement Section 6	10.7	9.9	11.2	9.9	12.8	9.9	10.9	9.9	9.9	9.9

The results in Table 33 show that the location-related COV of moisture content for the eight sections vary from 0.7% to 17.5%; while the location-related COV of moisture content vary from 1.4% to 9.9% for the micro-cracking sections (Table 34).

Analysis of E-Gauge Data

Like the NDG, the E-Gauge tests were also conducted on the constructed sections at ALF site. The dry density and moisture content are analyzed only for the location-related variability. The results for dry density are presented in Table 35 and Table 36, for the eight constructed sections and the three micro-cracking sections, respectively. The tables show that the location-related COV range from 0.1% to 9.3% for the eight constructed sections and from 1.1% to 2.9% for the three micro-cracking sections.

The location-related variability for the moisture content are presented in Table 37 and Table 38 for the eight constructed sections and the three micro-cracking sections, respectively. The tables show that the COVs range from 0.2% to 19.5% for the eight constructed sections and from 1.4% to 10.9% for the three micro-cracking sections.

Table 35. Summary of location-related variability of E-Gauge (dry density) for the eight constructed sections

Material	Location 1		Location 2		Location 3		Location 4	
	Avg. Dry Density	COV	Avg. Dry Density	COV	Avg. Dry Density	COV	Avg. Dry Density	COV
	pcf	%	pcf	%	pcf	%	pcf	%
Section 1	92.0	1.9	95.7	0.9	93.5	1.2	95.4	1.4
Section 2	94.4	3.1	100.5	0.9	103.0	1.2	100.2	1.4
Section 3	94.9	0.8	94.5	1.1	94.2	1.1	95.1	0.7
Section 4	67.7	0.3	75.2	9.3	69.7	8.9	61.0	4.6
Section A	76.4	0.1	68.5	1.3	75.9	4.2	74.4	0.3
Section B	77.8	0.7	77.2	0.5	72.9	4.7	77.5	2.9
Section C	97.3	1.2	105.5	1.6	132.9	1.5	102.2	2.1
Section D	98.2	4.3	93.0	0.5	94.2	4.5	92.0	0.2

Table 36. Summary of location-related variability of E-Gauge (dry density) for the three micro-cracking sections

Material	Location 1		Location 2		Location 3		Location 4		Location 5	
	Avg. Dry Density	COV	Avg. Dry Density	COV	Avg. Dry Density	COV	Avg. Dry Density	COV	Avg. Dry Density	COV
	pcf	%	pcf	%	pcf	%	pcf	%	pcf	%
Soil Cement Section 1	145.2	2.9	147.8	1.1	141.5	1.8	124.8	2.5	138.6	1.8
Soil Cement Section 4	135.3	2.6	152.6	1.5	143.2	1.7	128.6	2.8	128.9	2.0
Soil Cement Section 6	133.3	1.4	139.3	1.4	133.0	1.4	119.7	1.4	131.7	1.4

Table 37. Summary of location-related variability of E-Gauge (moisture content) for the eight constructed sections

Material	Location 1		Location 2		Location 3		Location 4	
	Moisture Content	COV	Dry Density	COV	Dry Density	COV	Dry Density	COV
	%	%	%	%	%	%	%	%
Section 1	20.8	19.5	19.5	0.8	21.7	4.0	20.6	4.4
Section 2	21.8	19.2	20.5	0.8	22.8	4.0	21.7	4.4
Section 3	19.5	2.8	20.1	1.3	19.6	1.6	20.4	1.2
Section 4	47.3	0.2	43.0	8.9	46.7	8.8	53.1	4.6
Section A	33.3	1.2	48.0	0.7	37.5	4.4	36.9	0.3
Section B	27.6	0.8	30.7	0.3	33.1	4.4	30.0	3.0
Section C	21.8	1.6	12.7	7.8	14.8	6.7	20.5	5.2
Section D	21.8	4.2	21.3	0.7	24.3	4.5	27.0	0.6

Table 38. Summary of location-related variability of COV of E-Gauge (moisture content) for the three micro-cracking sections

Material	Location 1		Location 2		Location 3		Location 4		Location 5	
	Avg. m.c.	COV	Avg. m.c.	COV	Avg. m.c.	COV	Avg. m.c.	COV	Avg. m.c.	COV
	%	%	%	%	%	%	%	%	%	%
Soil Cement Section 1	11.3	9.9	11.8	9.9	13.5	9.9	11.5	9.9	9.9	9.9
Soil Cement Section 4	15.9	8.2	13.7	10.9	15.1	7.2	14.5	7.8	15.9	8.2
Soil Cement Section 6	13.5	1.4	13.6	1.4	16.9	5.4	13.8	1.4	13.7	1.4

Analysis of Under-Constructed Field Tests

Analysis of the under-constructed field tests was performed using the second moment statistics, which is applied for Geogauge, LFWD, DCP, NDG and E-Gauge. There were two under-constructed sections at LA 98 and one under-constructed section at LA 417 on which the tests were performed. Table 39 presents the description of the three under-constructed sections at LA 98 and LA 417.

Table 39. Properties of the three under-constructed sections at LA 98 and LA 417

Section	Description of the sections
LA 98 Station 1	Cement stabilized base course material with 7% cement by volume
LA 98 Station 2	
LA 417	Cement stabilized subgrade material with 10% cement by volume

Analysis of Geogauge and LFWD Data

In order to assess the variability, the Geogauge and the LFWD tests were performed on different locations of the under-constructed sections. In this analysis, the operator and location-related variabilities were determined using the X-Bar/R and the ANOVA. The results of operator- and location-related variabilities for the Geogauge data are presented in Table 40 and Table 41, respectively. The tables indicate that the COVs of the operator and the location-related variabilities range from 20.3% to 32.5% and from 20.3% to 31.9, respectively. The maximum COV value is seen for operator 3 of LA 98 Station 2 (32.5%); while the lowest value of COV is noticed for location 5 of LA 417 (20.3%).

In the case of LFWD, the results of operator- and location-related variabilities are presented in Table 42 and Table 43, respectively. The tables show that the COVs for the operator-related variability range from 11.7% to 37.5%, whereas the COVs for the location-related variability range from 18.6% to 31.8%.

Table 40. Summary of operator-related variability of Geogauge

Material	Operator 1		Operator 2		Operator 3		Operator 4		Operator 5	
	Data Avg.	COV	Data Avg.	COV	Data Avg.	COV	Data Avg.	COV	Data Avg.	COV
	MPa	%	MPa	%	MPa	%	MPa	%	MPa	%
LA 98 Station 1	236.5	29.4	269.7	27.1	246.6	31.5	299.0	25.8	278.4	20.3
LA 98 Station 2	242.3	29.3	281.2	30.6	255.8	32.5	334.1	26.5	285.7	22.5
LA 417	267.5	24.4	272.0	28.2	246.6	31.5	299.0	25.8	273.3	20.4

Table 41. Summary of location-related variability of Geogauge

Material	Location 1		Location 2		Location 3		Location 4		Location 5	
	Data Avg.	COV	Data Avg.	COV	Data Avg.	COV	Data Avg.	COV	Data Avg.	COV
	MPa	%	MPa	%	MPa	%	MPa	%	MPa	%
LA 98 Station 1	282.4	29.1	251.6	25.9	238.4	25.5	284.2	31.7	258.0	20.5
LA 98 Station 2	313.2	29.9	244.8	25.5	272.7	31.0	312.6	31.9	245.1	20.4
LA 417	302.4	25.2	245.1	28.4	241.5	21.6	298.1	26.4	259.9	20.3

Table 42. Summary of operator-related variability of LFWD

Material	Operator 1		Operator 2		Operator 3		Operator 4		Operator 5	
	Data Avg.	COV	Data Avg.	COV	Data Avg.	COV	Data Avg.	COV	Data Avg.	COV
	MPa	%	MPa	%	MPa	%	MPa	%	MPa	%
LA 98 Station 1	182.9	21.3	208.9	17.4	188.8	21.3	202.2	23.8	143.0	11.7
LA 98 Station 2	192.7	24.2	219.4	18.9	198.3	23.1	212.6	24.8	150.2	13.3
LA 417	214.6	31.2	223.5	35.0	184.8	22.8	227.0	37.5	224.3	34.0

Table 43. Summary of location-related variability of LFWD

Material	Location 1		Location 2		Location 3		Location 4		Location 5	
	Data Avg.	COV	Data Avg.	COV	Data Avg.	COV	Data Avg.	COV	Data Avg.	COV
	MPa	%	MPa	%	MPa	%	MPa	%	MPa	%
LA 98 Station 1	188.0	23.2	183.9	22.7	205.8	24.7	152.4	20.0	180.6	23.8
LA 98 Station 2	197.7	27.5	192.5	22.7	217.3	25.9	164.7	25.2	186.7	26.8
LA 417	220.0	31.8	178.8	31.6	272.6	26.9	230.5	18.6	172.3	21.9

Analysis of Dynamic Cone Penetrometer (DCP) data

The DCP tests were performed at the center of each point of a location of station, and the COVs were determined for the whole station. Analysis of the DCP was performed using

the first-order second moment (FOSM) analysis. Figure 69 depicts the DCPI (mm/blow) profile for LA 98 Station 1, which was tested on five points. The base layer LA 98 Station 1 is about 10 in.. The average values of the DCPI (mm/blow) for each point are presented in the figure, in which the DCPI (mm/blow) varies from 4.1 mm/blow to 5.8 mm/blow for LA 98 Station 2 and LA 98 Station 1, respectively.

Figure 69. DCPI (mm/blow) profile of LA 98 station 1

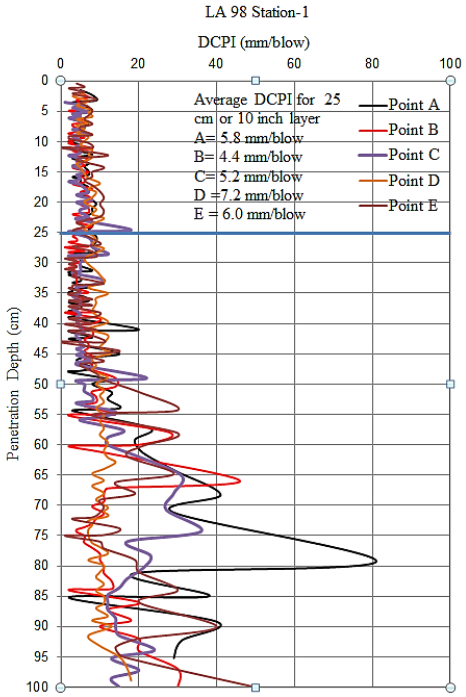

Summary of the COVs for all stations is shown in Table 44, where the maximum and the minimum values of COV are 29.8% and 15.4%, respectively. The maximum value of COV is seen for LA 98 Station 1; whereas, the minimum value of COV is observed for LA 98 Station 2.

Table 44. Summary of the DCPI variability for the under-constructed sections

Stations	DCPI Avg.	SD	COV
	mm/blow	mm/blow	%
LA 98 Station 1	5.8	0.9	15.4
LA 98 Station 2	4.1	1.2	29.8
LA 417	4.8	1.1	23.6

Analysis of Nuclear Density Gauge (NDG) Data

Although the Nuclear Density Gauge (NDG) was tested at the center of each point of a location of station, the location-related variability can be applied as measurements were taken three times. Table 45 and Table 46 show the location-related variability of the dry density and the moisture content, respectively. The tables show that the COVs for NDG range from 0.2% to 2.3% and from 0.8% to 10.2%, for the dry density and moisture content, respectively

Table 45. Summary of location-related variability of NDG (dry density) for the under-constructed sections

Material	Point A		Point B		Point C		Point D		Point E	
	Dry Density	CV	Dry Density	CV	Dry Density	CV	Dry Density	CV	Dry Density	CV
	pcf	%	pcf	%	pcf	%	pcf	%	pcf	%
LA 98 Station 1	99.5	2.3	99.3	0.8	105.1	0.8	99.1	1.4	99.1	1.4
LA 98 Station 2	101.7	1.4	101.2	0.6	102.3	0.6	106.5	0.4	115.7	1.7
LA 417	95.6	0.2	96.7	0.2	101.9	1.0	101.7	0.8	95.7	1.7

Table 46. Summary of location-related variability of NDG (moisture content) for the under-constructed sections

Material	Point A		Point B		Point C		Point D		Point E	
	Avg. m.c.	COV	Avg. m.c.	COV	Avg. m.c.	COV	Avg. m.c.	COV	Avg. m.c.	COV
	%	%	%	%	%	%	%	%	%	%
LA 98 Station 1	17.6	3.5	17.8	3.9	13.2	0.8	17.1	3.4	17.1	3.4
LA 98 Station 2	17.0	3.0	18.9	1.1	17.2	1.5	13.8	3.3	17.4	4.9
LA 417	14.3	2.7	14.3	5.4	15.4	10.2	14.7	9.3	15.3	8.7

Analysis of E-Gauge Data

The tests and analyses performed using the E-Gauge were similar to the NDG, in which tests were performed at the center of each point of a location of station. Table 47 and Table 48 present the summary of the COVs for the dry density and moisture content, respectively. As shown in the tables, the COVs range from 0.10% to 3.7% and from 0.8% to 12.0% for dry density and moisture content, respectively. The maximum COV values

for both the dry density and moisture content are observed for LA 417; while the minimum COV values for both the dry density and the moisture content are found for LA 417 and LA 98 Station 2, respectively.

Table 47. Summary of location-related variability of E-Gauge (dry density)

Material	Point A		Point B		Point C		Point D		Point E	
	Dry Density	COV	Dry Density	COV	Dry Density	COV	Dry Density	COV	Dry Density	COV
	pcf	%	pcf	%	pcf	%	pcf	%	pcf	%
LA 98 Station 1	105.9	0.3	102.4	0.9	99.3	1.1	105.5	2.1	104.8	1.5
LA 98 Station 2	107.5	1.1	107.4	0.2	107.6	0.7	110.0	1.0	96.5	2.1
LA 417	116.0	0.3	109.3	3.5	110.7	0.1	101.9	0.3	109.9	3.7

Table 48. Summary of location-related variability of E-Gauge (moisture content)

Material	Point A		Point B		Point C		Point D		Point E	
	Avg. m.c.	COV	Avg. m.c.	COV	Avg. m.c.	COV	Avg. m.c.	COV	Avg. m.c.	COV
	%	%	%	%	%	%	%	%	%	%
LA 98 Station 1	15.3	1.4	16.2	0.9	16.6	1.3	15.3	3.0	16.3	3.2
LA 98 Station 2	18.8	1.3	20.7	0.8	20.1	1.0	15.1	1.4	21.5	2.1
LA 417	3.5	8.2	5.5	4.2	3.6	3.2	3.4	12.0	3.8	1.5

Analysis of Lab Test Data

Analyses of lab tests have been performed based on the operator and specimen-related variability. The lab tests include the unconsolidated undrained (UU) triaxial, Atterberg limits, small direct shear, one-dimensional consolidation and California bearing ratio (CBR) tests.

Analysis of Unconsolidated Undrained (UU) Triaxial Test data

UU triaxial tests were performed by five different operators, in which each operator tested three specimens of the same soil type (low PI, high PI, and medium PI 1, 2 and 3 soils). The operator- and specimen-related variabilities were evaluated for the UU tests Bar/R and ANOVA, and the results are presented in Table 49 and Table 50, respectively. The tables show that the COVs of UU test results vary from 1.0% to 10.9% and from 3.8% to 17.1% for the operator and specimen-related variabilities, respectively.

Table 49. Summary of operator-related variability for UU tests

Material	Operator 1		Operator 2		Operator 3		Operator 4		Operator 5	
	Su, Avg.	COV	Su, Avg.	COV	Su, Avg.	COV	Su, Avg.	COV	Su, Avg.	COV
	psf	%	psf	%	psf	%	psf	%	psf	%
High PI (PI=53)	621.7	1.2	814.3	5.5	845.3	6.9	672.5	9.2	862.4	8.3
Low PI (PI=11)	3799.8	10.5	3984.8	6.4	3248.7	9.6	3209.3	1.0	3113.8	2.8
Medium PI 1 (PI=21)	2536.3	2.8	2521.2	6.1	2959.6	7.4	2659.1	7.1	2524.9	3.9
Medium PI 2 (PI=31)	2087.8	8.4	2195.3	1.4	2341.1	4.4	2257.2	10.9	2272.2	6.2
Medium PI 3	1888.6	5.8	1440.0	8.6	1736.9	4.5	1678.3	6.9	1675.2	4.3

Table 50. Summary of specimen-related variability of UU tests

Material	Specimen 1		Specimen 2		Specimen 3	
	Su, Avg.	COV	Su, Avg.	COV	Su, Avg.	COV
	psf	%	psf	%	psf	%
High PI (PI=53)	748.9	17.1	804.8	14.5	736.0	13.1
Low PI (PI=11)	3421.8	9.1	3488.5	15.6	3503.5	13.7
Medium PI 1 (PI=21)	2632.9	3.8	2689.0	10.4	2598.8	10.4
Medium PI 2 (PI=31)	2244.1	3.8	2228.5	6.5	2219.6	11.0
Medium PI 3 (PI=38)	1651.9	11.2	1666.0	10.6	1733.6	10.6

Analysis of Atterberg Limits Data

The Atterberg limit tests were performed by five operators to evaluate the operator-related variability in which each operator prepared three specimens to evaluate the specimen-related variability. Table 51 shows the summary of operator-related variability, and Table 52 presents the summary of specimen-related variability. The results show that the COVs of the liquid limit vary from 0.9% to 7.8%, and the COVs of the plastic limit range from 1.9% to 18.2%. Additionally, the COV of the plasticity index range from 1.1% to 26.4%.

Table 51. Summary of operator-related variability for the Atterberg limits

Material	Type	Operator 1		Operator 2		Operator 3		Operator 4		Operator 5	
		Avg.	COV	Avg.	COV	Avg.	COV	Avg.	COV	Avg.	COV
		%	%	%	%	%	%	%	%	%	%
Low PI (PI=11)	LL	32	1.8	31	3.2	31	3.7	35	1.7	34	7.8
	PL	21	4.8	20	2.8	18	8.6	18	11.4	20	2.9
	PI	11	10.8	11	14.3	13	4.4	16	14.1	14	16.9
Medium PI 1 (PI=21)	LL	42	5.5	41	1.4	43	4.0	41	2.4	39	6.8
	PL	26	5.9	26	7.7	21	2.8	25	18.2	19	6.0
	PI	16	9.8	15	13.6	22	6.8	19	11.9	20	10.6
High PI (PI=53)	LL	88	4.5	92	2.5	100	4.7	94	1.8	99	4.8
	PL	35	4.4	38	7.6	50	7.1	41	5.0	48	8.6
	PI	53	6.0	54	1.1	50	4.0	53	4.4	51	4.1
Medium PI 2 (PI=31)	LL	55	2.1	48	1.2	50	3.0	52	3.0	49	6.3
	PL	19	3.1	19	7.9	22	5.2	24	2.4	20	8.7
	PI	36	4.8	29	5.3	28	6.2	28	7.1	29	15.7
Medium PI 3 (PI=38)	LL	62	0.9	61	1.9	64	3.6	58	4.6	62	0.9
	PL	30	9.7	30	1.9	30	2.0	28	5.4	31	1.9
	PI	32	8.3	31	4.9	34	6.7	30	10.3	31	1.9

Note: LL = Liquid Limit, PL = Plastic Limit and PI = Plasticity Index

Analysis of Small Direct Shear Test Data

Small direct shear tests were conducted on both sand and clay soil types to evaluate the operator and specimen-related variability. In order to do so, five different operators conducted the tests on three specimens.

Figure 70 presents an example of direct shear test results on sand soil, and Figure 71 presents an example of direct shear test results on the low PI (PI=11) clay soil. The friction angle, ϕ, was determined for each test from the shear stress-normal stress plot.

The cohesion, c, for clay soils was determined for each test from the intercept of shear stress - normal stress line with the y-axis

Table 52. Summary of specimen-related variability for the Atterberg limits

Specimen-related Variability										
Material	Type	Specimen 1			Specimen 2			Specimen 3		
		Average	SD	COV	Average	SD	COV	Average	SD	COV
		%	%	%	%	%	%	%	%	%
Low PI (PI=11)	LL	33	2.2	6.6	33	2.2	6.6	32	1.9	5.8
	PL	19	1.8	9.3	20	1.1	5.8	20	2.3	11.7
	PI	14	1.5	11.2	13	2.6	19.6	12	2.8	22.5
Medium PI 1 (PI=21)	LL	42	1.5	3.6	41	2.9	7.0	41	1.5	3.7
	PL	22	3.4	15.6	24	3.4	14.1	25	4.2	17.2
	PI	20	2.6	13.1	17	4.4	26.4	16	3.9	24.6
High PI (PI=53)	LL	98	7.3	7.4	93	5.8	6.3	94	2.3	2.5
	PL	45	7.5	16.7	41	6.7	16.5	42	5.4	12.9
	PI	53	0.9	1.7	52	2.5	4.9	52	3.4	6.5
Medium PI 2 (PI=31)	LL	52	2.3	4.4	50	2.5	5.0	50	3.8	7.6
	PL	21	2.2	10.6	21	2.7	13.1	21	2.2	10.2
	PI	31	2.7	8.6	29	3.7	12.7	29	5.3	18.0
Medium PI 3 (PI=38)	LL	62	1.6	2.7	60	3.1	5.2	62	2.8	4.5
	PL	30	1.1	3.7	29	1.3	4.6	30	2.2	7.2
	PI	32	2.0	6.3	31	2.4	7.9	32	3.3	10.3

Figure 70. Example of direct shear test results on sand soil

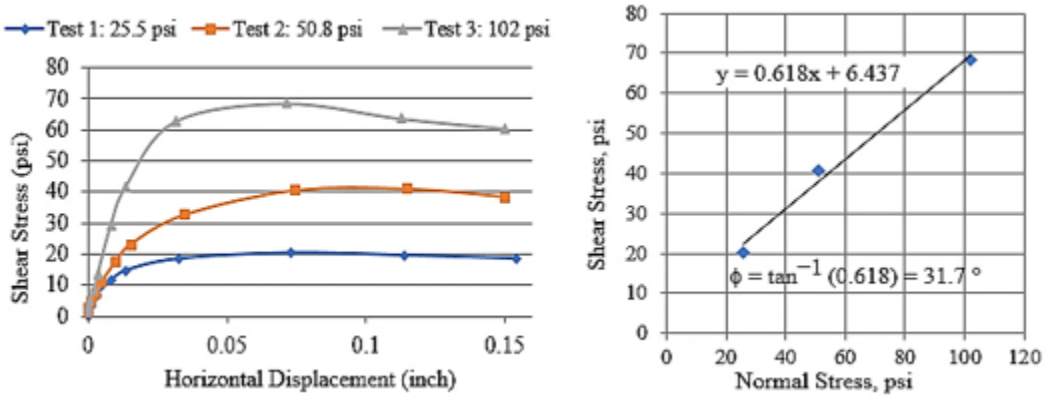

Figure 71. Example of direct shear test results on clay soil

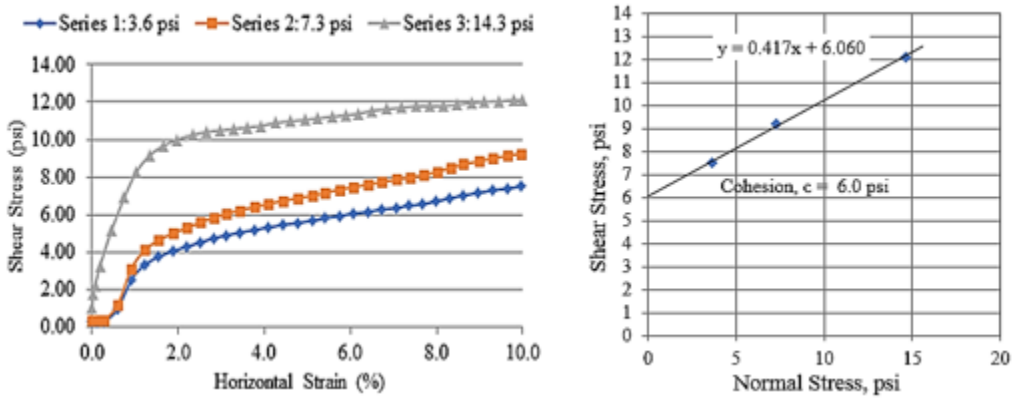

Table 53 presents the operator-related variability of small direct shear test on clay soil, which shows that the COVs of cohesion, c, range from 3.5% to 19.5%. Whereas Table 54 presents the specimen-related variability of small direct shear test on clay, which shows that the COVs of c range from 5.7% to 20.0%.

The operator-related and specimen-related variability of small direct shear test on sand soil are presented in Table 55 and Table 56, respectively. The tables show that the operator-related COVs of ϕ range from 0.4% to 1.8%, and the specimen-related COVs of ϕ range from 7.8% to 8.8%.

Table 53. Summary of operator-related variability of small direct shear test on clay

Material	Operator 1		Operator 2		Operator 3		Operator 4		Operator 5	
	Avg. c	COV	Avg. c	COV	Avg. c	COV	Avg. c	COV	Avg. c	COV
	psf	%	psf	%	psf	%	psf	%	psf	%
Low PI (PI=11)	816.0	13.4	868.8	9.1	868.8	14.1	897.6	15.8	859.2	14.6
Medium PI 1 (PI=21)	633.6	11.8	576.0	5.0	648.0	10.2	561.6	11.8	628.8	3.5
Medium PI 2 (PI=31)	436.8	5.0	446.4	14.1	422.4	12.0	484.8	7.5	436.8	8.3
Medium PI 3 (PI=38)	321.6	6.8	321.6	11.3	369.6	12.5	331.2	7.5	379.2	19.5
High PI (PI=53)	259.2	14.7	220.8	16.4	288.0	10.0	297.6	7.4	254.4	14.2

Table 54. Summary of specimen-related variability of small direct shear test for clay

Material	Specimen 1		Specimen 2		Specimen 3	
	Avg. Cohesion	COV	Avg. Cohesion	COV	Avg. Cohesion	COV
	psf	%	psf	%	psf	%
Low PI (PI=11)	933.1	5.7	751.7	8.8	901.4	8.9
Medium PI 1 (PI=21)	599.0	10.8	607.7	10.1	622.1	10.0
Medium PI 2 (PI=31)	460.8	9.4	463.7	7.7	411.8	8.4
Medium PI 3 (PI=38)	374.4	15.4	334.1	11.6	325.4	8.6
High PI (PI=53)	256.3	20.0	267.8	13.5	267.8	14.0

Table 55. Summary of operator-related variability of small direct shear test on sand

Material	Operator 1		Operator 2		Operator 3		Operator 4		Operator 5	
	Avg. φ	COV	Avg. φ	COV	Avg. φ	COV	Avg. φ	COV	Avg. φ	COV
	Degree	%	Degree	%	Degree	%	Degree	%	Degree	%
Sand	31.1	1.8	36.4	0.5	30.3	0.5	35.4	0.9	35.3	0.4

Table 56. Summary of specimen-related variability of small direct shear test for sand

Material	Specimen 1		Specimen 2		Specimen 3	
	Avg. φ	COV	Avg. φ	COV	Avg. φ	COV
	Degree	%	Degree	%	Degree	%
Sand	33.9	8.2	33.7	8.8	33.6	7.8

Analysis of One Dimensional Consolidation Test Data

One dimensional consolidation tests were conducted on clay specimens ranging from low PI (PI=11) to high PI (PI=53). This test was operated by three different operators to evaluate the operator-related variability; while every operator conducted this test three times to determine specimen-related variability. For geotechnical engineering, the significance of this test is to determine the consolidation parameters (coefficient of consolidation, C_v, compression index, C_c, recompression (or swelling) index, C_r, and preconsolidation pressure, P_c) that are needed to assess the magnitude and time rate of consolidation settlement of clay soils.

The coefficient of consolidation, C_v, can be evaluated for each load increment using log time (t) versus displacement, d; curve and evaluate the d_{50} and t_{50} (Terzaghi method) from $\sqrt{t}$ versus d; and evaluate d_{50} and $\sqrt{t_{90}}$ (Tylor method). In this method, Taylor method was used to evaluate the coefficient of consolidation, C_v, using the following equation:

$$c_v = \frac{T_{90}\ H_D^2}{t_{90}} \qquad [148]$$

where: T_{90} = time factor for 90 percent consolidation; t = time corresponding to the particular degree of consolidation; H_D = length of drainage path.

Table 57 and Table 58 present the operator and the specimen-related variability for the preconsolidation pressure (P_c). The tables show that the COVs of Pc range from 5.0% to 19.5%, and from 3.3% to 20.4% for the operator and specimen variations, respectively. From Table 57, the maximum and the minimum values of operator-related COV are seen for medium PI 2 (PI=31) and medium PI 3 (PI=38), respectively. However, from Table 58, the maximum and the minimum values of specimen-related COV are observed for high PI (PI=53) and low PI (PI=11) and medium PI 1 (PI=21), respectively.

The operator-related COVs for the compression index (C_c) are presented in Table 59, which vary from 1.4% to 16.8%; whereas the specimen-related COVs for C_c range from 0.8% to 18.4%, as shown in Table 60.

Table 57. Summary of operator-related variability of preconsolidation pressure (P_c)

Material	Operator 1			Operator 2			Operator 3		
	Pc (Avg.)	SD	COV	Pc (Avg.)	SD	COV	Pc (Avg.)	SD	COV
	tsf	tsf	%	tsf	tsf	%	tsf	tsf	%
Low PI (PI=11)	1.57	0.21	13.3	1.78	0.10	5.8	1.60	0.10	6.3
Medium PI 1 (PI=21)	1.35	0.22	16.1	1.48	0.20	13.6	1.42	0.10	7.3
Medium PI 2 (PI=31)	1.13	0.15	13.5	1.07	0.21	19.5	1.13	0.12	10.2
Medium PI 3 (PI=38)	1.28	0.18	13.7	1.52	0.08	5.0	1.43	0.15	10.7
High PI (PI=53)	0.65	0.05	7.7	0.68	0.12	16.9	0.48	0.03	6.0

Table 58. Summary of specimen-related variability of preconsolidation pressure (P_c)

Material	Specimen 1			Specimen 2			Specimen 3		
	Pc (Avg.)	SD	COV	Pc (Avg.)	SD	COV	Pc (Avg.)	SD	COV
	tsf	tsf	%	tsf	tsf	%	tsf	tsf	%
Low PI (PI=11)	1.58	0.18	11.1	1.73	0.06	3.3	1.63	0.23	14.1
Medium PI 1 (PI=21)	1.62	0.13	7.8	1.77	0.06	3.3	1.60	0.26	16.5
Medium PI 2 (PI=31)	1.13	0.21	18.4	1.07	0.12	10.8	1.13	0.15	13.5
Medium PI 3 (PI=38)	1.52	0.08	5.0	1.37	0.25	18.4	1.35	0.09	6.4
High PI (PI=53)	0.65	0.13	20.4	0.55	0.10	18.2	0.62	0.13	20.4

Table 59. Summary of operator-related variability of compression index (C_c)

Material	Operator 1			Operator 2			Operator 3		
	Cc (Avg.)	SD	COV	Cc (Avg.)	SD	COV	Cc (Avg.)	SD	COV
			%			%			%
Low PI (PI=11)	0.158	0.007	4.4	0.141	0.024	16.8	0.139	0.015	10.6
Medium PI 1 (PI=21)	0.189	0.015	8.1	0.199	0.016	7.9	0.208	0.016	7.7
Medium PI 2 (PI=31)	0.236	0.004	1.9	0.261	0.024	9.3	0.227	0.003	1.4
Medium PI 3 (PI=38)	0.289	0.031	10.5	0.263	0.015	5.7	0.284	0.029	10.2
High PI (PI=53)	0.448	0.023	5.1	0.414	0.021	5.0	0.377	0.006	1.5

Table 60. Summary of specimen-related variability of compression index (C_c)

Material	Specimen 1			Specimen 2			Specimen 3		
	Cc (Avg.)	SD	COV	Cc (Avg.)	SD	COV	Cc (Avg.)	SD	COV
			%			%			%
Low PI (PI=11)	0.128	0.024	18.4	0.138	0.015	10.7	0.138	0.015	10.9
Medium PI 1 (PI=21)	0.184	0.014	7.5	0.200	0.006	2.8	0.212	0.013	6.1
Medium PI 2 (PI=31)	0.233	0.002	0.8	0.244	0.021	8.7	0.247	0.030	12.2
Medium PI 3 (PI=38)	0.262	0.021	8.1	0.277	0.027	9.6	0.298	0.021	7.1
High PI (PI=53)	0.416	0.033	7.9	0.408	0.029	7.1	0.415	0.053	12.8

The operator and specimen-related variability for the recompression index (C_r) are presented in Table 61 and Table 62, respectively. The results show that the operator-related COVs for C_r range from 5.6% to 18.2%., while the specimen-related COVs for C_r range from 3.6% to 17.1%. The maximum operator and specimen COV values are seen for Low PI (PI=11) and Medium PI 1 (PI=21), respectively; and the minimum operator and specimen COV values are noticed for Medium PI 3 (PI=38) and Low PI (PI=11), respectively.

Table 61. Summary of operator-related variability of recompression index (C_r)

Material	Operator 1			Operator 2			Operator 3		
	Cr (Avg.)	SD	COV	Cr (Avg.)	SD	COV	Cr (Avg.)	SD	COV
			%			%			%
Low PI (PI=11)	0.021	0.003	11.8	0.022	0.004	18.2	0.016	0.003	16.8
Medium PI 1 (PI=21)	0.032	0.003	9.5	0.030	0.002	7.0	0.035	0.003	9.9
Medium PI 2 (PI=31)	0.041	0.007	16.8	0.038	0.002	5.7	0.042	0.003	7.5
Medium PI 3 (PI=38)	0.058	0.003	5.6	0.064	0.004	6.5	0.068	0.008	12.3
High PI (PI=53)	0.107	0.013	12.4	0.117	0.009	7.4	0.108	0.008	7.0

Table 62. Summary of specimen-related variability of recompression index (C_r)

Material	Specimen 1			Specimen 2			Specimen 3		
	Cr (Avg.)	SD	COV	Cr (Avg.)	SD	COV	Cr (Avg.)	SD	COV
			%			%			%
Low PI (PI=11)	0.014	0.001	3.6	0.017	0.002	13.8	0.022	0.001	6.6
Medium PI 1 (PI=21)	0.034	0.006	17.1	0.031	0.001	3.9	0.032	0.002	6.7
Medium PI 2 (PI=31)	0.039	0.003	7.9	0.038	0.002	5.7	0.044	0.005	10.7
Medium PI 3 (PI=38)	0.064	0.009	14.1	0.065	0.006	9.3	0.061	0.007	11.0
High PI (PI=53)	0.110	0.010	9.4	0.112	0.013	12.0	0.110	0.010	9.2

The operator and specimen-related variability for the coefficient of consolidation (C_v) are presented in Table 63 and Table 64, respectively. The tables show that the operator-related COVs of C_v range from 2.3% to 20.9%; while the specimen-related COVs for C_v range from 5.5% to 30.6%.

Table 63. Summary of operator-related variability of the coefficient of consolidation (C_v)

Material	Operator 1			Operator 2			Operator 3		
	Cv (Avg.)	SD	COV	Cv (Avg.)	SD	COV	Cv (Avg.)	SD	COV
	in²/min	in²/min	%	in²/min	in²/min	%	in²/min	in²/min	%
Low PI (PI=11)	0.101	0.016	15.4	0.127	0.024	19.2	0.147	0.011	7.2
Medium PI 1 (PI=21)	0.161	0.017	10.5	0.197	0.038	19.1	0.168	0.014	8.1
Medium PI 2 (PI=31)	0.118	0.003	2.3	0.108	0.014	13.0	0.120	0.025	20.9
Medium PI 3 (PI=38)	0.116	0.010	8.9	0.194	0.017	8.8	0.166	0.012	7.3
High PI (PI=53)	0.140	0.017	12.0	0.102	0.020	19.2	0.099	0.008	8.6

Table 64. Summary of specimen-related variability of the coefficient of consolidation (C_v)

Material	Specimen 1			Specimen 2			Specimen 3		
	Cv (Avg.)	SD	COV	Cv (Avg.)	SD	COV	Cv (Avg.)	SD	COV
	in²/min	in²/min	%	in²/min	in²/min	%	in²/min	in²/min	%
Low PI (PI=11)	0.126	0.030	23.5	0.122	0.029	23.9	0.127	0.028	22.0
Medium PI 1 (PI=21)	0.167	0.017	10.0	0.176	0.010	5.5	0.183	0.049	27.0
Medium PI 2 (PI=31)	0.092	0.028	30.6	0.117	0.013	10.9	0.127	0.010	8.2
Medium PI 3 (PI=38)	0.161	0.041	25.5	0.145	0.036	24.9	0.170	0.042	24.5
High PI (PI=53)	0.127	0.027	21.0	0.115	0.027	23.3	0.100	0.019	18.7

Analysis of California Bearing Ratio (CBR) Test Data

The California Bearing Ratio (CBR) test was conducted by five operators to evaluate the operator-related variability and on three specimens to evaluate the specimen-related variability. The tests were conducted in four different materials: Kentucky limestone, Mexican limestone, RAP, and sand soil. In order to analyze data, it was first required to correct the stresses if necessary. As shown in Figure 72, the adjusted origins have been formed from the slope of the curve and then the corrected stresses are found from the y-axis for 0.1-in. and 0.2-in. penetrations. The figure shows the plot of CBR test, which indicates the adjusted origins along with the corrected stresses for 0.1-in. and 0.2-in. penetration.

Figure 72. Resistance to penetration (psi) vesrus penetration plot for Kentucky limestone

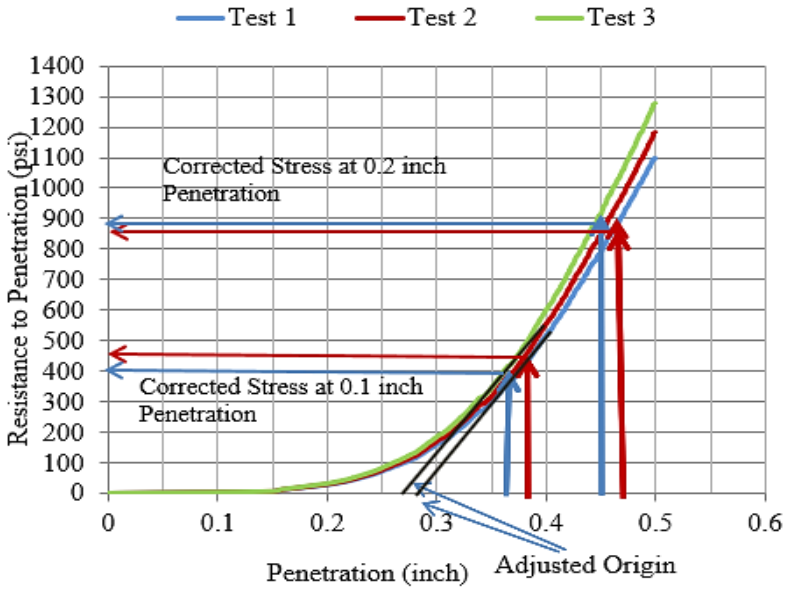

The operator and specimen-related variations of CBR results were evaluated and the results are summarized in Table 65 and Table 66, respectively. The results show that the operator-related COVs for CBR range from 4.2% to 15.6%, and the specimen-related COVs for CBR range from 5.7% to 16.0%. Furthermore, from Table 65, the maximum and minimum values of operator-related COVs are observed for sand and Mexican limestone, respectively. However, from Table 66, the maximum and the minimum values of specimen-related COVs are seen for Mexican Limestone and RAP, respectively.

Table 65. Summary of operator-related variability of CBR

Material	Operator 1		Operator 2		Operator 3		Operator 4		Operator 5	
	CBR (Avg.)	COV	CBR (Avg.)	COV	CBR (Avg.)	COV	CBR (Avg.)	COV	CBR (Avg.)	COV
	%	%	%	%	%	%	%	%	%	%
Kentucky Limestone	43.3	8.1	56.7	6.2	42.0	6.3	49.3	12.2	50.3	5.0
Mexican Limestone	40.0	6.6	50.3	6.1	39.3	5.3	36.7	4.2	39.3	6.4
RAP	25.7	11.9	24.0	8.3	23.7	10.6	23.7	10.6	24.3	8.6
Sand	13.7	11.2	12.7	12.1	11.7	4.9	12.3	4.7	13.3	15.6

Table 66. Summary of specimen-related variability of CBR

Material	Specimen 1		Specimen 2		Specimen 3	
	CBR (Avg.)	COV	CBR (Avg.)	COV	CBR (Avg.)	COV
	%	%	%	%	%	%
Kentucky Limestone	46.4	13.9	48.2	11.7	50.4	15.1
Mexican Limestone	40.8	10.2	40.6	14.6	42.0	16.0
RAP	23.6	8.8	22.8	5.7	26.4	5.7
Sand	12.4	9.2	12.6	14.4	13.2	9.9

Analysis of Combined Variability from AMRL and Lab Data

Analyses of combined variability from both the AASHTO Materials Reference Laboratory (AMRL) and lab test data can be determined using different statistical techniques. It is simple to calculate the coefficient of variations (COVs) when the average values and standard deviations are given for different dataset. The combined mean (or average), μ_a, of different combinations of datasets (μ_1 to μ_n) can be estimated statistically using the following equation:

$$\text{Average, } \mu_a = \frac{\mu_1 * n_1 + \mu_2 * n_2 + \mu_3 * n_3 + \ldots \mu_n * n_n}{n_1 + n_2 + n_3 + \ldots n_n} \quad [149]$$

In order to estimate the combined standard deviation (or combined pooled variance) of different population sets, samples taken from each population are first used to measure the variance, σ^2, for each set. The combined pooled variance, σ_p^2, can then be evaluated using the following equation:

$$\sigma_p^2 = \frac{\sum_{i=1}^{k} (n_i - 1)\sigma_i^2}{\sum_{i=1}^{k} (n_i - 1)} = \frac{(n_1 - 1)\sigma_1^2 + (n_2 - 1)\sigma_2^2 + \ldots + (n_k - 1)\sigma_k^2}{n_1 + n_2 + \ldots + n_k - k} \quad [150]$$

The collected data from AMRL and lab tests were analyzed to evaluate the combined variability for different tests. To estimate the combined variability, there are three group of datasets indicating set 1, set 2 and set 3. The AMRL data are composed of set 1 and set 2; whereas lab test data is incorporated with set 3. The collected AMRL data range from 2009–2010 to 2016–2017. Here, the Atterberg Limits and CBR tests are analyzed to evaluate the combined lab variability.

For each test, the mean (average) for each dataset is first calculated, and the combined mean, μ_a, of the three sets is evaluated using Equation 149. The standard deviation (or variance) is then calculated for each dataset. Finally, the combined variability is calculated and expressed in terms of standard deviation, σ, and the coefficient of variations, COV. Table 67 presents the calculation of combined variability of Atterberg limits of low PI soils for the combined AMRL 2016-2017 and lab test data. The combined COV for the liquid limit (LL) is 4.3%, and the combined COV for the plastic index (PI) is 6.7%. Table 68 summarizes the calculated COVs of Atterberg limits for different PI soils (Low, medium, and high PI) using the different AMRL datasets (2009-2010 to 2016-2017).

It can seen from Table 68 that the COVs vary from 4.3% to 8.4% for the LL, where the lowest and the highest COVs are for the 2016-17 and 2009-10 datasets, respectively. However, the COVs of the PL range from 6.7% to 9.4%, with the minimum and maximum of COVs for 2016-17 and 2013-14, respectively.

Table 67. Combined variability analysis of Atterberg limits for combined AMRL and lab data

Low PI (PI=11) Soil	AMRL Data 2016-2017						Lab Test Data			Combined Variability		
	Sample 1			Sample 2			Sample 3					
	No. of Data	Avg.	SD	No. of Data	Avg.	SD	No. of Data	Avg.	SD	Avg.	SD	COV
	n_1	μ_1	σ_1	n_2	μ_2	σ_2	n_3	μ_3	σ_3	μ	σ	%
LL	1588	33.1	1.4	1588	32.7	1.4	15	32.5	2.0	32.9	1.4	4.3
PI	1588	18.8	1.3	1588	18.8	1.3	15	19.5	1.7	18.8	1.3	6.7

*LL = Liquid Limit, PL = Plastic Limit and PI = Plasticity Index

Table 68. Summary of the COVs of Atterberg limit test for AMRL data

Year	Low PI (PI=11)		Medium PI 1 (PI=21)		Medium PI 2 (PI=31)		Medium PI 3 (PI=38)		High PI (PI=53)	
	LL	PL	LL	PL	LL	PL	LL	PL	LL	PL
	COV	COV	COV	COV	COV	COV	COV	COV	COV	COV
	%	%	%	%	%	%	%	%	%	%
2009-10	8.3	8.0	8.3	8.2	8.3	8.0	8.3	8.0	8.4	8.6
2010-11	7.7	7.4	7.7	7.5	7.7	7.4	7.7	7.4	7.7	7.9
2011-12	6.6	7.5	6.6	7.6	6.6	7.5	6.6	7.5	6.7	8.0
2012-13	5.9	7.8	5.9	8.0	5.9	7.9	5.9	7.8	6.0	8.2
2013-14	6.6	9.2	6.6	9.2	6.6	9.2	6.6	9.1	6.6	9.4
2014-15	7.4	8.5	7.4	8.6	7.4	8.5	7.4	8.4	7.4	8.9
2015-16	5.2	7.0	5.2	7.2	5.2	7.1	5.2	7.0	5.3	7.5
2016-17	4.3	6.7	4.3	6.8	4.3	6.8	4.3	6.7	4.4	7.0

The summary of COVs of CBR test from AMRL data for the different geomaterials (sand, RAP, Kentucky limestone, and Mexican limestone) are summarized in Table 69. The results show that the COVs range from 16.5% (for Mexican limestone and 2009-2010 AMR data) to 34.9% (for sand and 2012-2013 AMR data).

Table 69. Summary of COVs of CBR test for AMRL data

Year	Sand		RAP		Kentucky Limestone		Mexican Limestone	
	CBR at 0.1 inch	CBR at 0.2 inch	CBR at 0.1 inch	CBR at 0.2 inch	CBR at 0.1 inch	CBR at 0.2 inch	CBR at 0.1 inch	CBR at 0.2 inch
	COV %	COV %	COV %	COV %	COV %	COV %	COV %	COV %
2009-10	16.8	24.7	16.8	24.5	16.8	24.3	16.5	24.3
2010-11	31.8	30.5	31.7	30.3	31.5	24.6	31.6	24.7
2011-12	27.3	26.2	27.2	26.0	27.0	25.7	26.9	25.8
2012-13	34.9	32.9	34.8	32.4	34.4	32.0	33.7	31.3
2013-14	31.5	30.0	31.4	29.9	31.1	29.6	31.2	29.7
2014-15	33.1	24.3	31.9	28.5	30.4	28.1	30.4	28.2
2015-16	33.9	24.2	33.8	24.1	33.6	24.0	33.7	24.0
2016-17	33.3	22.9	33.2	22.9	33.0	22.7	33.1	22.8

Evaluation of Site Variability using Semivariogram

Site Variability from CPT data and LCPC- Pile CPT Method

To investigate site variability from the CPT data and its effect on the LRFD design of piles using the LCPC Pile-CPT design method, the corrected tip resistance, q_t, were collected from six different project sites (Metairie, ALF, US 90, and LA 85, Hammond, Bayou Lacassine, and LA 1) for evaluation per site. The CPT location points for each site are presented earlier in Figure 43. The soil profile, soil properties, CPT data and CPT soil classification for Metairie site with depth were presented earlier in Figure 45. The soil profiles, soil properties, CPT data, and CPT soil classifications for the other sites are presented in Appendix B. In order to investigate the effect of site variability for each site using the geo-statistics tools, all the collected data for each site need to be first transferred to stationary data without any trend prior to performing the semivariogram analyses. The

CPT data collected for Metairie site and ALF site (as examples) were transformed from nonstationary data (with trend) to stationary data for each layer by removing the trend values using the equations presented on Figure 73a and Figure 74a, respectively. The corresponding transformed CPT data from Metairie site and ALF site are shown in Figure 73b and Figure 74b, respectively. Data transformation from nonstationary data (with trend) to stationary data were also performed for the other four CPT sites in this study, following the same procedure done for Metairie and ALF sites, and are presented in Appendix D. All the data used to evaluate site variability from CPT data for the six sites are stationary data without any trend.

Figure 73. Transferring the data from non-stationary to stationary data for Matierie site: (a) non-stationary data with trend line; (b) stationary data

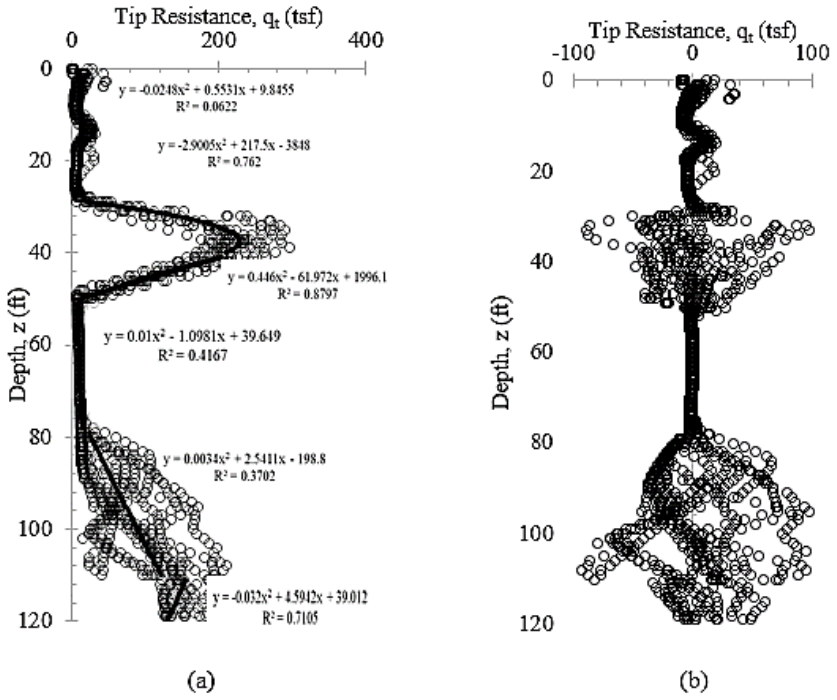

Semivariogram analyses were performed on the CPR-q_t data using the JeoStat software for each soil layer of the six CPT sites. The resulted experimental semivariograms for the six soil layers at Metairie site for vertical and horizontal directions are presented in Figure 75 and Figure 76, respectively. The spherical model presented in Equation 20 was adopted here to fit the model′s semivariogram with the experimental data to define the vertical and horizontal correlation ranges, a_v and a_h, for each soil layer. The results values of a_v and a_h for the six soil layers at Metairie site were determined as shown in the figures. The values of a_v for the Matierie site are 5.90 ft., 8.80 ft., 8.08 ft., 12.20 ft.,

12.40, and 8.0 ft. for the soil layers 1st, 2nd, 3rd, 4th, 5th and 6th layers, respectively. However, the values of a_h for the Matairie site are 100 ft., 150 ft., 110 ft., 100 ft., 117.5 ft. and 100 ft. for 1st, 2nd, 3rd, 4th, 5th and 6th layers, respectively. Apparently, the range of a_h values (100 to 150 ft.) is much higher than the range of a_v values (5.9 to 12.4 ft.) due to large spacing between the CPT test locations (≥24 ft.), which will result on minimal effect of the horizontal variability.

Figure 74. Transferring the data from non-stationary to stationary data for ALF Site: (a) non-stationary data with trend line; (b) stationary data

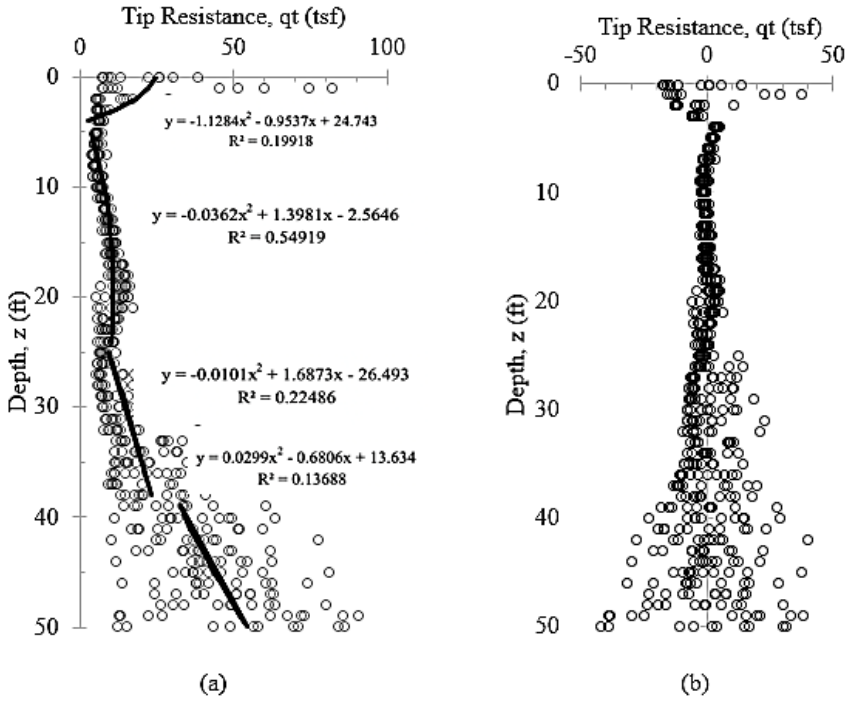

Semivariogram analyses were also conducted on LA 1 site to fit the experimental CPT-q_t data into spherical semivariograms, and to determine the ranges of vertical and horizontal correlation, a_v and a_h, for each soil layer. The resulted experimental vertical and horizontal semivariograms for the four soil layers at LA 1 site are presented in Figure 77 and Figure 78, respectively. The ranges of a_v for the LA 1 site are 5 ft., 11.5 ft., 10.4 ft., and 11.9 ft. for the 1st, 2nd, 3rd, and 4th layers, respectively; while the range of a_h are 12.5 ft., 13 ft., 14 ft., and 17.5 ft. for the 1st, 2nd, 3rd, and 4th layers, respectively. The horizontal correlation factors, a_h, for LA 1 are also higher than a_v. Similar semivariogram analyses were conducted on the other four CPT sites in this study, following the same procedure done for Metairie and LA 1 sites, and the results are presented in Appendix D.

Figure 75. Experimental and spherical vertical semivariogram models for the CPT-q_t data of soil layers at Metairie site

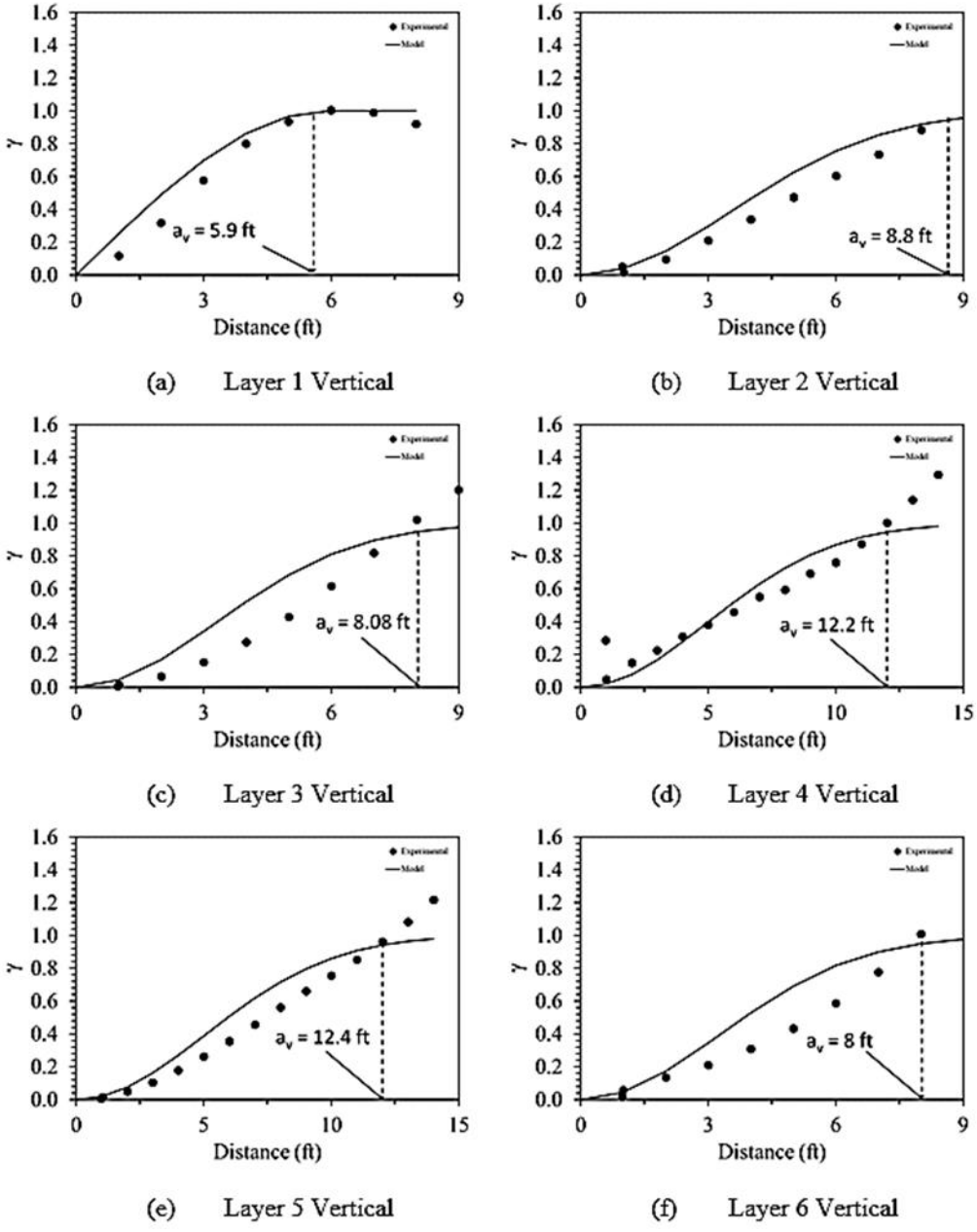

Figure 76. Experimental and spherical horizontal semivariogram models for the CPT-q_t data of soil layers at Metairie site

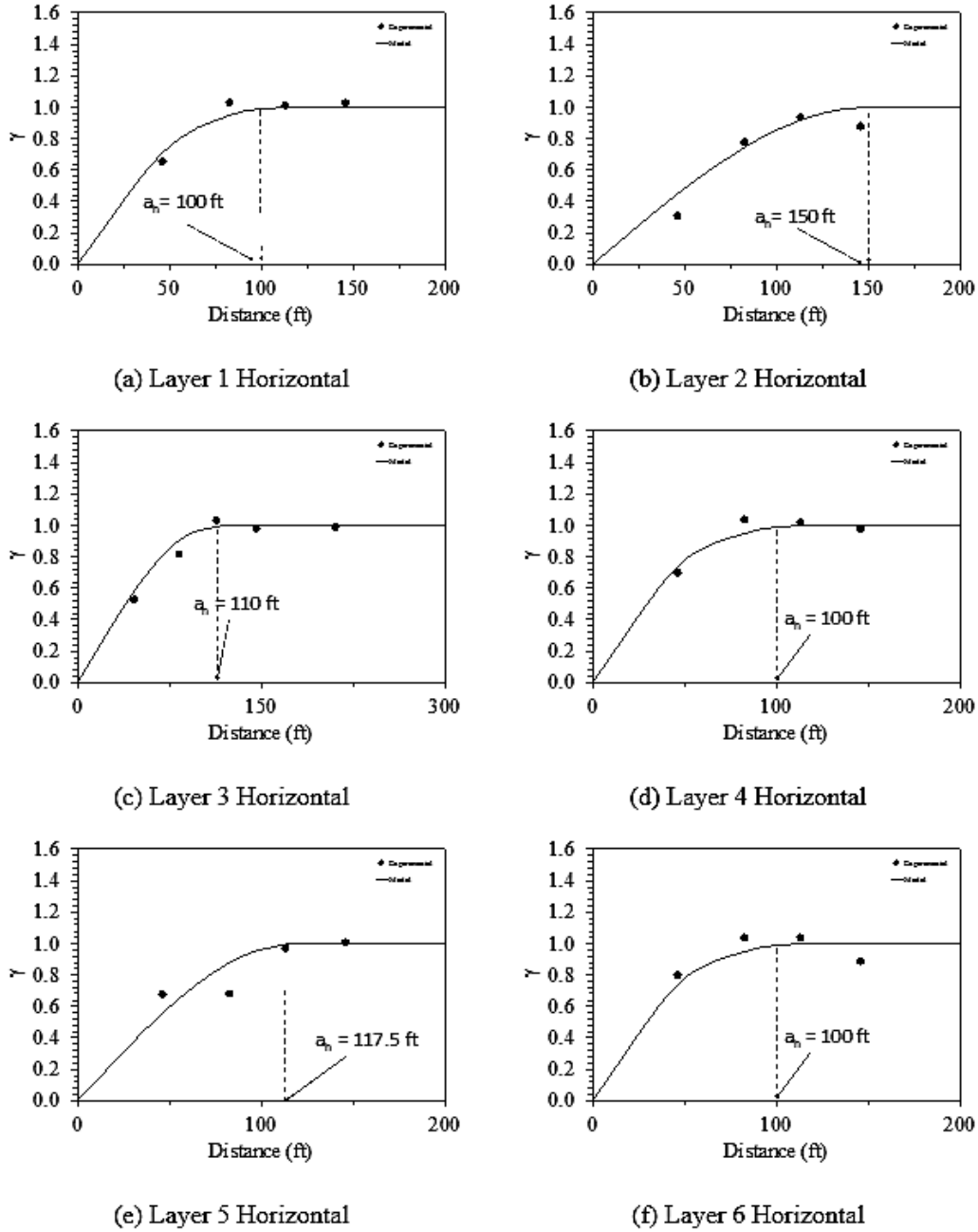

Figure 77. Experimental and spherical vertical semivariogram models for the CPT-q_t data of soil layers at LA 1 site

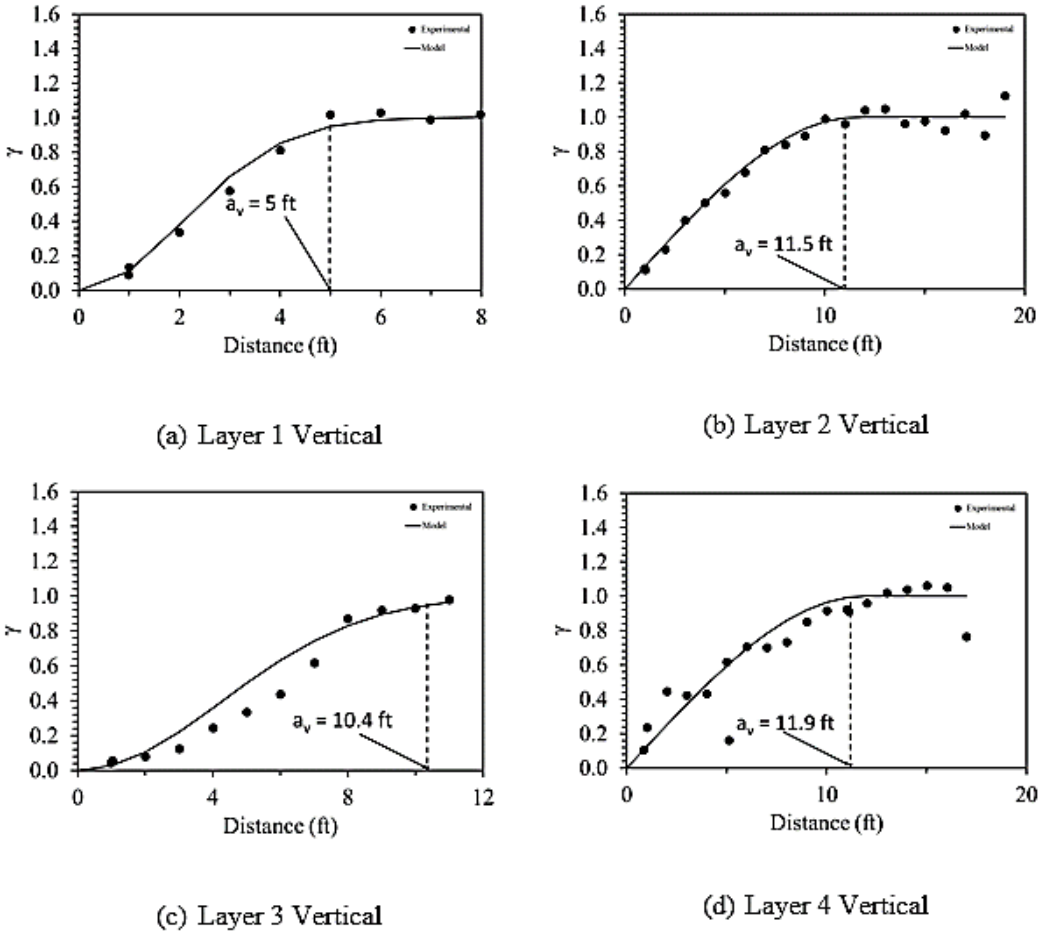

The variance reduction factor, α_r, depends on both the spatial correlation of variable (CPT-q_t) and the pile or shaft geometry. It can be calculated using $C(h_i)$ from Equation 17 and a set of relevant parameters L, D, a_v, and a_h. Figure 12 presents the relationship between $\alpha_r^{1/2}$ and the dimensionless ratios L/a_v and D/a_h [14]. The figure shows that α_r decreases with increasing of either L/a_v or D/a_h. When either L/a_v or D/a_h is very large (i.e., a variogram with very short range), α_r becomes very small (approaches zero). However, in situations were both L/a_v and D/a_h equal zero, there will be no effective averaging or variance reduction, resulting in $\alpha_r = 1$.

When considering the effect of horizontal site variability, generally, there will be two scenarios: (a) the horizontal range, a_h, is unknown (i.e., the horizontal distances between test points are large), and (b) the horizontal range, a_h, is determined.

Figure 78. Experimental and spherical horizontal semivariogram models for the CPT-q_t data of soil layers at LA 1 site

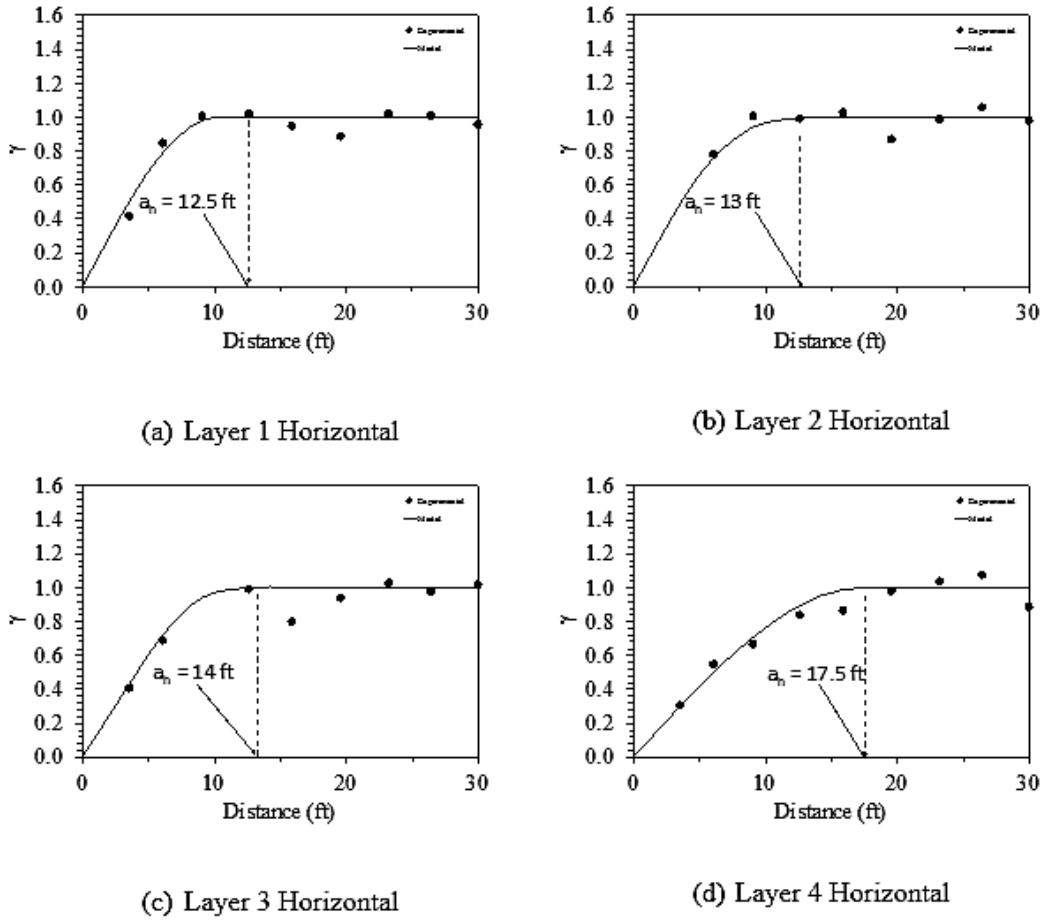

When the CPT tests and soil borings are located far away from each other, the resulting horizontal range, a_h, will be much larger than the vertical range, a_v (i.e., has negligible effect). For these conditions, the authors are recommending to assume a_h = (2-4) a_v (i.e., the horizontal range is two to four times of the vertical range) depending on the importance of the project. However, a conservative approach of $D/a_h \approx 0$ can also be adopted. Then the value $\alpha_r^{1/2}$ can be extracted by using the dimensionless variables L/a_v and D/a_h from Figure 12.

When the horizontal range, a_h, can be determined, such as the case for Metairie and LA 1 sites, both values of a_v and a_h will be used to evaluate α_r using Figure 12. To investigate site variability (including horizontal range) of the CPT-q_t data and its effect on the LRFD design of piles using the LCPC Pile-CPT design method, the q_t data collected from the two sites (Metairie and LA 1) will be evaluated separately. The CPT location points for

the two sites are presented earlier in Figure 43; and the soil profile, soil properties CPT data are presented in Figure 45 and Appendix B for the Metairie and LA 1 sites, respectively. The first step to investigate the effect of site variability for each site using the geo-statistics tools is to transfer the collected data to stationary data without any trend. Then develop the experimental vertical and horizontal semivariograms to evaluate the correlation factors a_v and a_h for each soil layer per site.

Once the values of a_v and a_h are evaluated for each site, the reduction factor, α_r can be determined using the dimensionless variables L/a_v and D/a_h and using Figure 12. The spatial coefficient of variation, $COV_{R,spatial}$, can be evaluated using Equation 19, and the load coefficient of variation, COV_Q, can be evaluated using Equation 23. Here, the layer wise, σ, and the mean, m, were calculated from the q_t data (using the JeoStat software). The resistance factor considering spatial variability, $\phi_{spatial}$, for each site was then evaluated using Equation 21.

The values of $COV_{R,spatial}$ for the Metairie site (from q_t data) using the generated a_h, $a_h=2a_v$, and $D/a_h\approx0$ were calculated to be 0.2167, 0.2149, and 0.20, respectively. The corresponding LRFD resistance factors based on spatial variability, $\phi_{spatial}$, are 0.7342, 0.7293, and 0.76, for the generated a_h, $a_h=2a_v$, and $D/a_h \approx0$, respectively.

The values of $COV_{R,spatial}$ for the LA 1 site (from q_t data) using the generated a_h, $a_h=2a_v$, and $D/a_h\approx0$ were calculated to be 0.1044, 0.1058 and 0.10, respectively. The corresponding LRFD resistance factors based on spatial variability, $\phi_{spatial}$, are 0.9229, 0.9206 and 0.93, for the generated a_h, $a_h=2a_v$, and $D/a_h \approx0$, respectively.

These resistance factors were calculated using the $COV_{R,spatial}$ only. The LRFD resistance factors were also calculated using the design method resistance coefficient of variation, $COV_{R,method}$, which is equal to 0.31 for LCPC pile CPT design method [57]. The corresponding method's resistance factor, ϕ_{method}, for LCPC design method equals 0.61, which is the same for all scenarios. In this study, the authors recommended earlier to incorporate both the site variability, $COV_{R,spatial}$, and the method variability, $COV_{R,method}$, in the LRFD calibration of resistance factor, ϕ_{total}, using the following proposed equation [143]:

$$COV_{R,total} = \frac{c1.COV_{R,spatial} + c2.COV_{R,method}}{c1 + c2} \quad [149]$$

The calculated COVs and the corresponding calibrated resistance factors (ϕ) for the different scenarios are summarized in Table 70. It is clear that when the site has lower

variability than the design method variability (i.e., $COV_{R,spatial} < COV_{R,method}$), the value of the $COV_{R,total}$ will be decreased and the corresponding resistance factor will be increased, and vice versa.

The table shows that the $COV_{R,spatial}$, $COV_{R,total,}$ and ϕ_{total} for Metairie site using the generated a_h are 0.2167, 0.2633, and 0.66, respectively. Using $a_h=2a_v$, the $COV_{R,spatial}$ = 0.2149, $COV_{R,total}$ =0.2624, and ϕ_{total} = 0.6582. However for the $D/a_h \approx 0$ case, the $COV_{R,spatial}$, $COV_{R,total,}$ and ϕ_{total}l are 0.20, 0.255, and 0.67, respectively.

For LA 1, the table shows that the values of $COV_{R,spatial}$, $COV_{R,total,}$ and ϕ_{total}l using the generated a_h are 0.1044, 0.2072, and 0.7498, respectively. When assuming $a_h=2a_v$, the $COV_{R,spatial}$ = 0.1058, $COV_{R,total}$ =0.2079, and the ϕ_{total} = 0.7486. Finally, the values of $COV_{R,spatial}$, $COV_{R,total}$, and ϕ_{total}l for the case of $D/a_h \approx 0$ are 0.10, 0.205, and 0.75, respectively. It can be seen from Table 70 that the effect of considering the horizontal range in analysis is not significant. Therefore, for simplification of the analysis, we can assume $D/a_h \approx 0$.

Table 70. Calibrated resistance factors, ϕ_R, for LCPC design method for Metairie and LA 1 sites

Parameters	Metairie			LA 1		
	Generated a_h	$a_h=2a_v$	$\frac{D}{a_h} \approx 0$	Generated a_h	$a_h=2a_v$	$\frac{D}{a_h} \approx 0$
$COV_{R,spatial}$	0.2167	0.2149	0.20	0.1044	0.1058	0.10
$COV_{R,method}$ (LCPC)	0.31					
$COV_{R,total}$	0.2633	0.2624	0.255	0.2072	0.2079	0.205
COV_Q^2	0.0111					
$\phi_{spatial}$	0.7342	0.7293	0.76	0.9229	0.9206	0.93
ϕ_{method} (LCPC)	0.61					
ϕ_{total}	0.660	0.6582	0.67	0.7498	0.7486	0.75

The variability analyses for the other four sites were done using the vertical range only (i.e., assuming D/ah ≈0), since the effect horizontal range is not significant. Additionally, the minimum spacing between the CPT test locations are considered large compared to the pile width used in these project.

The vertical ranges, a_v, for the ALF site are 3 ft., 12.7 ft., 3 ft., and 4 ft. for 1st, 2nd, 3rd, and 4th layers, respectively. In case of Bayou Laccassine, the vertical ranges, av, for the 1st, 2nd, 3rd, 4th and 5th layers are 4.35 ft., 10.50 ft., 6.7 ft., 11 ft. and 8.30 ft.,

respectively. The vertical ranges, a^v, for the US 90 and LA 85 site are 4.9 ft., 8.5 ft., 2.6 ft., 6.8 ft., 4.9 ft., and 4.8 ft. for 1st, 2nd, 3rd, 4th, 5th, and 6th layers, respectively. For Hammond site, the vertical ranges, av, for the 1st, 2nd and 3rd layers are 2.08 ft., 5.50 ft., and 1.5 ft., respectively.

The calculated coefficients of variabilities (COV) and the corresponding calibrated resistance factors (ϕ_R) for the four sites (ALF, Bayou Laccassine, US 90 and LA 85, and Hammond sites) are summarized in Table 71. It is clear that when the site has lower variability than the design method variability (i.e., $COV_{R,spatial} < COV_{R,method}$), the value of $COV_{R,total}$ decreases and the corresponding resistance factor increases, and vice versa.

Table 71. Calibrated resistance factors, ϕ_R, for LCPC design method for the other four sites

Parameters	ALF	BL	US 90	Hammond
$COV_{R,spatial}$	0.11	0.08	0.09	0.16
$COV_{R,method}$ (LCPC)	0.31			
$COV_{R,total}$	0.21	0.195	0.20	0.235
COV_Q^2	0.0111			
$\phi_{spatial}$	0.91	0.96	0.94	0.83
ϕ_{method} (LCPC)	0.61			
ϕ_{total}	0.74	0.77	0.76	0.70

The results in Table 71 show that the $COV_{R,spatial}$, $COV_{R,total}$, and ϕ_{total} for ALF site are 0.11, 0.21, and 0.74, respectively. For Bayou Lacassine site, the $COV_{R,spatial}$, $COV_{R,total}$, and ϕtotal are 0.08, 0195 and 0.77, respectively. The values of $COV_{R,spatial}$, $COV_{R,total}$, and ϕ_{total} for the US 90 and LA 85 site are 0.09, 0.20, and 0.76, respectively. Finally, for the Hammond site, the $COV_{R,spatial} = 0.16$, $COV_{R,total} = 0.235$, and the $\phi_{total} = 0.70$. It can seen from Table 70and Table 71 that the values of ϕ_{total} are different for the different sites, basically due to variability on the $COV_{R,spatial}$ of the sites. The relatively high site variability of Metairie resulted on lower resistance factor, $\phi_{total} = 0.67$, as compared to other sites; while the low site variability of Bayou Lacassine resulted on higher resistance factor, $\phi_{total} = 0.77$, than the other sites.

Site Variability and FHWA Static Pile Design Method

The FHWA pile design method adopted the Nordlund (effective stress) method for the sand layers and the α-Tomlinson (total stress) method for clay layers along the pile length. Usually, the SPT data are used to evaluate the friction angle in Nordlund method;

while the α-Tomlinson method is based on the undrained shear strength, S_u. For sites consist of sandy soils, the Nordlund design method is usually used for pile design; while for sites with cohesive clayey soils, the α-Tomlinson design method is usually used for pile design. However, for mixed soil conditions, both design methods are used.

Amongst the four sites evaluated in this study for soil borings, the subsurface soil conditions in three sites (i.e., Bayou Lacassine, Red River and Williams Boulevard) are clayey soils, and therefore the α-Tomlinson design method based on S_u will be used in these sites. However, the subsurface soil condition at Metairie sites consists of mixed soil layers, therefore, both the Nordlund and α-Tomlinson design methods will be analyzed.

Site Variability from Undrained Shear Strength and α-Tomlinson Method

To investigate site variability from undrained shear strength, S_u, data for the α-Tomlinson method, soil boring data were collected from three sites (i.e., Bayou Lacassine, Red River and Williams Boulevard). The distribution of soil borings for the three sites are shown in Figure 44. For Bayou Lacassine, the maximum, minimum, and average COV of S_u (COV_{Su}) from soil borings are 0.80, 0.29 and 0.51, respectively. For the Red River site, the maximum, minimum, and average of COV_{Su} are 0.91, 0.11, and 0.35, respectively. For the Williams Boulevard site, the maximum, minimum, and average of COV_{Su} are 0.39, 0.13, and 0.26, respectively. All the S_u data used in the study are stationary data without any trend. The profile of soil type/layers and S_u data for the Red River site (as an example) are shown in Figure 79. Experimental semivariogram analyses were performed using the JeoStat software to evaluate the vertical correlation range, a_v, for the soil layers of each site (as shown in Figure 80 for the Red River site). Analyses were done in the vertical direction only since the horizontal distance between the soil borings were very large. The spherical model, as described in Equation 20, was used to fit the spherical semivariogram model with the experimental S_u data, and to evaluate the vertical correlation range, a_v, for each soil layer. Figure 80 presents the semivariogram and corresponding a_v values for the four soil layers at the Red River site. The value of a_v are 7.0 ft., 10.7 ft., 5.5 ft., and 6.0 ft. for the 1st, 2nd, 3rd, and 4th soil layers, respectively.

Similar analyses were performed for the other two soil boring sites to fit the experimental data of S_u into spherical semivariograms, and to evaluate the vertical ranges, a_v, for each soil layer. For the Bayou Laccassine site, the vertical ranges, a^v, for the 1st, 2nd, 3rd, 4th and 5th layer are 3.20 ft., 5.90 ft., 6.10 ft., 9.50 ft., and 14.50 ft., respectively. The

vertical range, a_v, for the Williams Boulevard site are 19.50 ft., 24.0 ft., 24.0 ft., and 10.80 ft. for the 1st, 2nd, 3rd, and 4th layer, respectively.

Figure 79. Profile of soil layers and S_u data for the Red River site

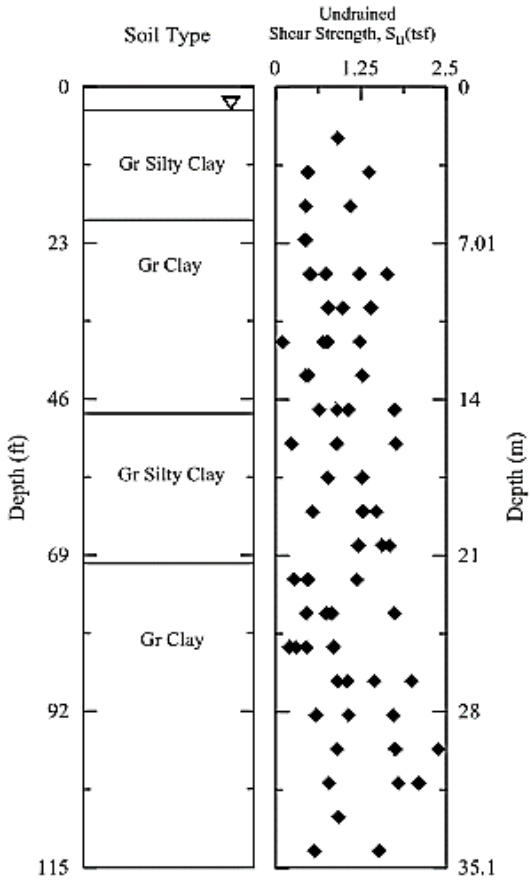

The values of a_v evaluated from the semivariograms analysis were used to calibrate the LRFD resistance factor, ϕ_R, as shown in Table 72. As described earlier, the value of reduction factor, α_r, for each soil layer was calculated using Equation 20. The spatial coefficient of variation, $COV_{R,spatial}$, for each site was evaluated using Equation 19, and the load coefficient of variation, COV_Q, was evaluated from Equation 23. Finally, the resistance factor considering spatial variability, $\phi_{spatial}$, for each site was calculated using Equation 21. The values of $COV_{R,spatial}$ for Bayou Laccasine, Red River and Williams Boulevard sites were calculated as 0.22, 0.19, and 0.14, respectively, as shown in Table 72. The corresponding LRFD resistance factors based on site variability only, $\phi_{spatial}$, are 0.61, 0.65, and 0.72 for Bayou Laccasine, Red River, and Williams Boulevard sites, respectively. The LRFD resistance factors for the α-Tomlinson method, ϕ_{method},

corresponding to the bias $\lambda_R = 0.87$ and $COV_{R,method} = 0.48$ is equal 0.34 [58]. To incorporate both the site variability, $COV_{R,spatial}$, and the method variability, $COV_{R,method}$, in the LRFD calibration of resistance factor, ϕ_{total}, Equation 21 was used to calculate $COV_{R,total}$, and to calibrate the corresponding ϕ_{total}. Table 72 summarizes the coefficients of variations (COV) and the corresponding calibrated resistance factors (ϕ_R) for the three project sites. Again, for sites with lower site variability than the design method variability (i.e., $COV_{R,spatial} < COVR_{,method}$), the value of the $COV_{R,total}$ decreased and the corresponding resistance factor, ϕ_{total}, increased, and vice versa. For the three investigated sites here, $COV_{R,spatial} < COV_{R,method}$, and therefore both the $\phi_{spatial}$ (0.61 to 0.72) and the ϕ_{total} (0.45 to 0.49) are higher than the ϕ_{method} (0.34).

Figure 80. Experimental and spherical semivariogram models for S_u data of the Red River site

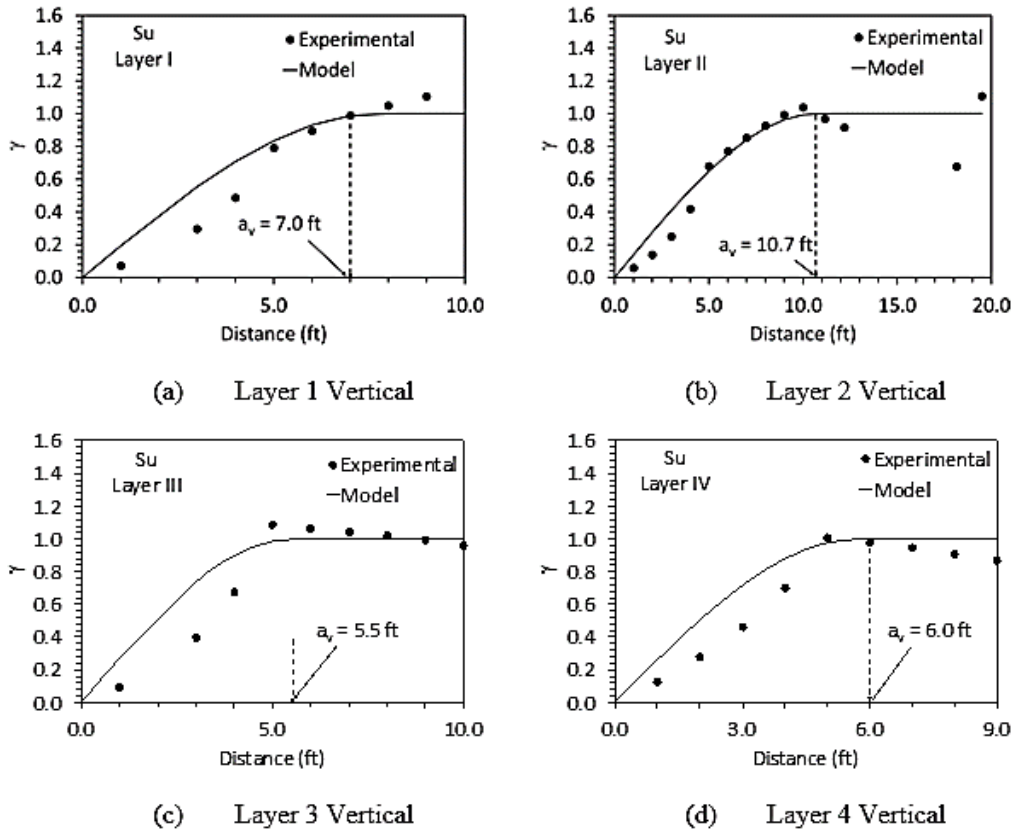

Site Variability of Mixed Soil at Metairie Site and Combined Static Method

The subsurface soil condition at Metairie site consists of four layers, two clayey layers (I: 0 to 29 ft. and III: 48 to 78 ft.), and two sandy layers (II: 29 to 48 ft. and IV: 78 to 105 ft.). For Layer I and III, the maximum, minimum, and average COV of S_u (COV_{Su}) from

soil borings are 0.67, 0.17 and 0.27, respectively. For Layer II and IV, the maximum, minimum, and average COV of SPT-N (COV_{SPT-N}) from soil borings are 0.70, 0.13, and 0.31, respectively. Therefore, the collected S_u data will be used to evaluate the site variability for Layers I and III for incorporation into the α-Tomlinson pile design method, and the collected SPT-N data will be used to evaluate the site variability for Layers II and IV for integration into the Nordlund pile design method, separately. This means we will calibrate two methods′ resistance factors; one for α-Tomlinson method ($\phi_{R,Tomlinson}$ method) and one for Nordlund method ($\phi_{R,Nordlund}$ method). In addition, the combined site variability from both the S_u and SPT-N collected data was used to calibrate the resistance factor for the combined static analysis method ($\phi_{R\text{-}static}$ method). A recent study by [57] calibrated the FHWA static method for piles driven in mixed soil conditions in Louisiana, and the values of λ_R and $COVR_{,Static}$ were calculated to be 0.91 and 0.42, respectively.

Table 72. Calibrated resistance factors, ϕ_R, for α-Tomlinson static design method

Parameters	Bayou Lacassine	Red River	Williams Blvd
$COV_{R,\ spatial}$	0.22	0.19	0.14
$COV_{R,\ method}$ (α method)	0.48		
$COV_{R,\ total}$	0.35	0.33	0.31
COV_Q^2	0.0111		
$\phi_{spatial}$	0.61	0.65	0.72
ϕ_{method} (α method)	0.34		
ϕ_{total}	0.45	0.47	0.49

The measured S_u data and SPT-N data collected from the different boreholes at Metairie site are plotted versus depth for the four layers as shown in Figure 81a and Figure 81b, respectively. All the S_u and SPT-N data used in Metairie site are stationary data without any trend. Experimental semivariogram analyses were performed using the JeoStat software for the four soil layers at Metairie site as shown in Figure 82. The analyses were done in the vertical direction only due to large horizontal distances between the soil borings. Spherical model (Equation 17) was used to fit the semivariogram model with the experimental S_u or SPT-N data, and to determine the vertical correlation range, a_v, for each soil layer. Figure 82a and Figure 82b present the semivariograms and the corresponding a_v values for the clay layers I and III, respectively. Figure 82c and Figure 82d present the semivariograms and the corresponding a_v values for the sand layers II and IV, respectively. The values of vertical range, a_v, for the soil layers I, II, III, and IV are 8.8 ft., 14.4 ft., 12.2 ft., and 24.0 ft., respectively.

Figure 81. Measured undrained shear strength, S_u, and SPT-N data for Metairie site

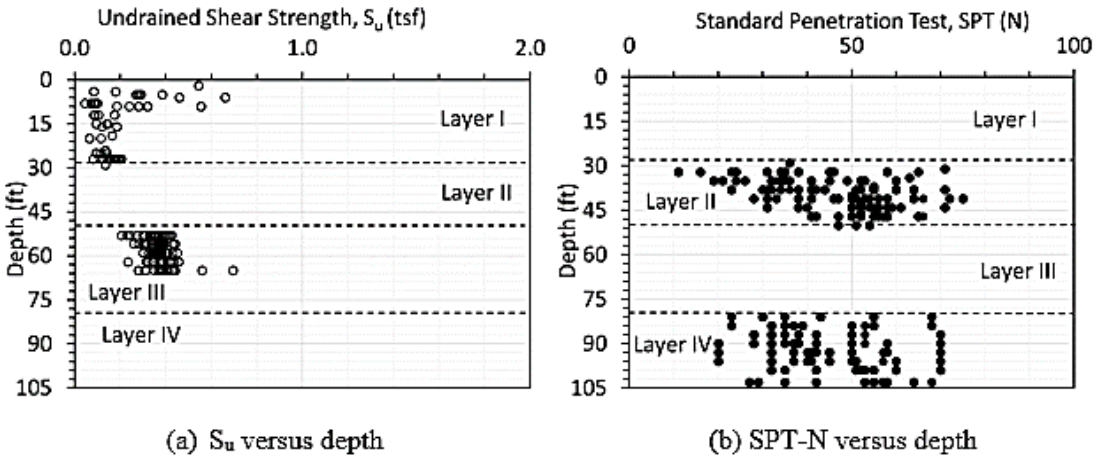

(a) S_u versus depth (b) SPT-N versus depth

Figure 82. Experimental and spherical semivariogram models for S_u data of the Metairie site

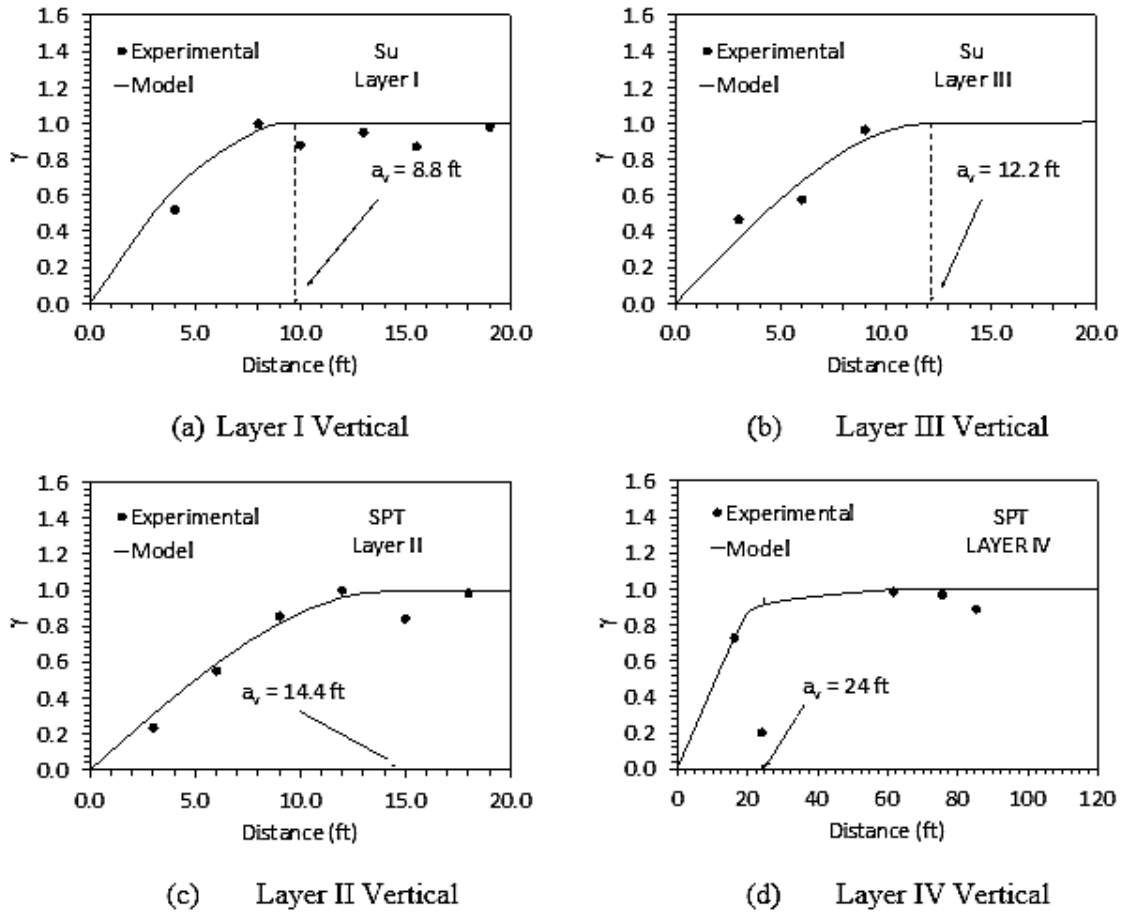

(a) Layer I Vertical (b) Layer III Vertical

(c) Layer II Vertical (d) Layer IV Vertical

The correlation vertical range, a_v, determined from the semivariogram were used to evaluate the reduction factor, α_r, for each soil layer and the spatial coefficient of variation, $COV_{R,spatial}$, (for both S_u and SPT-N) using Equation 20 and Equation 19, respectively. As shown in Table 73, the $COV_{R,spatial}$ for layers I and III, layers II and IV, and for Metairie site are 0.10, 0.17, and 0.166, respectively. The load coefficient of variation, COV_Q, was evaluated from Equation 23. The resistance factor considering to spatial variability, $\phi_{spatial}$, for α-Tomlinson method (layers I and III), Nordlund method (layers II and IV), and combined static method (all layers) were calculated using Equation 21. The corresponding resistance factors based on $\phi_{spatial}$ only are 0.82, 0.74, and 0.70 for the α-Tomlinson method, Nordlund method, and combined static method, respectively. The resistance factors for the methods, ϕ_{method}, are 0.34, 0.41, and 0.40, for the α-Tomlinson method Nordlund method, and combined static method, respectively. Equation 149 was then used to calculate the $COV_{R,\ total}$ to incorporate both site variabilities, $COV_{R,spatial}$, and $COV_{R,method}$, into the LRFD calibration of resistance factor, ϕ_{total}, assuming $c_1 = c_2 = 0.5$. Table 73 summarizes the coefficients of variations (COV) and the corresponding calibrated resistance factors (ϕ_R) for the α-Tomlinson method, Nordlund method, and combined static method. It is clear that the site variability for the Metairie site is lower than the design method variability (i.e., $COV_{R,spatial} < COV_{R\text{-}method}$), and therefore a credit will be given to the site by increasing the resistance factors, $\phi_{spatial}$ and ϕ_{total}, used for designing of pile foundations using α-Tomlinson method, Nordlund method, or combined static method. Both the $\phi_{spatial}$ (0.74 to 0.82) and the ϕ_{total} (0.58 to 0.62) are higher than the ϕ_{method} (0.34 to 0.41).

Table 73. Calibrated resistance factors, ϕ_R, for Metairie site

Parameters	α-Tomlinson Method (Layers I and III)	Nordlund Method (Layers II and IV)	Combined Static Method (All Layers)
$COV_{R,\ spatial}$	0.10	0.17	0.166
$COV_{R,\ method}$	0.48	0.48	0.42
$COV_{R,\ total}$	0.29	0.32	0.29
COV_Q^2	0.0111	0.0111	0.0111
$\phi_{spatial}$	0.82	0.74	0.70
ϕ_{method}	0.34	0.41	0.40
ϕ_{total}	0.62	0.58	0.53

Discussion of Semivariogram Analysis

The value of resistance factor, ϕ_R, in LRFD design of pile foundations is directly related to the resistance coefficient of variation (COV_R) due to uncertainty in subsurface soil resulting from spatial variability, statistical error, measurement error, and model bias. In this section, the CPT data (q_t) and soil borings data (S_u and SPT-N) were used to evaluate the site variability of different soil layers in combination with the variation reduction factor, α_r. The main sources of measurement errors in CPT are the soil formation and equipment error (i.e., cone type, calibration), with less effect of the operator on test results. However, the main measurement errors sources in S_u data are soil formation, soil sampling, specimen handling and transportation, and operator/equipment. In the case of SPT measurement, the soil formation and equipment error are the main sources of the measurement's errors. It is expected that the SPT equipment source of errors (discrete number of blows) are higher than the CPT equipment errors (continuous electrical measurement).

The results of site variability using semivariogram analysis showed there is little effect of the horizontal range, a_h, on evaluating the reduction factor, α_r, and the resistance factos (ϕ), since the distance between the CPT tests and soil borings are usually very large compared the pile diameter and the ratio $D/a_h \approx 0$. Therefore, for the simplification of the analysis, we can assume $D/a_h \approx 0$. Exploring the results presented for the ten sites, the reader can realize that the spatial resistance coefficient of variation, $COV_{R,spatial}$, from CPT-q_t data ranges from 0.08 to 0.20; the $COV_{R,spatial}$ from S_u data ranges from 0.14 to 0.22; and the $COV_{R,spatial}$ from SPT-N data for Metairie site is 0.17. Interestingly, the values of $COV_{R,spatial}$ for all ten sites (either from CPT or soil boring) are lower than the $COV_{R,method}$, which are evaluated from data collected from many sites at different locations nationwide [58] or statewide [57]. In $COV_{R,method}$, no consideration is given to the specific site variability, although variability between different sites in Louisiana were indirectly included in the LCPC pile-CPT method and the combined static method. Some researchers, like McVay et al. [14], used the $COV_{R,spatial}$ to calibrate the resistance factor, $\phi_{spatial}$, for use in LRFD design of piles for the specific site. The authors recommend using Equation 149 to evaluate the $COV_{R,total}$, which incorporates both the the $COV_{R,spatial}$ and the $COV_{R,method}$, and to calibrate the total resistance factor, ϕ_{total}, for use in LRFD design of pile foundations.

It is clear that for the sites with lower site variability than the design method variability (i.e., $COV_{R,spatial} < COV_{R\text{-}method}$), the value of the $COV_{R,total}$ decreased and the

corresponding resistance factor, ϕ_{total}, increased (as well as $\phi_{spatial}$), and vice versa. This means a credit will be given to low variability sites as compared to high variability sites in terms of increasing the resistance factors, either using $\phi_{spatial}$ or ϕ_{total}, for use in the design of pile foundations. Since the site variability from using CPT-q_t data is lower than soil boring data (S_u and SPT-N), the corresponding $\phi_{spatial}$, ϕ_{total}, for LCPC pile-CPT design method are higher than the static α-Tomlinson and the Nordlund design methods.

Evaluation of Site Variability using Bayesian Analysis

Geotechnical Characterization

In order to utilize the CPT data for estimating the ultimate pile capacity using any pile-CPT method, it is important to classify the soils and evaluate soil layering and type so that the proper correlation factors can be selected to evaluate the unit end bearing capacity and unit side resistance of the soil layers along the pile shaft, which are based on soil type, pile type, and installation method. In this study, the probabilistic region estimation CPT classification method introduced by Zhang and Tumay [134] was adopted in this study to classify the soil layers along piles' lengths. The probabilistic estimation method determines the probability of soil behavior (clay, sand, and silt). Figure 83 depicts an example of the soil description, moisture content, liquid limit, plastic limit, undrained shear strength, cone tip resistance, and the probability of soil behavior for a test pile located at the Houma I.C.W.W. Bridges project.

Bayesian Update on the New Sites

Houma I.C.W.W. Bridges Project in Terrebonne Parish

In this study, 33 sites out of the 34 total sites were considered as old sites that will be used as likelihood in level 1 of the Bayesian analysis, and the site at Houma I.C.W.W. Bridges project in Terrebonne Parish in Louisiana is considered and used as the likelihood in level 2 of the Bayesian analysis. In Houma bridge site, six pile load tests were performed. The Davisson's measured ultimate pile capacities, Q_m, for the 6 pile load tests were 110, 60, 117, 115, 107, and 170 tons, respectively. However, the estimate ultimate pile capacities, Q_p, using the LCPC methods for those piles were 115.5, 81, 95.9, 108.6, 77.3, and 117.9 tons, respectively. Therefore, the biases ($\lambda = Q_m/Q_p$) for 6 pile load tests are 0.95, 0.74, 1.22, 1.05, 1.38, and 1.44, and the corresponding mean bias (λ) and

standard deviation (σ) are 1.04 and 0.30, respectively, assuming lognormal distribution of data.

Figure 83. Subsurface soil condition at Houma I.C.W.W. Bridges project site

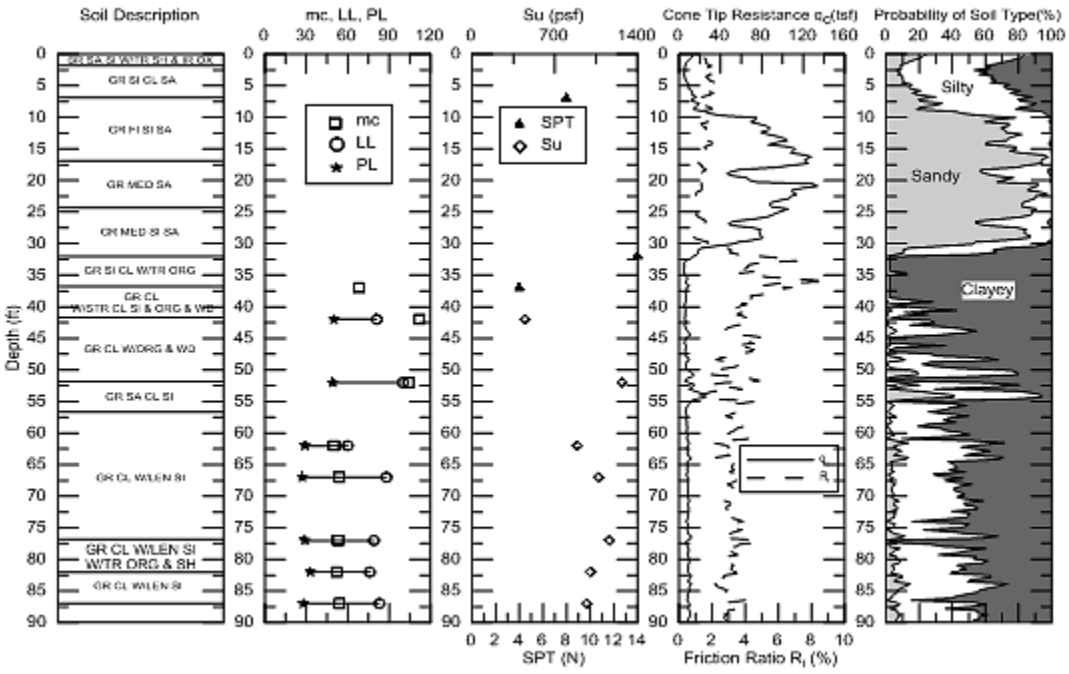

In level 1 of the Bayesian analysis, the previous data (33 sites out of 34 sites) is considered as the likelihood, with mean bias, λ= 1.03 (average $\lambda = Q_m/Q_p$) for pile load tests in 33 sites, and the corresponding standard deviation, σ = 0.32, assuming lognormal distribution of data. The prior parameter for this part of analysis is assumed to be λ= 0.8 and σ = 0.40 (conservative values) with lognormal distribution. It should be noted here that we could use other reliable data (say based on engineering judgement) as prior data for level 1 analysis. However, an accurate selection of the prior data in level 1 Bayesian analysis has insignificant impact on the posterior data of level 2 analysis [144]. After executing the level 1 analysis, we will generate the posterior data, which is in this case λ = 1.07 and σ = 0.38 with normal distribution, which will be considered as prior data in level 2 Bayesian analysis.

In level 2 Bayesian analysis, due to the framework of the code, the level 1 posterior data and parameters will be considered as prior data in this level. As stated earlier, the Houma bridges site in Louisiana will be considered as the likelihood for level 2 of the Bayesian analysis, with λ = 1.04 and σ = 0.30.

After level 2 analysis, we will generate the posterior data and parameter ($\lambda = 1.035$ and $\sigma = 0.31$) for the normal distribution. These updated posterior parameters (λ and σ) will be used for calibrating the LRFD resistance factor (ϕ_R) for use in the design of PPC based on LCPC pile-CPT design method. Figure 84a and Figure 84b present the distributions of the prior, likelihood and posterior data for level 1 and level 2, respectively, of the Bayesian analysis for the Houma bridge site.

Figure 84a shows that the prior data (λ=0.8 and σ=0.40) in level 1 Bayesian analysis has little impact on the posterior data (λ=1.07 and σ=0.38), when likelihood1 is given (λ=1.03 and σ=0.32). However, Figure 84b shows that in level 2, the posterior (λ=1.035 and σ=0.31) or the updated parameters for the Houma bridge site lie between the prior2 parameters (λ=1.07 and σ=0.38) and the likelihood2 parameters (λ=1.04 and σ=0.30) distribution, taking into consideration the specific site variability.

Gibson Highway at St. Mary Parish Project

To demonstrate the effectiveness of Bayesian analysis, another site in Gibson Highway (Morgan City) in St. Mary Parish in Louisiana is considered and used as the likelihood in level 2 of Bayesian analysis. In this site, 6 pile load tests were performed whose values of Q_m were 102.5, 518, 482, 568, 565, and 111 tons for piles TP1 to TP6, respectively. Meanwhile, the values of Q_p for those test piles estimated based on LCPC method were 121.4, 594.6, 615.4, 652.2, 771.9, and 115.6 tons. The corresponding biases ($\lambda = Q_m/Q_p$) for those piles are 0.84, 0.87, 0.78, 0.87, 0.73, and 0.96. Accordingly, the mean bias (λ) and standard deviation (σ) are 0.84 and 0.08, respectively, for lognormal distribution.

In level 1 of the Bayesian analysis, the data for the other 33 sites (out of 34 sites) is considered as the likelihood with mean bias, λ= 1.05, and corresponding standard deviation, σ = 0.33, and assuming lognormal distribution of data. The prior parameters for this part of analysis is assumed to be λ= 0.8 and σ = 0.40 with lognormal distribution. After executing the level 1 analysis, we will generate the posterior data, which is in this case λ = 1.09 and σ = 0.38 with normal distribution, which will be considered as prior data in level 2 Bayesian analysis.

In level 2 Bayesian analysis, the level 1 posterior data and parameters will be considered as prior data in this level. As stated earlier, the Gibson Highway in St. Mary Parish will be considered as the likelihood for level 2 of the Bayesian analysis, with λ = 0.84 and σ = 0.08 for Gibson Highway site, and lognormal distribution.

Figure 84. Prior, likelihood, and posterior distribution with mean at different Bayesian levels

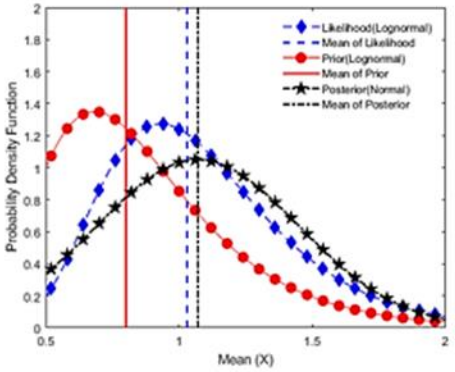

(a) Prior, likelihood and Posterior at Level 1 for Houma I.C.W.W. Bridge site

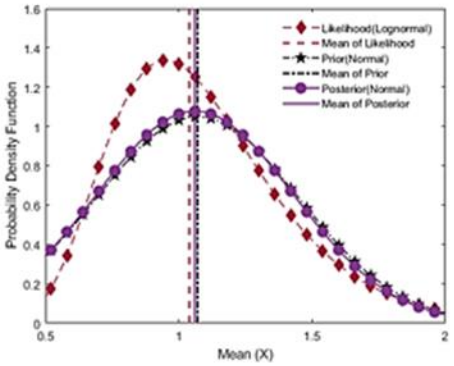

(b) Prior, likelihood and Posterior at Level 2 for Houma I.C.W.W. Bridge site

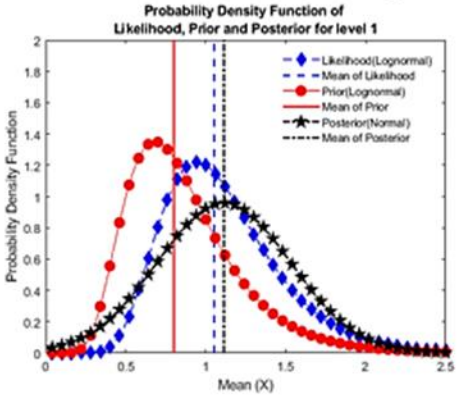

(c) Prior, likelihood and Posterior at Level 1 for Gibson Highway at St. Mary Parish

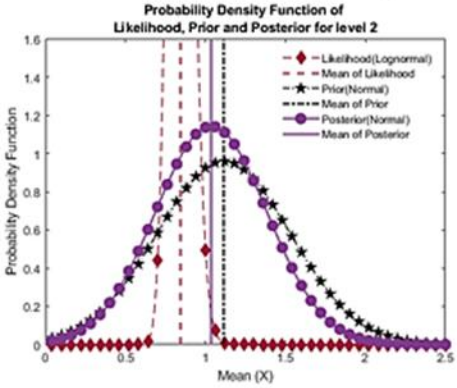

(d) Prior, likelihood and Posterior at Level 2 for Gibson Highway at St. Mary Parish

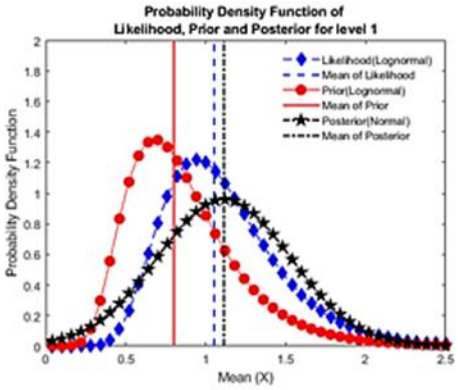

(e) Prior, likelihood and Posterior at Level 1 for Causeway Boulevard at Jefferson

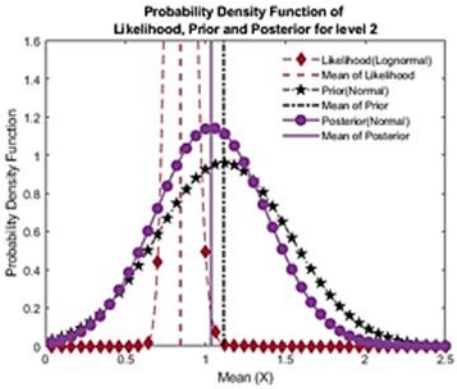

(f) Prior, likelihood and Posterior at Level 2 for Causeway Boulevard at Jefferson

After the level 2 analysis, we will generate the posterior data and parameter ($\lambda = 1.03$ and $\sigma = 0.31$) for the normal distribution. These updated posterior parameters (λ and σ) will be used for calibrating the LRFD resistance factor (ϕ) of LCPC design method. The prior,

likelihood and posterior distributions for level 1 and level 2 are presented in Figure 84c and Figure 84d, respectively. As shown in Figure 84c, the values of prior data (λ=0.8 and σ=0.40) in level 1 of Bayesian analysis has little impact on the posterior parameters (λ=1.09, σ=0.38) when likelihood1 is given (λ=1.05, σ=0.33). The results of Figure 84d shows that, the values of the updated posterior parameters Gibson Highway site in level 2 (λ=1.03, σ=0.31) lie between the prior2 parameters (λ=1.09, σ=0.38) and likelihood2 parameters (λ=0.84, σ=0.08) distribution that considers the specific site variability.

Causeway Boulevard at Jefferson Project

Another site is Causeway Boulevard in Jefferson Parish in Louisiana was also considered to demonstrate the effectiveness of Bayesian analysis. This site has 7 pile load tests with the measured capacities, Q_m, as 126, 97.5, 159, 134, 143, 149.5, and 110.5 tons, for test piles TP1 to TP7, respectively. The values of estimated pile capacities, Q_p, based on LCPC design method were 254.2, 148.2, 234.6, 172.5, 177.2, 165.6, and 139.4 tons. Therefore, the corresponding values of bias, λ, for these piles are 0.49, 0.66, 0.68, 0.78, 0.81, 0.90, and 0.79. The calculated mean bias (λ) and standard deviation (σ) for the Causeway Boulevard site are 0.73 and 0.13, with lognormal distribution.

In level 1 of the Bayesian analysis, the data from the other 33 sites (out of 34) is considered as the likelihood in the Bayesian analysis (with λ= 1.06 and σ = 0.32), and assuming lognormal distribution. The prior parameter for this analysis is assumed to be λ= 0.8 and σ = 0.40 with lognormal distribution. After executing the level 1 analysis, the posterior data will be generated, with values of λ = 1.08 and σ = 0.37 and normal distribution. These values will be considered as prior data in level 2 Bayesian analysis.

In level 2 Bayesian analysis, the level 1 posterior data and parameters will be considered as prior data in this level. As stated earlier, the Causeway Boulevard in Jefferson Parish will be considered as the likelihood for level 2 of the Bayesian analysis (with λ = 0.73 and σ = 0.13) with lognormal distribution.

After level 2 analysis, we will generate the posterior parameters as λ = 0.95 and σ = 0.30, for the normal distribution. These updated posterior parameters (λ and σ) will be used for calibrating the LRFD resistance factor (ϕ_R) for the LCPC pile-CPT design method. The prior, likelihood, and posterior distributions for level 1 and level 2 are presented in Figure 84e and Figure 84f, respectively. Again, Figure 84e demonstrated that the prior data (λ=0.8 and σ=0.40) in level 1 Bayesian analysis has insignificant impact on the posterior data (λ=1.08, σ=0.37), when likelihood1 is given (λ=1.06 and σ=0.32). However, Figure

84f shows that the values of updated posterior parameters in level 2 (λ=0.95, σ=0.30) are between the prior2 parameters (λ=1.08, σ=0.37) and likelihood2 parameters (λ=0.73, σ=0.13), which means the specific site variability was considered.

Effect of Confidence Bias Site Parameter

Generally, designers and researchers have more confidence on the test results for the new specific site (or data) than the previous test (or data) of other sites; therefore, it is rational to put more weight on the new test results for updating data within the Bayesian framework. In this study, the authors introduced a new term called confidence bias site parameter (w_b) to put more weight on the test results/data for the new specific site during the Bayesian updating process. In this study, the effect of weight parameter or confidence bias site parameter was checked for different scenarios with different site variabilities (i.e., low site variability, high site variability). Herein, the low site variability refers to site variability with mean bias, λ= 1.02, and standard deviation, σ = 0.20; while the high site variability represents site variability with λ= 1.10 and σ = 0.40. In this analysis, we divided the 80 pile load test database into two different sets: (i) we randomly selected 75 test piles as old database and 5 test piles for a new site; and (ii) we randomly selected 70 test piles as old database and 10 test piles for a new site.

In this part, the Bayesian analysis was also performed in two levels. The old database data are considered as likelihood at level 1, while the prior parameters for level 1 is taken as mean bias, λ= 0.8 and standard deviation, σ = 0.40. After level 1 analysis, we will get the posterior parameters (λ and σ); which will be considered as prior parameters in level 2 Bayesian analysis. Therefore, the new sites values will be used as likelihood data in level 2 analysis. After completing the level 2 Bayesian analysis, an updated posterior parameters (final λ and σ) will be delivered. Three different confidence bias site parameter, w_b, were considered in this analysis, i.e., w_b = 1.0, 1.5, and 2.0.

The results for the confidence bias site parameter, w_b = 1 is presented in Figure 85a. The figure shows that for the case of high site variability of old database and low site variability at new site; and when using 75 piles as old database and 5 piles for the new site, the resulted updated posterior parameters were mean bias, λ= 1.08, and standard deviation, σ = 0.36. Figure 85b presents the case for low site variability at old database, high site variability at new site with w_b = 1, and same split of pile load tests (75 for old database and 5 for new site). The results yield the updated posterior parameters values of λ= 1.05 and σ = 0.365. It can be concluded that without imposing any weight to new site data (i.e., w_b = 1), the updated posterior parameters will stay closer to the higher number

of pile, which is in this case, the old database. Figure 85c shows the result for the case when using 70 pile load tests with high site variability for the old database and 10 pile load tests with low site variability at the new site, and using $w_b = 1.0$. The resulted updated posterior parameters were $\lambda = 1.07$ and $\sigma = 0.34$. However, when using 70 piles with low site variability for old database and 10 piles with high site variability at the new site (Figure 85d), the results for $w_b = 1.0$ yield $\lambda = 1.04$ and $\sigma = 0.34$ as updated posterior parameters. Again, the results show that without considering any weight (i.e., $w_b = 1$), the updated posterior parameters will stay closer to the higher number of piles, which is the old database in this case. However, when the number of piles for the new site increases, the updated posterior parameters tend to shift toward the new site parameters, as expected.

Figure 85. Probability density function at different site variability when confidence bias site parameter, $w_b = 1$

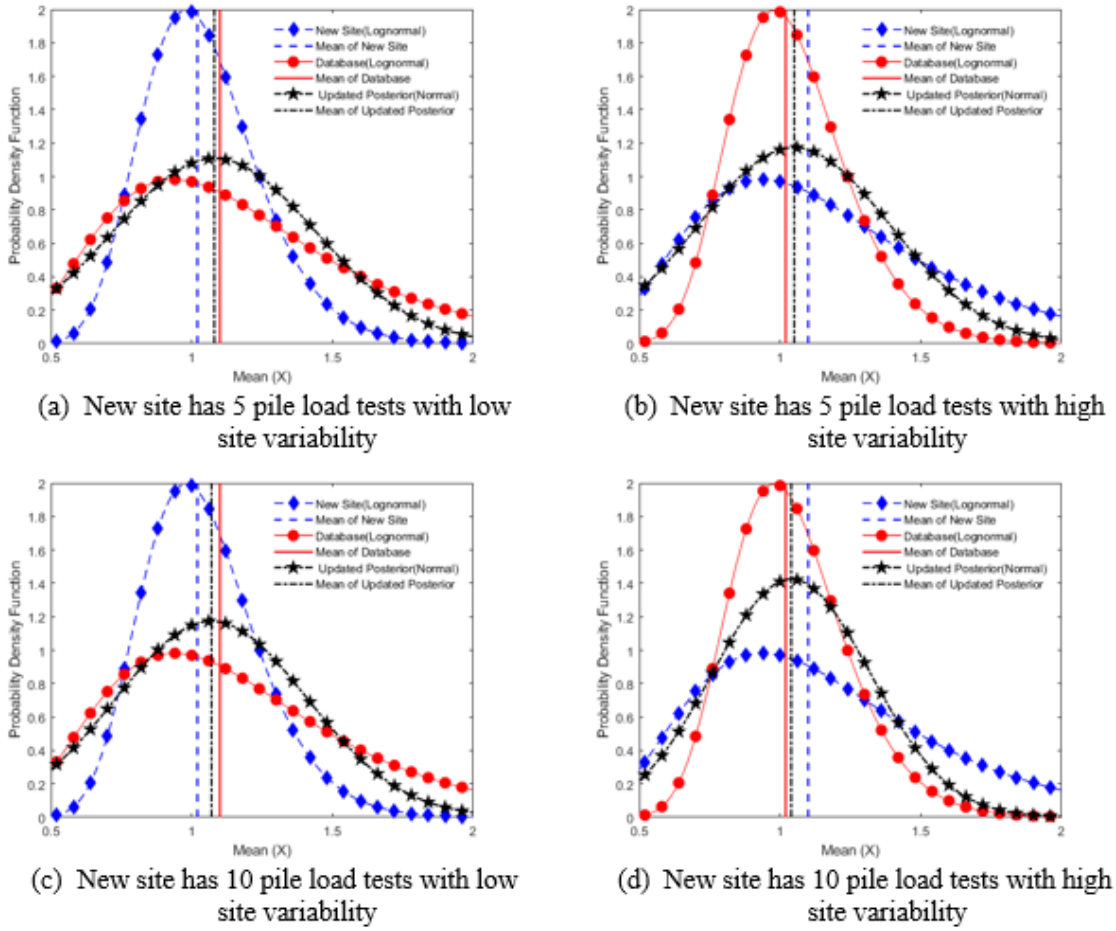

(a) New site has 5 pile load tests with low site variability

(b) New site has 5 pile load tests with high site variability

(c) New site has 10 pile load tests with low site variability

(d) New site has 10 pile load tests with high site variability

As discussed earlier, it is logic to apply weight (i.e., $w_b > 1.0$) on the test results of the new site, giving it more importance than the old database. In this study, three values of confidence bias site parameter, w_b, are considered on the test results of new site, i.e., w_b = 1, 1.5 and 2. The effect of w_b on the updated posterior parameters were evaluated for two sets of data: 75 piles for old database versus 5 piles for new site, and 70 piles for old database versus 10 piles for new site (selected randomly). Two site variabilities were considered for each case, low and high site variabilities. The updated posterior parameters obtained at different w_b values and different site variabilities for the two sets of data are summarized in Table 74. As shown in the table, the updated values of the posterior parameters when using $w_b = 1.0$ are $\lambda = 1.08$ and $\sigma = 0.36$ for the case of 75 pile tests of high site variability for old database and 5 pile tests of low site variability at the new site; while for the same dataset case but using $w_b = 1.5$, the values of updated posterior parameters are $\lambda = 1.062$ and $\sigma = 0.31$. However, when using $w_b = 2$ for the same dataset, the values of updated posterior parameters reduce to $\lambda = 1.05$ and $\sigma = 0.28$.

The values of updated posterior parameters (λ and σ) for the same set of data (i.e., 75 piles for old database and 5 piles for the new site), but with low site variability of old site and high site variability at the new site are also presented in Table 74, which shows an increase of updated λ and σ from (1.05, 0.365) to (1.07, 0.36) with increasing w_b from 1 to 2. The results for the second set of data (i.e., 70 piles for old database and 10 piles for the new site) for different site variabilities and different wb values are also presented in Table 74, which gave the same trend of results. For the case of high site variability of old site and low site variability at new site, the values of updated λ and σ reduced from (1.07, 0.34) to (1.04, 0.27) with increasing w_b from 1 to 2. However, for the case of low site variability of old site and high site variability at new site, the updated values of increased from (1.04, 0.34) to (1.075, 0.37) with increasing w_b from 1 to 2.

It can be concluded that when applying the confidence bias site parameter, w_b, to the new site data, the updated λ and σ parameters shift toward the new site values, which is rationale and will result on updating the LRFD resistance factors (that are calibrated nationwide or statewide) taking into consideration the specific site variability. The use of $w_b = 1.0$ means that the pile load tests at the new specific site are treated at the same level of confidence as the prior pile load test values from nationwide or statewide database. Since the variability of the model bias factor within a specific site is often smaller than that of a region, most of the time uncertainties will be lower in the new site. Therefore, when the new site's pile load test (likelihood2) is completed, more consideration should be given to the new test data in the Bayesian analysis. Unfortunately, there is no

guidelines in literature on the proper selection of wb value. Any value between 1 and 2 can be adopted for w_b, depending on the specific site condition and the extent of testing. The authors recommend using a confidence bias site parameter, $w_b = 1.5$, as a starting point.

Effect of λ and σ Parameters on LRFD Design of Piles

The resistance factor, ϕ_R, for pile design according to the load and resistance factor design (LRFD) method can be calculated using the following modified first order second moment method (MFOSM) calibration equation proposed by McVay et al. [14]:

$$\phi_R = \frac{\lambda_R \left(\gamma_D \frac{Q_D}{Q_L} + \gamma_L\right) \sqrt{\frac{1 + COV_Q^2}{1 + COV_R^2}}}{\left(\lambda_{QD} \frac{Q_D}{Q_L} + \lambda_{QL}\right) \exp\left(\beta_T \sqrt{\ln(1 + COV_R^2)\left(1 + COV_Q^2\right)}\right)} \quad [150]$$

λ_R is the resistance bias factor; Q_D is the dead load and Q_L is the live load; β_T is the target reliability index; γ_D is the dead load factor and γ_L is the live load factor; λ_{QD} is the dead load bias factor (measured divided by predicted) and λ_{QL} is the live load bias factor. COV_{QD} is for the dead load and COV_{QL} is for the live load. The Q_D/Q_L is the ratio of dead and live load (which is assumed to be 3 in this study). The coefficient of variation of the random loads, COV_Q, was introduced by McVay et al. [14] using the following equation:

$$COV_Q = \sqrt{\frac{\frac{{Q_D}^2}{{Q_L}^2}{\lambda_{QD}}^2 COV_{QD}^2 + {\lambda_{QL}}^2 COV_{QL}^2}{\frac{{Q_D}^2}{{Q_L}^2}{\lambda_{QD}}^2 + 2\frac{Q_D}{Q_L}\lambda_{QD}\lambda_{QL} + {\lambda_{QL}}^2}} \quad [151]$$

where, COV_{QD} is for the dead load and COV_{QL} is for the live load. According to the FHWA [59], the dimensionless parameters in the above equations can be defined as the follows:

$$\gamma_L = 1.75;\ \lambda_{QL} = 1.15;\ COV_{QL} = 0.18;\ \gamma_D = 1.25;\ \lambda_{QD} = 1.08;\ COV_{QD} = 0.128$$

In this study, we will consider the LCPC method [56] to design piles from CPT data. The LCPC is a direct Pile-CPT method that showed one of the best performance Pile-CPT methods on estimating the ultimate resistance for piles driven in Louisiana soils [57]. The mean resistance bias, λ_R, and COV_R for the LCPC method are 1.04 and 0.31, respectively.

Table 74. Updated parameters at different site variability for different w_b parameter levels

Database			New site			Updated Parameters		COV_R	Resistance Factor (ϕ_R)	Efficiency Factor (ϕ_R/λ)
No. of piles	Parameters		No. of piles	Parameters		Mean Bias (λ)	Standard Deviation (σ)			
Confidence Bias site Parameter, w_b = 1										
When new site has lower number of piles; Low site variability										
75	λ	1.10	5	λ	1.02	**1.08**	**0.36**	0.33	**0.56**	0.52
	σ	0.40		σ	0.20					
When new site has lower number of piles; High site variability										
75	λ	1.02	5	λ	1.10	**1.05**	**0.365**	0.35	**0.54**	0.52
	σ	0.20		σ	0.40					
When new site has higher number of piles; Low site variability										
70	λ	1.10	10	λ	1.02	**1.07**	**0.34**	0.32	**0.58**	0.54
	σ	0.40		σ	0.20					
When new site has higher number of piles; High site variability										
70	λ	1.02	10	λ	1.10	**1.04**	**0.34**	0.33	**0.57**	0.55
	σ	0.20		σ	0.40					
Confidence Bias site Parameter, w_b = 1.5										
When new site has lower number of piles; Low site variability										
75	λ	1.10	5	λ	1.02	**1.062**	**0.31**	0.29	**0.62**	0.58
	σ	0.40		σ	0.20					
When new site has lower number of piles; High site variability										
75	λ	1.02	5	λ	1.10	**1.056**	**0.35**	0.33	**0.56**	0.54
	σ	0.20		σ	0.40					
When new site has higher number of piles; Low site variability										
70	λ	1.10	10	λ	1.02	**1.06**	**0.30**	0.28	**0.63**	0.60
	σ	0.40		σ	0.20					
When new site has higher number of piles; High site variability										
70	λ	1.02	10	λ	1.10	**1.05**	**0.32**	0.30	**0.60**	0.57
	σ	0.20		σ	0.40					
Confidence Bias site Parameter, w_b = 2										
When new site has lower number of piles; Low site variability										
75	λ	1.10	5	λ	1.02	**1.05**	**0.28**	0.27	**0.65**	0.62
	σ	0.40		σ	0.20					
When new site has lower number of piles; High site variability										
75	λ	1.02	5	λ	1.10	**1.07**	**0.36**	0.34	**0.56**	0.52
	σ	0.20		σ	0.40					
When new site has higher number of piles; Low site variability										
70	λ	1.10	10	λ	1.02	**1.04**	**0.27**	0.26	**0.67**	0.64
	σ	0.40		σ	0.20					
When new site has higher number of piles; High site variability										
70	λ	1.02	10	λ	1.10	**1.075**	**0.37**	0.34	**0.55**	0.51
	σ	0.40		σ	0.20					

However, when using the Bayesian analysis, the values of λ_R and corresponding standard deviation, σ_R (and $COV_R = \sigma_R/\lambda_R$), will be updated to λ and σ based on number of pile load tests and variability of the specific new site. In this case, the COV_R will be also updated from σ/λ. So the updated λ and updated COV_R will be used to recalibrate the resistance factor (ϕ_R) for the specific new site. For example, the updated $posterior_2$ values of (λ, COV_R) for Houma bridge site are (1.035, 0.31); the updated posterior2 values of (λ, COVR) for Gibson Highway site are (1.03, 0.31); and the updated posterior2 values of (λ, COVR) for Causeway Boulevard site are (0.95, 0.30).

Table 74 presents the summary of the variable parameters (λ, σ, COV_R) for the different scenarios (number of old piles versus number of piles at new site, different site variability, and different confidence bias site parameter) and the corresponding LRFD calibration resistance factors (ϕ_R) and efficiency factors (ϕ_R/λ). It can been seen from the table that the resistance factor increases with decreasing variability of the new specific site, which is also affected by the ratio of old piles versus new piles and the value of confidence bias site parameter, w_b. More credit will be given to sites (in terms of ϕ_R) for low variability sites with lager number of piles and using $w_b > 1$.

Evaluation of Site Variability using Probabilistic Analysis

Probabilistic analysis were performed on LA 1 CPT site using the SGeMS software. The software provides confidence intervals (CI) to the estimated data in between the test points. When a cumulative distribution has been determined, the operator can choose from a range of confidence limits ranging from 0 to 100 percent. At LA 1 site, 13 CPT tests (75 ft. deep) were performed at different locations as described in Figure 48. The subsurface soil for each CPT test location was divided into four soil layers (0-10 ft., 10-34 ft., 34-46 ft. and 46-75 ft.), based on CPT soil classification. For each soil layer of the CPT test, the average CPT-q_t value was calculated and then incorporated into the SGeMS data format as input in X, Y, and Z, in which X is the latitude, Y is the longitude, and Z is the data (here the average CPT-q_t). Then the data will be plotted in the SGeMs. After plotting the data, variogram analysis will be performed. From the results of variogram analysis, kriging analysis can be performed on the data space. In this study, we followed the ordinary kriging. Next step, we generated fifty realizations of CPT-q_t data distribution using the sequential Gaussian simulation (SGS), so that we can do the probabilistic analysis.

SGS Simulations

The SGeMs software was used to simulate the CPT test data from the 13 test locations at LA 1 site. The simulated values of CPT generated 2176 (64×34) cells. Given our knowledge of the site, every image is a plausible depiction of the real parameter distribution. Fifty realizations were generated using the SGS algorithm. Figure 86 depicts five images of these realizations for the 1st layer at LA 1 site.

Figure 86. Five realizations (out of 50 realizations) at the 1st layer of LA 1 site

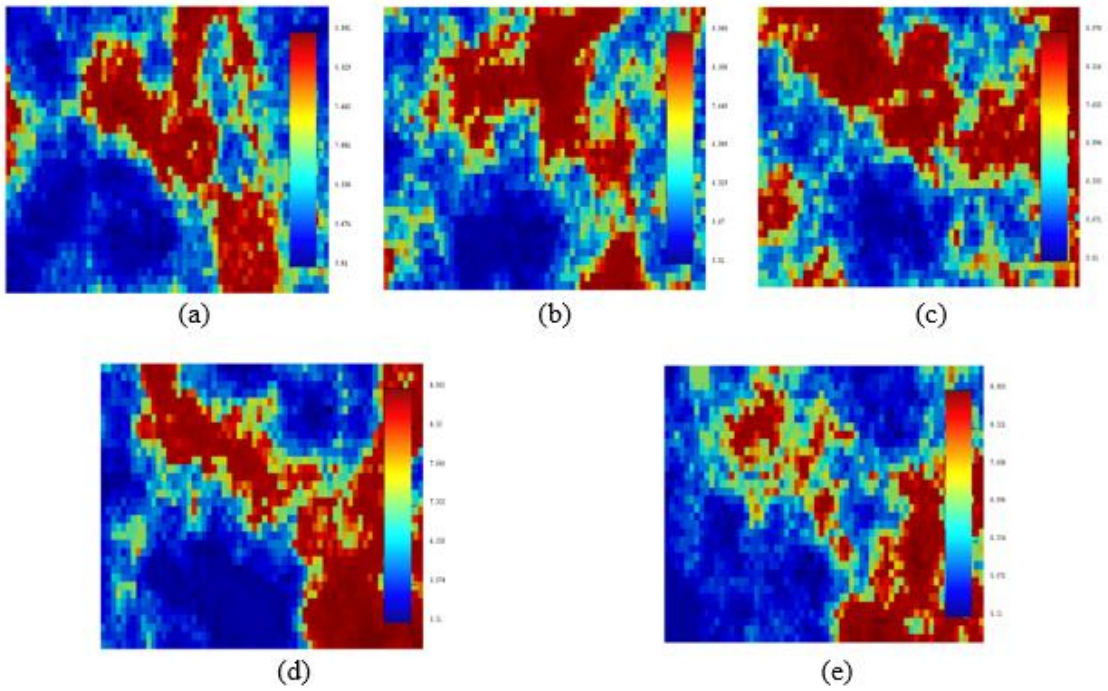

Estimation/Mean vs Ordinary Kriging

One of the goals of simulation was to obtain the estimation/mean map from the 50 realizations. The estimation/mean map is a map that resulted from averaging the 50 realizations. Since the estimation/mean map is the average of all realizations, the results is expected to be similar to the kriging map [106]. Figure 87 compares the kriged plan versus the estimation/mean map for each soil layer of the LA 1 site. As shown in the figure, the results of estimation through simulation and kriging are very close (almost same).

Figure 87. Estimation/mean of the 50 realizations versus ordinary kriging

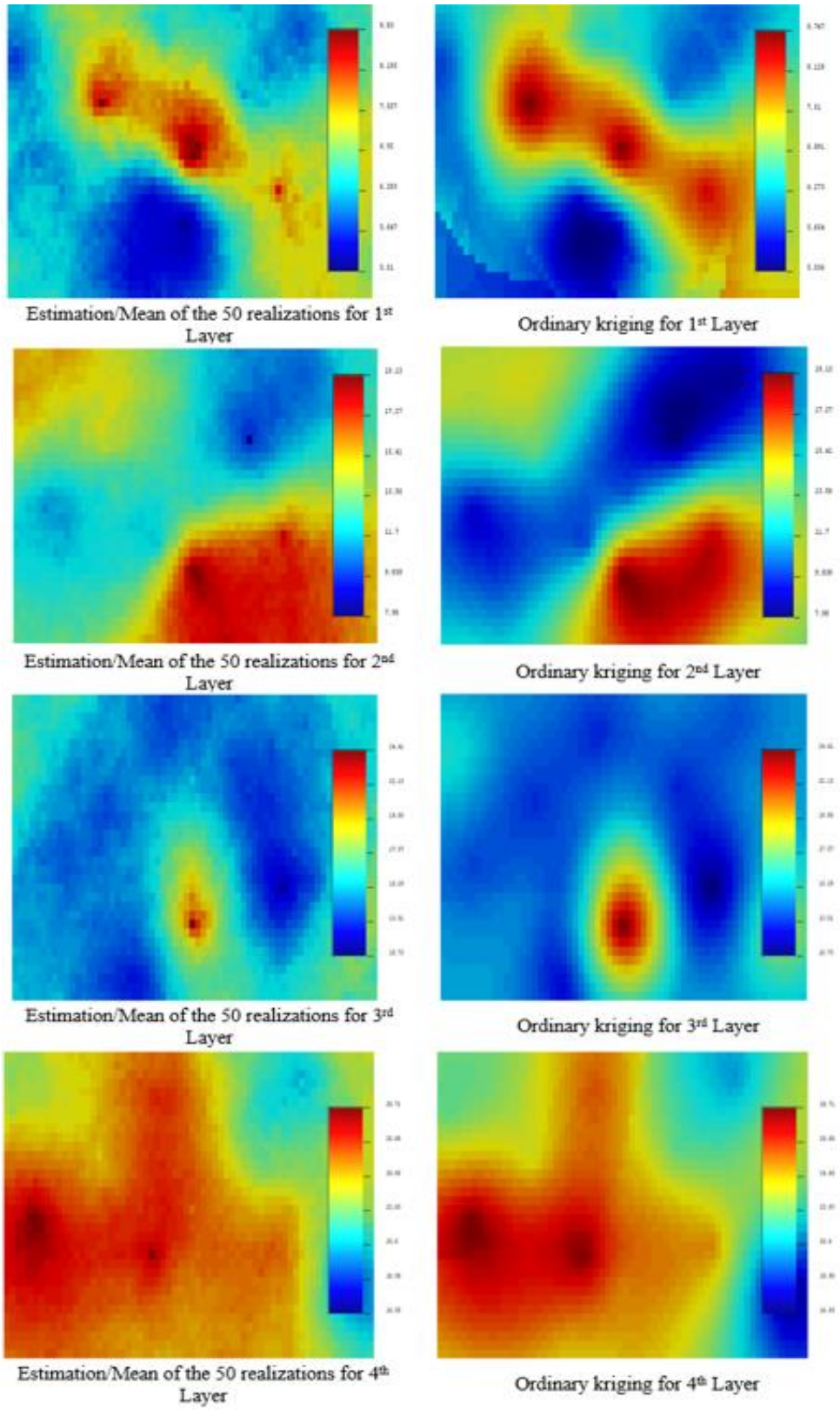

Estimation/Mean of the 50 realizations for 1st Layer

Ordinary kriging for 1st Layer

Estimation/Mean of the 50 realizations for 2nd Layer

Ordinary kriging for 2nd Layer

Estimation/Mean of the 50 realizations for 3rd Layer

Ordinary kriging for 3rd Layer

Estimation/Mean of the 50 realizations for 4th Layer

Ordinary kriging for 4th Layer

Figure 88 presents the data points, estimation/mean map of 50 simulations and the Varance of the 50 simulations for the CPT-q_t data for the 1st soil layer at LA 1 site, respectively. The figure shows that when we have q_t data available on some points (area), or even in the surrounding location (red to yellow areas), the realization gives low variance. However, when we do not have q_t data available close to some points (blue areas), the resulted variance will be high.

Figure 88. (a) Data points, (b) Estimation/mean map of 50 simulations, and (c) Variance of 50 simulations for the CPT data of LA 1 site

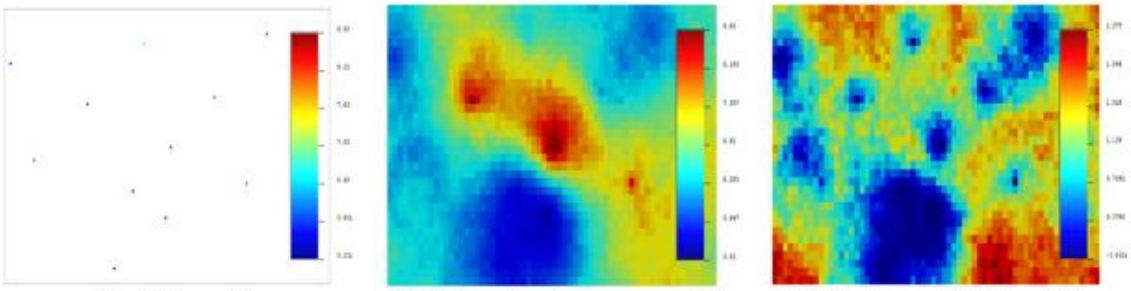

(a) Data points (b) Estimation/mean map of 50 simulations for 1st layer (c) Variance of 50 simulations for 1st layer

Probability Analysis

For the probability analysis, we need to find the probability that the value of corrected cone tip resistance, q_t, fall between $q_{t\text{-}avg} - \sigma < q_t < q_{t,avg} + \sigma$, on a given location (i.e., black circled), where σ is the standard deviation of q_t values. For this analysis we have to develop two realizations using the previous 50 realizations. The first one is the probability of the CPT-q_t lower than $q_{t\text{-}avg} - \sigma$, and another one is the probability of CPT-qt data lower than $q_{t,avg} + \sigma$. Figure 89 presents the data points, probability of $q_t < q_{t\text{-}avg} - \sigma$, and probability of $q_t < q_{t,avg} + \sigma$ for each of the four soil layers at LA 1 site. Table 75 presents the values of the different parameters for each layer.

For the CPT points of layer 1 of LA 1 site, the values of $q_{t,avg}$, σ, $q_{t,avg} - \sigma$, and $q_{t,avg} + \sigma$ are 6.66, 1.24, 5.41, and 7.90, respectively. Using the values of $q_{t,avg} - \sigma$, and $q_{t,avg} + \sigma$ data into Equation 126, we got the probability that q_t will fall within the range $q_{t,avg} - \sigma < q_t < q_{t,avg} + \sigma$ is 78%. For the the CPT points of layer 2, the values of $q_{t,avg}$, σ, $q_{t,avg} - \sigma$, and $q_{t,avg} + \sigma$ are 12.64, 3.42, 9.22, and 16.06, respectively. Using the values of $q_{t,avg} - \sigma$, and $q_{t,avg} + \sigma$ data into Equation 126, we will obtain the probability that q_t will fall within the range $q_{t,avg} - \sigma < q_t < q_{t,avg} + \sigma$ is 70%. For the CPT points of layer 3, the values of

$q_{t,avg}$, σ, $q_{t,avg}$ - σ, and $q_{t,avg}$ + σ are 15.04, 3.46, 11.58, and 18.51, respectively. Using the values of $q_{t,avg}$ - σ and $q_{t,avg}$ + σ data into Equation 126, we will got the probability of q_t fall between $q_{t,avg}$ - σ and $q_{t,avg}$ + σ is 87%. For the CPT points of layer 4, the values of $q_{t,avg}$, σ, $q_{t,avg}$ - σ, and $q_{t,avg}$ + σ are 24.17, 3.18, 21.00, and 27.35, respectively. Using $q_{t,avg}$ - σ and $q_{t,avg}$ + σ data into Equation 126, we got the probability that q_t lies within the range of $q_{t,avg}$ - σ < q_t < $q_{t,avg}$ + σ is 73%. After complete analysis, we can say that the prediction probability of $[q_{t,avg} - \sigma \leq q_t \leq q_{t,avg} + \sigma\ ]_{xo}$ for each layer of LA 1 site ranges from 70% to 87%.

Table 75. Layer-wise data analysis and the probability

Parameters	1st Layer	2nd Layer	3rd Layer	4th Layer
$q_{t,avg}$ (tsf)	6.66	12.64	15.04	24.17
$st.dev$ (tsf)	1.24	3.42	3.46	3.18
$q_{t,avg} - st.dev$	5.41	9.22	11.58	21.00
$q_{t,avg} + st.dev$	7.90	16.06	18.51	27.35
$Prob\ [z \leq q_{t,avg} - st.dev\ ]_{x_0}$	5%	28%	8%	2%
$Prob\ [z \leq q_{t,avg} + st.dev\ ]_{x_0}$	83%	98%	95%	75%
$Prob\ [q_{t,avg} - st.dev\ \leq q_t \leq q_{t,avg} + st.dev\ ]_{x_0}$	78%	70%	87%	73%

Incorporating SGS Simulations into LRFD (Resistance Factor)

From the results in Table 75, we can see that the prediction probabilities of $[q_{t,avg} - \sigma \leq q_t \leq q_{t,avg} + \sigma]_{xo}$ for LA 1 site are 78%, 70%, 87% and 73% for the 1st, 2nd, 3rd and 4th layer, respectively. The thickness of the 1st, 2nd, 3rd and 4th layer is 10ft., 24ft., 12ft. and 29ft., respectively. So, the weighted average prediction probability for LA 1 site is 75%.

In order to calibrate the resistance factor for the LCPC Pile-CPT design method taking into consideration the probabilistic SGS simulation of site variability at LA 1 site, the value of special COV of resistance ($COV_{R,spatial}$) and the $COV_{R,total}$ were updated for LA 1 to be 0.13 and 0.22, respectively, using the prediction probability of 75%. The corresponding resistance factors $\phi_{spatial}$ and ϕ_{total} were calibrated to be 0.87 and 0.73, respectively. These values are higher than the LCPC resistance factor of ϕ_{method} (LCPC) = 0.61. Table 76 depicts the calibrated resistance factors, $\phi_{spatial}$ and ϕ_{total}, after modifying the $COV_{R,spatial}$, as compared to the ϕ_{method} (LCPC).

Figure 89. (a) Data points, (b) Probability of q_t below $q_{t\text{-}avg}$-σ, and (c) Probability of q_t below $q_{t,avg}$+σ

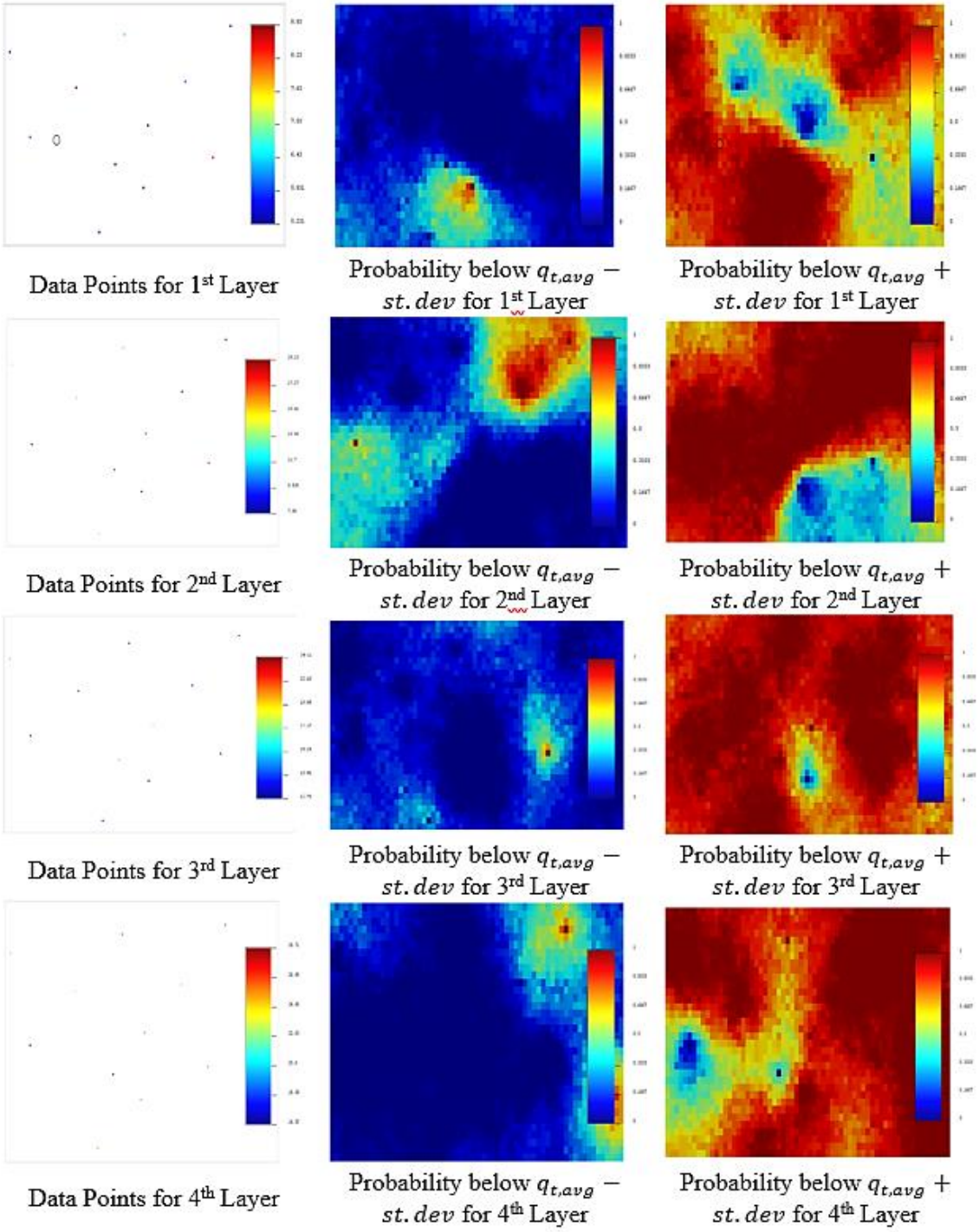

Table 76. Calculated resistance factors, ϕ_R, after modifying $COV_{R,spatial}$

Parameters	LA 1 Including SGS (Modifying $COV_{R,spatial}$)
$COV_{R,spatial}$	0.13
$COV_{R,method}$ (LCPC)	0.31
$COV_{R,total}$	0.22
COV_Q^2	0.0111
$\phi_{spatial}$	0.87
ϕ_{method} (LCPC)	0.61
ϕ_{total}	0.73

Application of Site Variability in Slope Stability Analysis

Drained Condition

Variation of Friction Angle

Different scenarios were modeled in this section to study the effect of variability in friction angle of the soil layers on the slope stability of embankment. Here, the COV of unit weight and cohesion were kept constant as 5% and 20%, respectively. In the first part of analysis, the vertical correlation length was changed from 15 ft. (5 m) (low vertical variability) to 1 ft. (0.3 m) (high vertical variability). The correlation length in the horizontal direction was selected to be 60 ft. (20 m). The Bishop simplified, Janbu simplified, and Spencer method were used in this analyses. In this study, 15 scenarios were ran to investigate the effect of site variability (by increasing the COV of friction angle and changing the vertical correlation length) on the factor of safety for slope stability. Table 5 summarizes the material properties considered in the analyses of drained condition. In the case of the spatial variability analyses, the statistics tool in the Slide 2018 2D software was activated. The COVs of the material properties were put as value of the standard deviation for each single soil property. Latin-Hypercube probabilistic analysis sampling method was used to accomplish the probabilistic analysis. A 1000 samples were generated and used in the analyses for each scenario. The log normal sample distribution was used. Figure 90 presents the factor of safety versus COV of friction angle at different vertical variability levels of the drained condition.

For the scenarios 1, 2, 3, 4, and 5, the COVs for friction angle were 5%, 10%, 15%, 20%, and 25%, respectively; while the COVs for unit weight and cohesion were kept constant as 5% and 20%, respectively. In these cases, the vertical and horizontal correlation

lengths of 6 ft. (2 m) (medium vertical variability) and 60 ft. (20 m), respectively, were assumed. For the scenarios 6, 7, 8, 9, and 10, the values COV for the friction angle were 5%, 10%, 15%, 20%, and 25%, respectively, and the COVs for unit weight and cohesion were kept constant as 5% and 20%, respectively. In these cases, the vertical and horizontal correlation lengths were assumed as 1 ft. (0.3 m) (high vertical variability) and 60 ft. (20 m), respectively. For the scenarios 11, 12, 13, 14, and 15, the COVs for friction angle were 5%, 10%, 15%, 20%, and 25%, respectively; while the COVs for unit weight and cohesion were kept constant as 5% and 20%, respectively. In these cases, the vertical and horizontal correlation lengths were assumed to be 15 ft. (5 m) (low vertical variability) and 60 ft. (20 m), respectively. In these scenarios, the main objective was to investigate the effect of variation in the COV of friction angle and vertical correlation length on the mean factor of safety for slope stability of drained condition. The slope stability results for scenarios 1 to 15 are shown in Figure 90**.** The figure clearly shows that the factor of safety for all methods decreases with increasing the COV of friction angle. For the same COV, the figure shows that the factor of safety increasing with increasing the vertical correlation length. Out of the three analysis methods, Janbu simplified method gives lower factor of safety than other two methods (Bishop simplified and Spencer), which can be seen in the Figure 90. Table 85 of Appendix E shows the factor of safety versus COV of friction angle, ϕ, at different vertical variability levels for the drained condition.

Variation of Unit Weight

Different scenarios were model to study the effect of variability in unit weight of the soil layers on the embankment slope stability. Here, the COV of friction angle and cohesion were kept constant as 10% and 20 %, respectively. In this part of the analysis, the vertical correlation length was changed from 15 ft. (5 m) (low vertical variability) to 1 ft. (0.3 m) (high vertical variability). The Bishop simplified, Janbu simplified, and Spencer method were used in the analyses. A total of 15 scenarios were run to investigate the effect of site variability in terms of increasing the COV of unit weight for different vertical correlation lengths on the factor of safety for slope stability. Table 86 presents the summary of all the scenarios considered in this analyses. The spatial variability analyses were performed using the Slide 2018 2D software. A 1000 samples were generated and used in the analyses for each scenario. The resulted factor of safety versus COV of unit weight at different vertical variability levels are presented in Figure 91.

Figure 90. Factor of safety vs COV of ϕ at different vertical variability levels of drained condition

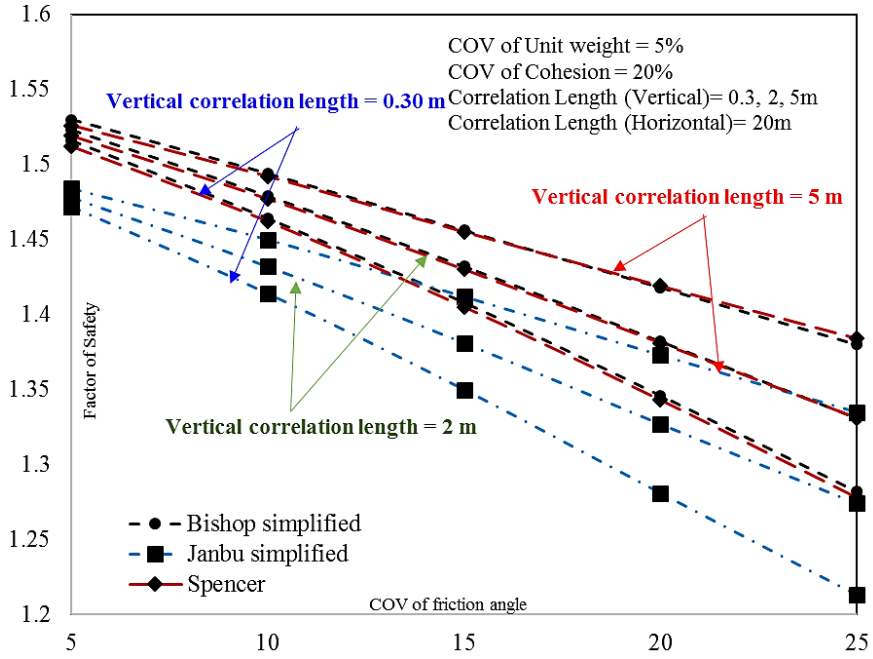

Figure 91. Factor of safety vs COV of unit weight at different vertical variability levels of drained condition

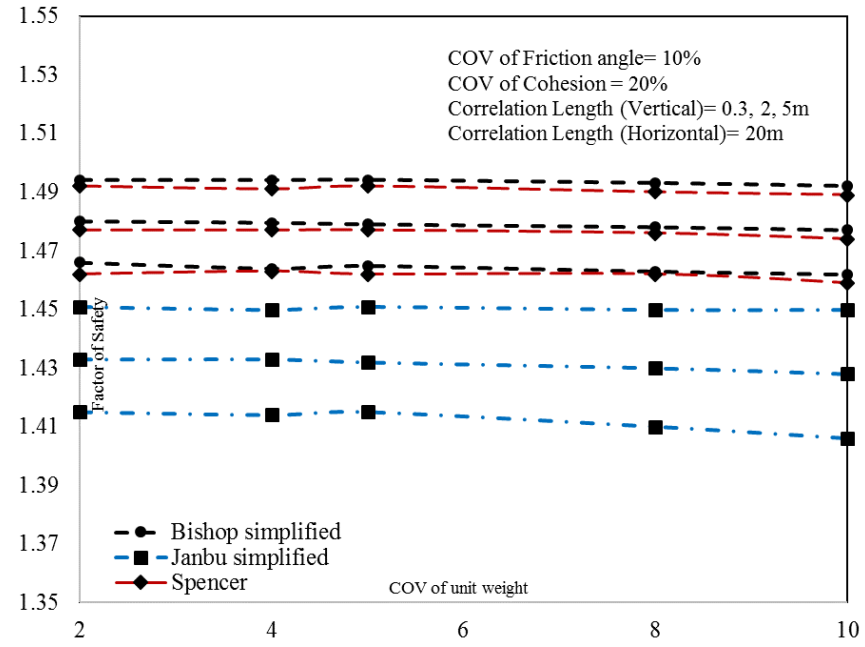

For the scenarios 16, 17, 18, 19, and 20, the values of COV of unit weight were 2%, 4%, 5%, 8%, and 10%, respectively; while the COV of friction angle and cohesion were kept

constant as 10% and 20%, respectively. In these cases, the vertical and horizontal correlation lengths were assumed as 6 ft. (2m) (medium vertical variability) and 60 ft. (20 m), respectively. For the scenarios 21, 22, 23, 24, and 25, the values of COV for unit weight were 2%, 4%, 5%, 8%, and 10%, respectively; while the COVs of variation for friction angle and cohesion were kept constant as 10% and 20%, respectively. In these cases, the vertical and horizontal correlation lengths were assumed as 1 ft. (0.3 m) (high vertical variability) and 60 ft. (20 m), respectively. For the scenarios 26, 27, 28, 29, and 30, the values of COVs of the unit weight were 2%, 4%, 5%, 8%, and 10%, respectively; while the COVs for friction angle and cohesion were kept constant as 10% and 20%, respectively. In these cases, the vertical and horizontal correlation lengths were assumed to be 15 ft. (5 m) (low vertical variability) and 60 ft. (20 m), respectively. The results of slope stability analysis for scenario 16 to 30 are shown in Figure 91. The figure shows that the factor of safety for all scenarios did not change significantly when COV of unit weight was increased from 2% to 10%. The figure also show that the factor of safety increases with increasing the vertical correlation length (i.e., vertical variability changes from high to low). Again, out of three methods, Janbu simplified method gave lower factor of safety than the other two methods. Table 86 of Appendix E presents the factor of safety versus COV of unit weight at different vertical variability levels of the drained condition.

Variation of Cohesion

Different scenarios were model to study the effect of variability in cohesion of soil layers on the slope stability of embankment. Here, the COV of friction angle and unit weight were kept constant as 10% and 5%, respectively. In this analysis, the vertical correlation length was changed from 15 ft. (5 m) (low vertical variability) to 1 ft. (0.3 m) (high vertical variability). A total of 15 scenarios were run to investigate the effect of COV of cohesion and the vertical correlation length on factor of safety for slope stability using the Slide 2018 2D software. A total of 1000 samples were generated and used in the analyses for each scenario. The resulted factor of safety versus COV of cohesion at different vertical correlation lengths are presented in Figure 92.

For the scenarios 31, 32, 33, 34, and 35, the COVs for cohesion were 10%, 20%, 30%, 40%, and 50%, respectively; while the COVs for friction angle and unit weight were kept constant as 10% and 5%, respectively. In these cases, the vertical and horizontal correlation lengths were taken as 6 ft. (2 m) (medium vertical variability) and 60 ft. (20 m), respectively. For the scenarios 36, 37, 38, 39, and 40, the COVs for cohesion were assumed as 10%, 20%, 30%, 40%, and 50%, respectively, and the COVs for friction

angle and unit weight were kept constant as 10% and 5%, respectively. In these cases, the vertical and horizontal correlation lengths were assumed as 1 ft. (0.3 m) (high vertical variability) and 60 ft. (20 m), respectively. For the scenarios 41, 42, 43, 44, and 45, the COV values for cohesion were assumed as 10%, 20%, 30%, 40%, and 50%, respectively; and the COVs for friction angle and unit weight were kept constant at 10% and 5%, respectively. In these cases, vertical and horizontal correlation lengths were assumed as 15 ft. (5 m) (low vertical variability) and 60 ft. (20 m), respectively. The results of slope stability analysis for scenario 31 to 45 are presented in Figure 92. The figure shows that the factor of safety for all scenarios did not change significantly when the COV of cohesion were increased from 10% to 50%. Meanwhile, the factor of safety increased with increasing the vertical correlation length (i.e., decreasing vertical variability). Again, the Janbu simplified method has lower factor of safety than the other two methods. Table 87 of Appendix E presents the factor of safety versus COV of cohesion at different vertical variability levels for the drained condition.

Figure 92. Factor of safety vs COV of cohesion at different vertical variability levels of drained condition

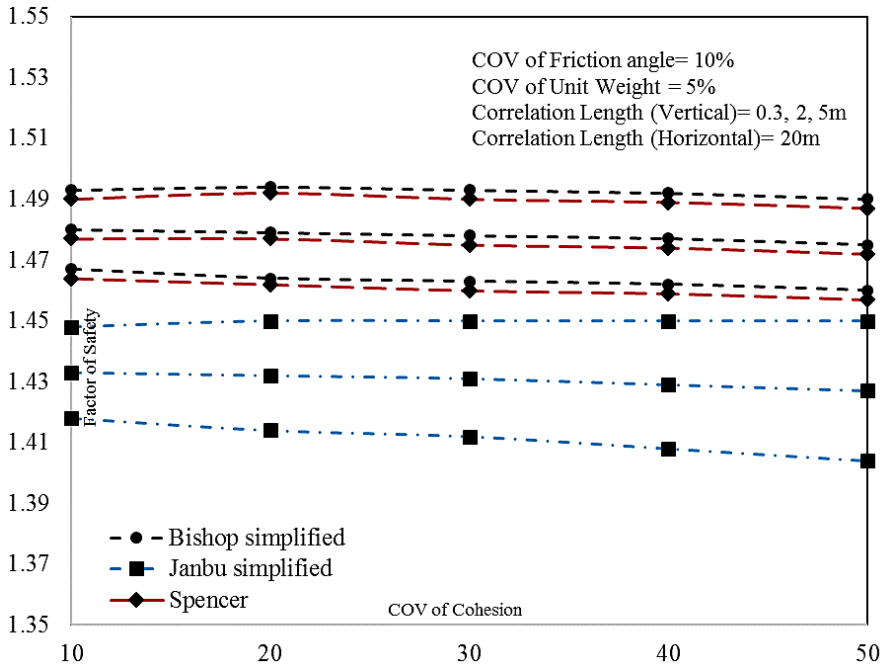

Undrained Condition

High Vertical Variability of Undrained Cohesion

Different scenarios were modeled to study the effect of variability in the undrained cohesion (C or S_u) of the clay soil layer on the slope stability of embankment. Here, the COV of undrained cohesion was ranged from 10% to 50%, while the COV of ϕ (for sand and embankment fill) and unit weight were kept constant as 10% and 5%, respectively. In this analysis, the vertical correlation length was assumed to be 1 ft. (0.3) (for high vertical variability) and the horizontal correlation length was changed from 60 ft. (20 m) to 180 ft. (60 m). The Bishop simplified, Janbu simplified, and Spencer method were used in the analyses. In this study 15 scenarios were run to investigate to the effect of site variability (by increasing COV of cohesion and changing the horizontal correlation length) on the factor of safety for slope stability. The spatial variability analyses were performed using the Slide 2018 2D software. A total of 1000 samples were generated and used in the analyses for each scenario.

For the scenarios 46, 47, 48, 49, and 50, the vertical and horizontal correlation lengths were assumed to be 1 ft. and 60 ft., respectively. For the scenarios 51, 52, 53, 54, and 55, the values of vertical and horizontal correlations were taken as 1 ft. and 120 ft., respectively. For the scenarios 56, 57, 58, 59, and 60, the vertical and horizontal correlation lengths were assumed to be 1 ft. and 180 ft., respectively. The results of slope stability for scenario 46 to 60 are shown in Figure 93. The figure shows that the factor of safety decreases with increasing the COV of undrained cohesion and increases with increasing the horizontal correlation length. However, the degree in the effect of variability in undrained cohesion depends on the length of failure surface within the clay layer. Out of three methods, Janbu simplified method has lower factor of safety than the other two methods. Table 88 of Appendix E shows the factor of safety versus the COV of undrained cohesion for the high vertical variability of undrained condition.

Medium Vertical Variability of Undrained Cohesion

In this part, the COV of undrained cohesion was ranged from 10% to 50%; while the COV of ϕ (for sand and embankment fill) and unit weight were kept constant at 10% and 5%, respectively. Here, the vertical correlation length was assumed to be 6 ft. (2 m) (for medium vertical variability) and the horizontal correlation length was changed from 60 ft. (20 m) to 180 ft. (60 m). 15 different scenarios were run to investigate the effect of COV of undrained cohesion and the horizontal correlation length on the factor of safety for slope stability. A total of 1000 samples were generated and used in the analyses for each scenario.

Figure 93. Factor of safety vs COV of undrained cohesion for high vertical variability and different horizontal correlation lengths of the undrained condition

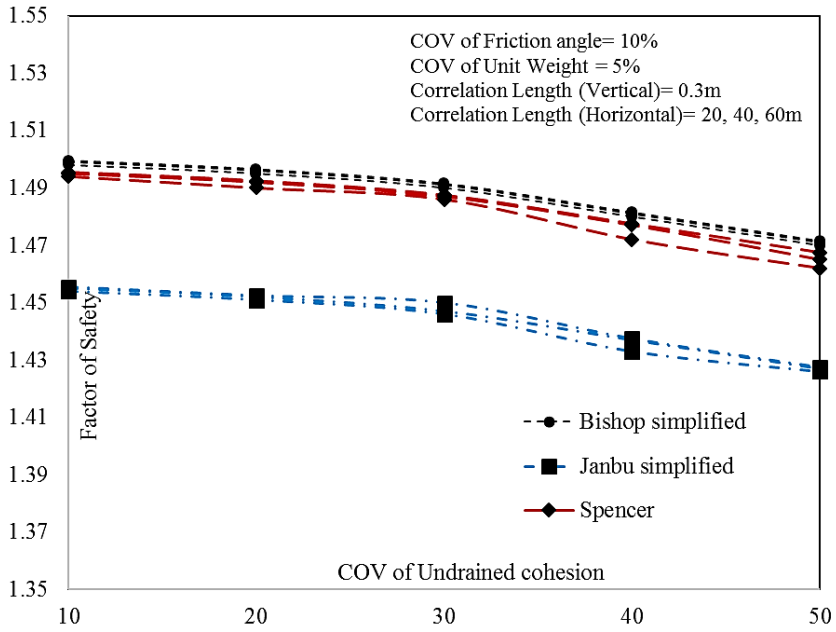

For the scenarios 61, 62, 63, 64, and 65, the vertical and horizontal correlation lengths were assumed to be 6 ft. and 60 ft., respectively. For the scenarios 66, 67, 68, 69, and 70, the vertical and horizontal correlation lengths were assumed to be 6 ft. and 120 ft., respectively. For the scenarios 71, 72, 73, 74, and 75, the vertical and horizontal correlation lengths were assumed to be 6 ft. and 180 ft., respectively. The results of slope stability analysis on these scenarios are presented in Figure 94, which shows that the factor of safety for all cases decreases with increasing the COV of undrained cohesion and increases with increasing the horizontal correlation length. Again the degree of variability effect depends on the length of failure surface within the clay layer. Again, the Janbu simplified method has lower factor of safety than the other two methods. Table 89 of Appendix E presents the factor of safety versus the COV of undrained cohesion for the medium vertical variability of undrained condition.

Figure 94. Factor of safety vs COV of undrained cohesion for medium vertical variability and different horizontal correlation lengths of the undrained condition

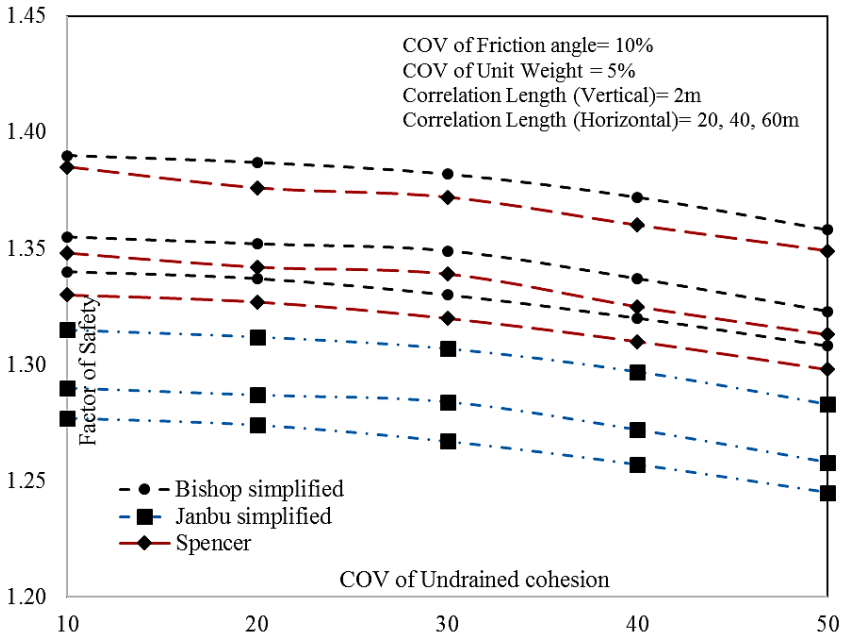

Low Vertical Variability of Undrained Cohesion

Here the COV of undrained cohesion was ranged from 10% to 50%; while the COV of ϕ (for sand and embankment fill) and unit weight were kept constant at 10% and 5%, respectively. The vertical correlation length was assumed to be 15 ft. (5 m) (for low vertical variability) and the horizontal correlation length was changed from 60 ft. (20 m) to 180 ft. (60 m). 15 different scenarios were run to investigate the effect of COV of the undrained cohesion and the horizontal correlation length on the factor of safety for slope stability. A total of 1000 samples were generated and used in the analyses for each scenario.

For the scenarios 76 to 80, the values of vertical and horizontal correlations were taken as 15 ft. and 60 ft., respectively. For the scenarios 81 to 85, the values of vertical and horizontal correlations were taken as 15 ft. and 120 ft., respectively. And for scenarios 86 through 90, the vertical and horizontal correlation lengths were assumed to be 15 ft. and 180 ft., respectively. The results of slope stability for the scenario 76 to 90 are presented in Figure 95. The figure demonstrated that the factor of safety decreases with increasing the COV of undrained cohesion and increases with increasing the horizontal correlation

length. The effect of variability in undrained cohesion depends on the length of failure surface within the clay layer. As for the other cases, the Janbu simplified method has lower factor of safety than the other two methods. Table 90 of Appendix E shows the factor of safety versus the COV of cohesion for the low vertical variability of undrained condition.

Proportional COV

High Vertical Variability

In this part of analysis, different scenarios were modeled to study the effect of soil variability (in terms of cohesion, unit weight and friction angle) of the soil layers on the slope stability of embankments. Here, increment no. 1 means the COV of cohesion, unit weight and friction angle are 20%, 2%, and 5%, respectively. Increment no. 2 means the COV of cohesion, unit weight and friction angle are 30%, 4%, and 15%, respectively. Then, increment no. 3 means the COV of cohesion, unit weight and friction angle are 40%, 8%, and 20%, respectively. Finally, increment no. 4 means the COV of cohesion, unit weight and friction angle are 50%, 10%, and 25%, respectively. This means we increased the COV values of cohesion, unit weight and friction angle in each increment. Here, the vertical correlation length was assumed to be 1 ft. (0.3 m) (for high vertical variability) and the horizontal correlation length was changed from 60 ft. (20 m) to 180 ft. (60 m). Bishop simplified, Janbu simplified, and Spencer methods were used in the analyses. A total of 12 scenarios were run to investigate the effect of site variability (by increasing COV of cohesion, unit weight, and friction angle and changing the horizontal correlation length) on the factor of safety for slope stability. The Slide 2018 2D software was used for the spatial variability analyses. A total of 1000 samples were generated and used in the analyses for each scenario, assuming log normal sample distribution.

For the scenarios 91 through 94, the vertical correlation length was assumed to be 1 ft. (0.3) (for high vertical variability) and the horizontal correlation length was assumed to be 60 ft. (20 m). For the scenarios 95 to 98, the vertical correlation length was assumed to be 1 ft. (0.3) (for high vertical variability) and the horizontal correlation length was assumed to be 120 ft. (40 m). For the scenarios 99 through 102, the vertical correlation length was assumed to be 1 ft. (0.3) (for high vertical variability) and the horizontal correlation length was assumed to be 180 ft. (60 m). The results of slope stability analysis for the scenarios 91 to 102 are shown in Figure 96. As shown in the figure, the factor of safety for all cases were decreased with the increase in the COV from increment 1 to 4. However, the figure also shows that the change in horizontal correlation length from 60

ft. to 180 ft. is not significant. Again, the Janbu simplified method gave lower factor of safety than the other two methods (Bishop simplified and Spencer). Table 91 of Appendix E shows the factor of safety versus the COV of increment for the high vertical variability.

Figure 95. Factor of safety vs COV of undrained cohesion for low vertical variability and different horizontal correlation lengths of the undrained condition

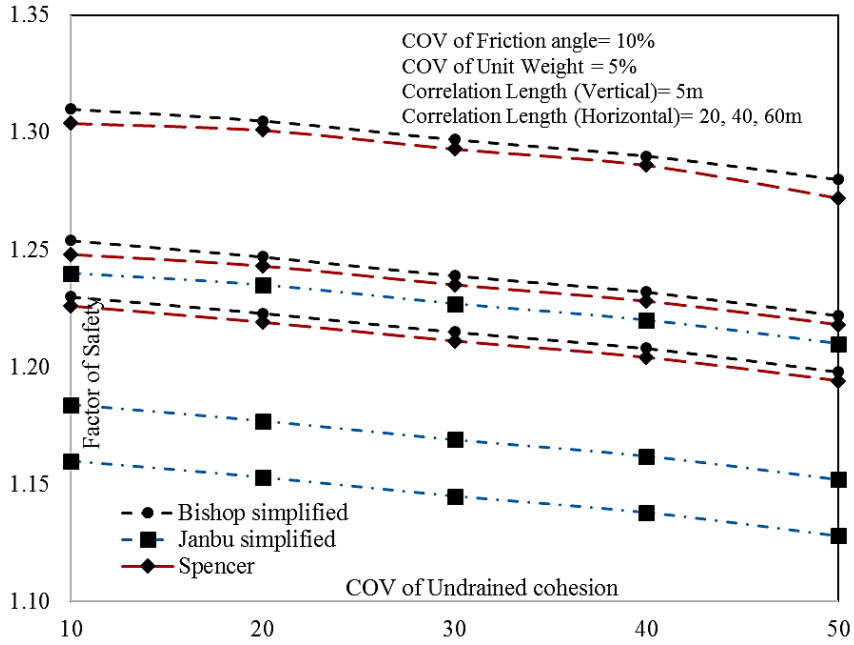

Figure 96. Factor of safety vs COV of cohesion, unit weight and friction angle at different horizontal variability levels (for high vertical variability)

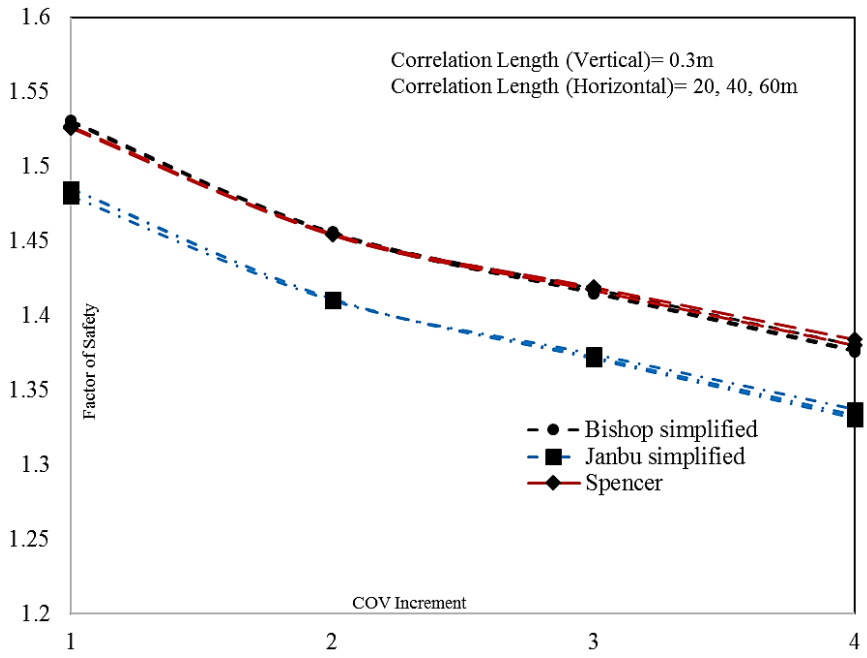

Medium Vertical Variability

Different scenarios were modeled here to study the effect of soil variability (cohesion, unit weight and friction angle) of the soil layers on the slope stability of embankments. The COVs for the different increments in this analysis are the same as for the high vertical variability, in which the COVs of cohesion, unit weight and friction angle were increased in each increment. The vertical correlation length was assumed to be 6 ft. (0.3 m) (for medium vertical variability) and the horizontal correlation length was changed from 60 ft. (20 m) to 180 ft. (60 m). Bishop simplified, Janbu simplified and Spencer methods were used in the analyses. A total of 12 scenarios were run to investigate the effect of site variability on the factor of safety for slope stability through increasing COVs of soil properties and changing the horizontal correlation length. The Slide 2018 2D software was used for the spatial variability analyses.

For the scenarios 103 to 106, the vertical correlation length was assumed to be 6 ft. (2 m) (for medium vertical variability); while the horizontal correlation length was assumed to be 60 ft. (20 m). For the scenarios 107 to 110, the values of vertical and horizontal correlation lengths were assumed to be 6 ft. (2 m) and 120 ft. (40 m), respectively. For the scenarios 111 to 114, the vertical correlation length was assumed to be 6 ft. (2 m) and the horizontal correlation length was assumed to be 180 ft. (60 m). Figure 97 presents the results of slope stability analysis for scenarios 103 to 114. The figure demonstrates that the factor of safety decreases with increasing the COV of soil properties from increment

1 to 4, and that the effect of changing the horizontal correlation length from 60 ft. to 180 ft. is not significant. Again, the factor of safety of Janbu simplified method is lower than the other two methods (Bishop simplified and Spencer).

Table **92** of Appendix E depicts the factor of safety versus COV of increments for the medium vertical variability.

Low Vertical Variability

In this part of analysis, the effect of the low vertical variability of the soil layers on the slope stability of embankments was investigated using a vertical correlation length of 15 ft. (5 m) (for low vertical variability) and changing the horizontal correlation length from 60 ft. (20 m) to 180 ft. (60 m). Bishop simplified, Janbu simplified, and Spencer methods were used in the analyses. A total of 12 scenarios were run using the Slide 2018 2D software to investigate the effect of site variability on the factor of safety for slope stability through increasing COVs of soil properties and changing the horizontal correlation length. A total of 1000 samples were generated and used in the analyses for each scenario, assuming log normal sample distribution.

Figure 97. Factor of safety vs COV of cohesion, unit weight and friction angle at different horizontal variability levels (for medium vertical variability)

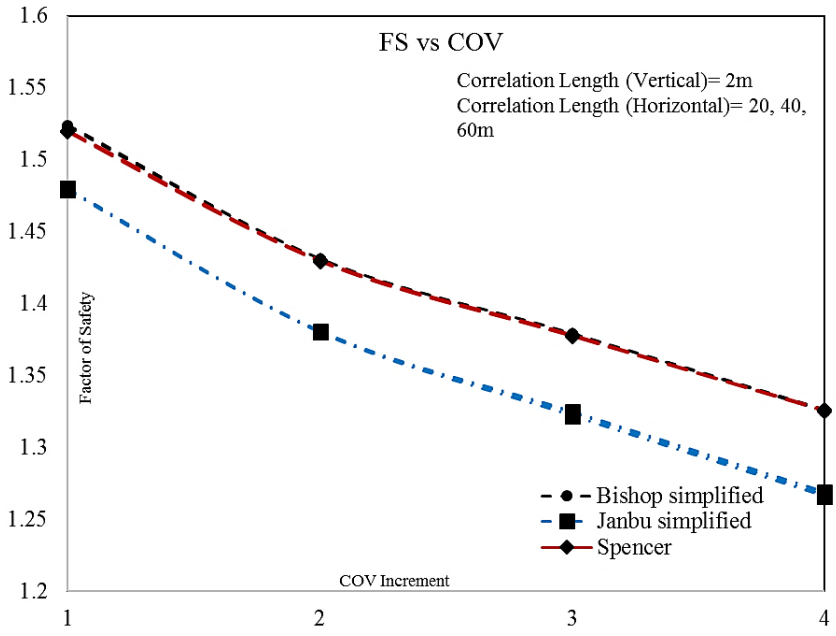

For the scenarios 115 to 118, the vertical and horizontal correlation lengths were assumed to be 15 ft. (5 m) (for low vertical variability) and 60 ft. (20 m), respectively. For the

scenarios 119 through 122, the vertical correlation length was assumed to be 15 ft. (5 m) and the horizontal correlation length was assumed to be 120 ft. (40 m). For the scenarios 123 to 126, the vertical and horizontal correlation lengths were assumed to be 15 ft. (5 m) and 180 ft. (60 m), respectively. The results of slope stability analysis are presented in Figure 98 which shows that the factor of safety were decreased with the increase in the COV from increment 1 to 4, and also demonstrates that changing in horizontal correlation length from 60 ft. to 180 ft. is not significant. Again, the Janbu simplified method gave the lowest factor of safety of slope stability. Table 93 of Appendix E presents the factor of safety versus the COV of increment for the low vertical variability.

Figure 98. Factor of safety vs COV of cohesion, unit weight and friction angle at different horizontal variability levels (for low vertical variability)

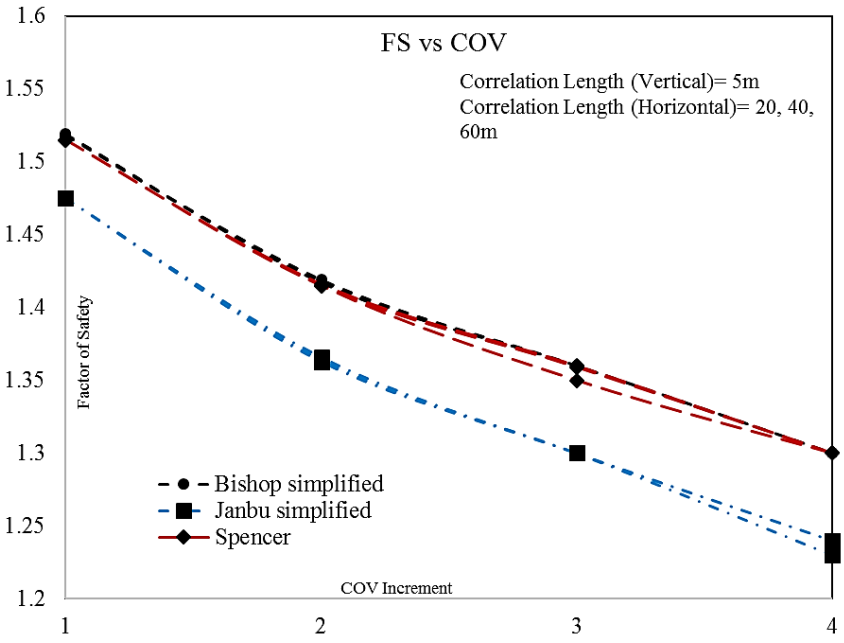

Application of Site Variability in Shallow Foundation

Effect of Site Variability on the Bearing Capacity (Second Moment Analysis)

The effect of site variability on the bearing capacity of shallow foundations was first investigated here using the second moment statistical analysis and Vesper 6 software on a 6' × 6' foundation with a FS = 3. The undrained shear strength (S_u) presented in Table 7

was used for the soil profile (here medium PI 1 soil), and the schematic diagram of the foundation example is described in Figure 55.

The plot of the semivariogram for the S_u data below the footing is presented in Figure 99. The range of influence (a_v) and the scale of fluctuation (θ) for the spherical model are 4.2 feet and 3.2 feet, respectively. Scale of fluctuation is determined from Table 3. Once the scale of fluctuation is known, the plot of variance reduction factor, Γ^2, against influence depth below footing for the S_u profile can be developed by assuming hypothetical lengths below footing and substituting the θ value of S_u into the following equation:

$$\Gamma^2(L)=\left[\frac{\theta}{L}\left(1-\frac{\theta}{4L}\right)\right]^{\frac{1}{2}} \quad \text{for } L/\theta > 1/2 \qquad [152a]$$

$$\Gamma^2(L)=1 \quad \text{for } L/\theta \leq 1/2 \qquad [152b]$$

Figure 99. Plot of semivariogram from S_u data

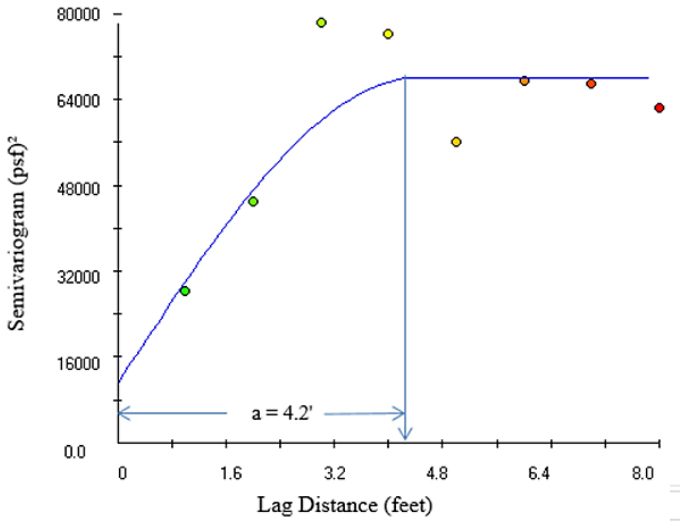

The plots of variance reduction factor, Γ^2, against averaging length, L, for S_u is presented in Figure 100. The variance reduction factor of S_u for 9 feet length below footing is ~ 58%.

The ultimate bearing capacities of square can be calculated using the following equation:

$$q_u=1.3\ c'N_c+qN_q+0.4\gamma N_q \qquad [153]$$

where c' = cohesion, q = effective stress at the level of the bottom of the foundation, γ = unit weight of soil and N_c, N_q, N_γ = bearing capacity factors.

For undrained condition, ϕ' = zero, N_c =5.14, N_q =1 and N_γ=0. The mean value, mean + 1 standard deviation (σ), and mean value -1 σ of q_u were analyzed to calculate a new (updated) standard deviation as presented in Table 77. The mean, mean + σ, mean - σ of q_u are presented in Table 78 for the second moment and the spatially averaged values.

Figure 100. Variance reduction factor versus influence depth below footing

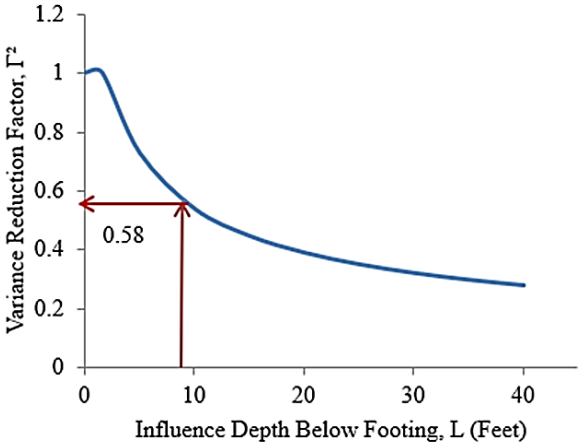

Table 77. New standard deviation from variance reduction factor

Material	q_u	q_u (Mean)	Standard Deviation	Variance	Variance Reduction Factor	New Variance	New Standard Deviation
	psf	psf	psf				
Medium PI 1(PI=21)	18761.3	20220.3	1899.7	3608783.0	0.58	2093094	1447
	19800.0						
	19073.7						
	20159.2						
	17895.3						
	19246.7						
	20472.1						
	23389.2						
	23184.7						

Table 78. Probability of failure calculation

#	Property	Mean	+ σ	- σ	Mean	+ σ	- σ
		S_u - Second Moment			S_u - Spatially-Averaged		
1	q_u (psf)	20220.3	22119.9	18320.6	20220.3	21667.0	18773.5
2	q_{all} (psf)	6740.1	7373.3	6106.9	6740.1	7222.3	6257.8

#	Property	Mean	+ σ	- σ	Mean	+ σ	- σ
3	Q_u (lbs)	727929.4	796317.9	659540.9	727929.4	780012.5	675846.3
4	Q_{all} (lbs)	242643.1	265439.3	219847.0	242643.1	260004.2	225282.1
5	FS	3.0	3.0	3.0	3.0	3.0	3.0
6	Δ_{FS}	0.8			0.6		
7	σ_{FS}	0.3986			0.3076		
8	COV_{FS}	0.1329	13.3%	$P_f = 0$	0.1025	10.3%	$P_f = 0$

For the determination of the reliability assessment, the allowable bearing capacity for the mean, Q_{all} is assumed as the applied stress, Q_{app}. The values in the above table were computed using the following formulas: #1 - 4: computed from the generalized bearing capacity equation; #5: $FS = Q_{ult} / Q_{app}$; #6: $\Delta FS = FS_{max} - FSmin$; #7: $\sigma_{FS} = [(\Delta FS / 2)^2]^{0.5}$, the standard deviation of FS; #8: COV_{FS} = coefficient of variation of FS; and P_f: probability of failure obtained from the standard lognormal Table 79 using mean FS and COV_{FS}.

Table 79. Probability of failure chart for bearing capacity analysis [55]

	Coefficient of Variation of Factor of Safety (V_F)														
F_{MLV}	2%	4%	6%	8%	10%	12%	14%	16%	20%	25%	30%	40%	50%	60%	80%
1.05	0.8%	12%	22%	28%	33%	36%	39%	41%	44%	47%	49%	53%	55%	58%	61%
1.10	0.00%	0.9%	6%	12%	18%	23%	27%	30%	35%	40%	43%	48%	51%	54%	59%
1.15	0.00%	0.03%	1.1%	4%	9%	13%	18%	21%	27%	33%	37%	43%	48%	51%	56%
1.16	0.00%	0.01%	0.7%	3%	8%	12%	16%	20%	26%	32%	36%	42%	47%	50%	56%
1.18	0.00%	0.00%	0.3%	2%	5%	9%	13%	17%	23%	29%	34%	41%	45%	49%	55%
1.20	0.00%	0.00%	0.13%	1.2%	4%	7%	11%	14%	21%	27%	32%	39%	44%	48%	54%
1.25	0.00%	0.00%	0.01%	0.3%	1.4%	4%	6%	9%	15%	22%	27%	35%	41%	45%	51%
1.30	0.00%	0.00%	0.00%	0.06%	0.5%	1.6%	3%	6%	11%	17%	23%	31%	37%	42%	49%
1.35	0.00%	0.00%	0.00%	0.01%	0.2%	0.7%	1.9%	4%	8%	14%	19%	28%	34%	40%	47%
1.40	0.00%	0.00%	0.00%	0.00%	0.04%	0.3%	1.0%	2%	5%	11%	16%	25%	32%	37%	45%
1.50	0.00%	0.00%	0.00%	0.00%	0.00%	0.04%	0.2%	0.7%	3%	6%	11%	19%	27%	32%	41%
1.60	0.00%	0.00%	0.00%	0.00%	0.00%	0.01%	0.05%	0.2%	1.1%	4%	7%	15%	22%	28%	38%
1.70	0.00%	0.00%	0.00%	0.00%	0.00%	0.00%	0.01%	0.06%	0.5%	2%	5%	12%	19%	25%	34%
1.80	0.00%	0.00%	0.00%	0.00%	0.00%	0.00%	0.00%	0.01%	0.2%	1.2%	3%	9%	16%	22%	31%
1.90	0.00%	0.00%	0.00%	0.00%	0.00%	0.00%	0.00%	0.00%	0.08%	0.65%	2%	7%	13%	19%	29%
2.00	0.00%	0.00%	0.00%	0.00%	0.00%	0.00%	0.00%	0.00%	0.03%	0.36%	1.3%	5%	11%	17%	26%
2.20	0.00%	0.00%	0.00%	0.00%	0.00%	0.00%	0.00%	0.00%	0.01%	0.10%	0.56%	1.3%	8%	13%	22%
2.40	0.00%	0.00%	0.00%	0.00%	0.00%	0.00%	0.00%	0.00%	0.00%	0.03%	0.23%	1.9%	5%	10%	19%
2.60	0.00%	0.00%	0.00%	0.00%	0.00%	0.00%	0.00%	0.00%	0.00%	0.01%	0.09%	1.1%	4%	7%	16%
2.80	0.00%	0.00%	0.00%	0.00%	0.00%	0.00%	0.00%	0.00%	0.00%	0.00%	0.04%	0.66%	3%	6%	13%
3.00	0.00%	0.00%	0.00%	0.00%	0.00%	0.00%	0.00%	0.00%	0.00%	0.00%	0.02%	0.39%	1.8%	4%	11%

Note: F_{MLV} = factor of safety computed using most likely values of parameters.

It can be seen from Table 78 that including variability into bearing capacity analysis reduces the COV. Here, the calculated probability of failure is zero. From the lognormal probability Table 79, the reader can realize that when the COV decreases, the probability of failure also decreases. Hence, it can be concluded from Table 78 that incorporating variability into bearing capacity of shallow foundations can reduce both COV and probability of failure.

Effect of Site Variability on the Bearing Capacity (Fenton and Griffiths Method)

Different scenarios were considered in this part of study to investigate the effect of variation in cohesion and friction angle of foundation soil, for both drained and undrained conditions, on the resistance factors of shallow foundations using a 6 ft. wide and 3 ft. depth strip footing.

Sandy Soil

In this analysis, researchers studied the effect of the coefficient of variation of friction angle, COV_ϕ, on the bearing capacity of shallow foundation. Here the COV_ϕ was increased from 0 to 25% with 5% increase increment. The ultimate bearing capacity was normalized by dividing the respective bearing capacity to the initial (with zero site variability) bearing capacity (q_{ref}) (in percent). For example, for the dense sand, to get the normalized bearing capacity for COV_ϕ=25, the bearing capacity for COV_ϕ=25 (which is 1374 psf) was divided by the bearing capacity of COV_ϕ=0 (which is 1664 psf), eventually resulting in 82.6%. The COV of the bearing capacity can be extracted from the Rbear2D software using the mean and standard deviation of soil properties.

Figure 101 presents the ultimate bearing capacity versus COV_ϕ for three different sandy soils (loose, medium and dense). The figure shows that the bearing capacity for the three sandy soils decreases with increasing the COV_ϕ. As expected, the magnitude of bearing capacity for dense soil gives higher capacity than the medium dense and loose sands. The normalized bearing capacity versus COV_ϕ for different sandy soils is presented in Figure 102. The figure shows that, for all sandy soils, the normalized bearing capacity decreases with increasing the COV_ϕ. However, for the dense and medium dense sand the normalized bearing capacity decreases more with increasing the COV_ϕ as compared to loose sand.

Figure 101. Ultimate bearing capacity versus COV_ϕ for different sands

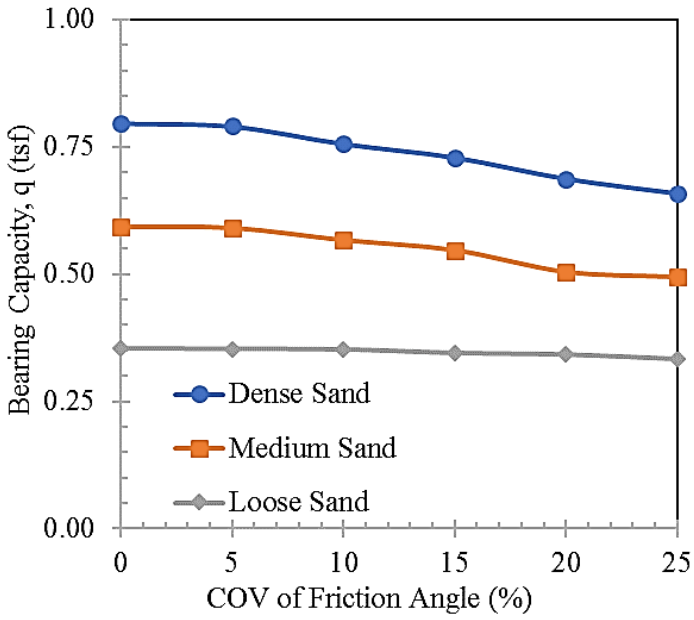

Figure 102. Normalized ultimate bearing capacity versus COV_ϕ for different sands

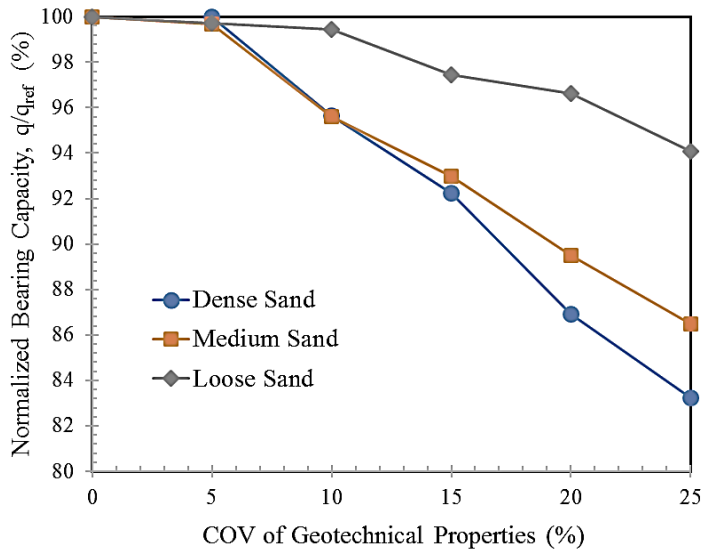

The relationship between the COV of the bearing capacity and COV_ϕ for the different sandy soils is presented in Figure 103. The figure demonstrated that the COV of the bearing capacity increases with increasing the COV_ϕ.

Figure 103. COV of bearing capacity versus COV_ϕ for different sands

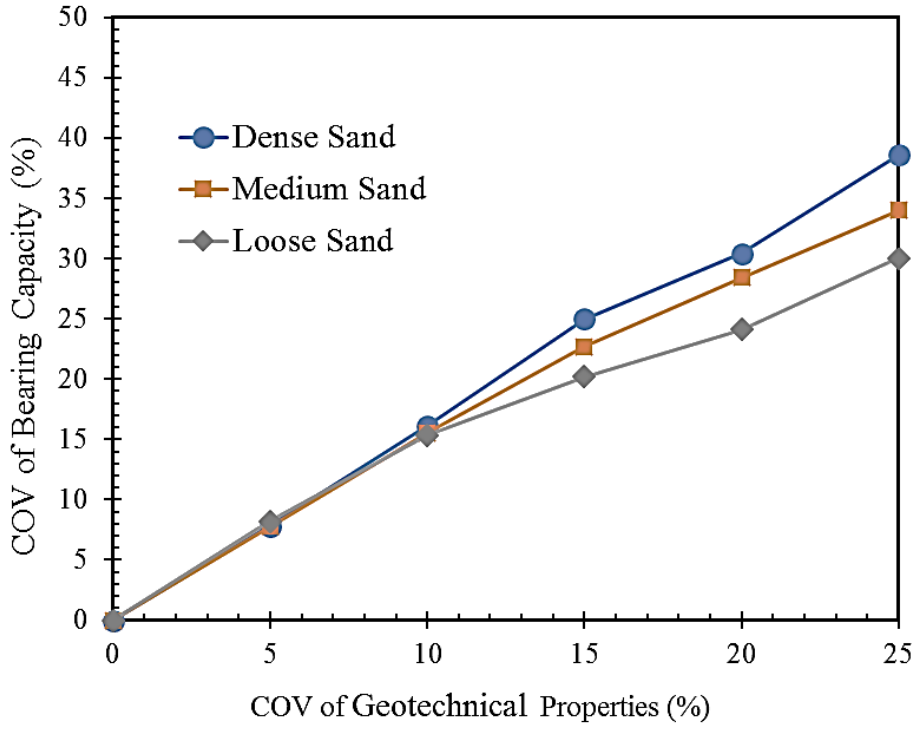

Clayey Soil (Drained Condition)

In this part, researchers studied the effect of changing the COV of cohesion, COV_c, and COV of friction angle, COV_ϕ, on the bearing capacity of our footing model for different clay (soft, medium and stiff) soils for drained condition. The COV_c was ranged from 0 to 50% with an increment increase of 10%, and the COV_ϕ was ranged from 0 to 20%, with an increment increase of 10%. Here, the COV_ϕ was fixed with varying the COV_c.

Figure 104 presents the ultimate bearing capacity versus COV_c for different clay soils, which shows that the bearing capacity for the three clay soils decreases with increasing the COV_c. The magnitude of ultimate bearing capacity depends on the soil type. For example, stiff clay gives higher capacity than the medium stiff and soft clays. The normalized bearing capacity versus COV_c for the three clay soils is presented in Figure 105, which demonstrates a decrease in the normalized bearing capacity with the increase in COV_c for all clay soils for the drained condition.

Figure 106 presents the COV of the bearing capacity versus the coefficient of variation of cohesion, COV_c, for different clay soils. The figure clearly shows that the COV of bearing capacity increases with the increasing the COV_c for the three clay soils. In the three figures, the bearing capacity and the normalized bearing capacity decrease with increasing the COV_ϕ, and that the COV of bearing capacity increases with increasing COV_ϕ.

Figure 104. Ultimate bearing capacity versus COV_ϕ for different clay soils (drained condition)

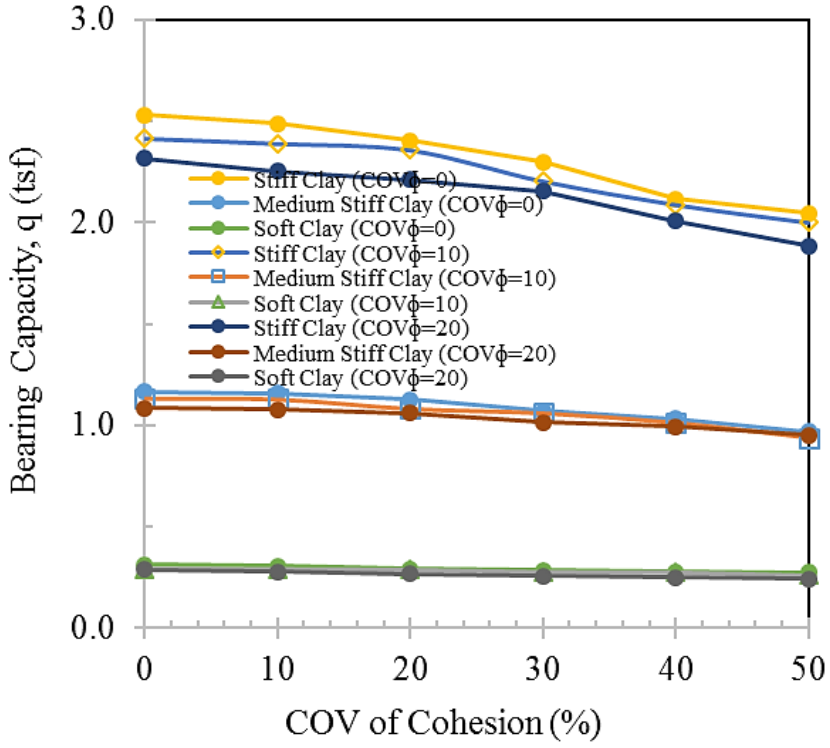

Figure 105. Normalized bearing capacity versus COV_ϕ for different clay soils (drained condition)

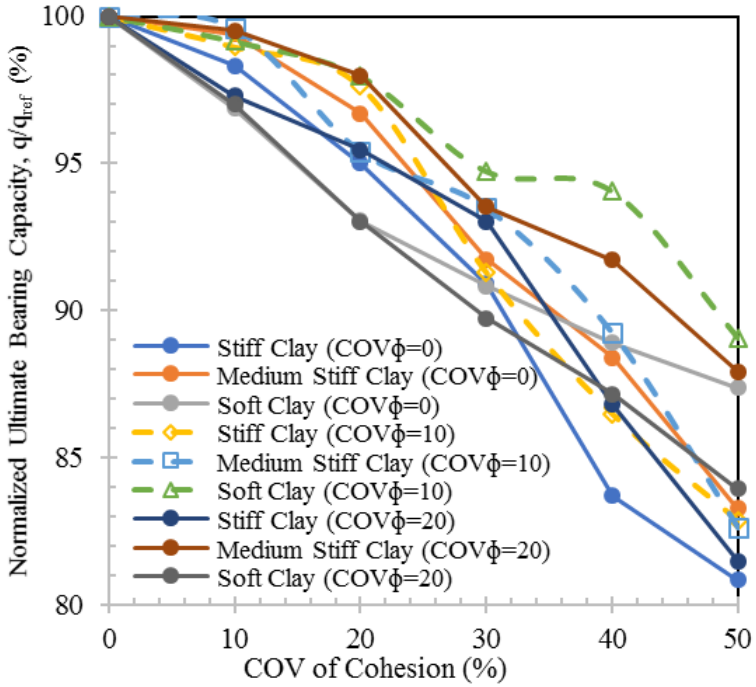

Figure 106. COV of bearing capacity versus COV_ϕ for different clay soils (drained condition)

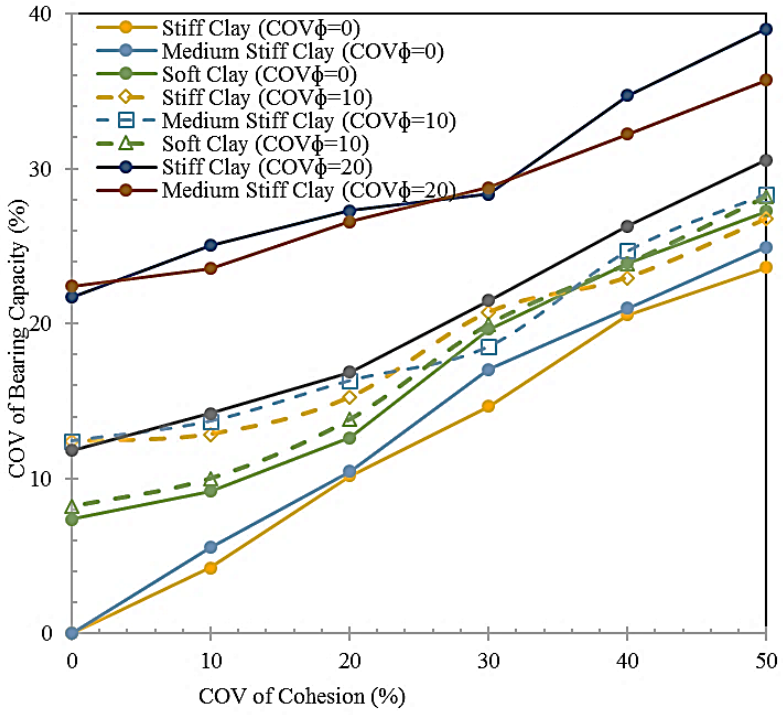

Clayey Soil (Undrained Condition)

In this section, we studied the effect of varying the COV of undrained cohesion (or undrained shear strength for $\phi = 0$) on the ultimate bearing capacity of our footing model for different clay soils (soft, medium and stiff) at the undrained condition. The selected range of COV of undrained cohesion was selected to be from 0 to 50%, with 10% increase increment.

The ultimate bearing capacity versus the COV of undrained cohesion for the three clay soils under undrained condition is presented in Figure 107. The figure show that the bearing capacity decreases with increasing the COV of undrained cohesion, and that the magnitude of bearing capacity changes with the clay soil type. For example, stiff clay gives higher capacity than the medium stiff clay and soft clay. Figure 108 presents the normalized bearing capacity versus the COV of undrained cohesion for the three clay soils, which clearly demonstrates that the normalized bearing capacity decreases with increasing COV of undrained cohesion. The relationship between the COV of the bearing capacity and the COV of undrained cohesion is presented in Figure 109. It is clear that the COV of bearing capacity increases with increasing the COV of undrained cohesion.

Figure 107. Ultimate bearing capacity versus COV_c for different clay soils (undrained condition)

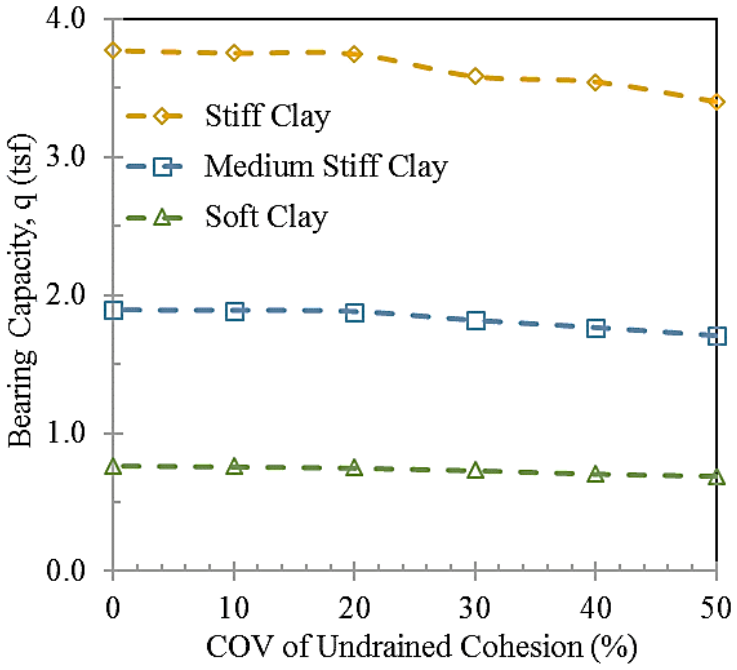

Figure 108. Normalized bearing capacity versus COV_c for different clay soils (undrained condition)

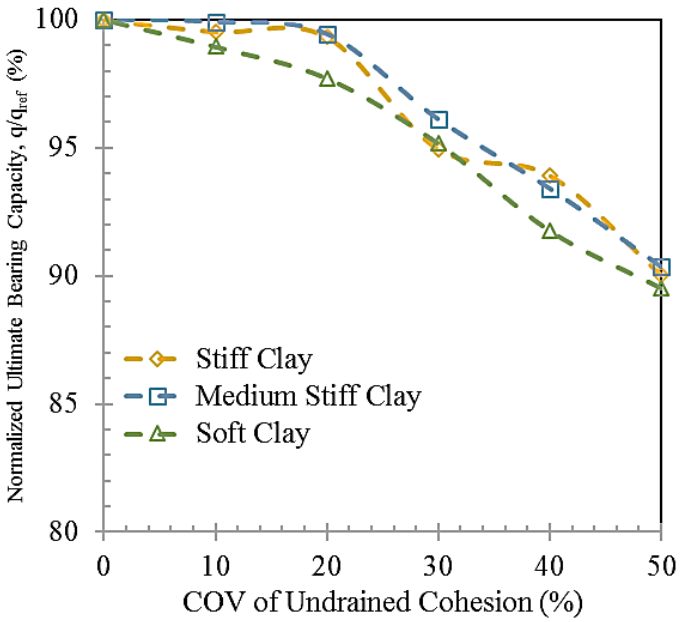

Figure 109. COV of bearing capacity versus COV_c for different clay soils (undrained condition)

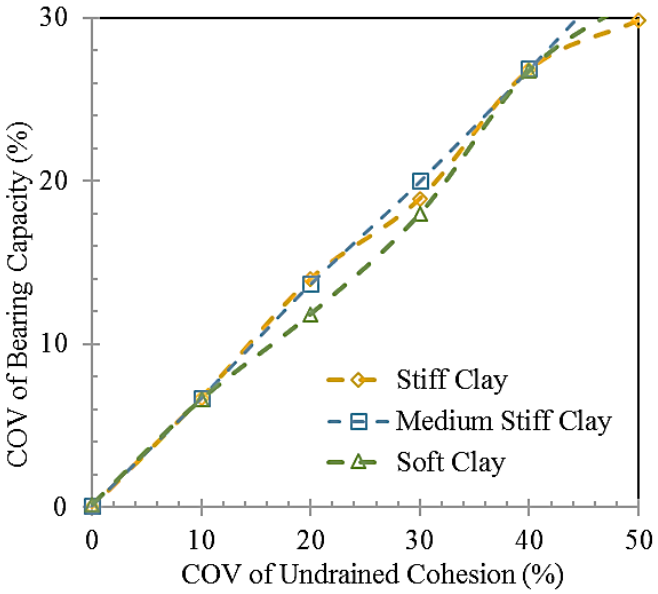

Effect of Site Variability on Resistance Factor (Fenton and Griffiths Method)

Different scenarios were considered in this study to investigate the effect of variation in cohesion and friction angle of foundation soil on the resistance factors of shallow foundations. The values of resistance factors, ϕ_{sf}, were calculated at different sampling borehole location radii 16.4 ft. (5 m), 32.8 ft. (10 m), 49.2 ft. (15 m), 65.6 ft. (20 m) and 82 ft. (25 m) from the center of foundation, at different correlation lengths (0 m to 40 m), and for different values of soil cohesion, c, with different COV_c (0%, 10%, 20%, 30%, 40% and 50%), and for different values of soil friction angle, ϕ, with different, COV_ϕ (0%, 5%, 10%, 15%, 20% and 25%).

Sandy Soil

In this part, analysis was performed for the medium sand (ϕ= 38^o) and the properties shown in Table 8. The soil friction angle, ϕ, was considered for different COV_ϕ (0%, 5%, 10%, 15%, 20% and 25%).

As shown in Figure 110, the resistance factor, ϕ_{sf}, decreased dramatically as the correlation length increased from 0 about 6-16 ft. (2-5 m), then started to increase beyond this correlation range. For all sampling radius, the shape of the resistance factor versus the correlation length curves are similar, but the values of minimum resistance factors decreased as the location of sampling borehole was far from the foundation. Figure 111 presents the effect of the distance of borehole on the resistance factor for the different COV_ϕ levels, which demonstrates a decrease in resistance factor of shallow foundations with the increase in COVϕ and the distance from the borehole.

Figure 110. Resistance factor versus correlation length of medium sand for single boring

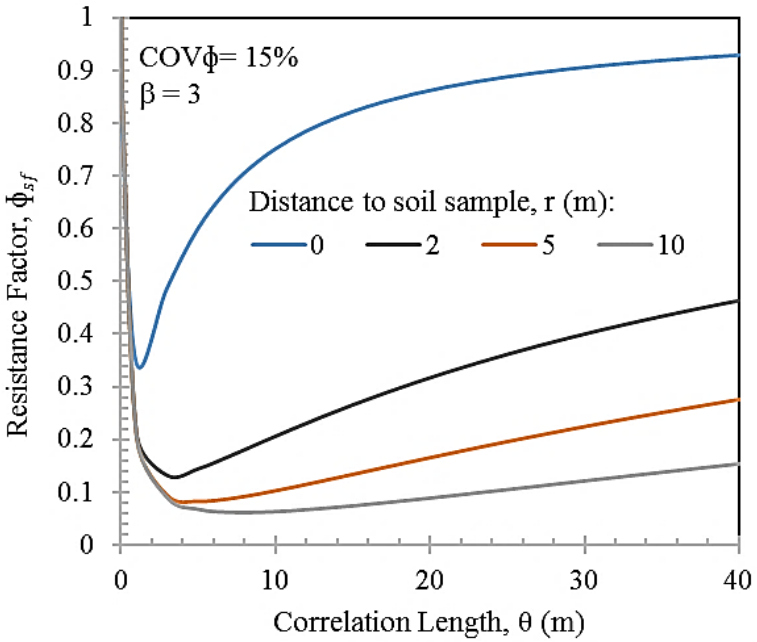

Figure 111. Resistance factor versus distance from borehole for medium sand at different COV_{ϕ} levels

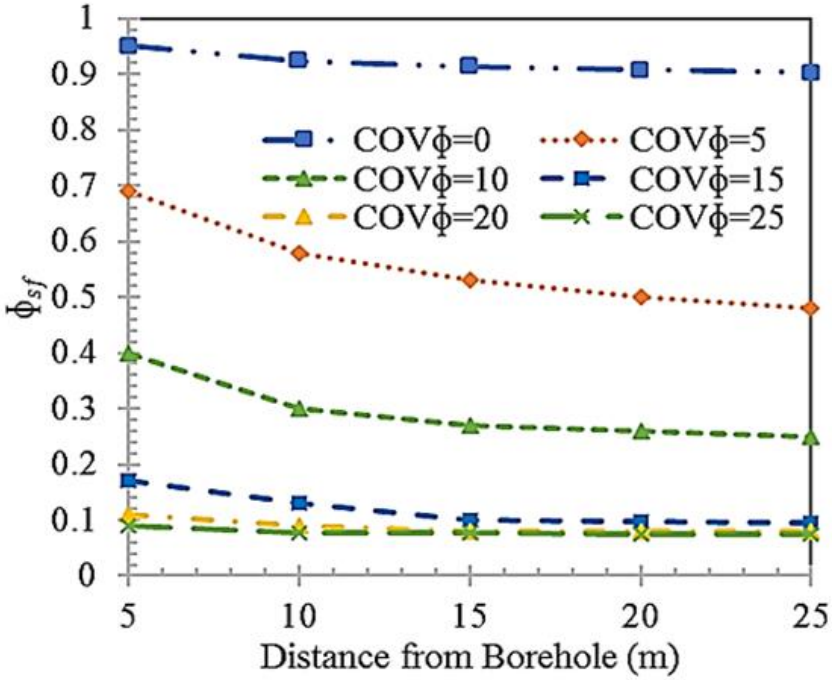

Clayey Soil (Drained Condition)

The analysis here was performed for the medium stiff clay [$\phi = 30^o$ and c = 83.5 psf (4 kPa)] and using the properties shown in Table 9. The soil friction angle, ϕ, was considered with different COV_ϕ (0%, 5%, 10%, 15%, 20% and 25%) and the cohesion, c, was considered with different COVc (0%, 10%, 20%, 30%, 40% and 50%).

Analysis shows that the resistance factor decreased dramatically as the correlation length increased from 0 to about 6-26 ft. (2-8 m), which started to increase after that as shown in Figure 112. The shape of the resistance factor versus the correlation length curves is the same for all sampling radii. However, the values of resistance factors decrease with the increase of the location of sampling borehole from the foundation. Figure 113 presents the effect of the distance of borehole on the resistance factor for different COV_ϕ levels, which shoes a decrease in resistance factor of shallow foundations with the increase in COV_ϕ as well as the distance from the borehole. Figure 114 presents the effect of the distance of borehole on the resistance factor for different COV_c levels, which also demonstrates a significant decrease in the resistance factor of shallow foundations with the increase in COV_c and the distance from the borehole.

Clayey Soil (Undrained Condition)

Analysis was performed here for medium stiff clay (cohesion = 36 kPa) and the using the properties in Table 10. Cohesion, c, was considered with different coefficients of variation, COV_c (0%, 10%, 20%, 30%, 40% and 50%). The results of resistance factor, ϕ_{sf}, versus correlation length of medium stiff clay for single boring of drained condition are shown in Figure 115, which clearly show that the ϕ_{sf} dramatically decreases with increasing the correlation length up to about 6-16 ft. (2-5 m), then after that it starts to increase with increasing the correlation range. For all sampling radii, the shape of the resistance factor versus correlation length curves are similar, but the values of ϕ_{sf} decreases as the distance of sampling borehole was far increases from the foundation. The effect of the distance of borehole on the resistance factor for different COVc levels are presented in Figure 116, which clearly shows a significant decrease in the resistance factor of shallow foundations with the increase in distance of the borehole and COV_c.

Figure 112. Resistance factor versus correlation length of medium stiff clay for single boring (drained condition)

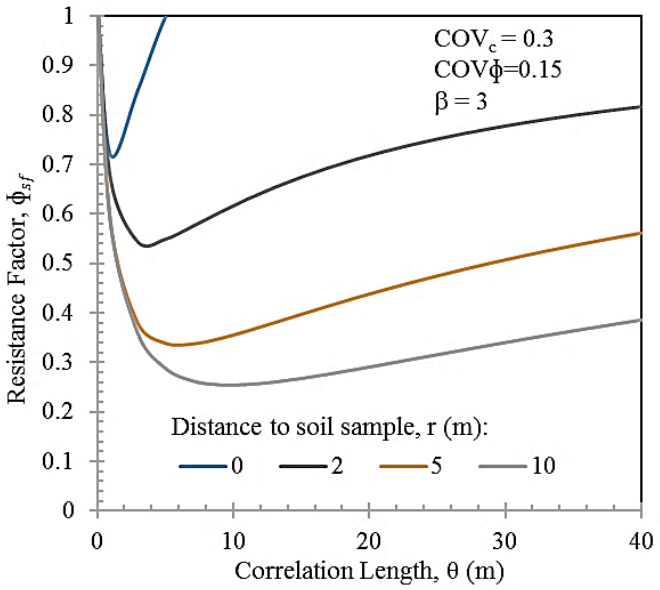

Figure 113. Resistance factor versus distance from borehole for medium stiff clay at different COV$_\phi$ levels (drained condition)

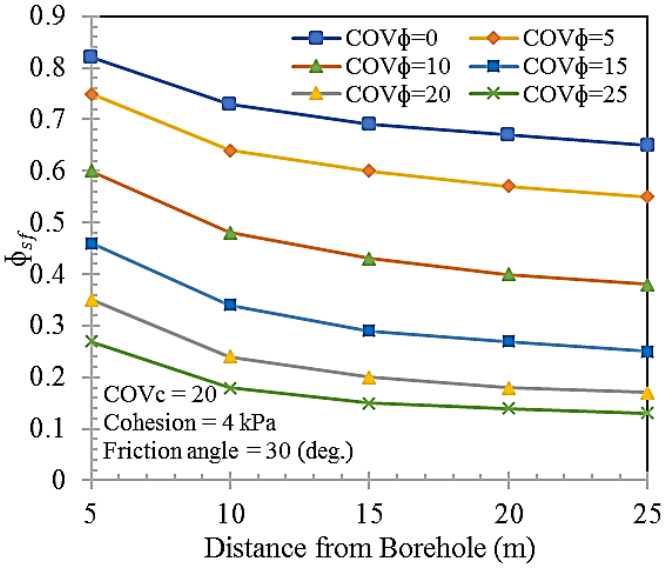

Figure 114. Resistance factor versus distance from borehole for medium stiff clay at different COV_c levels (drained condition)

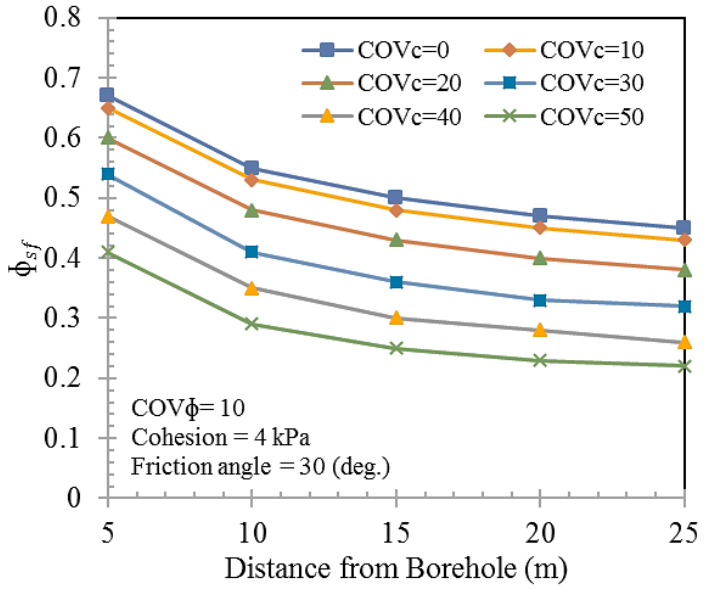

Figure 115. Resistance factor versus correlation length for medium stiff clay at different COV_ϕ levels (undrained condition)

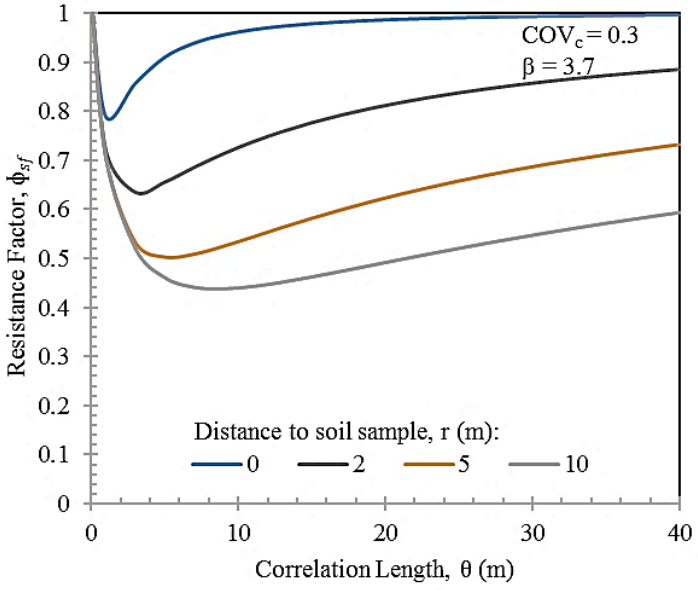

Figure 116. Resistance factor versus distance from borehole for medium stiff clay at different COV_c levels (undrained condition)

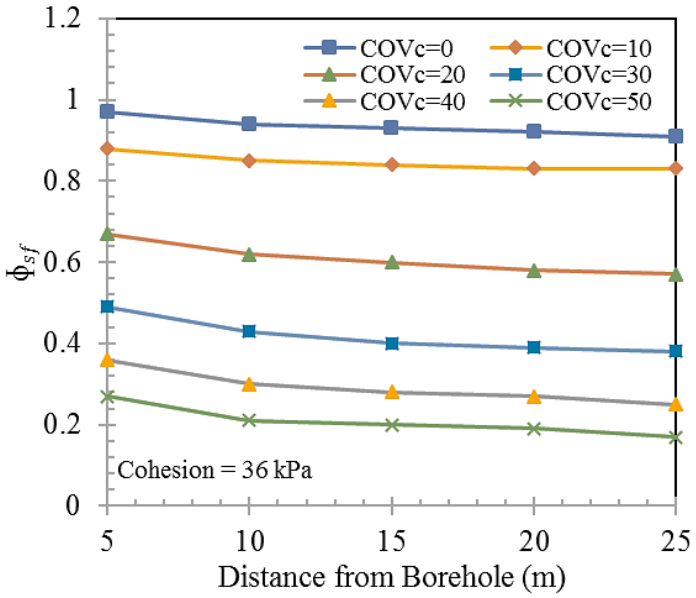

Effect of Site Variability on Reliability Index and Probability of Failure

Different scenarios were analyzed here to study the effect of variability of the soil properties (in terms of cohesion, friction angle, unit weight and friction angle) on the reliability index and probability of failure of the foundation. Here, variability increment no. 1 represents the case when the COVs of cohesion, unit weight and friction angle are 10%, 2% and 5%, respectively. In variability increment no. 2, the COVs of cohesion, unit weight and friction angle were taken as 20%, 4% and 10%, respectively. The variability increment no. 3 represents the case for the COVs of cohesion, unit weight and friction angle are 30%, 6% and 15%, respectively. The COVs for cohesion, unit weight and friction angle in variability increment no. 4 are 40%, 8% and 20%, respectively. Finally, in variability increment no. 5, the COVs of cohesion, unit weight and friction angle were selected as 50%, 10% and 25%, respectively. This means that we increased the COV values for cohesion, unit weight and friction angle simultaneously in each variability increment. In this analysis, for each vertical load of 27.4 kips/ft. (400 kN/m), 34.3 kips/ft. (500 kN/m), and 41.1 kips/ft. (600 kN/m), we calculated the reliability index for each variability increment and the corresponding probability of failure. In this study 15 different scenarios were run to investigate the effect of site variability (by increasing COVs of cohesion, unit weight and friction angle and changing the vertical load) on the Hasofer-Lind reliability index. A matlab code was developed for use in this analysis.

The relationship between the reliability index/probability of failure and the variability increment for the 15 different scenarios are shown in Figure 117. The results show that the reliability indexes were decreased and the probability of failure were increased when the values of COV were increased from variability increment 1 to variability increment 5, and also with increasing vertical load.

Application of Site Variability in Deep Foundation

The method proposed by Naghibi [131] and Naghibi and Fenton [18] were used here to analyze and evaluate the effect of site variability on the design of deep foundation for both the cohesive and cohesionless soils. Additionally, we used our expanded approach of Naghibi's [131] method for analyzing the mixed soils.

Analysis without End Bearing

Cohesive Soil Condition

In this part of analysis, the Red River site was used to study the effect of site variability on deep foundations for cohesive soil condition without considering the end bearing capacity. As stated earlier, eight soil borings were performed at different locations down to 105 ft. depth.

Figure 117. Reliability index vs probability of failure at different COV (at different loading levels)

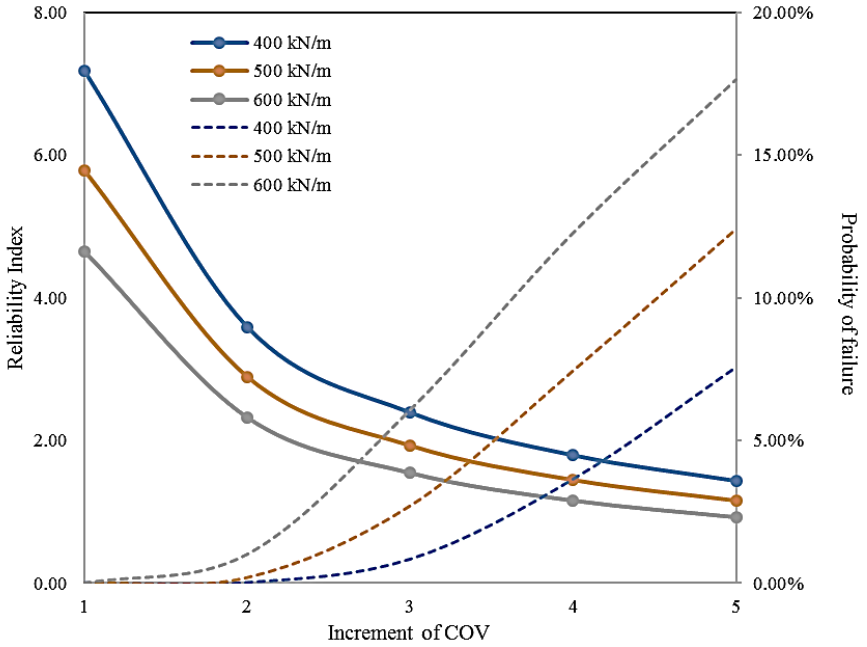

For analysis purpose, we assumed the pile is located at the black (round) point, and calculating the distances of soil borings to the pile as R1, R2, … and R8 shown earlier in Figure 63 (a-c). As shown in Table 80, the distances of the pile from the soil boring locations, R_1, R_2, R_3, R_4, R_5, R_6, R_7, and R_8 are 40.5 ft. (12.33 m), 46.8 ft. (14.27 m), 14.23 ft. (4.34 m), 25.4 ft. (7.74 m), 51.0 ft.(15.55 m), 84.4 ft. (25.72 m), 82.1 ft. (25.02 m), and 120.0 ft. (36.57 m), respectively. The average value of S_u and COV_{Su} was determined for each soil boring. Moreover, the inverse distance weighted (IWD) values of S_u (IDW) and COV_{Su} (IDW) were determined for the whole site. The resistance factors, ϕ_{df} for each soil boring was calculated using Equation 73 and the corresponding distance from the pile location for a reliability index, $\beta = 2.33$. The average of ϕ_{df} for all soil borings was calculated as 0.79. The resistance factor, ϕ_{df}, for the entire site, was also calculated using the S_u (IDW) and COV_{Su} (IDW) values as 0.77. As shown in Table 80, the calculated resistance factor, ϕ_{df}, for each soil boring depends on the distance between the pile and the location of the soil boring and the COV_{Su}.

Table 80. Calculation of resistance factor for the Red River site

Soil Boring	Distance from pile (ft.)	Average S_u	S_u (IDW)	COV_{Su}	COV_{Su} (IDW)	Resistance Factor, ϕ_{df} (β=2.33)	Average ϕ_{df} (all borings)	IDW Resistance Factor, ϕ_{df} (β=2.33)
R 1	40.5	105.39	80.90	0.31	0.32	0.78	**0.79**	**0.77**
R 2	46.8	84.92		0.25		0.86		
R 3	14.23	54.89		0.48		0.71		
R 4	25.4	98.97		0.19		0.89		
R 5	51.0	88.14		0.21		0.87		
R 6	84.4	64.72		0.07		0.93		
R 7	82.1	124.65		0.19		0.84		
R 8	120.0	92.08		0.47		0.47		

Cohesionless Soil Condition

Site variability analysis was performed here on a cohesionless soil site with an average value of friction angle of ϕ=30° without considering the end bearing. Different coefficients of variation of ϕ, COV_ϕ (i.e., 0%, 10%, 20%, 30%, 40% and 50%), was considered in this analysis. In addition, soil borings with different locations and sampling distances [i.e., 16.4 ft. (5 m), 32.8 ft. (10 m), 49.2 (15 m), 65.6 ft. (20 m), and 82.0 ft. (25 m) from the pile location were considered. The resistance factors, ϕ_{df}, for the pile in cohesionless soil (without end bearing) for the different COV_ϕ scenarios and distance of boring from pile were calculated using Equation 88, and the results are presented in

Figure 118. The figure clearly demonstrates a significant decrease in the resistance factor of pile in cohesionless soil with the increase in COV_ϕ and the distance from the boring location.

Mixed Soil Condition

In this part of analysis, we considered the Metairie site for the mixed soil condition without considering the end bearing capacity. Fifteen soil borings were performed at different locations in Metairie site down to 105 ft. depth as shown in Figure 44a. As described earlier, the Metairie site consists of two clay layers and two sand layers. The soil layering and properties are presented in Figure 45.

Figure 118. Resistance factor of pile in cohesionless soil for different COV_ϕ scenarios

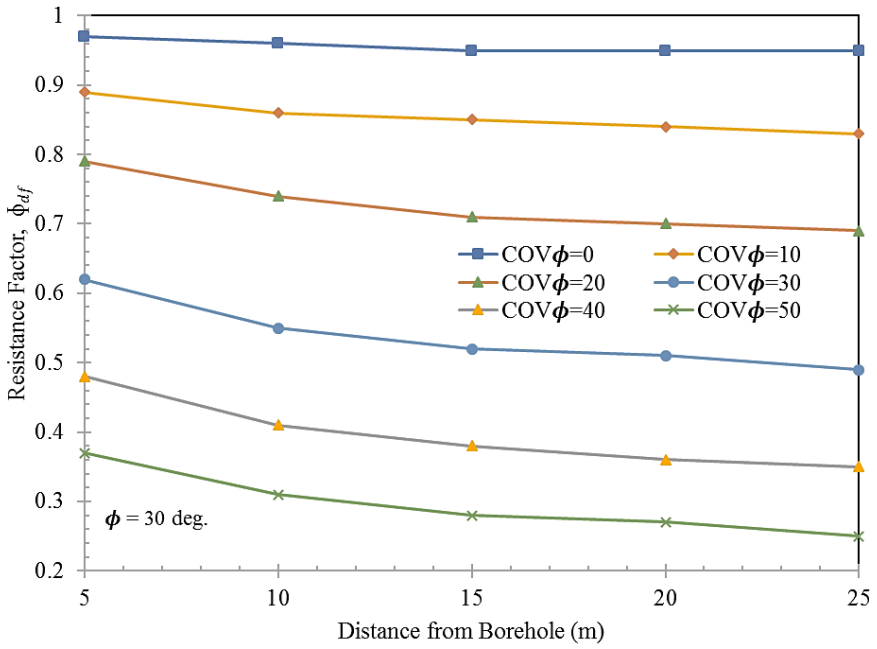

For analysis purpose, we assumed the pile is located at the black (round) point, and calculating the distances of soil borings to the pile as M1, M2, … and M15 shown earlier in Figure 64(a-c). The distances of the pile from the soil boring locations are presented in Table 81. The average value of S_u, COV_{Su}, ϕ and COV_ϕ were determined for each soil boring location. In addition, the inverse distance weighted (IWD) values of S_u (IDW), COV_{Su}(IDW), ϕ (IDW) and COV_ϕ(IDW) were calculated for the entire site. The resistance factor, ϕ_{df}, corresponding to β=2.33 was calculated for each soil boring location based on the distance of soil boring from the pile location using Equations 73

and 88. The average of ϕ_{df} for all soil borings was calculated to be 0.65. Meanwhile, the resistance factor, ϕ_{df}, for the entire site, was calculated using the S_u (IDW), COV_{Su}(IDW), ϕ (IDW) and COV_{ϕ}(IDW) as 0.71. The table shows that the resistance factor, ϕ_{df}, for each soil boring depends on the distance of the pile from the soil boring and the COV_{Su} and COV_{ϕ}.

Table 81. Calculation of resistance factor for the Metairie site (without end bearing)

Soil Boring	Distance from Pile (ft.)	Undrained Shear Strength, S_u (kPa)	COV_{Su}	Friction Angle, ϕ (deg.)	COV_{ϕ}	Resistance Factor, ϕ_{df} (β=2.33)	Average ϕ_{df} (all borings)	IDW Resistance factor, ϕ_{df}
M 1	188.0	32.98	0.35	37.50	0.23	0.55		
M 2	190.5	37.45	0.42	36.07	0.21	0.52		
M 3	158.0	33.86	0.31	32.31	0.27	0.55		
M 4	113.8	28.13	0.29	33.38	0.18	0.66		
M 5	72.3	25.56	0.44	40.42	0.11	0.64		
M 6	91.4	34.74	0.29	40.82	0.09	0.74	**0.65**	
M 7	24.6	30.48	0.25	41.93	0.09	0.78		
M 8	49.8	30.72	0.34	38.86	0.12	0.71		
M 9	179.0	28.25	0.36	45.79	0.07	0.66		
M 10	153.1	27.41	0.38	41.50	0.10	0.64		
M 11	129.2	24.30	0.37	36.82	0.13	0.66		
M 12	148.6	27.77	0.45	40.33	0.10	0.61		
M 13	121.8	28.25	0.37	42.50	0.14	0.666		
M 14	77.8	30.32	0.48	41.33	0.11	0.608		
M 15	110.5	31.00	0.34	45.00	0.17	0.622		
IDW		**30.17**	**0.31**	**40.92**	**0.11**			**0.71**

Another analysis was conducted for the Metairie site using the average S_u and ϕ values for the four soil layers (two clay and two sand layers). The weighted average of S_u, COV_{Su}, and σ_{Su} for the clay layers are 480.4 psf (23.0 kPa), 0.27 and 5.85, respectively; and for the sandy layers, the weighted average of ϕ, COV_{ϕ}, and σ_{ϕ} are 39°, 0.35 and 13.06, respectively. Different sampling location distances [16.4 ft. (5 m), 32.8 ft. (10 m), 49.2 ft. (15 m), 65.6 ft. (20 m), and 82.0 ft. (25 m)] were considered. The calculated resistance factors for the mixed soil (without considering end bearing) at different COV_{ϕ} (i.e., 0%, 10%, 20%, 30%, 40% and 50%) and COV_{Su} (i.e., 0%, 10%, 20%, 30%, 40%

and 50%) scenarios are presented in Figure 119. The figure presents the effect of the distance of borehole on the resistance factor for different COVϕ and COV_{Su} levels, which clearly demonstrates a significant decrease in the resistance factor of mixed soil with the increase in either the COV_{ϕ} or COV_{Su} levels and the increase of distance between the pile and soil boring.

Figure 119. Calculated resistance factor for the mixed soil at different COV_{ϕ} and COV_{Su} scenarios (without end bearing)

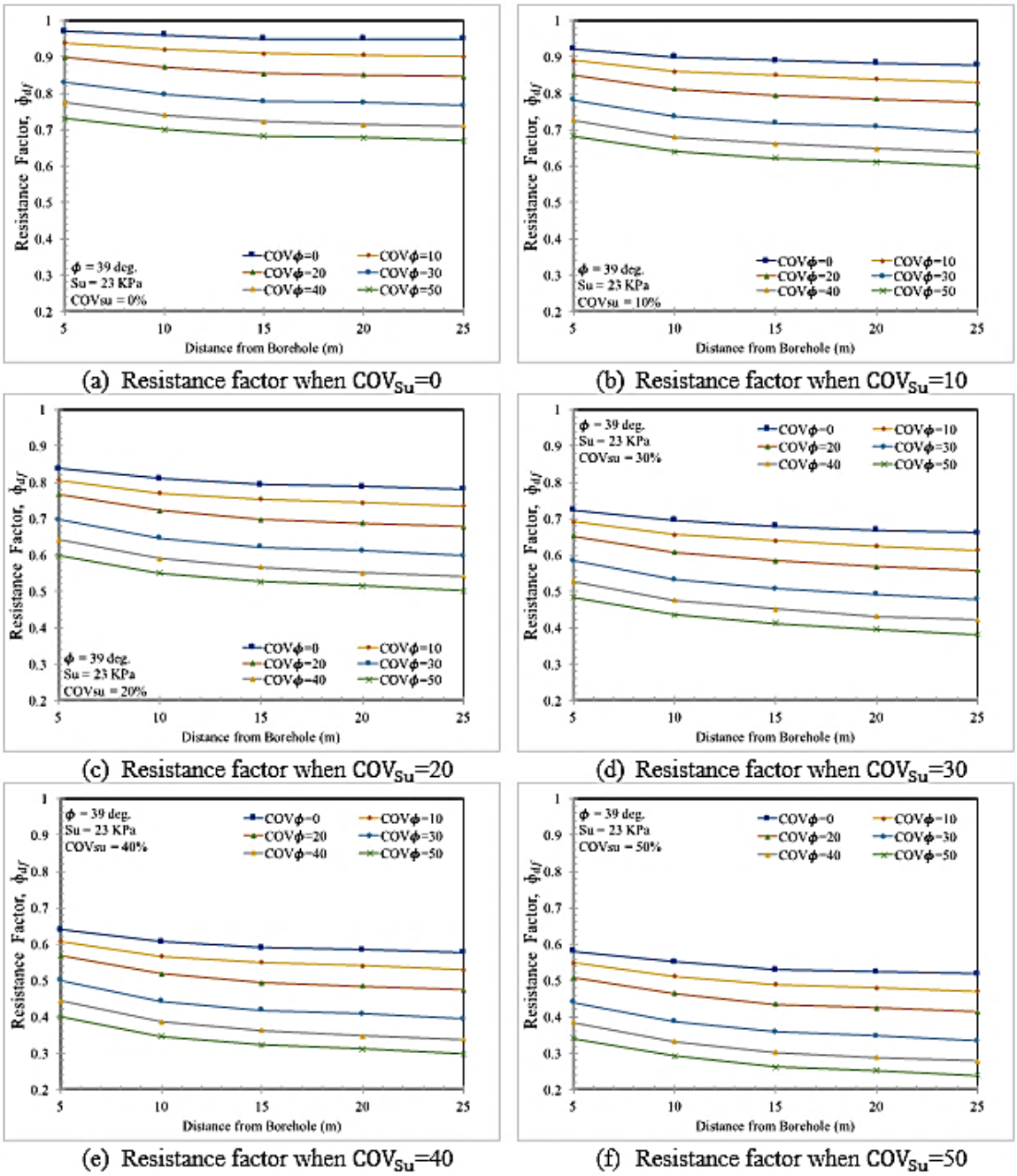

Analysis Including End Bearing

Cohesive Soil Condition

In this part of analysis, the Red River site was used again to study the effect of site variability on deep foundations for cohesive soil condition, but with including the end bearing capacity. We followed the same procedure we did before by assuming the pile to be located at the black point, and calculating the distances of soil borings to the pile (R1 to R8), as described earlier in Figure 63 (a-c). The distances of soil borings were calculated as R1 = 40.5 ft. (12.33 m), .., and R8 = 120.0 ft. (36.57 m), as shown in Table 82. The average value of S_u and COV_{Su} were calculated for each soil boring. The values of S_u (IDW) and COV_{Su} (IDW) were also determined for the whole site using the inverse distance weighted method. The resistance factor, ϕ_{df} (for β=2.33) was calculated for each boring location considering the end bearing capacity using Equation 138. The average ϕ_{df} for all soil layers was estimated to be 0.8. Additionally, the value of ϕ_{df} for the whole site was determined using the S_u (IDW) and COV_{Su} (IDW), and the results are presented in Figure 120, which shows that the ϕ_{df} value for each boring location depends on the distance between the pile and soil boring and the COV_{Su}. The resistance factor, ϕ_{df}, was increased from 0.77 to 0.78 for the Red River site, when the end bearing was considered.

Table 82. Calculation of resistance factor for the Red River site (considering end bearing)

Soil Boring	Distance from pile (ft.)	S_u	S_u (IDW)	S_u (Tip)	S_u (Tip) (IDW)	COV_{Su}	COV_{Su} (IDW)	Resistance Factor, ϕ_{df} (β=2.33)	Average ϕ_{df} (all soil borings)	ϕ_{df} (IDW)
R 1	40.5	105.39	80.90	60.0	35.35	0.31	0.32	0.81	0.80	0.78
R 2	46.8	84.92		25.0		0.25		0.88		
R 3	14.23	54.89		30.0		0.48		0.73		
R 4	25.4	98.97		35.0		0.19		0.89		
R 5	51.0	88.14		40.0		0.21		0.88		
R 6	84.4	64.72		35.0		0.07		0.94		
R 7	82.1	124.65		45.0		0.19		0.84		
R 8	120.0	92.08		15.0		0.47		0.47		

Cohesionless Soil Condition

A cohesionless soil site with an average friction angle of ϕ=30° was selected here to study the effect of site variability on deep foundation with considering the end bearing capacity. To do so, different values of COV of ϕ were selected (i.e., COVϕ = 0%, 10%, 20%, 30%, 40% and 50%) in this analysis. Additionally, different locations and sampling distances

soil borings from the pile location [i.e., 16.4 ft. (5 m), 32.8 ft. (10 m), 49.2 (15 m), 65.6 ft. (20 m), and 82.0 ft. (25 m) were considered. The resistance factors, ϕ_{df}, for pile in cohesionless soil were calculated again for the different COVϕ scenarios, but with considering the end bearing capacity, using Equation 146. The resulted values of ϕ_{df} are presented in Figure 120, which shows that the resistance factor, ϕ_{df}, decreases with the increasing the COV_{ϕ} and the distance from the soil boring location.

Figure 121 presents the effect of the distance between the soil boring and the pile on the resistance factor, ϕ_{df}, for different side and tip COV_{ϕ} levels. Here the COV_{ϕ} for both the side and the tip were selected as 0%, 20%, and 40%. The figure clearly shows significant decrease in ϕ_{df} with the increase in the COV_{ϕ} (side), COV_{ϕ} (tip), and the distance of borehole location from the pile.

Figure 120. Resistance factor of pile in cohesionless soil for different COV_{ϕ} scenarios (considering end bearing)

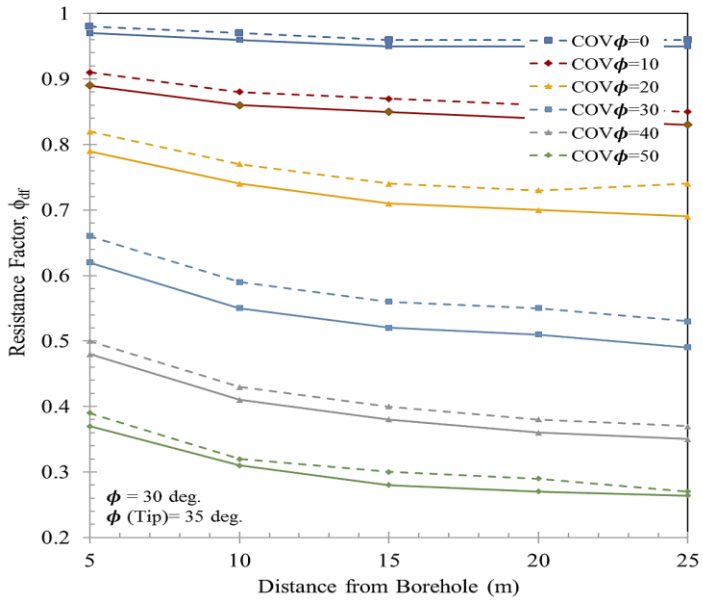

Figure 121. Resistance factor of pile in cohesionless soil for different COV_ϕ scenarios (considering end bearing)

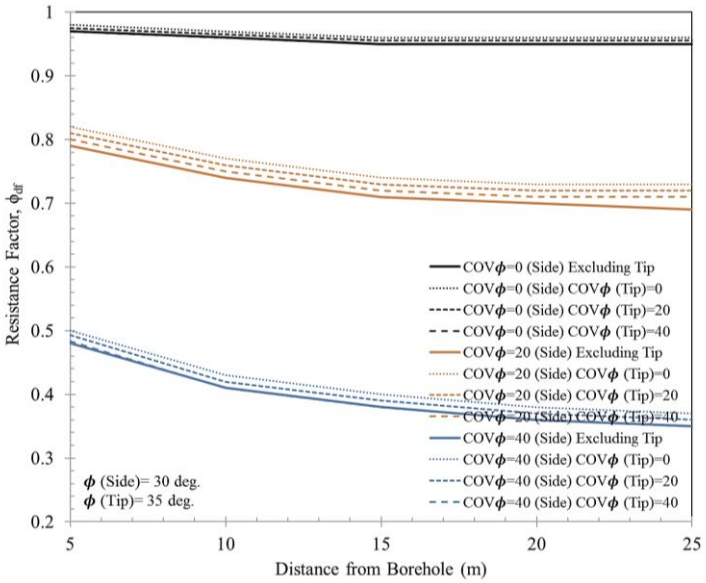

Mixed Soil Condition

The Metairie site was considered again for the mixed soil condition, but with considering the end bearing capacity this time. Analysis was performed for the pile located at the black (round) point described earlier in Figure 64(a-c), and calculating the distances of soil borings from the pile as M1, M2, … and M15 (as presented in Table 83). The values of S_u, COV_{Su}, ϕ and COV_ϕ were determined for each soil boring. Also, The values of S_u (IDW), COV_{Su}(IDW), ϕ (IDW) and COV_ϕ(IDW) were also determined for the entire site using the inverse distance weighted method. The resistance factor, $\phi_{df,}$ for each soil boring locations were calculated at β=2.33 using equations 73 and 88 and the corresponding distance from pile. The average ϕ_{df} for all soil borings was calculated to be 0.66. The resistance factor, ϕ_{df}, for the entire site was calculated using the S_u (IDW), COV_{Su}(IDW), ϕ (IDW) and COV_ϕ(IDW) as 0.74. The results are presented in Figure 122, which shows that ϕ_{df} for each soil boring is depend on the distance between the pile and soil boring and the COV_{Su} and COV_ϕ. The value of ϕ_{df} for the entire site (based on IDW) increased from 0.71 to 0.74 when the end bearing is considered.

Table 83. Calculation of resistance factor for the Metairie site (including end bearing)

Soil Boring	Distance from Pile (m)	Su (kPa)	COV_{Su}	Friction Angle, ϕ (deg.)	COV_{ϕ}	ϕ_R (Tip)	Resistance factor, ϕ_{df}	Average ϕ_{df} (all soil borings	ϕ_{df} (IDW)
M 1	57.31	32.98	0.35	37.50	0.23	42.0	0.58	0.66	0.74
M 2	58.07	37.45	0.42	36.07	0.21	38.0	0.552		
M 3	48.15	33.86	0.31	32.31	0.27	37.0	0.578		
M 4	34.70	28.13	0.29	33.38	0.18	32.0	0.692		
M 5	22.03	25.56	0.44	40.42	0.11	40.0	0.636		
M 6	27.85	34.74	0.29	40.82	0.09	36.0	0.744		
M 7	7.49	30.48	0.25	41.93	0.09	46.0	0.8		
M 8	15.18	30.72	0.34	38.86	0.12	35.0	0.722		
M 9	54.55	28.25	0.36	45.79	0.07	50.0	0.656		
M 10	46.66	27.41	0.38	41.50	0.10	44.0	0.644		
M 11	39.37	24.30	0.37	36.82	0.13	32.0	0.66		
M 12	45.30	27.77	0.45	40.33	0.10	38.0	0.61		
M 13	37.12	28.25	0.37	42.50	0.14	36.0	0.666		
M 14	23.70	30.32	0.48	41.33	0.11	35.0	0.608		
M 15	33.70	31.00	0.34	45.00	0.17	40	0.666		
IDW		**30.17**	**0.31**	**40.92**	**0.11**	**41.82**			

The Metairie site was analyzed again with considering end bearing using the average S_u and ϕ values for the four soil layers (two clay and two sand layers). The weighted average of S_u, and COV_{Su} for the clay layers are 480.4 psf (23.0 kPa) and 0.27, respectively; and the weighted average of ϕ and $COV\phi$ for the sandy layers are 39° and 0.35, respectively. Different sampling location distances were considered [from 16.4 ft. (5 m) to 82.0 ft. (25 m)]. The resistance factors, ϕ_{df}, for the mixed soil (including the end bearing) were calculated at different $COV\phi$ (0%, to 50%) and different COV_{Su} (0% to 50%) scenarios using Equations 138 and 146, and are presented in Figure 122. The figure shows that the resistance factor, ϕ_{df}, for the mixed soil decreases with increasing either the COV_{ϕ} or the COV_{Su} levels and with increasing the distance between the soil boring and the pile.

Figure 122. Calculated resistance factor for the mixed soil at different COV_{ϕ} and COV_{Su} scenarios (including the end bearing)

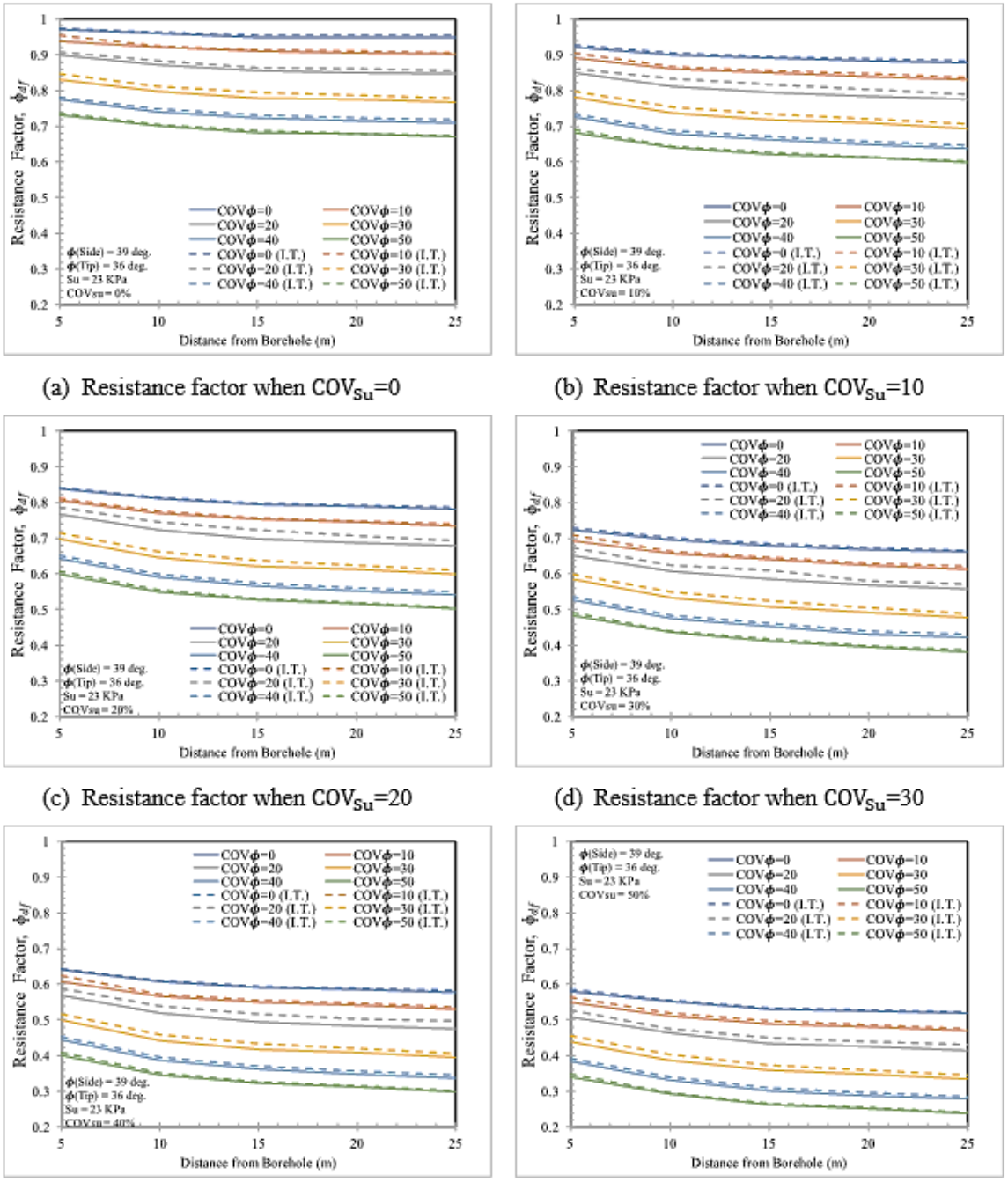

(a) Resistance factor when COV_{Su}=0

(b) Resistance factor when COV_{Su}=10

(c) Resistance factor when COV_{Su}=20

(d) Resistance factor when COV_{Su}=30

(e) Resistance factor when COV_{Su}=40

(f) Resistance factor when COV_{Su}=50

Conclusions

Different approaches and techniques were examined to evaluate the spatial variability of soil properties and the different sources of geotechnical variability, and to quantify the soil variabilities for incorporation in analysis and design of different geotechnical engineering applications. This includes conducting in-box laboratory tests on different soil types using different devices such as Geogauge, LFWD, D-SPA and DCP; conducting field tests using Geogauge, LFWD and DCP on constructed sections at ALF site and under-construction sections from different projects; and conducting typical laboratory tests, such as unconsolidated undrained (UU), direct shear and tests, and consolidation tests were conducted, on different soil types. Different geostatistic methods and techniques were used to incorporating the effect of site variability from soil borings and in-situ CPT tests into different geotechnical engineering applications, such as ultimate capacity of pile foundations, ultimate bearing capacity of shallow foundations, and slope stability analysis. The incorporated geostatistic techniques include X-Bar/R, ANOVA, second moment statistical analysis, spatial correlation and semivariogram modeling, Bayesian technique, probabilistic approach, and Fenton and Griffiths [133] modeling. Based on the findings of this study, the following conclusions can be made:

- When comparing variabilities among the different devices, the in-box and field tests showed range values of coefficient of variation (COV). For the in-box test, the COV of Geogauge varied from 5.1% to 15.3% using the X-Bar/R method, whereas it ranged from 7.4% to 18.1% using the ANOVA method. For the LFWD, the COV ranged from 7.4% to 14.3% and 8.2% to 24.4% for the X-Bar/R and ANOVA methods, respectively. In the case of the Dirt Seismic Portable Analyzer (D-SPA), the COV differed from 4.2% to 9.6% for the X-Bar/R method; while the COVs varied from 6.7% to 15.4% for the ANOVA method. However, the ranges of the COVs of Geogauge, LFWD, and D-SPA devices evaluated using the second moment statistics were 6.7% to 15.6%, 10.9% to 20.8% and 5.9% to 13.4%, respectively. For the case DCP test, it was found that the COV of DCPI range from 1.6% to 16.4%, and 0.4% to 18.1%, for the operator and the location-related variability, respectively. For the case of the Nuclear Density Gauge (NDG), the COV ranged from 0.5% to 6.1% and from 2.4% to 25.1% for the dry density and the moisture content, respectively. When analyzing data using the E-Gauge device, the COVs ranged from 0.41% to 4.02% and from 1.76% to 18.8% for the dry density and for the moisture content, respectively.

- The field tests performed by different devices were grouped into the constructed and under-construction sections. In the case of constructed sections at ALF site, the COV of Geogauge varied from 7.7% to 21.0% using the X-Bar/R method, whereas the COV ranged from 11.4% to 23.6% using the ANOVA method. For the LFWD, the COVs ranged from 7.3% to 20.3% and from 7.9% to 18.9% for the X-Bar/R method and the ANOVA method, respectively. However, when analyzing data using the second moment statistical analysis, the ranges of COVs for the Geogauge and LFWD were 11.1% to 20.2% and 7.0% to 16.7%, respectively. When comparing the operator and the location-related variabilities of the DCPI, it was found that the COVs ranged from 3.2% to 20.3%, and 2.6% to 29.4%, respectively. The COVs for the dry density and moisture content evaluated using the Nuclear Density Gauge (NDG) ranged from 0.2% to 4.2% and from 0.7% to 17.5%, respectively. In the case of the E-Gauge device, the COVs differed from 0.1% to 9.3% and from 0.2% to 19.5% for the dry density and the moisture content, respectively.

- The result of field tests conducted in three under-construction sections at LA highway showed that the COVs of Geogauge varied from 20.3% to 32.5% and from 20.3% to 31.9% for the operator and the location-related variabilities, respectively. When assessing data for the LFWD, the COVs ranged from 11.7% to 37.5% and from 18.6% to 31.8%, for the operator and the location-related variabilities, respectively. Analysis of DCP tests showed that the COV of DCPI for the whole section ranged from 15.4% to 29.8%. The COVs for the dry density and moisture content measured using the Nuclear Density Gauge (NDG) ranged from 0.2% to 2.3% and from 0.8% to 10.2%, respectively. In the case of the E-Gauge, the COVs ranged from 0.10% to 3.7% and from 0.8% to 12.0% for the dry density and the moisture content, respectively.

- Analysis of laboratory test results showed that the COVs of the UU tests varied from 1.0% to 10.9% and from 3.8% to 17.1% for the operator and specimen-related variabilities, respectively. The results of Atterberg Limits data showed that the COVs of liquid limit varied from 0.9% to 7.8%; the COVs of plastic limit ranged from 1.9% to 18.2%, and the COVs of plasticity index ranged from 1.1% to 26.4%. For the small direct shear tests, the results showed that the operator-related and specimen-related variabilities COVs of friction angle, ϕ, ranged from 0.4% to 1.8%, and from 7.8% to 8.8%, respectively. Meanwhile, the COVs of the cohesion, c, ranged from 3.5% to 19.5%, and 5.7% to 20.0% for the operator and specimen-related variabilities, respectively. For the one-dimensional consolidation test, the

operator and specimen-related COVs for the compression index (C_c) varied from 1.4% to 16.8%, and 0.8% to 18.4%, respectively. The operator and specimen-related COVs for C_r ranged from 5.6% to 18.2%., and 3.6% to 17.1%, respectively. Meanwhile the COVs for the coefficient of consolidation (C_v) varied from 2.3% to 20.9% and 5.5% to 30.6% for the operator and specimen-related variabilities, respectively. Analysis of CBR test data showed that the COVs varied from 4.2% to 15.6%, and 5.7% to 16.0% for the operator and specimen-related variabilities, respectively.

- Analysis of different AMRL test datasets (2009-2010 to 2016-2017) showed that the COV for the liquid limit, LL, varied from 4.3% to 8.4%; while the COV for the plastic limit, PL, varied from 6.7% to 9.4%. However, analysis of combined AMRL and lab test data showed that the combined COV for the LL is 4.3%, and the combined COV for the 6.7%. Analysis of the AMRL CBR test data showed that the COVs range from 16.5 % for Mexican limestone using the 2009-2010 AMRL data to 34.9% for the RAB material using the 2012-2013 AMRL data.

- The results of this study demonstrated that the spatial site variability can be evaluated from site exploration program involved multi CPT tests and/or multi soil borings with laboratory tests performed at different locations within the specific site.

- The effect of site variability of soil properties can be implemented into LRFD design of pile foundations through evaluating the spatial and/or the total coefficients of variation ($COV_{R,spatial}$, $COV_{R,total}$) of the site using the semivariogram approach, which can be used as input parameters in Equation 21 to calibrate the resistance factor ($\phi_{spatial}$ or ϕ_{total}) for the specific site.

- For sites that have site variability lower than the design method variability (i.e.,$COV_{R,spatial} < COV_{R,method}$), the total coefficient of variation ($COV_{R,total}$) decreases and the corresponding resistance factor ($\phi_{spatial}$ or ϕ_{total}) increases, and vice versa. Hence, giving a credit to low variability sites as compared to high variability sites in terms of increasing either $\phi_{spatial}$ or ϕ_{total}, for use in the design of pile foundations.

- The CPT equipment source of errors are expected to be lower than the SPT equipment source of errors. Furthermore, the site variability from using CPT-q_t data are usually lower than the site variability from using soil boring data (SPT-N or S_u). Therefore, the corresponding resistance factors ($\phi_{spatial}$, ϕ_{total}) for LCPC pile-CPT

design method are higher than the resistance factors for the static α-Tomlinson and Nordlund static design methods.

- The results show that the selection of prior data in level 1 of Bayesian analysis has little effect on the updated posterior data of the new specific site, and hence the updated bias mean (λ) and COV of the measured/predicted pile capacity, and the updated resistance factor for the specific site. In general, the updated posterior parameters for the new specific site in Bayesian analysis lie between the $prior_2$ parameters and the $likelihood_2$ parameters, taking into consideration the specific site variability.

- The authors introduced a new term called confidence bias site parameter (w_b) to put more weight on the test data for the new specific site during the Bayesian updating process high as compared to database collected from previous sites.

- When the soil variability of the new specific site increases from low to high as compared to previous sites data, the corresponding updated resistance factor (ϕ_R) decreases and vice versa. Meanwhile, when the number of tested piles in the new site increases, the value of ϕ_R increases for low specific site variability, while decreases for high specific site variability. As an example, for $w_b = 1.5$, and lower number of piles in the new site, if we change the variability of new site from low to high, the values of ϕ_R reduced from 0.62 to 0.56. However, if we increase the number of piles in the new site (at low site variability) the value of ϕ_R increases from 0.62 to 0.63. Meanwhile, for the case of high site variability of old site and low site variability and lower number of piles at new site, the values of ϕ_R increased from 0.56 to 0.65 with increasing w_b from 1 to 2.

- The probabilistic analysis method can used to develop the estimation/mean map by taking the average of all realizations simulation the sequential Gaussian simulation. The results of sequential Gaussian simulation were compared with kriging mapping, which shows that the simulation and kriging estimation are nearly identical.

- The prediction probability of corrected cone tip resistance $[q_{t,avg\ -st.dev} \leq q_t \leq q_{t,avg)+st.dev}\ ]_{x0}$ for LA 1 site for 1^{st}, 2^{nd}, 3^{rd} and 4^{th} soil layers are 78%, 70%, 87% and 73%, respectively. The weighted average prediction probability for LA 1 site is 75%, and the corresponding resistance factors ($\phi_{spatial}$, ϕ_{total}) for LCPC pile-CPT design method are 0.87 and 0.73, respectively.

- This effect of site variability on the slope stability analysis was investigated. In case of drained condition, the factor of safety for the three slope stability analysis methods decreased when the COV of friction angle, ϕ, was increased from 5% to 25%. For the same COV, the factor of safety increased with increasing the vertical correlation length (i.e., decrease in vertical variability). However, in case of unit weight and cohesion, the factor of safety did not change significantly when the COV of unit weight was increased from 2% to 10%, and when the COV of cohesion was increased from 10% to 50%. Out of three slope stability analysis methods, the Janbu simplified's factor of safety was less than the other two methods (Bishop simplified and Spencer).

- In case of undrained condition, the factor of safety for the three slope stability analysis methods decreased with increasing the COV of undrained cohesion, increased with increasing the vertical correlation length (i.e., decrease in vertical variability), and slightly increased with increasing the horizontal correlation length (i.e., decrease in horizontal variability). The effect of variability in undrained cohesion depends on the length of failure surface within the clay layer.

- For the cases of proportion COVs of friction angle, cohesion, and weight, the results showed that the factor of safety for the three slope stability methods was decreased when the COV values were increased from the low variability increment 1 to the high variability increment 4. In addition, the factor of safety did not change significantly when the horizontal correlation length was changed from low to high variability.

- The results of bearing capacity analysis of shallow foundations on medium dense sand (ϕ=38^o) clearly demonstrates a significant decrease in the resistance factor, ϕ_{sf}, of the shallow foundation with the increase in either the COV_ϕ or the distance of foundation from the soil boring.

- For all sandy soils, the results showed that the normalized ultimate bearing capacity decreases with the increasing the COV_ϕ. However, for the dense and medium dense sands, the rate of decrease in normalized ultimate bearing capacity with the increase in COV_ϕ was higher than the loose sand. For all sandy soils, the coefficient of variation of bearing capacity was increased with increasing the COV_ϕ.

- Analysis of bearing capacity of shallow foundations using Fenton and Griffiths [133] method on medium stiff clay for drained condition [$\phi = 30^o$ and cohesion = 83.5 psf (4 kPa)] showed that the ultimate bearing capacity and the resistance factor, ϕ_{sf}, of the shallow foundation decreases with increasing either the COV_ϕ or the distance of foundation from soil boring.

- For all clayey soils under drained condition, analysis showed that the normalized ultimate bearing capacity decreases with increasing the COV_ϕ and/or COV_c. Additionally, the COV of bearing capacity was increased with increasing either the $COV\phi$ or the COV_c.

- Analysis of bearing capacity of shallow foundations on medium stiff clay for undrained condition [cohesion = 752 psf (36 kPa)] also demonstrated significant decrease in the ultimate bearing capacity and the resistance factor, ϕ_{sf}, of the shallow foundation with increasing of either the COV_ϕ or the distance of foundation from soil boring.

- For all clayey soils under undrained condition, the normalized ultimate bearing capacity decreased with increasing the COV_c. Moreover, the COV of the bearing capacity was increased with the increasing the COV_c for all clayey soils.

- For all soil types/conditions, the results showed that the resistance factor, ϕ_{sf}, decreased dramatically as the correlation length increased from 0 to about 6-16 ft. (2-5 m), then started to increase beyond this correlation range. For all sampling radii, the shape of the resistance factor ϕ_{sf}, versus the correlation length curves are similar in the shape.

- The results of reliability analysis for the different scenarios of proportion COVs of friction angle, cohesion, and weight, considered in this study, showed that the reliability index was decreased and the probability of failure was increased when the proportional COVs were increased from increment 1 (low variability) to 5 (high variability), and with increasing the vertical load.

- Analysis of bearing capacity of deep foundations in cohesive soils based on Naghibi's [131] and Naghibi and Fenton [18] approach showed that the ultimate bearing capacity and the resistance factor, ϕ_{df}, decrease with increasing the COV of undrained shear strength, S_u, and with increasing the distance between the pile and soil boring. For the case of multi soil borings. The value of ϕ_{df}, can be calculated for

each soil boring based on the distance of pile from soil borings and calculate the average of all soil borings. Another approach is to calculate the inverse distance weighted values of S_u(IDW) and COV_{Su}(IDW) for the site, and use these values to calculate the resistance factors, ϕ_{df}. For the cohesive soil site at river, the ϕ_{df} corresponding to β=2.33 was calculated to be 0.78.

- For cohesionless soils, the results clearly demonstrates that both the ultimate bearing capacity and the resistance factor, ϕ_{df}, decreased significantly with the increase in COV_{ϕ} and/or the distance between pile and the soil boring.

- For the case of mixed soil condition, the results also showed significant decrease in the ultimate bearing capacity and the resistance factor, ϕ_{df}, with the increase in the COV_{ϕ}, COV_{Su}, and the distance between the pile and soil boring. The ϕ_{df} for multi soil borings in Metairie site was first calculated for each soil boring based the distance between the pile and each soil boring, and then the average of all soil borings was calculated. The ϕ_{df} value for Metairie site was also calculated through evaluating the inverse distance weighted values of S_u(IDW), COV_{Su}(IDW), ϕ(IDW) and COV_{ϕ}(IDW) for the site, which gave a resistance factor, ϕ_{df}, that corresponds to β=2.33 as 0.74.

Recommendations

Based on the results of this research study, the following recommendations are offered to DOTD engineers:

- It is recommended that the DOTD engineers to start assessing and using the variability of soil properties evaluated in the laboratory tests and AMRL for geotechnical engineering analysis and design for different applications.

- Since remolded soil specimens were used in this study, it is recommended in future research to include Shelby-tube specimens to evaluate the variability of soil properties for different laboratory tests.

- It is recommended that the DOTD engineers to start considering the variability of measurements by the different devices (DCP, Geogauge, LFWD, NDG, E-Gauge) in different geotechnical engineering applications.

- Since only three under-construction sections were tested in this study to evaluate the variability of compacted soil. It is recommended to consider testing more under-construction sections in a future study to better evaluate the quality control variability of compacted soil properties and variability of measurements from different in situ testing devices.

- It is highly recommended to implement the semivariorgam analysis to evaluate the site variability from multi CPT tests and/or multi soil borings for use in different geotechnical engineering applications, especially to evaluate the site's resistance factor for designing of deep foundations.

- It is recommended to evaluate and apply the Bayesian analysis method to incorporate site variability for updating the State's resistance factor, as more data are available, and to update the resistance factor for the new specific site.

- It is recommended to explore the applicability of the probabilistic analysis approach to evaluate the specific site variability and its application in geotechnical engineering analysis and design.

- It is highly recommended to consider variability in soil properties in evaluating the slope stability analysis of slopes, embankments and MSE walls.

- It is recommended to evaluate variability in the soil properties of fill materials for better analyzing the slope stability analysis of slopes and MSE walls.
- It is recommend to explore using Fenton and Griffiths [133] method to incorporate the variability in soil properties and distance from soil boring(s) for analysis and design of shallow foundations.
- It is recommend to explore using Naghibi [131] and Naghibi and Fenton [18] method to incorporate the variability in soil properties and distance from soil boring(s) for analysis and design of deep foundations.

Acronyms, Abbreviations, and Symbols

Term	Description
a	Correlation length
AASHTO	American Association of State Highway and Transportation Officials
A_c	Area of cross-section of the cone
ACF	Autocorrelation Function
a_h and a_v	Correlation ranges in horizontal and vertical directions
ALF	Accelerated load facility
AMRL	AASHTO Materials Reference Laboratory
A_n	Area of cross-section and the projected area of the load cell
ANOVA	Analysis of variance
AV	Reproducibility or the operator variability
B	Footing width
c	Cohesion
$\hat{c}$	Weighted average of cohesion
CBR	California bearing ratio
C(h)	Spatial covariance function
C_c	Compression index
CCDF	Conditional cumulative distribution function
cm	Centimeter
Cov	Covariance
COV	Coefficient of variation
COV_c	Coefficient of variation of cohesion
$COV_{R,spatial}$	Spatial coefficient of variation
COV_ϕ	Coefficient of variation of friction angle
CPT	Cone penetration test
C_r	Recompression index
c_v	Coefficient of consolidation
CV_q	Measurement variability
CV_R	Resistance variability

Term	Description
D	Pile diameter
$\bar{d}$	Average distance
d_c, d_q and d_γ	Depth factors
DCP	Dynamic cone penetrometer
DCPI	Dynamic cone penetrometer index
D_f	Depth of footing
DOTD	Department of Transportation and Development
D-SPA	Dirt seismic portable analyzer
d_2	Bias Correction Factor
E	Modulus of elasticity
E_{LFWD}	Surface modulus from LFWD
E_{PLT}	Plate load test modulus
E_{usw}	Young modulus from USW
EV	Repeatability or equipment variability
f	Trend component
f_r	Frequency
$\hat{F}_D$	Dead load (characteristic)
$\hat{F}_L$	Live load (characteristic)
ft.	foot (feet)
FDOT	Florida Department of Transportation
F_{dr}	Force applied by shaker
FEM	Finite element method
FHWA	Federal Highway Administration
FOSM	First-order second-moment
FS	Factor of safety
G	Shear modulus
g	Performance function
GIS	Geographic Information Systems
GRR	Gauge R&R
H	Height

Term	Description
h	Thickness
H_{dr}	Length of the drainage path
IWD	Inverse distance weighted
K	Geogauge stiffness
k	Modulus of subgrade reaction
k_D	Dead load bias factor
K_{flex}	Stiffness of the flexible plate
k_L	Live load bias factor
kN	Kilo newton
kPa	Kilo pascal
ksi	Kip per square inch
K_{soil}	Stiffness of soil
LFWD	Light falling weight deflectometer
L	Length
LAS	Local average subdivision
$\widehat{L_t}$	Characteristic load
LL	Liquid Limit
L_{ph}	Wavelength
LRFD	Load and resistance factor design
LTRC	Louisiana Transportation Research Center
m	meter
mm	Millimeter
MC	micro cracking
m.c.	Moisture content
MCMC	Markov chain Monte Carlo
MPa	Mega Pascal
MSA	Measurement System Analysis
MSE	Mechanically stabilized earth
N_c, N_q and N_γ	Bearing capacity factors
NDG	Nuclear density gauge

Term	Description
OLS	Ordinary Least Squares
P	Applied load on plate
p_f	Probability of failure
p(θ)	Prior distribution
p(y|θ)	Likelihood function
p(θ|y)	Posterior function
PI	Plasticity index
P_c	Preconsolidation pressure
pcf	Pound per cubic foot
PDF	Probability density function
PLT	Plate load tests
PR	Penetration rate
$Prob$	Cumulative probability distribution
P_S	Vertical load
psi	Pound per square inch
psf	Pound per square foot
q	Overburden stress
q_c	Cone tip resistance
Q_D	Dead load
Q_L	Live load
q_t	Corrected tip resistance
q_u	Ultimate bearing capacity
R	Radius
R_{EB}	Unit end bearing capacity
RFEM	Random finite element method
RLEM	Random limit equilibrium method
RBD	Reliability-based design
R_u	Ultimate resistance
$\hat{R}_u$	Resistance of the soil
s_c, s_q and s_γ	Shape factors

Term	Description
SD	Standard deviation
SGeMS	Stanford Geostatistical Modeling Software
SGS	Sequential Gaussian Simulation
SM	Second moment
SPT	Standard penetration test
S_u	Undrained shear strength
SV	Specimen variability
SVF	Semivariogram function
t	Time
TV	Total variation
tsf	Ton per square foot
u_2	Porewater pressure
UU	Unconsolidated undrained
USW	Ultrasonic Surface Wave
V_1	Velocity at rigid plate
V_2	Velocity at flexible plate
V_p	Compression wave velocity
V_{ph}	Average phase velocity
V_R	Surface wave velocity
V_s	Shear wave velocity
z	Depth
W	Influence depth
w_b	Confidence bias site parameter
in.	inch(es)
2D	Two dimensional
α	Empirical correction factor
α_i	Load factor
α_r	Reduction factor
β	Reliability index
β_{HL}	Hasofer-Lind reliability index

Term	Description
δ_c	Center deflection
δ_v	Vertical scale of fluctuation
$\gamma(h)$	Variogram
λ	Mean bias
λ_R	Resistance bias factor
ν	Poison's ratio
ε	Random component
ϕ	Friction angle
$\overline{\phi}$	Equivalent friction angle
Φ_{df}	Resistance factor for deep foundation
ϕ_{method}	Resistance factor for the design method
ϕ_R	Resistance factors
Φ_{sf}	Resistance factor for shallow foundation
μ	Mean
μ_D	Mean of the dead load
μ_L	Mean of the live load
Γ^2	Variance reduction factor
γ	Unit soil weight
$\gamma_{lnc}(D)$	Variance reduction factor
ψ	Phase difference
ρ	Mass density
$\rho(h)$	Spatial correlation function
σ	Standard deviation
σ_{app}	Applied stress
σ_w	Inherent soil variability
θ	Scale of fluctuation

References

[1] S. Kumar, R. Lal and D. Liu, "A geographically weighted regression kriging approach for mapping soil organic carbon stock," *Geoderma,* Vols. 189-190, p. 627–634, 2012.

[2] S. Zhang, Y. Huang, C. Shen, H. Ye and Y. Du, "Spatial prediction of soil organic matter using terrain indices and categorical variables as auxiliary information," *Geoderma,* vol. 171–172, p. 35–43, 2012.

[3] H. Ye, C. Shen, Y. Huang, W. Huang, S. Zhang and X. Jia, "Spatial variability of available soil microelements in an ecological functional zone of Beijing," *Environmental Monitoring and Assessment,* vol. 187, no. 2, pp. 1-12, 2015.

[4] S. Lacasse and F. Nadim, "Uncertainties in characterising soil properties," *Geotechnical Special Publication,* vol. 58, pp. 49-75, 1996.

[5] T. Elkateb, R. Chalaturnyk and P. Robertson, "An Overview of Soil Heterogeneity: Quantification and Implications on Geotechnical Field Problems," *Canadian Geotechnical Journal,* vol. Vol. 40, pp. 1-15, 2003.

[6] K. K. Phoon and F. H. Kulhawy, "Characterization of geotechnical variability," *Canadian Geotechnical Journal,* vol. 36, no. 4, pp. 612-624, 1999.

[7] K. K. Phoon and F. H. Kulhawy, "Evaluation of Geotechnical Property Variability," *Canadian Geotechnical Journal,* vol. 36, no. 4, pp. 625-639, 1999.

[8] G. B. Baecher and J. T. Christian, Reliability-Based Design in Geotechnical Engineering: Computations and Applications, London: CRC Press, 2008.

[9] A. S. Fotheringham, "Spatial analysis in GIS. Spat Anal GIS," *Spat Anal GIS,* vol. 181, 1994.

[10] L. A., W. J. and Q. X., "Multivariate and geostatistical analyses of the spatial distribution and origin of heavy metals in the agricultural soils in Shunyi, Beijing, China," *Sci Total Environ,* vol. 425, p. 66–74, 2012.

[11] F. Moore, V. Sheykhi, M. Salari and A. Bagheri, "Soil quality assessment using GIS-based chemometric approach and pollution indices, Nakhlak mining district, Central Iran," *Environ Monit Assess,* vol. 188, no. 2, 2016.

[12] P. Goovaerts, A. Soares, G. H. and R. Froidevaux, "Kriging vs stochastic simulation for risk analysis in soil contamination," in *GeoENV I geostatistics Environ Appl Proceedings*, Lisbon, Port, 1996.

[13] S. Onyejekwe, X. Kang, L. Ge and R. Stephenson, "Variability Analysis of Undrained Shear Strength for Reliability-Based Design," in *Geo-Frontiers 2011, Advances in Geotechnical Engineering, GSP 211*, Dallas, Texas, 2011.

[14] M. McVay, H. Klammler, D. Bloomquist, J. Otero and M. Faraone, "Modifications of LRFD Resistance Factors Based on Site Variability," FDOT Report BD545-76, Florida Department of Transportation, Tallahassee, FL, 2009.

[15] J. K. Otero, . Development of a rational design approach (LRFD phi) for drilled shafts considering redundancy, Gainesville, Florida: PhD Dissertation, University of Florida, 2007.

[16] M. A. Faraone, Geostatistical analysis for reliability based design of foundations, Gainesville, Florida: PhD dissertation, University of Florida, 2014.

[17] G. A. Fenton and D. V. Griffiths, "Bearing-capacity prediction of spatially random c − φ soils," *Canadian Geotechnical Journal,* vol. 40, pp. 54-65, 2003.

[18] N. Naghibi and F. Fenton, "Geotechnical resistance factors for ultimate limit state design of deep foundations in cohesive soils," *Canadian Geotechnical Journal,* vol. 48, no. 11, p. 1729–1741, 2011.

[19] D. V. Griffiths and G. A. Fenton, "Probabilistic Slope Stability Analysis by Finite Elements," *J. Geotech. Geoenviron. Eng,* vol. 5, pp. 507-518, 2004.

[20] D. V. Griffiths and R. M. Marquez, "Three-dimensional slope stability analysis by elasto-plastic finite element," *Geotechnique,* vol. 57, no. 4, pp. 537-546, 2007.

[21] S. Jiang, D. Li, L. Zhange and C. Zhou, "Slope reliability analysis considering spatially variable shear strength parameters using a non-intrusive stochastic finite element method," *Engineering Geology,* vol. 168, pp. 120-128, 2014.

[22] L. Bjerrum, A. Casagrande, R. B. Peck and S. A., From Theory to Practice in Soil Mechanics; Selection from the Writings of Karl Terzaghi, Wiley, 425 pp., 1960.

[23] G. A. Fenton and E. H. Vanmarcke, "Simulation of Random Field via Local Average Subdivision," *Journal of Engineering Mechanics,* vol. 116, no. 8, pp. 1733-1749, 1990.

[24] D. V. Griffiths, G. A. Fenton and H. R. Ziemann, "Seeking Out Failure: The Random Finite Element Method RFEM in Probabilistic Geotechnical Analysis," in *GeoCongress: Geotechnical Engineering in the Information Technology Age, Proceedings of Mini-Symposium on Numerical Modeling and Analysis*, Atlanta, Georgia, 2006.

[25] R. V. Whitman, "Organizing and Evaluating Uncertainty in Geotechnical Engineering," in *In Uncertainty in the Geological Environment: From Theory to Practice, Geotechnical Special Publication No. 58*, New York, 1996.

[26] DNV, "Recommended Practice: Statistical Representation of Soil Data (DNV-RPC207)," Det Norske Veritas, Hovik, Norway, 2007.

[27] A. L. Jones, S. L. Kramer and P. Arduino, "Estimation of Uncertainty in Geotechnical Properties for Performance-Based Earthquake Engineering," PEER Report 2002-16. : Pacific Earthquake Engineering Center, Berkeley, CA, 2002.

[28] E. H. Vanmarcke, "Probabilistic Modeling of Soil Profiles," *Journal of Geotechnical Engineering,* vol. 103, no. 11, p. 1227 – 1246, 1997.

[29] M. B. Jaksa, W. S. Kaggwa and P. I. Brooker, "Experimental Evaluation of the Scale of Fluctuation of a Stiff Clay," in *Proceedings of the 8th International Conference on Applications of Statistics and Probability to Soil and Structural Engineering*, Rotterdam: Balkema, 2000.

[30] G. .. Baecher, "Statistical methods in site characterization," in *Proceedings of the Engineering Foundation Conference on Updating Subsurface Exploration and Testing for Engineering Purposes*, Santa Barbara, CA, 1982.

[31] H. H. Einstein and G. B. Baecher, "Probabilistic and Statistical Methods in Engineering Geology," *Rock Mechanics and Rock Engineering,* vol. 16, no. 1, pp. 39-72, 1983.

[32] G. B. Baecher, Site Exploration: A Probabilistic Approach, Massachusetts Institute of Technology, Massachusetts Institute of Technology: Thesis work in completion of PhD, 515 p., 1972.

[33] G. B. Baecher, "Simplified geotechnical data analysis," *In Reliability Theory and Its Application in Structural and Soil Mechanics,* pp. 257-277, 1983.

[34] G. Baecher, "Error Analysis for Geotechnical Engineering," US Army Corps of Engineers, GL-87-3, 126 pp, 1987.

[35] J. T. Christian, C. C. Ladd and G. B. Baecher, "Reliability Applied to Slope Stability Analysis,," *Journal of Geotechnical Engineering,* vol. 120, no. 12, pp. 2180-2207, 1994.

[36] G. B. Baecher and J. T. Christian, Reliability and Statistics in Geotechnical Engineering, New York: John Wiley, 2003.

[37] I. Hacking, The Emergence of Probability, , 246 pp., Cambridge, UK: Cambridge University Press, 1975.

[38] K. K. Phoon and F. H. Kulhawy, "On Quantifying Inherent Soil Variability," *Geotechnical Special Publication,* vol. 58, pp. 326-340, 1996.

[39] E. Vanmarcke, Random Fields: Analysis and Synthesis, World Scientific, 347 pp., 2010.

[40] G. A. Fenton, "Estimation for Stochastic Soil Models," *Journal of Geotechnical and Geoenvironmental Engineering,* vol. 125, no. 6, pp. 470-485, 1999.

[41] G. A. Fenton, "Random Field Modeling of CPT Data," *Journal of Geotechnical and Geoenvironmental Engineering,* vol. 125, no. 6, pp. 486-498, 1999.

[42] H. Kim, Spatial variability in soils: stiffness and strength, Atlanta, GA: Georgia Institute of Technology, 2005.

[43] S. Nazarian, M. Mazari, I. Abdallah, A. Puppala, L. Mohammad and M. Abu-Farsakh, "Modulus-based construction specification for compaction of earthwork and unbound aggregate," Transportation Research Board, Washington, DC, 2015.

[44] E. Vanmarcke, "Random fields: analysis and synthesis," *Bull. Amer. Math. Soc,* vol. 13, pp. 57-62, 1985.

[45] M. Down, F. Czubak, G. Gruska, S. Stahley and D. Benham, "Measurement System Analysis - Reference Manual:," Ford Motor Company, General Motors Corporation, United States, 2010.

[46] C. J. Orchant, F. H. Kulhawy and C. H. Trautmann, "Critical evaluation of in-situ test methods and their variability," Electric Power Research Institute, Report EL-5507, vol. 2., Palo Alto, 1988.

[47] F. H. Kulhawy and C. H. Trautmann, "Estimation of in-situ test uncertainty," in *Uncertainty in the geologic environment: From theory to practice*, 1996.

[48] M. Uzielli, S. Lacasse, F. Nadim and K. K. Phoon, "Soil Variability Analysis for Geotechnical Practice," in *Proceedings of the 2nd International Workshop on Characterisation and Engineering Properties of Natural Soils*, Singapore, 2007.

[49] L. Rethati, Probabilistic Solutions in Geotechnics, Amsterdam: Elsevier, 1988.

[50] D. J. DeGroot, "Analysing Spatial Variability of In Situ Soil Properties," in *In Uncertainty in the Geological Environment: From Theory to Practice, Geotechnical Special Publication*, C. D. Shackleford, P. P. Nelson, and M. J. S. Roth, 1996.

[51] F. H. Kulhawy and P. W. Mayne, "Manual on Estimating Soil Properties for Foundation Design, Report No. EL-6800," Electric Power Research Institute, Palo Alto, CA, 1990.

[52] H. El-Ramly, N. R. Morgenstern and D. M. Cruden, "Probalistic Slope Stability Analysis for Practice," *Canadian Geotechnical Journal,* vol. 39, pp. 665-683, 2002.

[53] I. Clark, Practical Geostatistics, LOndon: Applied Science, 1979.

[54] S. Onyejekwe, Characterization of soil variability for reliability-based design, Rolla, Missouri: Missouri University of Science and Technology, 2012.

[55] J. M. Duncan, "Factors of safety and reliability in geotechnical engineering," *Journal of geotechnical and geoenvironmental engineering,* vol. 126, no. 4, pp. 307-316, 2000.

[56] M. Bustamante and L. Gianeselli, "Pile bearing capacity prediction by means of static penetrometer CPT," in *Proceedings of the 2nd European Symposium on Penetration Testing*, 1982.

[57] M. Amirmojahedi and M. Abu-Farsakh, "Evaluation of 18 Direct CPT Methods for Estimating the Ultimate Pile Capacity of Driven Piles," *Transportation Research Record,* vol. 2673, no. 9, p. 127–141, 2019.

[58] S. Paikowsky, M. McVay, T. Nguyen, K. Steneren, K. O'Malley, L. Chernauskas and M. O"Neil, "Load and resistance factor design (LRFD) for deep foundations," Transportation Research Board, Washington, DC US, 2004.

[59] J. Withiam, E. Voytko, J. Duncan, R. Barker, B. Kelly, S. Musser and V. Elias, "NHI Course No. 132068, Load and Resistance Factor Design (LRFD) for Highway Bridge Substructures, Reference Manual and Participant Workbook," FHWA, Office of Technology Applications, Washington, DC, 1998.

[60] R. A. Fisher, Statistical Methods for Research Workers, New York, NY: Springer, 1970.

[61] J. O. Berger and R. L. Wolpert, The Likelihood Principle, Hayward, CA: Institute of Mathematical Statistics, 1988.

[62] A. W. Edwards, Likelihood, Baltimore, MD: Johns Hopkins University Press, 1992.

[63] P. S. Bandyopadhyay and M. R. Forster, Philosophy of Statistics, Amsterdam, Netherlands: Elsevier, 2011.

[64] L. Zhang, "Reliability verification using proof pile load tests," *Journal of Geotechnical and Geoenvironmental Engineering,* vol. 130, no. 11, p. 1203–121, 2004.

[65] G. B. Baecher and R. Rackwitz, "Baecher, G. B., & Rackwitz, R. (1982). Factors of safety and pile load tests," *International Journal for Numerical and Analytical Methods in Geomechanics,* vol. 6, no. 4, p. 409–424, 1982.

[66] J. H. Park, D. Kim and C. K. Chung, "Implementation of Bayesian theory on LRFD of axially loaded driven piles," *Computers and Geotechnics,* vol. 42, p. 73–80, 2012.

[67] A. H. Ang and W. H. Tang, Probability concepts in engineering planning and design (Issue BOOK)., Hoboken, NJ: Wiley, 1984.

[68] R. W. Cheung and W. H. Tang, "Realistic assessment of slope reliability for effective landslide hazard mangement," *Geotechnique,* vol. 55, no. 1, p. 85–94, 2005.

[69] W. H. Tang and R. B. Gilbert, "Case study of offshore pile system reliability," in *Offshore Technology Conference*, Houston, Texas, 1993.

[70] S. Lacasse and F. Nadim, "Reliability issues and future challenges in geotechnical engineering for offshore structures," *International Journal of Rock Mechanics and Mining Sciences and Geomechanics Abstracts,* vol. 8, no. 32, p. 400A, 1995.

[71] R. B. Gilbert and W. H. Tang, "17. (1995). Model uncertainty in offshore geotechnical reliability," in *Offshore Technology Conference*, Houston, Texas, 1995.

[72] C. H. Juang, S. H. Yang and H. Yuan, "Model uncertainty of shear wave velocity-based method for liquefaction potential evaluation," *Journal of Geotechnical and Geoenvironmental Engineering,* vol. 131, no. 10, p. 1274–1282, 2005.

[73] L. Zhang, Probabilistic study of slope stability under rainfall condition, Hong Kong: Hong Kong University of Science and Technolog, 2005.

[74] J. Ching, H. D. Lin and M. T. Yen, "Model selection issue in calibrating reliability-based resistance factors based on geotechnical in-situ test data," *Structural Safety,* vol. 31, no. 5, p. 420–431, 2009.

[75] A. Etz, "Introduction to the concept of likelihood and its applications," *Advances in Methods and Practices in Psychological Science,* vol. 1, no. 1, p. 60–69, 2018.

[76] Y. Wang, K. Huang and Z. Cao, "Probabilistic identification of underground soil stratification using cone penetration tests," *Canadian Geotechnical Journal,* vol. 50, no. 7, p. 766–776, 2013.

[77] Y. Wang and Z. Cao, "Probabilistic characterization of Young's modulus of soil using equivalent samples," *Engineering Geology,* vol. 159, p. 106–118, 2013.

[78] G. B. Baecher and J. T. Christian, Reliability and statistics in geotechnical engineering, Hoboken, NJ: John Wiley & Sons, 2005.

[79] Z. Cao, Y. Wang and D. Li, "Quantification of prior knowledge in geotechnical site characterization," *Engineering Geology,* vol. 203, p. 107–116, 2016.

[80] D. Sivia and J. Skilling, Data analysis: a Bayesian tutorial, Oxford, UK: Oxford University Press, 2006.

[81] Y. Wang, Z. Cao and D. Li, "Bayesian perspective on geotechnical variability and site characterization," *Engineering Geology,* vol. 203, p. 117–125, 2016.

[82] A. Abdideh and M. Ghasemi, "A comparison of various statistical and geostatistical methods in estimating the geomechanical properties of reservoir rocks," *Petroleum Science and Technology,* vol. 32, no. 9, pp. 1058-1064, 2014.

[83] V. Elumalai, K. Brindha, B. Sithole and E. Lakshmanan, "Spatial interpolation methods and geostatistics for mapping groundwater contamination in a coastal area," *Environmental Science and Pollution Research,* vol. 24, no. 2, pp. 11601-11617, 2017.

[84] S. Zarco-Perello and N. Simões, "Ordinary kriging vs inverse distance weighting: Spatial interpolation of the sessile community of Madagascar reef, Gulf of Mexico," *PeerJ,* vol. 30, no. 5, 2017.

[85] H. Ozturk and M. Erkayaoglu, "Interpretation of variability of rock mass rating by geostatistical analysis: A case study in Western Turkey," *Arabian Journal of Geosciences,* vol. 11, no. 13, 2018.

[86] F. Veronesi, R. Corstanje and T. Mayr, "Mapping soil compaction in 3D with depth functions," *Soil and Tillage Research,* vol. 124, pp. 111-118, 2012.

[87] I. Aghamolaie, G. Lashkaripour, M. Ghafoori and N. Moghaddas, "3D geotechnical modeling of subsurface soils in Kerman city, southeast Iran," *Bulletin of Engineering Geology and the Environment,* vol. 78, no. 3, pp. 1385-1400, 2018.

[88] C. Zhang and W. Li, "Regional-scale modelling of the spatial distribution of surface and subsurface textural classes in alluvial soils using Markov chain geostatistics," *Soil Use and Management,* vol. 24, no. 3, pp. 263-272, 2008.

[89] Y. Leung, W. Liu, Y. Lei and S. Hsu, "Quantifying cost-effectiveness of subsurface strata exploration in excavation projects through geostatistics and spatial tessellation," *Automation in Construction,* vol. 90, pp. 243-252, 2018.

[90] H. Kim, C. Chung and H. Kim, "Geo-spatial data integration for subsurface stratification of dam site with outlier analyses," *Environmental Earth Sciences,* vol. 75, no. 2, pp. 1-10, 2016.

[91] D. Krige, "A Statistical Approaches to Some Basic Mine Valuation Problems on the Witwatersrand," *Journal of the Chemical, Metallurgical and Mining Society of South Africa,* vol. 52, pp. 119-139, 1951.

[92] R. Webster and M. Oliver, Geostatistics for Environmental Scientists Statistics in Practice, Chichester, United Kingdom: Wiley, 2001.

[93] C. Cambardella, M. T., P. T., K. D., N. J., T. R. and K. A., "Field-Scale Variability of Soil Properties in Central Iowa Soils," *Soil Science Society of America Journal,* vol. 58, no. 5, 1994.

[94] P. Burrough and R. McDonnell, Principles of Geographical Information Systems, Oxford, UK: Oxford University Press, 1998.

[95] N. Facas, A. Michael and F. Reinhard, "Anisotropy in the Spatial Distribution of Roller-Measured," *International Journal of Geomechanics,* vol. 10, no. 4, pp. 129-135, 2010.

[96] I. Clark and W. Harper, Practical Geostatistics 2000, Ohio, USA., 2001.

[97] ESRI, "Understanding ordinary kriging-ArcGIS Pro | ArcGIS Desktop," <http://pro.arcgis.com/en/pro-app/help/analysis/geostatistical-analyst/understanding-ordinary-kriging.htm> , 2018.

[98] M. Pinheiro, X. Emery, T. Miranda, L. Lamas and M. Espada, "Modelling geotechnical heterogeneities using geostatistical simulation and finite differences analysis," *Minerals,* vol. 8, no. 5, 2018.

[99] R. Dimitrakopoulos, " Conditional simulation algorithms for modelling orebody uncertainty in open pit optimization," *International Journal of Surface Mining, Reclamation and Environment,* vol. 12, no. 4, pp. 173-179, 1998.

[100] X. Emery, "Properties and limitations of sequential indicator simulation," *Stochastic Environmental Research and Risk Assessment,* vol. 18, no. 6, pp. 414-424, 2004.

[101] H. Rahimi, O. Asghari and F. Hajizadeh, "Selection of optimal thresholds for estimation and simulation based on indicator values of highly skewed distributions of ore data," *Natural Resources Research,* vol. 27, no. 4, pp. 437-453, 2018.

[102] A. Journel and C. Huijbregts, Mining Geostatistics, London, UK: Academic Press, 1978.

[103] G. Fenton, "Probabilistic methods in geotechnical engineering," in *ASCE GeoLogan'97 Conference*, Logan, Utah, 1997.

[104] E. Isaaks and R. Srivastava, An Introduction to Applied Geostatistics, Oxford, UK: Oxford University, 1989.

[105] P. Dowd, "A review of recent developments in geostatistics," *Computers and Geosciences,* vol. 17, no. 10, pp. 1481-1500, 1991.

[106] C. Deustch and A. Journel, GSLIB, Geostastical Software Library and user's guide, Oxford, UK: Oxford Univ. Press, 1992.

[107] P. Goovaerts, Geostatistics for Natural Resources Evaluation, Oxford, UK: Oxford University Press, 1997.

[108] H. Li, Z. Lin and S. Liu, "Application of Kriging technique in estimating soil moisture in China. Geographical Research," *Geographical Research,* vol. 20, no. 4, p. 446–452, 2001.

[109] H. Gan and L. Peng, "Spatial variability of nutrients in cultivated soils of Xinhui District, Jiangmen City," *Chinese Journal of Applied Ecology,* vol. 16, no. 8, p. 1437–1443, 2005.

[110] M. Delbari, P. Afrasiab and W. Loiskandl, "Using sequential Gaussian simulation to assess the field-scale spatial uncertainty of soil water content," *Catena,* vol. 79, p. 163–69, 2009.

[111] G. Szatmári, K. Barta, A. Farsang and L. Pásztor, "Testing a sequential stochastic simulation method based on regression kriging in a catchment area in Southern Hungary," *Geologia Croatica,* vol. 68, no. 3, pp. 273-283, 2015.

[112] D. Griffiths and G. Fenton, "Influence of soil strength spatial variability on the stability of an undrained clay slope by finite elements. In Slope stability 2000 (pp. 184-193).," in *Geo-Denver 2000*, Denver, Co., 2000.

[113] L. Li, Y. Wang and Z. Cao, "Probabilistic slope stability analysis by risk aggregation," *Engineering Geology,* vol. 176, pp. 57-65, 2014.

[114] S. Jiang, D. Li, Z. Cao, C. Zhou and K. Phoon, "Efficient system reliability analysis of slope stability in spatially variable soils using Monte Carlo simulation," *Journal of Geotechnical and Geoenvironmental Engineering,* vol. 141, no. 2, 2015.

[115] S. Javankhoshdel, N. Luo and R. Bathurst, "Probabilistic analysis of simple slopes with cohesive soil strength using RLEM and RFEM," *Georisk: Assessment and Management of Risk for Engineered Systems and Geohazards,* vol. 11, no. 3, pp. 231-246, 2017.

[116] Y. Cheng and C. Lau, Slope stability analysis and stabilization; new methods and insight, London, UK: Scitech Book News, 2008.

[117] E. Shamekhi and D. Tannant, "Probabilistic assessment of rock slope stability using response surfaces determined from finite element models of geometric realizations," *Computers and Geotechnics,* vol. 69, pp. 70-81, 2015.

[118] L. Lu, Z. Wang, M. Song and K. Arai, "Stability analysis of slopes with ground water during earthquakes," *Engineering Geology,* vol. 193, pp. 288-296, 2015.

[119] K. Shou and C. Wang, "Analysis of the Chiufengershan landslide triggered by the 1999 Chi-Chi earthquake in Taiwan," *Engineering Geology,* vol. 68, no. 3-4, pp. 237-250, 2003.

[120] D. Leynaud and N. Sultan, "3-D slope stability analysis: a probability approach applied to the nice slope (SE France)," *Marine Geology,* vol. 269, no. 3, pp. 89-106, 2010.

[121] J. Stankovic, S. Filipovic, R. Rajkovic, L. Obradovic, V. Marinkovic and R. Kovacevic, "Risk and reliability analysis of slope stability deterministic and

probabilistic method," *Trends in the Development of Machinery and Associated Technoloy,* vol. 17, no. 1, pp. 11-26, 2013.

[122] D. Griffiths and G. Fenton, "Bearing capacity of spatially random soil: the undrained clay Prandtl problem revisited," *Geotechnique,* vol. 51, no. 4, pp. 351-359, 2001.

[123] G. Fenton, D. Griffiths and X. Zhang, "Load and resistance factor design of shallow foundation against bearing capacity," *Canadian Geotechnical Journal,* vol. 45, pp. 1556-1571, 2008.

[124] K. Terzaghi, Theoretical soil mechanics., New York, NY: Wiley, 1943.

[125] G. Fenton, "Estimation for stochastic soil models," *Journal of Geotechnical and Geo Environmental Engineering,* vol. 125, no. 6, p. 470–485, 1999.

[126] D. Griffiths and I. Smith, Numerical Methods for Engineers. (2nd Ed.), Boca Raton, FL: Chapman & Hall/CRC Press Inc., 2006.

[127] G. Fenton, X. Zhang and D. Griffiths, "Reliability of shallow foundations designed against bearing failure using LRFD.," *Georisk,* vol. 1, no. 3, pp. 202-215, 2007.

[128] O. Ditlevsen, Uncertainty modeling with applications to multidimensional civil engineering systems, New York: McGraw-Hill International Book Company, 1981.

[129] B. Lafifi and A. Rouaiguia, "Investigation of reliability analysis of shallow foundation by combining Hasofer-Lind index, response surface methodology and multi-objective genetic algorithm," *International Journal of Reliability and Safety,* vol. 15, no. 1-2, pp. 18-36, 2021.

[130] G. Fenton and D. Griffiths, "Reliability-based deep foundation design," *Geotechnical Special Publication 170. Probabilistic Applications in Geotechnical Engineering,* pp. 1-2, 2007.

[131] M. Naghibi, Geotechnical resistance factors for ultimate limit state design of deep foundations under axial compression loading, MS Thesis: Dalhousie University, Halifax, Nova Scotia., 2010.

[132] P. Hannigan, G. Goble, G. Thendean, G. Likins and F. Rausche, "Design and construction of driven pile foundations-volume I. Report No. FHWA-NHI-16-009," Federal Highway Administration, Washington, DC, 1998.

[133] G. Fenton and V. Griffiths, Risk assessment in geotechnical engineering. John Wiley & Sons New Jersey., 2008.

[134] Z. Zhang and M. Tumay, "Statistical to Fuzzy Approach Toward CPT Soil Classifcation," *Journal of Geotechnical and Geoenvironmental Engineering,* vol. 125, no. 3, p. 179–186, 1999.

[135] P. Robertson, "Soil classification using the cone penetration test," *Canadian geotechnical journal,* vol. 27, no. 1, pp. 151-158, 1990.

[136] A. International, Standard test method for deep foundations under static axial compressive load, ASTM International, 2013.

[137] M. Davisson, "High capacity piles," Proc. Innovations in Found. Const., 1972.

[138] M. Amirmojahedi, "Estimation of the axial and lateral capacity of driven piles from the results of cone penetration test and finite element analysis," Ph.D. Dissertation. Louisiana State University, Baton Rouge, LA, 2020.

[139] J. Goodman and J. Weare, "Ensemble samplers with affine invariance," *Communications in Applied Mathematics and Computational Science,* vol. 51, no. 1, p. 65–80, 2010.

[140] A. Grinsted, GWMCMC: An implementation of the Goodman and Weare MCMC sampler for MATLAB, GitHub Repository., 2015.

[141] M. Shahin and E. Cheung, "Stochastic design charts for bearing capacity of strip footings," *Geomechanics & engineering,* vol. 3, no. 2, pp. 153-167, 2011.

[142] A. Skempton, "The bearing capacity of clays," *Selected papers on soil mechanics,* pp. 50-59, 1951.

[143] I. Ghaaowd, A. Faisal, M. H. Rahman and M. Abu-Farsakh, "Evaluation of Site Variability Effect on the Geotechnical Data and Its Application," *Geotechnical Testing Journal,* vol. 44, no. 4, pp. 971-985, 2020.

[144] A. Gelman, D. Simpson and M. Betancourt, "The prior can often only be understood in the context of the likelihood," *Entropy,* vol. 19, no. 10, p. 555, 2017.

[145] S. Fiedler, M. Main and A. DiMillio, "In-place stiffness and modulus measurements," in *Specialty Conference on Performance Confirmation of Constructed Geotechnical Facilities*, 2000.

[146] Humboldt Mfg., "Humboldt soil stiffness gauge (Geogauge) user guide: version 3," Humboldt Mfg. Co., Elgin, Illinois, 1999.

[147] A. Benedetto, F. Tosti and L. Di Domenico, "Elliptic model for prediction of deflections induced by a Light Falling Weight Deflectometer," *Journal of Terramechanics,* vol. 49, no. 1, pp. 1-12, 2012.

[148] Y. Huang, "Pavement analysis and design. Prentice-Hall, Inc. Englewood Cliffs, `New Jersey.," Prentice-Hall, Inc., Englewood Cliffs, New Jersey, 1993.

[149] E. Kleyn, J. Maree and P. Savage, "The Application of a Portable Pavement Dynamic Cone Penetrometer to Determine In Situ Bearing Properties of Road Pavement Layers and Subgrades in South Africa., (No. Monograp," in *Transportation Research Board*, Washington, D.C., 1982.

[150] A. Ahsan, Pavement performance monitoring using Dynamic Cone Penetrometer and Geogauge during construction (Master's Thesis), Arlington, TX: The University of Texas at Arlington, 2015.

[151] R. Embacher, "Duration of spring thaw recovery for aggregate-surfaced roads," *mbacher, R. A. (2006). Duration of spring thaw recovery for aggregate-surfaced roads. Transportation research record, 1967(1), 27-35. ,* vol. 1967, no. 1, pp. 27-35, 2006.

[152] L. Mohammad, A. Herath, M. Abu-Farsakh, K. Gaspard and R. Gudishala, "Prediction of resilient modulus of cohesive subgrade soils from dynamic cone penetrometer test parameters," *Journal of Materials in Civil Engineering,* vol. 19, no. 11, pp. 986-992, 2007.

[153] A. Rodriguez, H. Castillo and G. Sowers, "Soil mechanics in highway engineering.," Clausthal-Zeellerfeld, Federal Republic of Germany: Trans Tech Publications, Germany, 1988.

[154] E. Yoder and M. Witczak, Principles of pavement design, New York, NY: John Wiley & Sons, 1975.

[155] M. Abu-Farsakh, K. Alshibli, M. Nazzal and E. Seyman, "Assessment of in-situ test technology for construction control of base courses and embankments," Report No, FHWA/LA.04/389, Louisiana Transportation Research Center, Baton Rouge, LA, 2004.

[156] D. Chen, W. Wu, R. He, J. Bilyeu and M. Arrelano, "Evaluation of in-situ resilient modulus testing techniques," *Geotechnical Special Publicatio,* vol. 86, pp. 1-11, 1999.

[157] G. R. Development, "PSPA & SPA Manager Manua," El Paso, TX, 2007.

[158] S. Nazarian, D. Yuan and V. Tandon, "Structural field testing of flexible pavement layers with seismic methods for quality control," *Transportation Research Record,* vol. 1654, no. 1, pp. 50-60, 1999.

[159] S. Nazarian, Y. D., T. V. and A. M., "Quality management of flexible pavement layers with seismic methods. Center for Transportation Infrastructure Systems," Research Report 0-1735-3. The University of Texas at El Paso, El Paso, TX, 2005.

[160] H. Azari, S. Nazarian and D. Yuan, "Assessing sensitivity of impact echo and ultrasonic surface waves methods for nondestructive evaluation of concrete structures," *Construction and Building Materials,* vol. 74, pp. 384-391, 2014.

[161] M. Sansalone and W. Streett, "Impact-Echo Condition Assessment of Structures," *Structural Engineering International,* vol. 6, no. 4, pp. 282-4, 1996.

[162] I. Troxler Electronic Laboeratories, "Manual of Operation and Instruction, Model 3430 Plus and 3440 Plus Surface Moisture-Density Gauge," Tro, Research Triangle Park, NC, 2009.

[163] J. Krahn, "The 2001 R.M. Hardy Lecture: The Limits of Limit Equilibrium Analyses," *Canadian Geotechnical Journal,* vol. 40, pp. 643-660, 2003.

[164] J. Duncan, S. Wright and T. Brandon, Soil strength and slope stability, New York, NY: John Wiley & Sons, 2014.

[165] W. Fellenius, "Calculation of stability of earth dam. In Transactions," in *2nd Congress Large Dams*, Washington, DC, 1936.

[166] E. Spencer, "A method of analysis of the stability of embankments assuming parallel inter-slice forces," *Geotechnique,* vol. 17, no. 1, pp. 11-26, 1967.

Appendix A

In-Box and Field Testing Devices

This section covers the review of all devices (i.e. Geogauge, Light Falling Weight Deflectometer, Dynamic Cone Penetrometer, Dirt Seismic Portable Analyzer, Plate Load Test, Nuclear Density Gauge and E-Gauge) used in this research study for in-box and field tests.

Geogauge Device

The Geogauge device, or Soil Stiffness Gauge, is a hand-held portable device that renders rapid and precise means of measuring soil stiffness and soil modulus. The development of this device was initiated by the Federal Highway Administration (FHWA) and the U.S. Department of Defense to locate buried landmines. The FHWA research program including the cooperation between Bolts, Beranek and Newman of Cambridge, MA, CNA consulting engineers of Minneapolis, MN and Humboldt introduced the Soil Stiffness Gauge (SSG) known as Geogauge [145], which is presented in Figure 123.

Figure 123. Geogauge device

The Geogauge device measures the in-situ stiffness of compacted soil at a rate of about 1.5 minutes per test. It has an annular ring that connects soil with an outside diameter of 4.50 in. (114 mm), an inside diameter of 3.50 in. (89 mm), and a thickness of 0.50 in. (13 mm).

Principle of Operation

The Geogauge device applies a dynamic force to the soil, which generates very small displacement (< 1.27 x 10^{-6} m or <.00005") at 25 steady state frequencies in 4 Hz increments between 100 and 196 Hz. The stiffness is determined at each frequency and the average is displayed. The entire process takes about 1½ minutes. It is designed in a way that the highway traffic will not have influence on its measurement as the frequency generated by traffic is as low as 30 Hz, which is below the operating frequency of Geogauge [146].

The shaker applies a small force, and this force is transferred to the ground, which is measured by differential displacement across the flexible plate by two velocity sensors (Figure 124). The expression can be expressed as follows:

$$F_{dr} = K_{flex} \times (X_2 - X_1) = K_{flex} \times (V_2 - V_1) \quad [A1]$$

where F_{dr} = force applied by shaker; K_{flex} = stiffness of the flexible plate; X_1 = displacement at rigid plate; X_2 = displacement at flexible plate; V_1 = velocity at rigid plate; and V_2 = velocity at flexible plate

Each compacted layer in a construction site can be thought of being a spring, which distributes the load to the lower layers. As for the springs:

$$K_{soil} = \frac{F_{dr}}{X1} \quad [A2]$$

where K_{soil} = stiffness of soil

Now, the soil stiffness can be expressed as:

$$K_{soil} = K_{flex} \left\{ \sum_1^n \frac{\frac{(X2-X1)}{X1}}{n} \right\} = K_{flex} \left\{ \sum_1^n \frac{\frac{(V2-V1)}{V1}}{n} \right\} \quad [A3]$$

where n is the number of frequencies.

Figure 124. Schematic of the Geogauge [146]

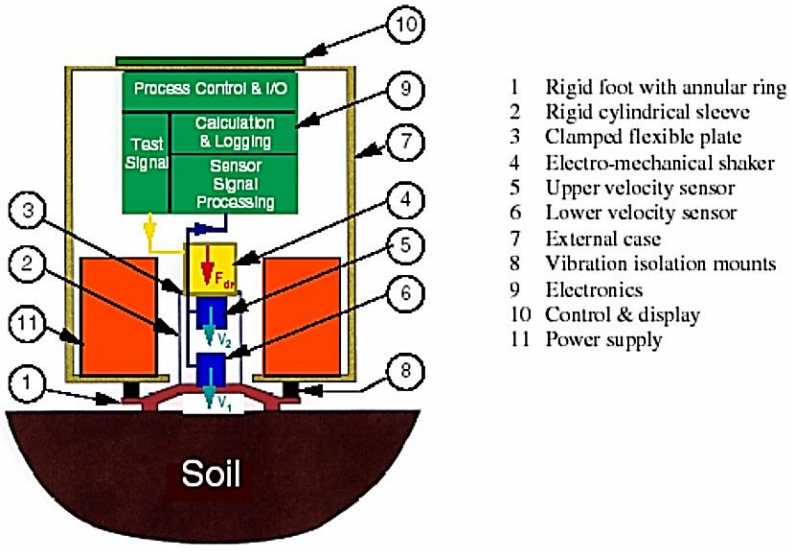

Geogauge Stiffness and Soil Modulus

The elastic modulus of soil can be calculated from the measured Geogauge stiffness. If the soil is a linear elastic, homogeneous and isotropic half space, the relationship between the Geogauge stiffness and soil elastic modulus can be presented as:

$$K=\frac{ER}{(1-\nu^2).\ \omega(n)} \qquad [A4]$$

where E = modulus of elasticity; ν = Poison's ratio; R = outside radius of the annular ring (2.25 in.); and ω(n) = a function of the ratio of the inside diameter and the outside diameter of the annular ring.

From the geometry of Geogauge, the value of ω (n) is equal to 0.565. So,

$$K=\frac{1.77ER}{(1-\nu^2)} \qquad [A5]$$

Stiffness is measured with the Geogauge by assuming proper Poison's ratio for the treated material. If Poison's ratio is assumed to be 0.35, a factor of 8.67 can be used to convert the Geogauge Stiffness (MN/m) into Stiffness Modulus (MPa). It is recommended from the Geogauge Manufacturer that Geogauge should not involve in

testing if measured layer stiffness and in-situ moduli value greater than 70 MN/m and 610 MPa, respectively.

Light Falling Weight Deflectometer

The Light Falling Weight Deflectometer (LFWD) is a portable device that measures deflection using falling weight, the degree of compaction and the dynamic modulus of soil. It was developed in Germany as an alternative to the plate load test to overcome accessibility problems for roads and highways under construction. There are different versions of LFWDs currently used, which are based on different manufacturers and different countries, but they are following the similar principle. Previously conducted studies include German Dynamic Plate (GDP), the Transport Research Laboratory (prototype) Foundation Tester (TFT), and the Prima 100 LFWD.

The LFWD device used in this research is the Zorn ZFG 3000 GPS, which is presented in Figure 125. The device has three major elements: a pulse-inducing weight, the loading plate and a set of geophone sensors (one in the center of the plate and others in lateral positions; seismic velocity transducers, accuracy ±2%, resolution 1 lm, frequency range 0.2–300 Hz to determine settlement) [147]. The LFWD device weighs 26 kg and has a 10 kg falling height, which impacts on a spring to create pulses of 18 milliseconds, and a guide rod (720 mm drop height) supported with lock pin and loading plate (100 mm, 200 mm and 300 mm).

Figure 125. Light falling weight deflectometer

Principle of Operation

During a test procedure, the loading plate measures the center deflection and LFWD elastic modulus. The measured deflection at the center of the plate is used to calculate the surface modulus E_{LFWD} using Boussinesq's solution as follows [148]:

$$E_{LFWD} = \frac{k(1-\nu^2)\sigma_{app}R}{\delta_c}$$

[A6]

where: k = π/2 or 2 for rigid and flexible plates, respectively; c = center deflection; ν = Poisons ratio, σ_{app} = applied stress; and R = radius of the plate.

Dynamic Cone Penetrometer

The Dynamic Cone Penetration (DCP) test was first introduced in South Africa for evaluation of pavement strength. In 1969, Dr. Van Vuuren introduced a new form of DCP with a 30° cone. According to him, the DCP is a tool to measure the in-situ shear resistance of soil as soil's shearing ability is to withstand load when it is applied. Kleyn et al. [149] suggested based on DCP that there is a minimum strength or suitability of the base course when sound pavement section is compared with a failed pavement section. Since then, DCP has been comprehensively used in South Africa, United Kingdom, Australia, New Zealand and several states in the U.S.A. The DCP device has been adopted as an effective tool in the assessment of the strength of pavements and subgrades.

The DCP test requires less time for field application, needs less maintenance and performs on a pavement with higher accuracy. Operation of DCP replaces manually driven mechanisms. One of the advantages of DCP over other in-situ tests is that it can detect weak zones inside the pavement layer. Figure 126 presents the schematic of the Dynamic Cone Penetrometer.

The Dynamic Cone Penetrometer consists of 8 kg (22lb) weights, which falls freely from an upper shaft at a distance of 22.6 in., and exerts dynamic energy of about 78.5 N. Specification of DCP are shown in Table 84.

Figure 126. Schematics of the dynamic cone penetrometer

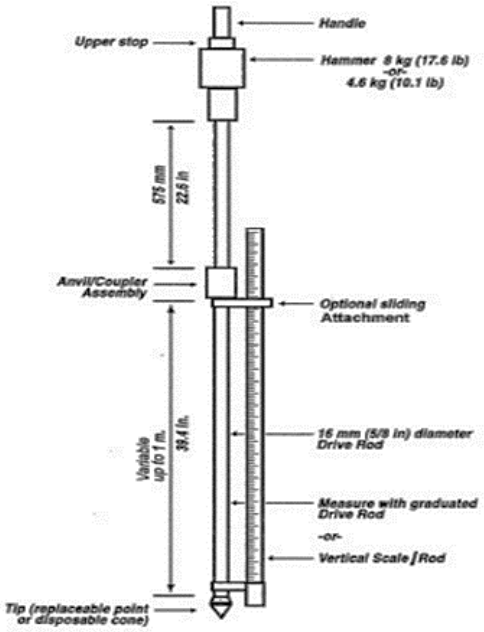

Principle of the DCP Test

The Dynamic Cone Penetrometer test is executed by dropping a hammer of a specific weight with a certain height, which resembles both the SPT and CPT tests. The DCP includes features of SPT in a way that both tests require penetration depth per blow up to a certain depth. In DCP test, a cavity is created using a 60˚ cone, which is similar to CPT.

The DCP test can take continuous measurement of the subgrade and pavement layers. The free-falling weight impacts on an anvil and the cone penetrates into the ground. The cone attached to the lower shaft needs to be replaced after one test. The entire process is repeated until the desired depth is achieved and the penetration depth for each blow is measured for each hammer drop.

Table 84. Specification of DCP [150]

Standard Hammer Mass	17.6 lbs (8kg) or 10.1 lbs (4.6 kg) for weaker soil
Hammer Falling Height	22.6 in. or 575 mm
Anvil	3.2 in. or 81 mm
Driving Rod Diameter	16 mm
Lower Shaft (Typical)	39.4 in. or 1000.76 mm
Replaceable Cone Apex Angle	60 degrees
Replaceable Cone Diameter	0.8 in. or 20 mm

DCP Penetration Index (DCPI)

In order to determine the layer thickness, we need to find the slope of the curve between number of blows and depth of penetration (mm/blow), which is denoted as the DCP Penetration Index (DCPI). Test procedure and typical DCPI profile are given in Figure 127 and Figure 128. The DCPI can be calculated using the following equation [151]:

$$DCPI = \frac{P(i+1)-P(i)}{B(i+1)-B(i)} \quad [A7]$$

where: DCPI = Dynamic Cone Penetration Index (mm/blow); P = Penetration at i^{th} or $(i+1)^{th}$ hammer drops (mm); and B = blow count for the i^{th} or $(i+1)^{th}$ hammer drops.

A representative value of DCPI for a certain amount of depth can be obtained using the following equation:

$$DCPI_{avg} = \sum_{N}^{i} (DCPI)/N \quad [A8]$$

Where: N = Total number of DCPI recorded for a given depth

Figure 127. The dynamic cone penetration (DCP) test procedure

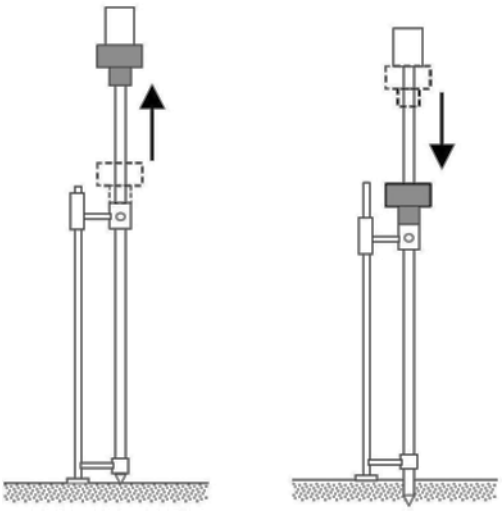

Figure 128. Typical DCPI profile [152]

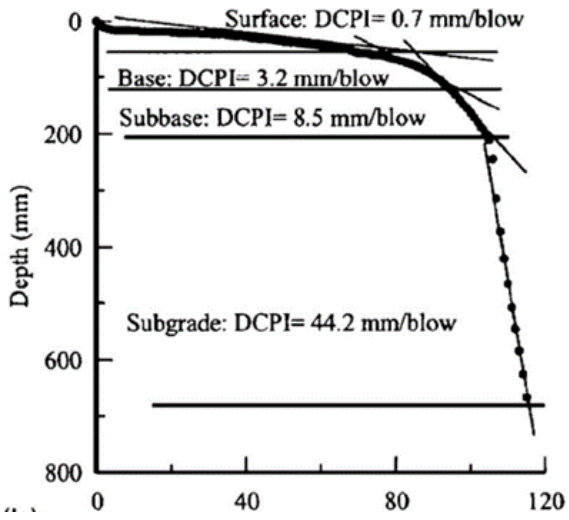

Plate Load Test

The Plate Load Rest (PLT) has been considered as a useful device for evaluating pavement structure in many European countries. It is a widely known test for measuring the bearing capacity of soil and modulus of subgrade reaction for pavement. This test is more time-consuming test than other in-situ testing devices, like Geogauge, LFWD, and DCP. Currently, it has been widespread used on both rigid and flexible pavement. The

influence depth of PLT test is about 1.5 to 2 times the diameter of the plate. Usually, plate diameter of 30 in. (76.2 cm) is used for runways, but for roadways smaller diameter of 12 in. (30.5 cm) can also be used.

During testing, smaller diameter plates are placed on the top of the plate to avoid bending. A hydraulic jack applies load on the plate and the load is then transferred to the soil by the plate. Measurements from four dial gauge readings indicate the settlement of the plate. These dial gauges are placed on horizontal beams, at right angles to each other [153].

Principle of Operation

The PLT test method is performed in accordance with ASTM D1194. During this test, a load is applied until settlement increment comes to a steady magnitude. In order to perform this test, load increments are applied and maintained until all settlements become stable. Then, loads are removed in the same manner until the rebound curve is achieved. This process can be progressed for the next cycle until the desired curve is achieved.

PLT Moduli Calculation

The modulus of subgrade reaction of a tested material can be determined by the PLT, using the following equation [154]:

$$k = \frac{P}{\delta_c} \qquad [A9]$$

where: P = applied load on plate (psi), δ_c = deflection of center of plate (in.).Additionally, the elastic modulus of the tested soil can be evaluated from the PLT.

The relationship from which the elastic modulus can be obtained is given as follows [154]:

$$E_{PLT} = \frac{1.18\ P.R}{\delta_c} \qquad [A10]$$

where: R = radius of plate.

Figure 129 presents an example of PLT results, where the initial modulus, $E_{PLT(i)}$, can be determined from the slope of the first loading cycle, and the reloading modulus, $E_{PLT(R2)}$ is determined from the second cycle.

Figure 129. Typical results of plate load test [155]

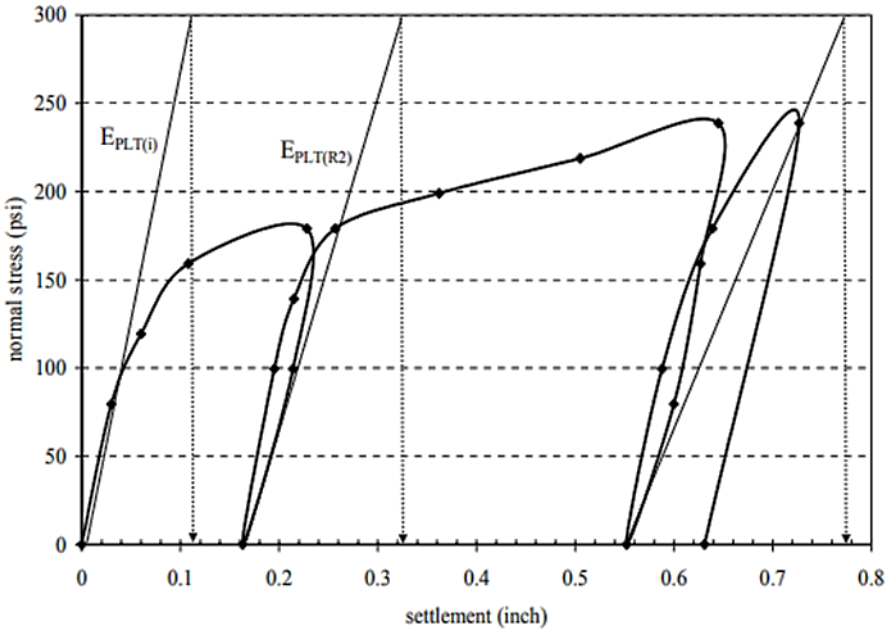

Dirt Seismic Portable Analyzer (D-SPA)

The Seismic Properties Analyzer (SPA) is a device for measuring vibrations (sonic, ultrasonic and resonant vibrations) to evaluate the average modulus of concrete pavements and structures, asphalt pavements, base materials and compacted subgrade materials. The SPA device was designed and developed by Dr. Soheil Nazarian of the University of Texas at El Paso [156].

D-SPA Operating Principles

D-SPA operates based on generating and detecting stress waves in a medium. When a vertical impact on the ground surface disturbs an elastic half-space, two types of waves will travel in the medium: the body wave, which is composed of compression and shear waves, and the surface wave. Among these waves, the compression waves are the fastest waves that travel through the ground, and occur when the material displacement takes place back and forth along the direction of wave propagation. The shear waves travel slower than the compression waves through the ground and occur when material displacement happens perpendicular to the direction of travel of the wave. The surface waves, primarily Rayleigh waves, are the slowest waves that travel along the surface of the ground and occur when the material is displaced in a cylindrical motion [157].

Two receivers usually collect outputs after the arrival of compression, shear and surface waves, which are marked in Figure 130. Reliable estimation of compression wave is difficult as only less than 10 percent of seismic energy propagates in this form. Shear wave energy is about one-fourth of the seismic energy and can be easily identified in the record. As the speed of shear waves and surface waves are close to each other, it is difficult to separate shear waves from surface waves. Surface waves contain about two-thirds of the seismic waves and it is easy to measure them.

Figure 130. Typical time records from D-SPA [158]

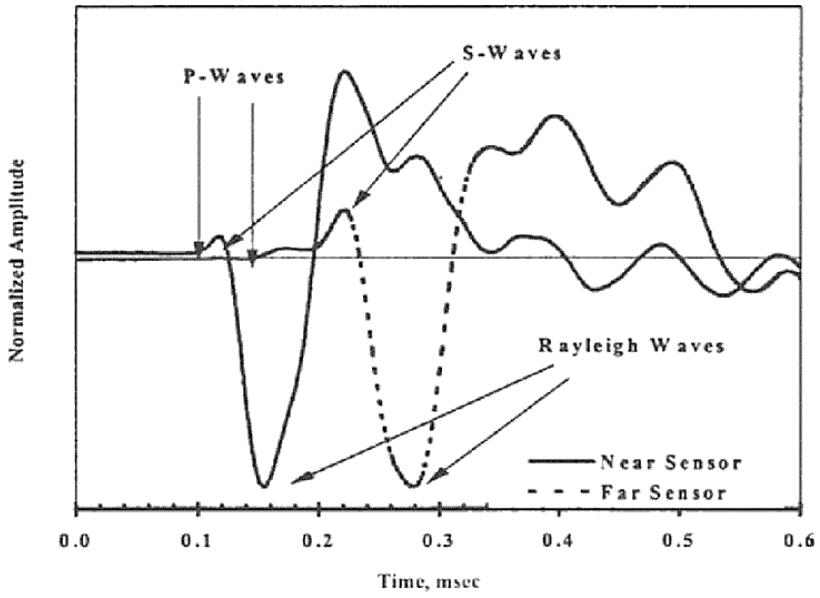

Data reduction can be done in either the time domain or the frequency domain. In time domain analysis, time is recorded when seismic energy arrives at each sensor. The relation between velocity and time can be expressed as [159]:

$$V = \frac{\Delta X}{\Delta t} \qquad [A11]$$

Where: V = Propagated velocity of any of the three waves (i.e. compression waves, Vp; shear waves, V_S; or surface (Rayleigh) wave, V_R); ΔX = Receiver spacing; and Δt = Travel time.

If the Poison's ratio of soil and shear modulus are known, the Young modulus can be calculated using the following equation:

$$E = 2\,(1+\nu)\,G \qquad [A12]$$

Where: ν = Poison's ratio of soil; G = Shear modulus; and E = Young's modulus

The shear modulus can be calculated from shear velocity and mass density using:

$$G = \rho\, V_s^2 \qquad [A13]$$

Since the surface wave velocity can be measured more accurately than shear velocity, V_R is then converted to shear wave velocity, and the expression is as follows:

$$V_S = V_R \times (1.13-0.16\,\nu) \qquad [A14]$$

So, if it is assumed that the properties of the upper most layer are uniform, the shear wave velocity can be calculated from Equation A13. Then, the Young's modulus of the top layer can be calculated by combining Equations A12 and A13:

$$E = 2\,\rho\, V_s^2\,(1+\nu) \qquad [A15]$$

Where: V_S = Velocity of shear waves, ρ = Mass density and ν = Poison's ratio.

Ultrasonic Surface Wave Method

The Ultrasonic Surface Wave (USW) method can measure seismic modulus process by performing Fourier transformation on the two signals. Fourier transformation disintegrates the time record into components of different frequencies and analyzes each frequency component. Each component of the signal has an amplitude, frequency and wavelength. Fourier approach is included in the USW method based on the fact that longer wavelengths of a component are more affected by values of modulus from deeper beneath the surface, which is presented in Figure 131.

After the data is collected from far and near receivers, the data is then reduced and a diagram of phase difference or phase versus frequency is constructed. Phase difference or phase curve is then analyzed to determine a value for seismic modulus at each frequency. If the phase difference (ψ) and frequency (f_r) are known from a phase diagram (Figure 132), travel time (Δt) can be calculated using the following formula:

$$\Delta t = \frac{\psi}{360 f_r} \qquad [A16]$$

Figure 131. Signal amplitude versus depth for different wavelengths [157]

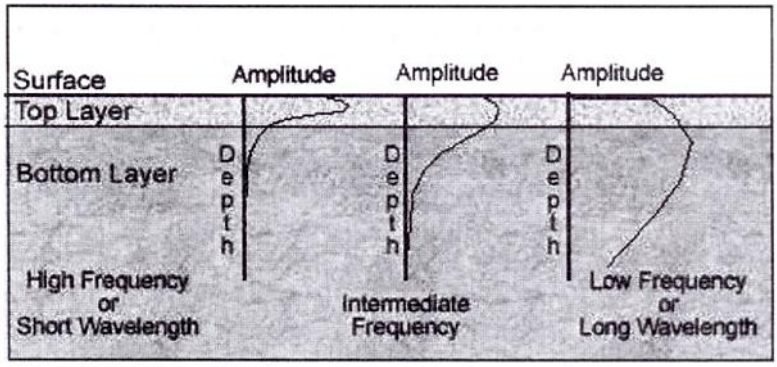

Figure 132. Phase difference versus frequency [157]

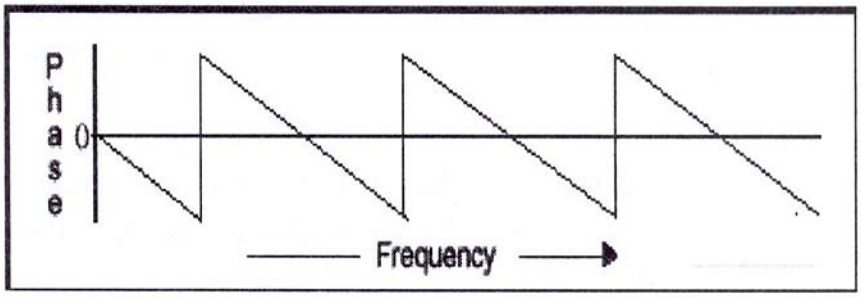

Phase velocity (Propagation of velocity inside a medium) can be determined from Equation A16. After knowing the phase velocity using travel time (Δt), the wavelength can be determined using the following equation:

$$L_{ph} = V_{ph}/f_r \quad [A17]$$

Where: L_{ph} = wavelength of the propagated velocity; and v_{ph} = Average phase velocity of the top layer [158].

Now, the dispersion curve can be constructed using phase velocity (V_{ph}) and wavelength (L_{ph}), and the Young Modulus is calculated using the following equation:

$$E_{usw} = 2\,\rho\,(1+\nu).(V_R(1.13-0.16\,\nu))^2 \quad [A18]$$

Impact-Echo Method

The Impact-Echo method is widely accepted as a nondestructive evaluation method. In this test, signals or disturbances (mechanical or stress waves at a frequency in the range of 20-30 kHz) are transferred from the bottom of the source, which propagates outward from the contact point through the ground [160]. If the ground layer overlies with another layer, one disturbance is reflected back to the D-SPA and the remaining signal is transmitted into the second layer (Figure 133) [157].

Figure 133. Path of D-SPA disturbances [157]

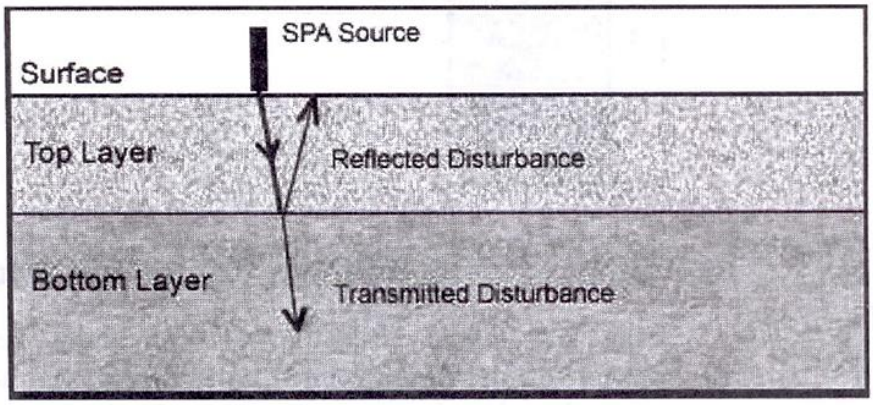

The reflected signal is collected by the receivers. Some of this energy is reflected from the surface and starts a second downward propagation. This process proceeds several times creating multiple echoes of the initial signal, which is shown in Figure 134 [157].

The time-domain signal is then converted into a frequency-domain signal by using Fourier analysis. Frequency-domain function and frequency-domain signal are monitored to detect the maximum frequency with maximum energy (referred to as peak frequency). Peak frequency (f) is then used to measure the thickness (h) of the soil layer using the following equation [160]:

$$h = \alpha \frac{V_p}{2f_r} \qquad [A19]$$

Where: V_p = compression wave velocity that can be measured from the surface wave velocity; α = empirical correction factor, which is 0.96 for plate-like structure [161]. The above equation is based on the assumption that compression is uniform throughout the

depth of the tested material. Uncertainty may increase if heterogeneity exists inside the material [160].

Figure 134. D-SPA "echoes" from multiple reflections [157]

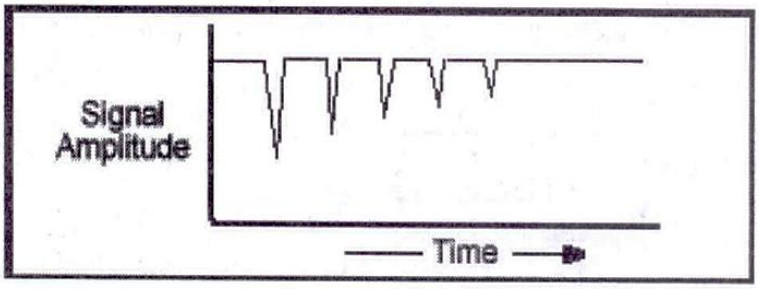

Nuclear Density Gauge

The Model 3430 Surface Moisture-Density Gauge known as Nuclear Density Gauge has been adopted for this study. The Moisture-Density Gauge can rapidly and unequivocally figure out dampness and thickness for soils, soil bases, aggregate, cement and asphaltic cement without the utilization of core samples or other ruinous techniques. Utilizing direct transmission or backscattered gamma radiation, the 3430 measure measures the thickness of materials by tallying the number of photons discharged by a cesium-137 source. Geiger-Mueller (G-M) identifiers situated in the check base identify the gamma radiation and a microprocessor changes over the tallies into a density reading. Figure 135 shows the working application of the Nuclear Density Gauge.

Utilizing the standard of neutron thermalization, the model 3430 measures the moisture content for soils and soil-like materials. Hydrogen (water) in the material moderates neutrons transmitted from an americium-241: beryllium source (or californium-252 in the Model 3430-M). Helium-3 indicators situated in the measure base identify the moderated neutrons.

The nuclear strategy for testing thickness and dampness has been affirmed by the American Society of Testing and Materials (ASTM). The Model 3430 meets or surpasses every one of the prerequisites of ASTM Standards C1040, D2922, D2950, and D3017 [162].

Figure 135. Direct transmission geometry of the nuclear density gauge [162]

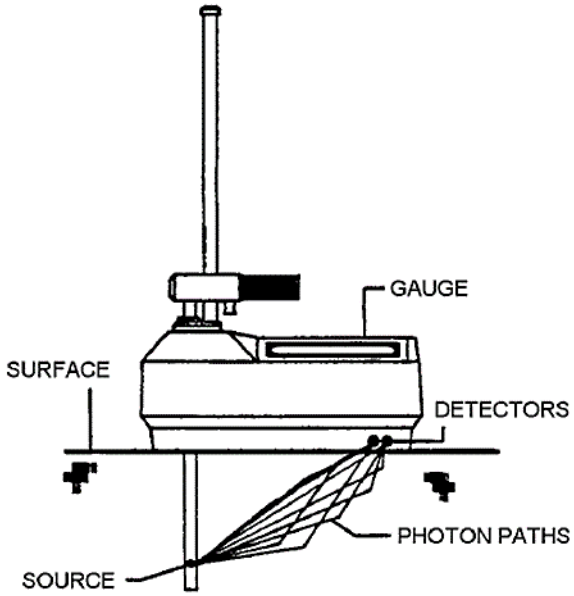

E-Gauge

The Troxler E-Gauge, Nuclear Density Gauge uses a low movement gamma beam source to play out the thickness estimations. The Cesium 137 source and the delicate identifier cooperate to give solid thickness readings, which are in the same class as the nuclear gauge. Figure 136 show the schematic of the E-Gauge.

Because of the plain low source action, it is important to nearly screen foundation radiation. Whenever the material estimated changes or when moving to another job site, it is important to play out a foundation tally at the estimation area over the readied gap. It is likewise important that any known wellsprings of radioactive material be kept no less than 30 ft. (10 m) away amid standard tallies, foundation checks and estimation tallies (for instance: other nuclear gauges). Thickness estimations can be performed between 2 in. (5 cm) and 8 in. (20 cm) inside and out, that isn't a backscatter estimation position. The E-Gauge is as of now offered as an 8-in. skilled thickness measure for soil thickness estimation with a non-nuclear moisture test frill, which measures moisture at a profundity of 4-5 in. (Troxler E-Measure Manual).

Figure 136. Schematic of the E-Gauge [162]

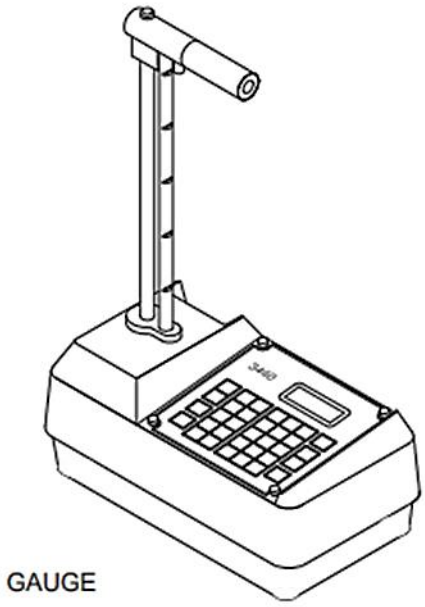

Appendix B

Profiles of Soil Boring Data, CPT Data and CPT Soil classification for the Different Sites

Figure 137. Profiles of soil boring data, CPT data, and CPT soil classification at Bayou Laccassine

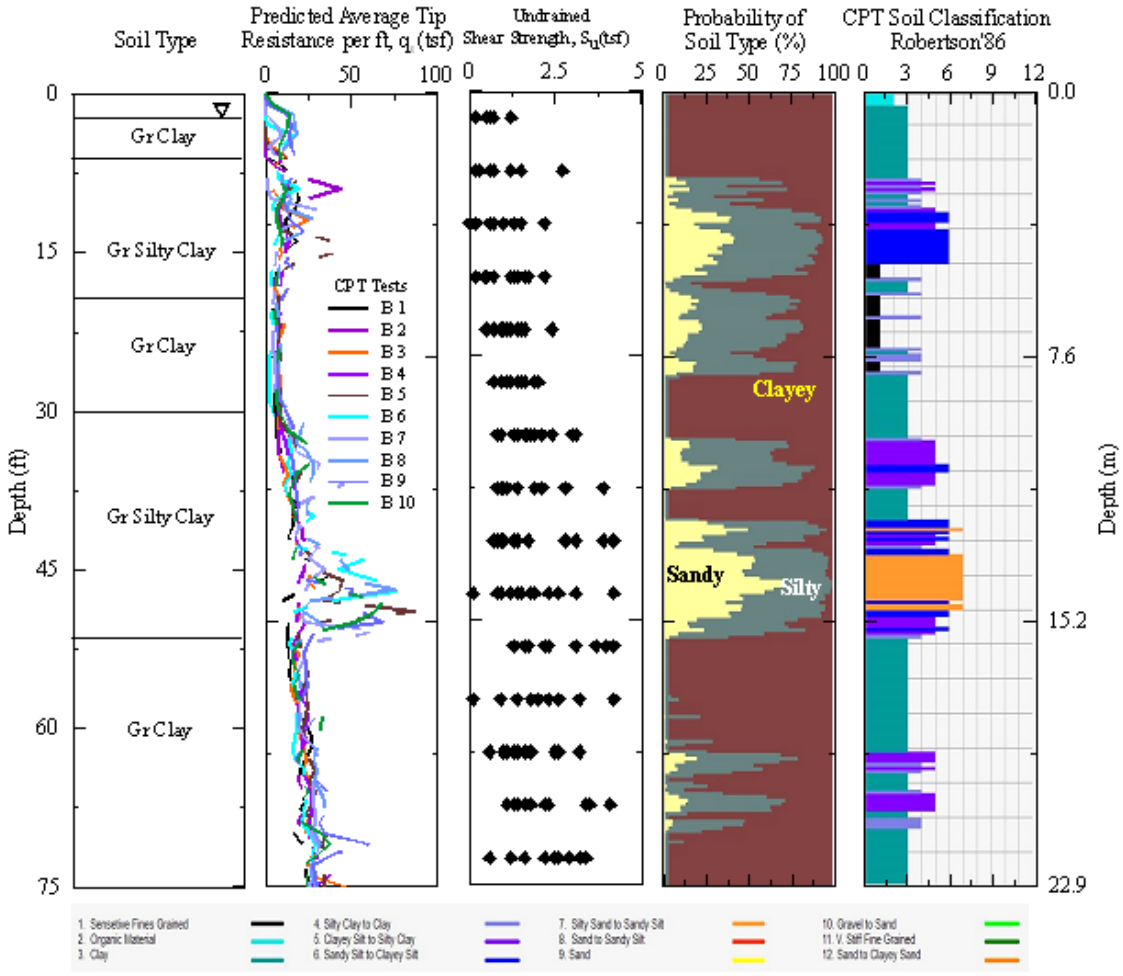

Figure 138. Profiles of CPT data, and CPT soil classification at ALF

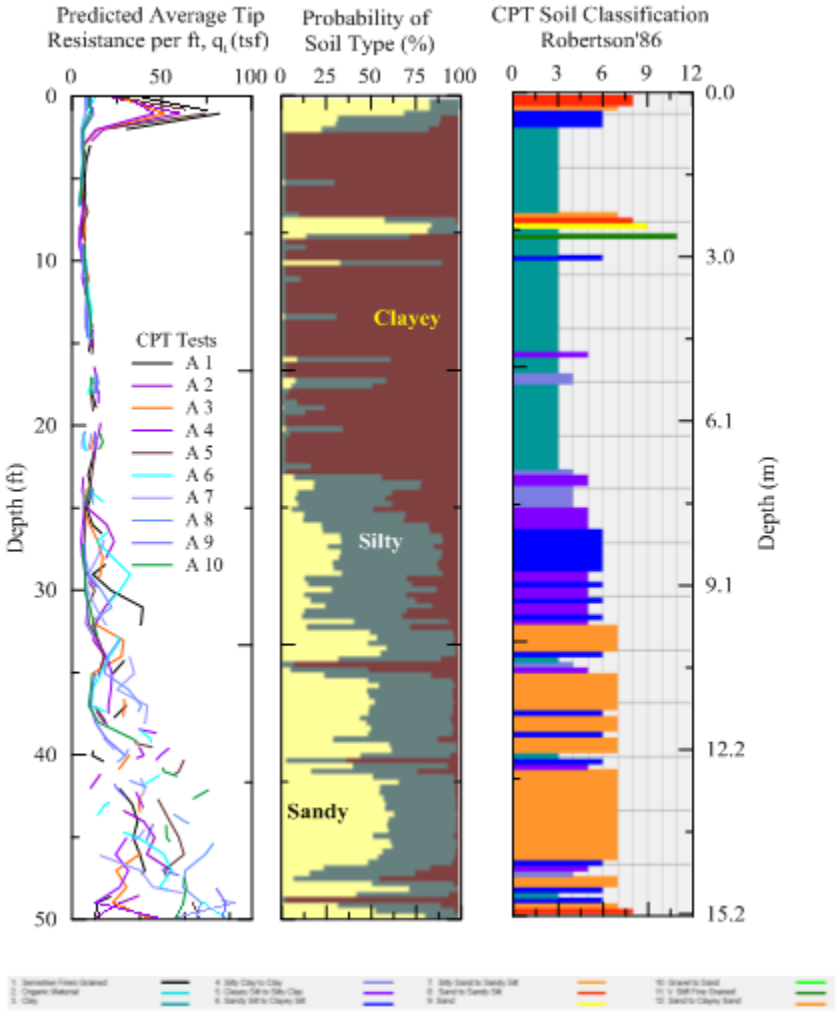

Figure 139. Profiles of CPT data, and CPT soil classification at US 90 & LA 85

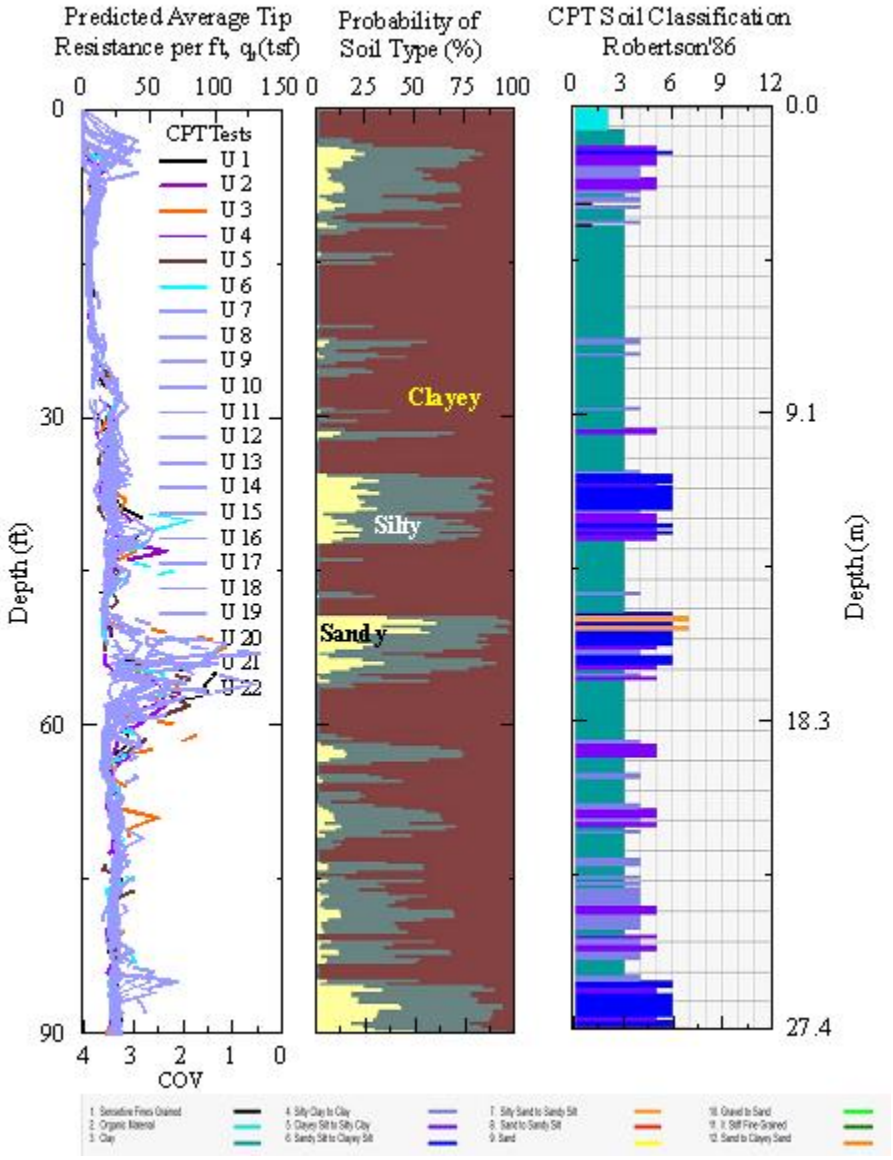

Figure 140. Profiles of CPT data, and CPT soil classification at Hammond

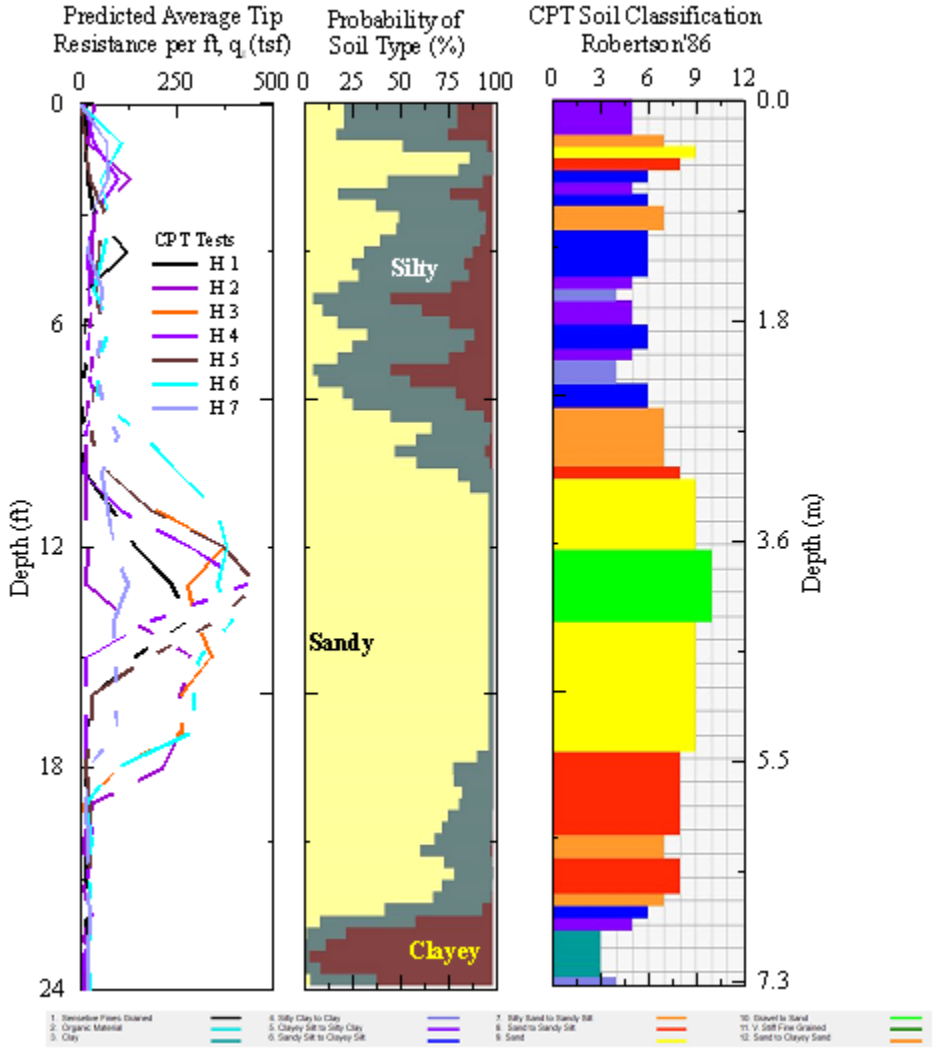

Figure 141. Profiles of CPT data, and CPT soil classification at LA 1

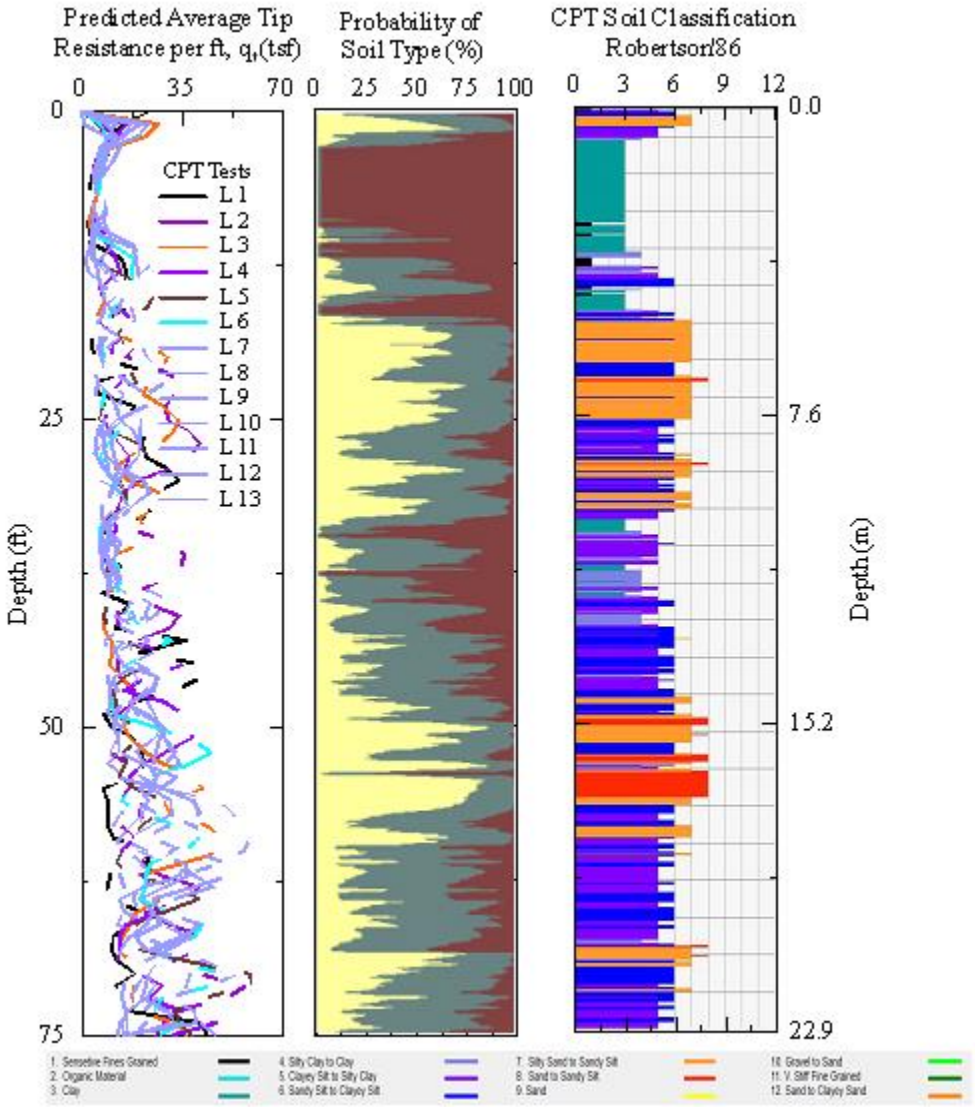

Figure 142. Profiles of soil type, soil layering and S_u data at Red River

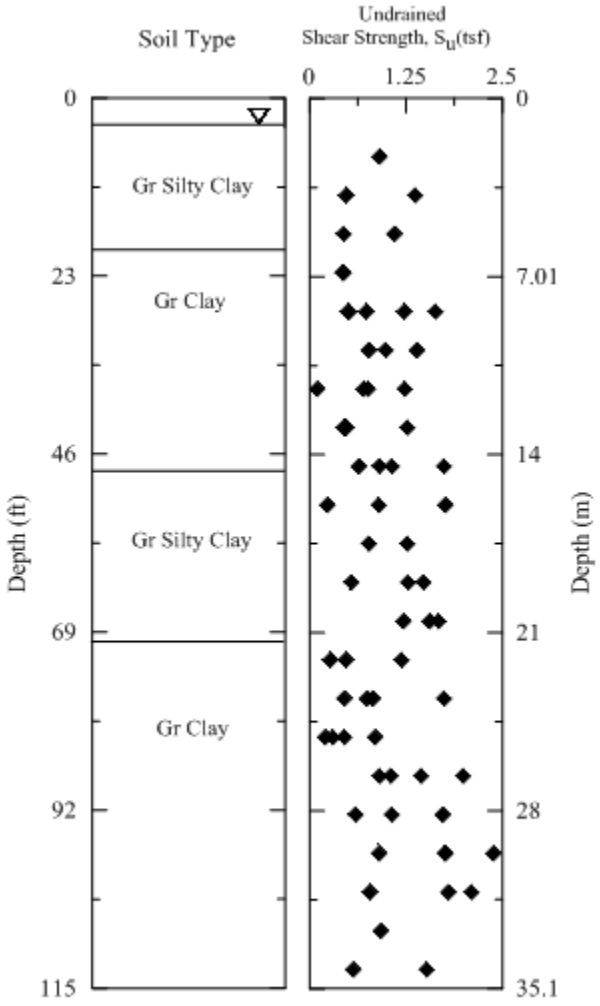

Figure 143. Profiles of soil type, soil layering and S_u data at Williams Blvd.

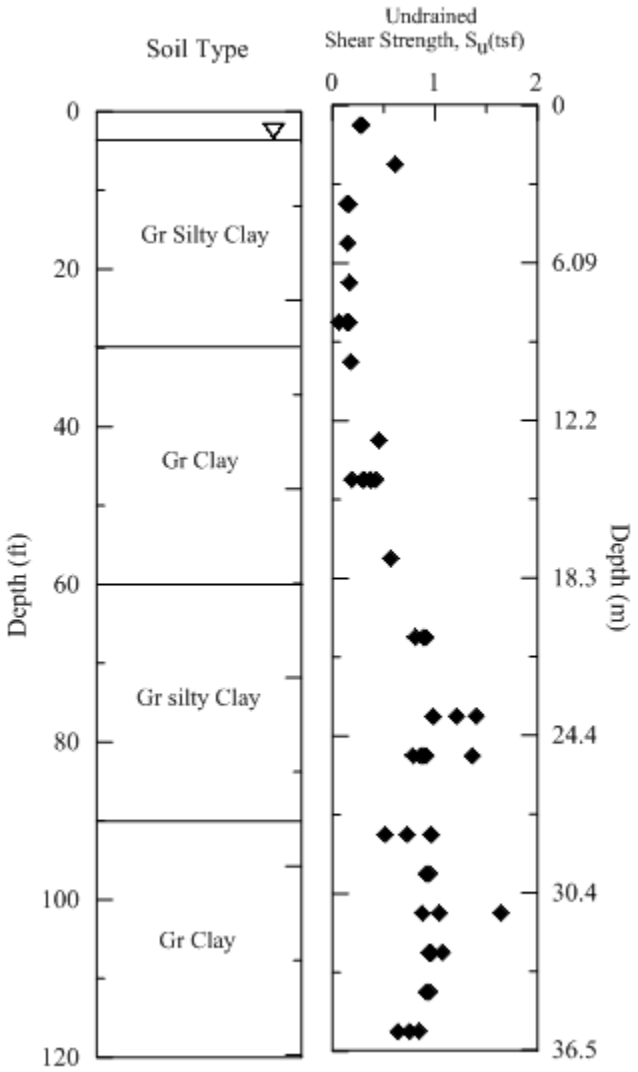

Appendix C

Typical Slope Stability Methods – Methods of Slices

A number of solution techniques have been developed for slice methods. The equations of the considered statics, the incorporated interslice normal and shear forces, and the anticipated correlation between the inner slice forces are the key differences among all techniques [163]. Figure 144 shows a typical slice in a hypothetical sliding mass, along with the forces operating on the slice. The number of slices used is determined by the geometry and profile of the slope earthfill [164].

Figure 144. Slicing and forces acting in a sliding mass

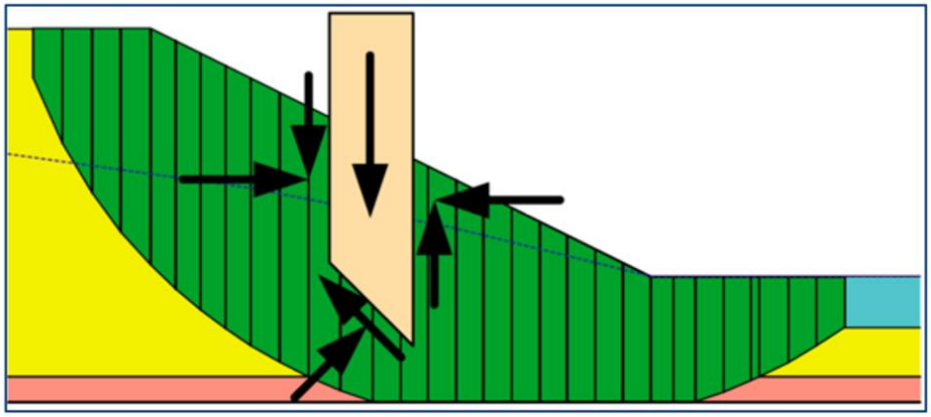

The assumption that the slip surface being a circular slip surface is utilized by some slices approaches to define a slope stability problem, whereas others accept a noncircular slip surface. The former considers the balance of moments around the circle's center, whereas the later does it in terms of individual slices [164].

Ordinary Method of Slices

The Fellenius method [165], or Swedish method of slices, is another name for this method. This approach is a slicing operation that ignores the forces on the slices' sides (Figure 145). The failing surface is divided into a number of imaginary upright slices, as shown in Figure 145(a).

Figure 145. Ordinary method of slices (a) different slices (b) forces acting on a single slice [165]

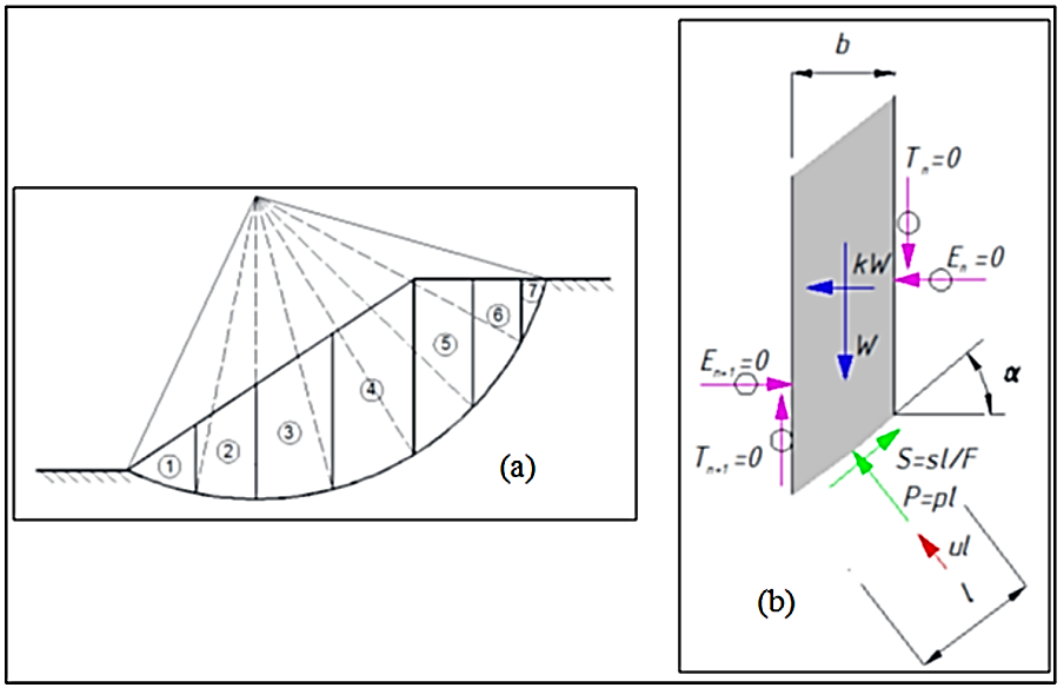

Bishop's Simplified Method

Professor Bishop of Imperial College in London devised a system in the 1950s that took into account interslice normal forces but overlooked interslice shear forces. By summing slice forces in the vertical direction, Bishop devised an equation for the normal at the slice base. As a result, the base normal is transformed into a function of the factor of safety. As a result, the factor of safety equation is nonlinear (FS appears on both sides of the equation), necessitating an iterative technique to determine the factor of safety.

In the absence of pore-water pressure, a basic form of Bishop's Simplified factor of safety equation is:

$$FS = \frac{1}{\sum W sin\alpha} \sum \left[\frac{c\beta + W tan\phi - \frac{c\beta}{FS} sin\alpha \, tan\phi}{m_\alpha} \right] \qquad [C1]$$

where, c = cohesion, β= slice base length, ϕ= friction angle, W= slice weight, and, α = slice base inclination. FS is on both sides of the equation as noted above. The equation is

not unlike the Ordinary factor of safety equation except for the m_α term, which is defined as:

$$m_\alpha = cos\alpha + \frac{sin\alpha\ tan\phi}{FS} \qquad [C2]$$

To find the Bishop's Simplified factor of safety, you must first guess the value of FS. The first guess is used as the Ordinary factor of safety in Slide2d. To compute m, the initial guess for FS is used, and then a new FS is computed. The new FS is then used to compute m, followed by another new FS. The operation is continued until the most recent computed FS is within a specified tolerance of the most recent computed FS. Fortunately, reaching a convergent solution usually only takes a few iterations.

When we look at the slice free body diagrams and forces polygons for the same slices as the Ordinary approach, we can detect a significant difference (Figure 146). The typical free body diagram and force polygon for the Bishop's simplified method is presented in Figure 147. With the addition of the interslice normal forces, the force polygon closure is now fairly good. The interslice shear forces are not there, as Bishop assumed, but the interslice normal forces are.

Figure 146. Case for hand calculation in Bishop's simplified method

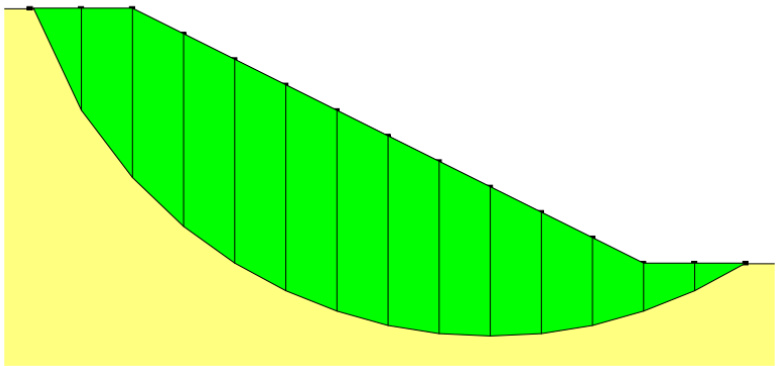

Figure 147. Typical free body diagram and force polygon for the Bishop's simplified method

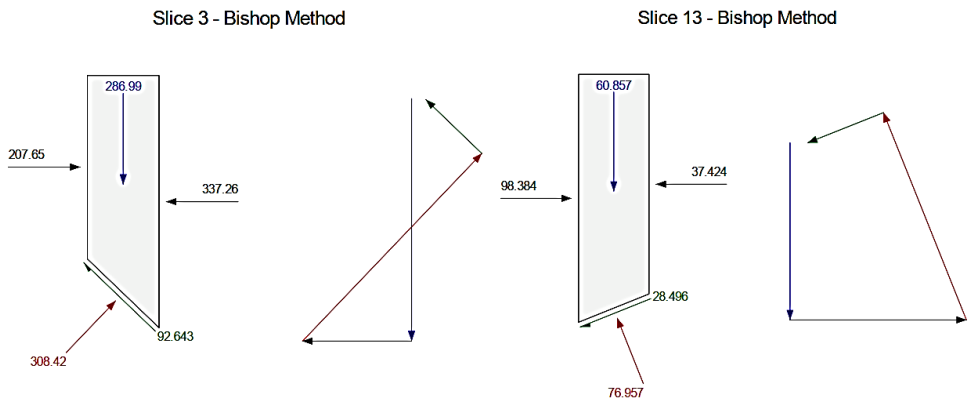

In summary, the Bishop's Simplified technique (1) takes normal interslice forces into account but overlooks interslice shear forces, and (2) achieves over all moment equilibrium but not overall horizontal force equilibrium.

Janbu's Simplified Method

The Janbu's Simplified approach is a noncircular method. It is similar to the Bishop's Simplified method, except that it only achieves overall horizontal force equilibrium rather than overall moment equilibrium.

The Janbu's Simplified method's free body diagrams and force polygons are shown in Figure 148. The Bishop's Simplified technique is actually better than the slice force polygon closure. However, using Bishop's Simplified approach, the factor of safety is 1.16 instead of 1.36. This is a substantial difference. Even though the slices are in force equilibrium, Janbu's Simplified factor of safety is actually too low.

Figure 148. Typical free body diagram and force polygon for the Janbu's simplified method

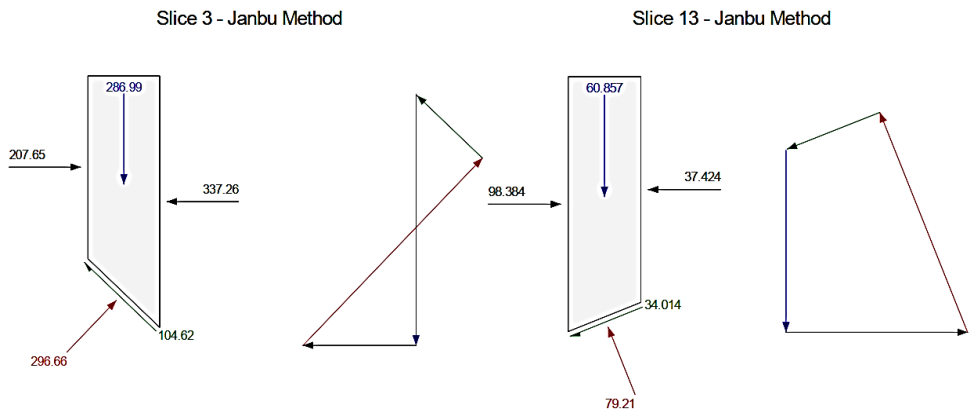

In summary, the Janbu's Simplified technique (1) takes into account normal interslice forces but ignores interslice shear forces, and (2) satisfies over all horizontal force equilibrium but not over all moment equilibrium.

Spencer Method

Spencer [166] is another noncircular method. It creates two factor-of-safety equations, one for moment equilibrium and the other for horizontal force equilibrium. He used a constant relationship between the interslice shear and normal forces and changed the interslice shear to normal ratio using an iterative approach until the two safety factors were equal. Finding the shear/normal ratio that equalizes the two safety factors indicates that both moment and force equilibrium have been achieved. This approach can also be used to simulate noncircular surfaces, with the assumption that all forces on the slice's sides are parallel. The slice forces provide more evidence of the link between the interslice shear and normal forces. A typical slice is shown in Figure 149.

It's worth mentioning that the force polygon closure is excellent when both interslice shear and normal forces are considered. The Spencer technique, in summary, takes into account both shear and normal interslice forces, achieves moment and force equilibrium, and assumes a constant interslice force function.

Figure 149. Typical free body diagram and force polygon for the Spencer method

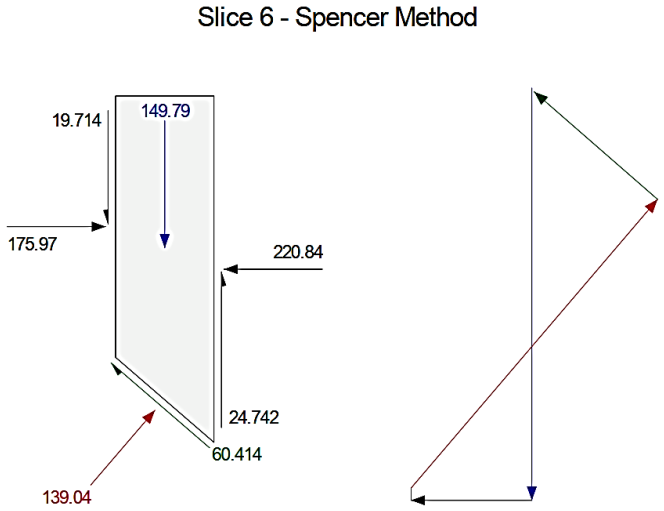

Appendix D

Data Transfer to Stationary and Semivariogram Models

Figure 150. Transferring the data from non-stationary to stationary data for Hammond site: (a) non-stationary data with trend line; (b) stationary data

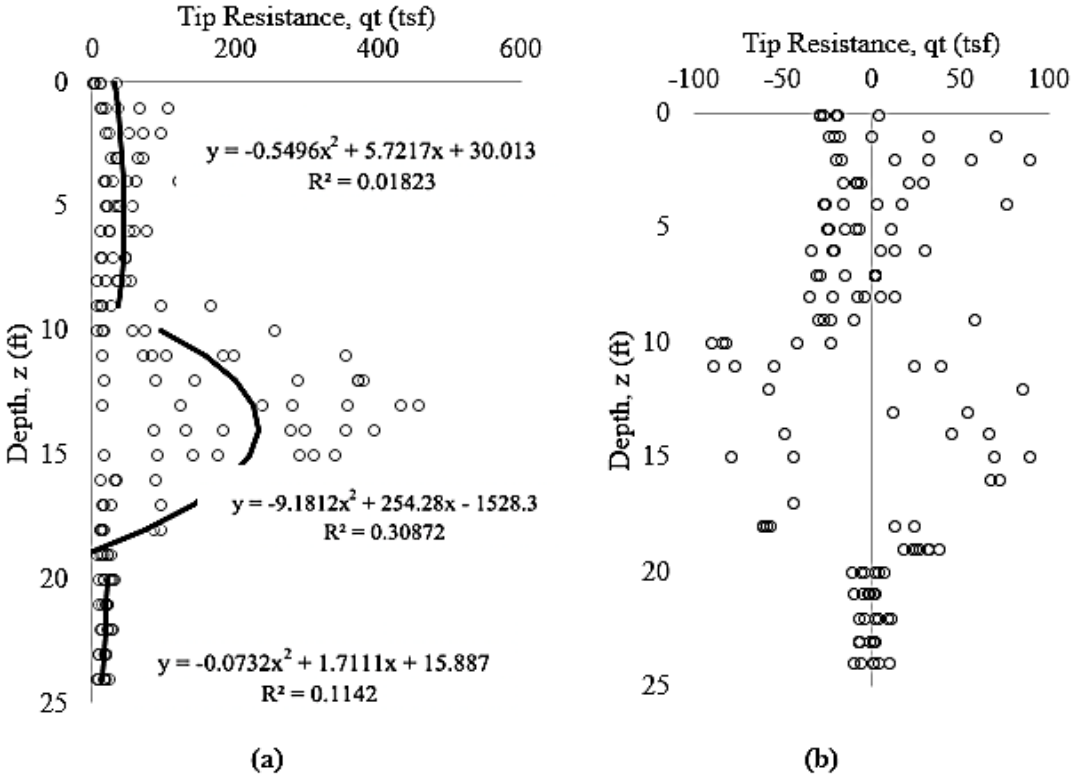

Figure 151. Transferring the data from non-stationary to stationary data for LA 1 site: (a) non-stationary data with trend line; (b) stationary data

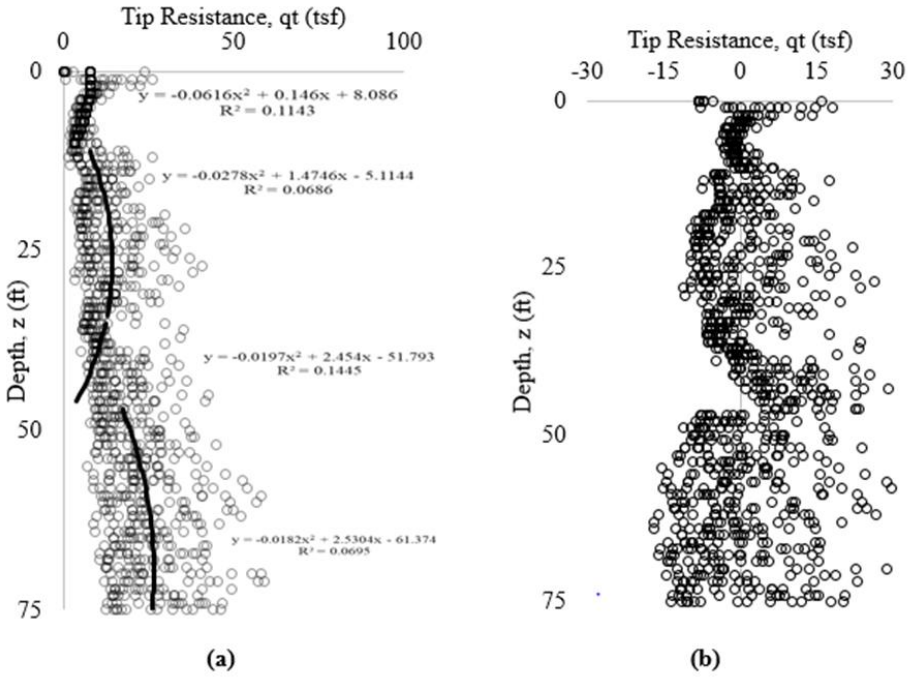

Figure 152. Transferring the data from non-stationary to stationary data for US90 & LA85 site: (a) non-stationary data with trend line; (b) stationary data

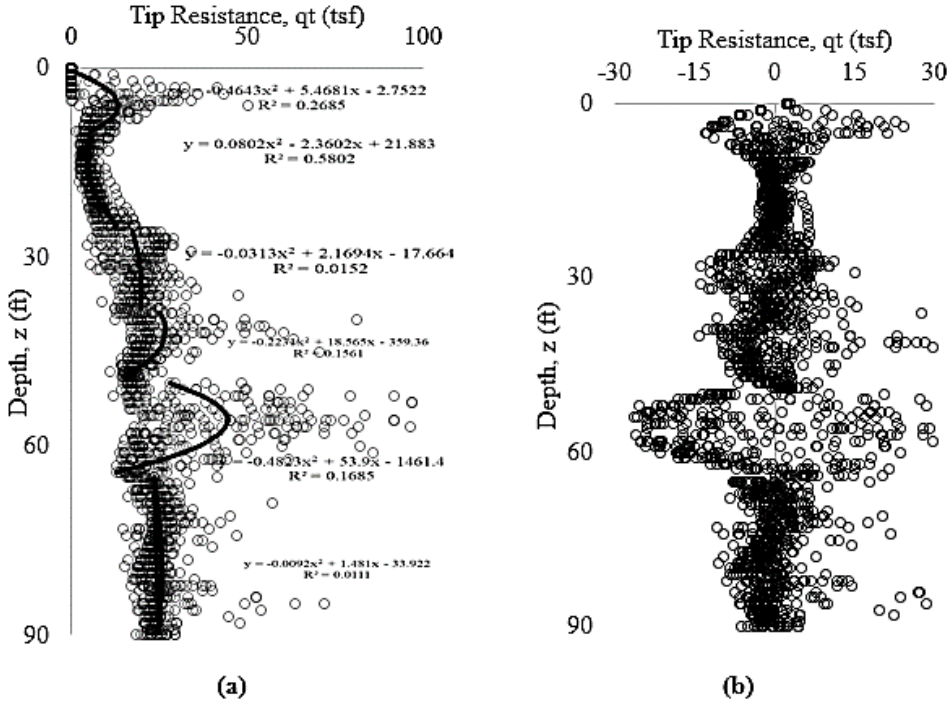

Figure 153. Transferring the data from non-stationary to stationary data for Bayou Laccassine site: (a) non-stationary data with trend line; (b) stationary data

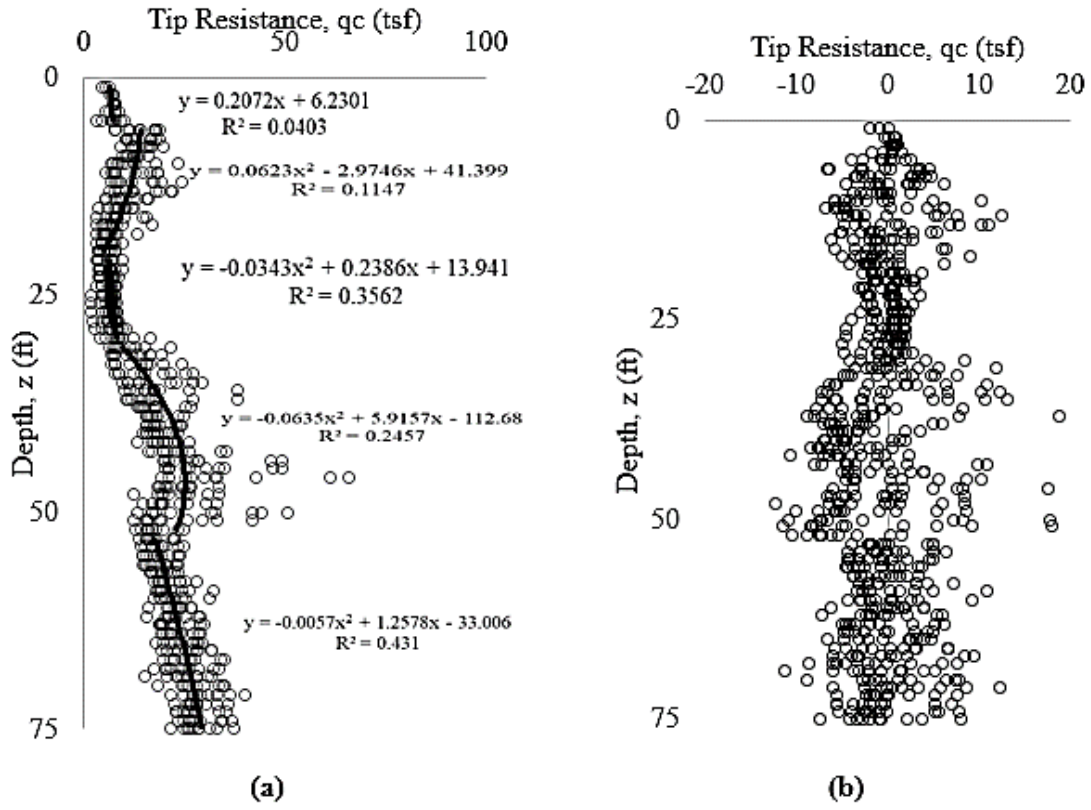

Figure 154. Experimental and spherical semivariogram models for the CPT-q_t data of soil layers at

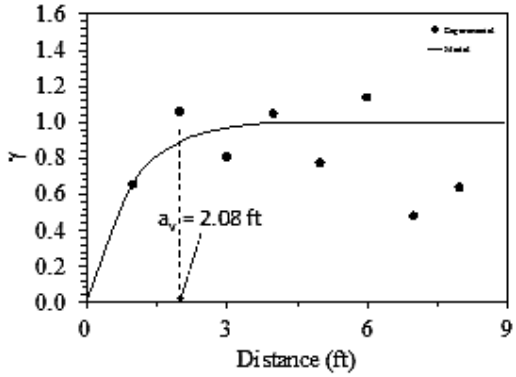

Layer 1 Vertical

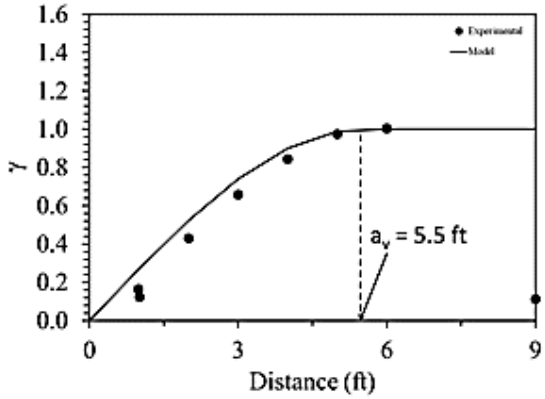

Layer 2 Vertical

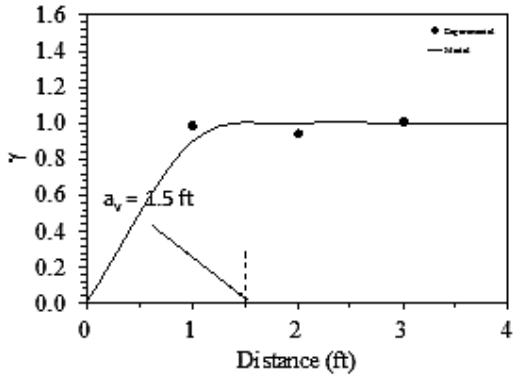

Layer 3 Vertical

Figure 155. Experimental and spherical semivariogram models for the CPT-q_t data of soil layers at ALF site

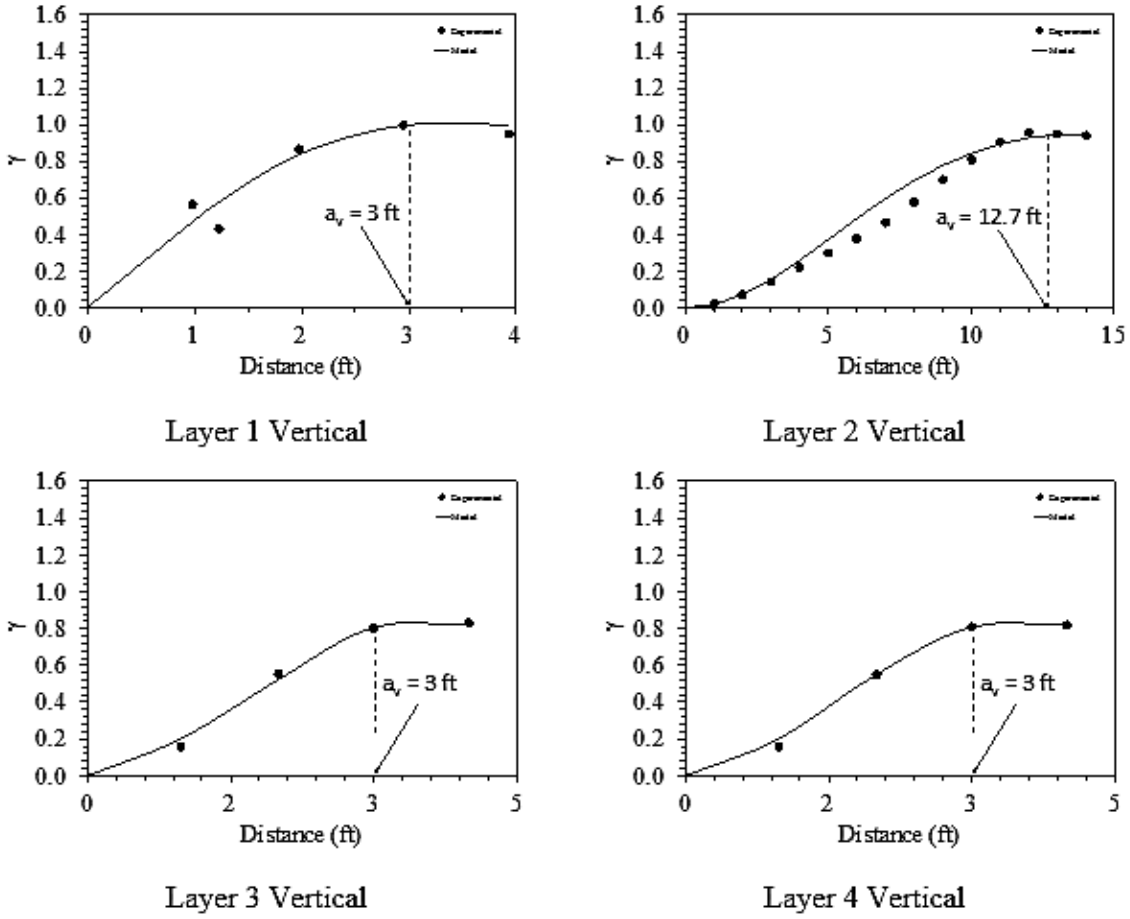

Figure 156. Experimental and spherical semivariogram models for the CPT-q_t data of soil layers at US 90 & LA 85 site

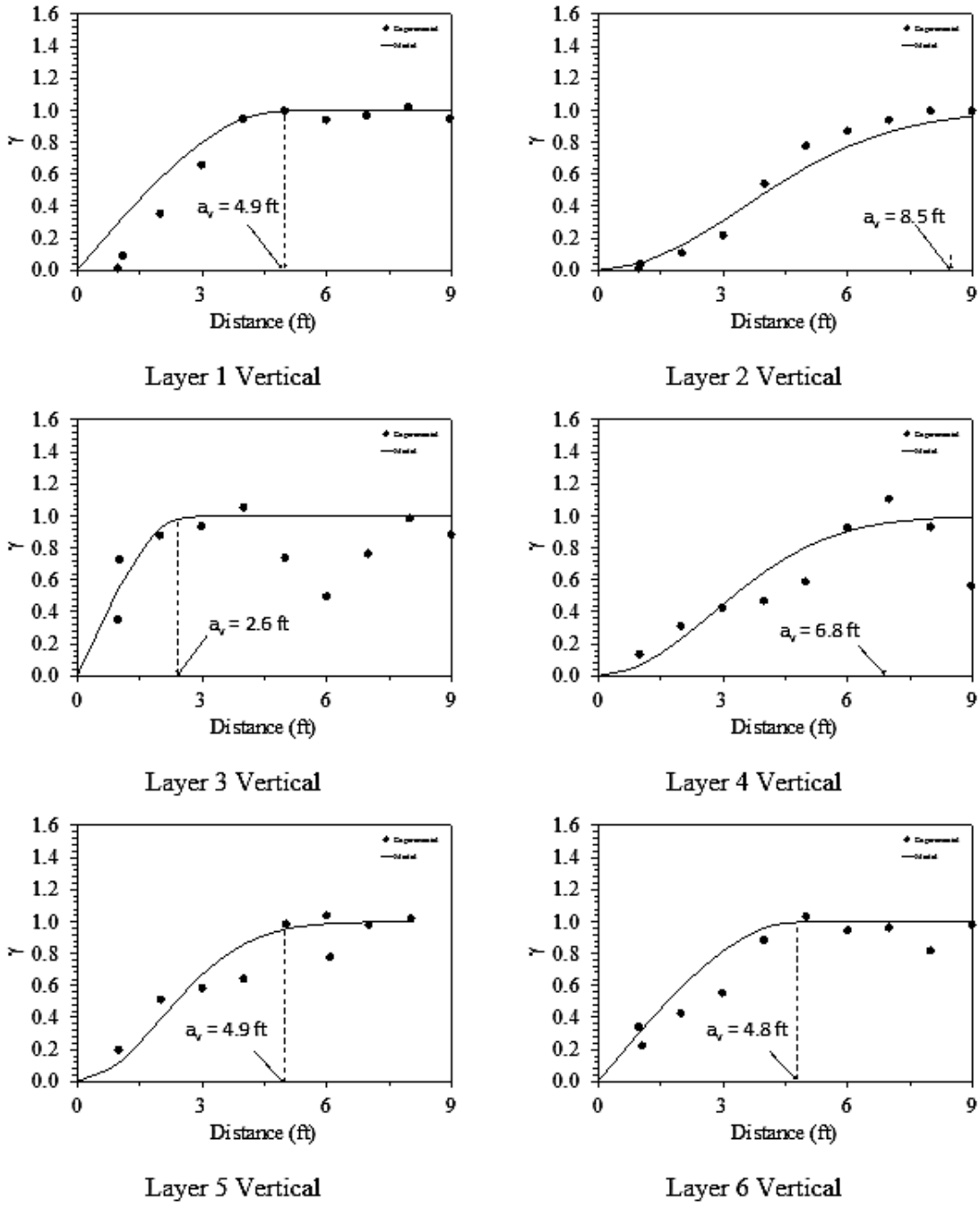

Figure 157. Experimental and spherical semivariogram models for the CPT-q_t data of soil layers at Bayou Laccassine site

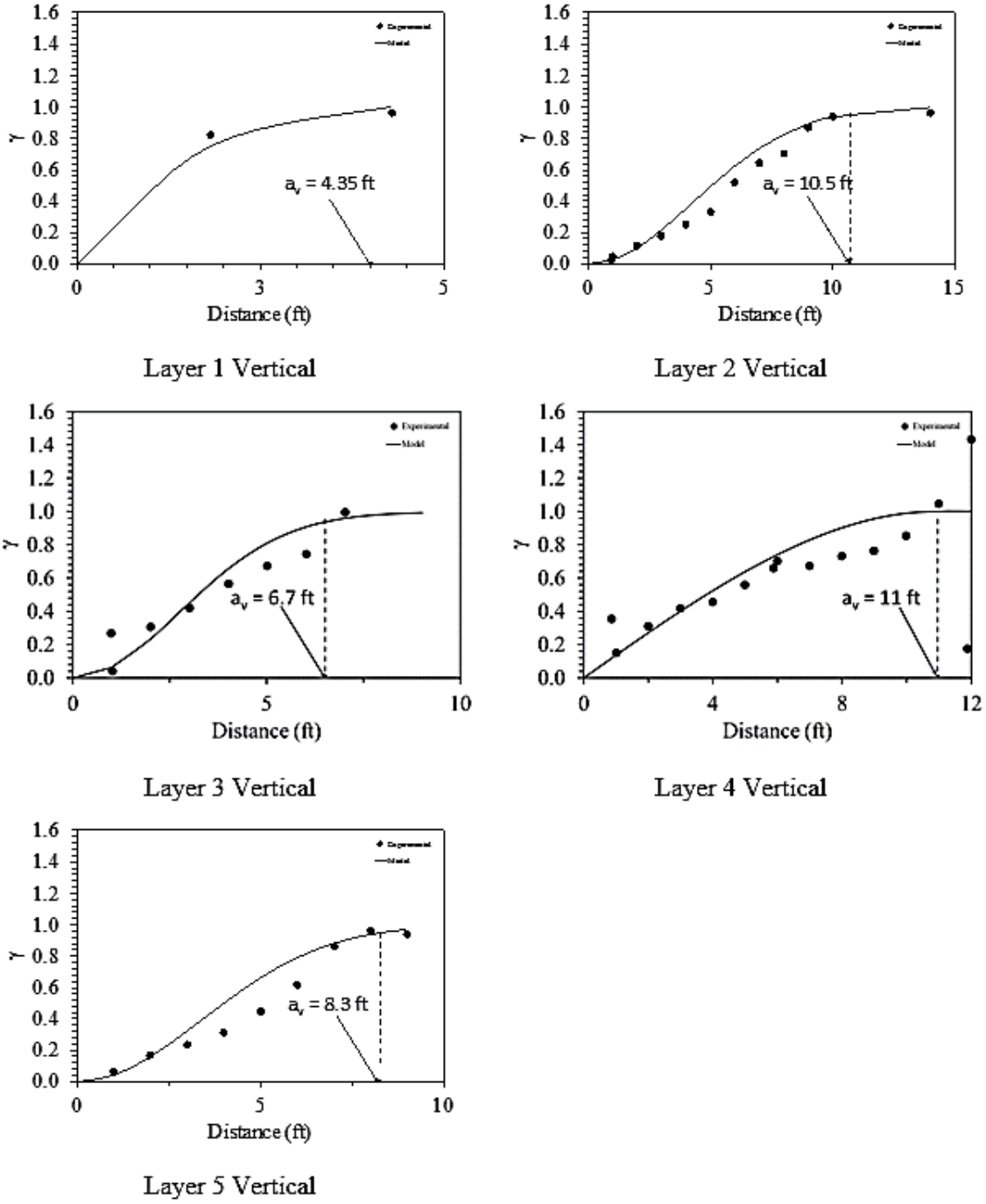

Figure 158. Experimental and spherical semivariogram models for the S_u data of the four soil layers at Williams Blvd site

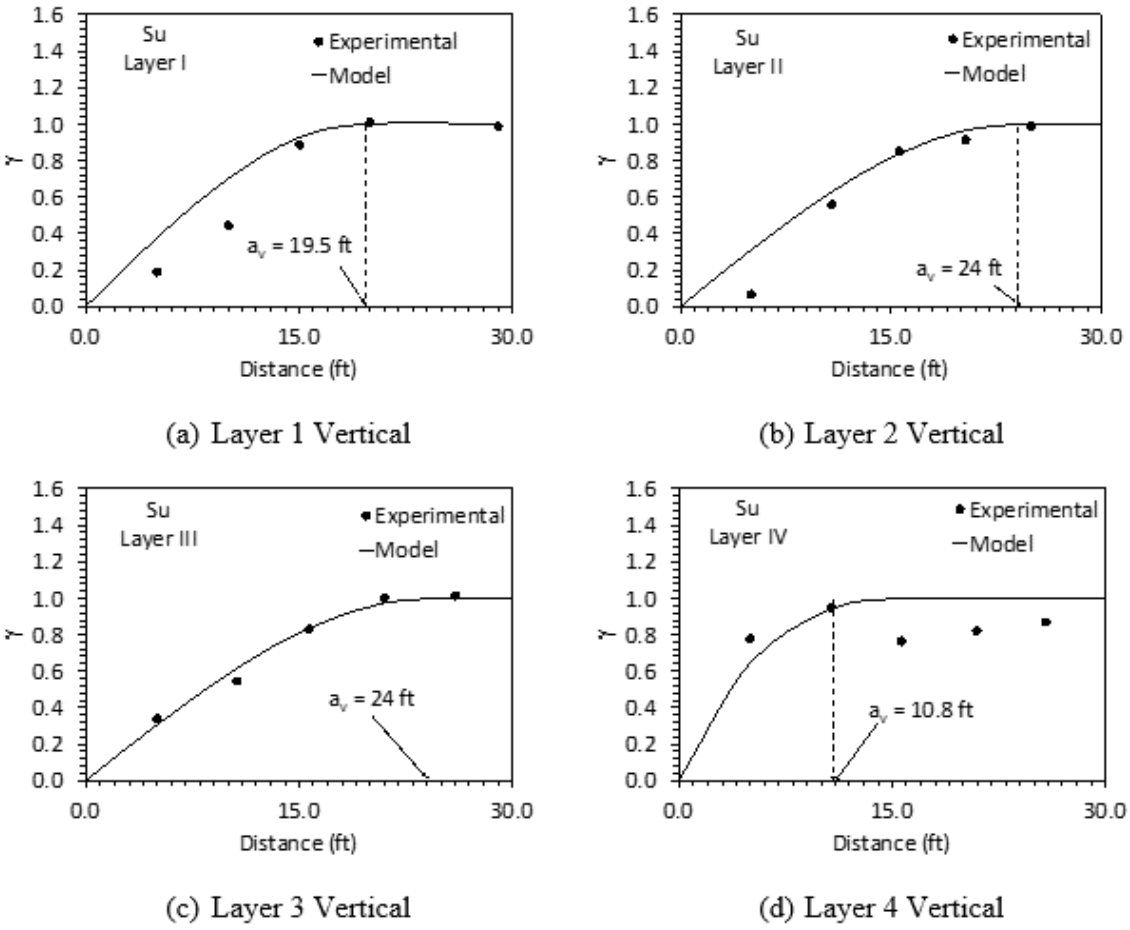

Figure 159. Experimental and spherical semivariogram models for the S_u data of the four soil layers at Bayou Laccassine site

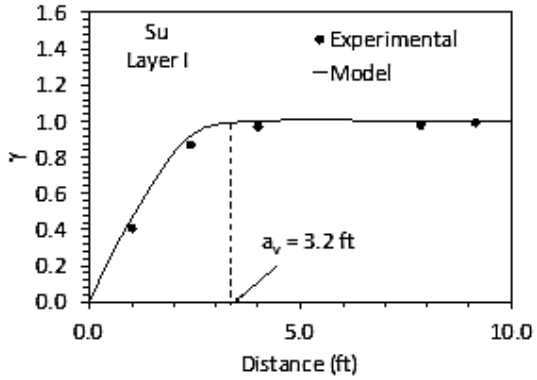

(a) Layer 1 Vertical

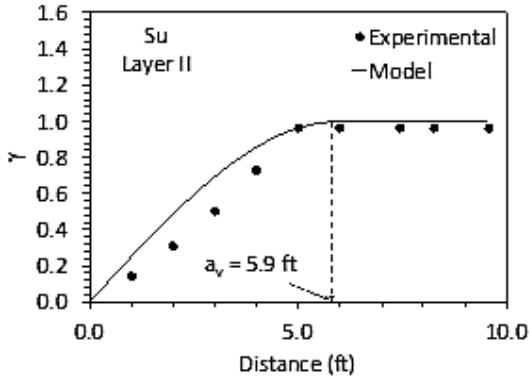

(b) Layer 2 Vertical

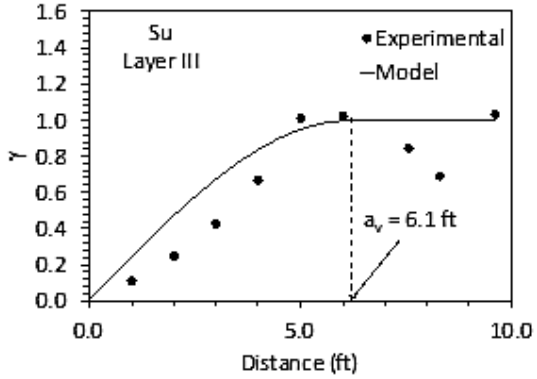

(c) Layer 3 Vertical

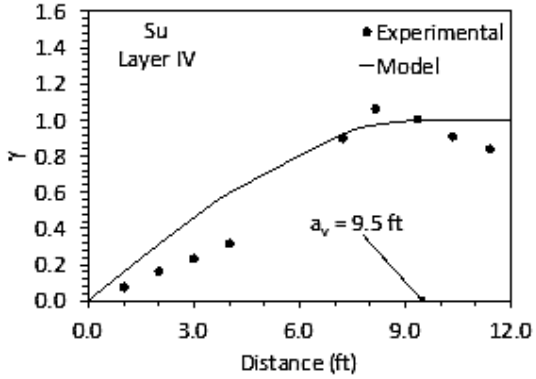

(d) Layer 4 Vertical

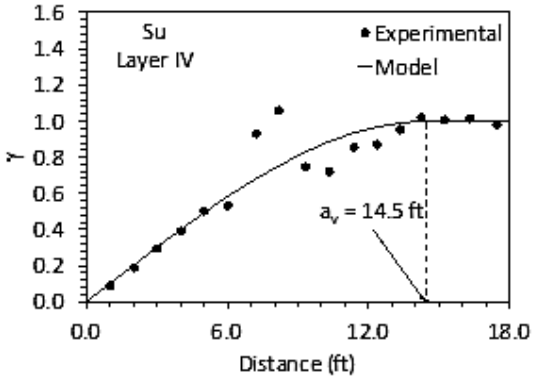

(e) Layer 5 Vertical

Appendix E

Results for Slope Stability Analysis for Drained and Undrained Conditions

Table 85. Factor of safety vs COV of ϕ at different vertical variability levels for drained condition

Scenario No.	Coefficient of variation			Correlation length		Factor of Safety		
	Unit weight	Friction Angle	Cohesion	Vertical	Horizontal	Bishop simplified	Janbu simplified	Spencer
1	5	5	20	2	20	1.523	1.478	1.519
2	5	10	20	2	20	1.479	1.432	1.477
3	5	15	20	2	20	1.432	1.381	1.43
4	5	20	20	2	20	1.38	1.327	1.381
5	5	25	20	2	20	1.331	1.274	1.331
6	5	5	20	0.3	20	1.516	1.472	1.512
7	5	10	20	0.3	20	1.464	1.414	1.462
8	5	15	20	0.3	20	1.408	1.35	1.405
9	5	20	20	0.3	20	1.346	1.281	1.343
10	5	25	20	0.3	20	1.282	1.213	1.278
11	5	5	20	5	20	1.53	1.484	1.526
12	5	10	20	5	20	1.494	1.45	1.492
13	5	15	20	5	20	1.456	1.412	1.455
14	5	20	20	5	20	1.418	1.373	1.419
15	5	25	20	5	20	1.38	1.335	1.384

Table 86. Factor of safety vs COV of unit weight at different vertical correlations levels for drained condition

Scenario No.	Coefficient of variation			Correlation length		Factor of Safety		
	Unit weight	Friction Angle	Cohesion	Vertical	Horizontal	Bishop simplified	Janbu simplified	Spencer
16	2	10	20	2	20	1.48	1.433	1.477
17	4	10	20	2	20	1.4795	1.433	1.477
18	5	10	20	2	20	1.479	1.432	1.477
19	8	10	20	2	20	1.478	1.43	1.476
20	10	10	20	2	20	1.477	1.428	1.474
21	2	10	20	0.3	20	1.466	1.415	1.462
22	4	10	20	0.3	20	1.464	1.414	1.463
23	5	10	20	0.3	20	1.4649	1.415	1.462
24	8	10	20	0.3	20	1.463	1.41	1.462
25	10	10	20	0.3	20	1.462	1.406	1.459
26	2	10	20	5	20	1.494	1.451	1.492
27	4	10	20	5	20	1.494	1.45	1.491
28	5	10	20	5	20	1.4941	1.451	1.492
29	8	10	20	5	20	1.493	1.45	1.49
30	10	10	20	5	20	1.492	1.45	1.489

Table 87. Factor of safety vs COV of cohesion at different vertical variability levels for drained condition

Scenario No.	Coefficient of variation			Correlation length		Factor of Safety		
	Unit weight	Friction Angle	Cohesion	Vertical	Horizontal	Bishop simplified	Janbu simplified	Spencer
31	5	10	10	2	20	1.48	1.433	1.477
32	5	10	20	2	20	1.479	1.432	1.477
33	5	10	30	2	20	1.478	1.431	1.475
34	5	10	40	2	20	1.477	1.429	1.474
35	5	10	50	2	20	1.475	1.427	1.472
36	5	10	10	0.3	20	1.467	1.418	1.464
37	5	10	20	0.3	20	1.464	1.414	1.462
38	5	10	30	0.3	20	1.463	1.412	1.46
39	5	10	40	0.3	20	1.462	1.408	1.459
40	5	10	50	0.3	20	1.46	1.404	1.457
41	5	10	10	5	20	1.493	1.448	1.49
42	5	10	20	5	20	1.494	1.45	1.492
43	5	10	30	5	20	1.493	1.45	1.49
44	5	10	40	5	20	1.492	1.45	1.489
45	5	10	50	5	20	1.49	1.45	1.487

Table 88. Factor of safety vs COV of undrained cohesion at high vertical variability levels for undrained condition

Scenario No.	Coefficient of variation			Correlation length		Factor of Safety		
	Unit weight	Friction Angle	Cohesion	Vertical	Horizontal	Bishop simplified	Janbu simplified	Spencer
46	5	10	10	0.3	20	1.498	1.454	1.494
47	5	10	20	0.3	20	1.495	1.451	1.490
48	5	10	30	0.3	20	1.490	1.446	1.486
49	5	10	40	0.3	20	1.480	1.433	1.472
50	5	10	50	0.3	20	1.470	1.426	1.462
51	5	10	10	0.3	40	1.496	1.452	1.492
52	5	10	20	0.3	40	1.491	1.447	1.487
53	5	10	30	0.3	40	1.481	1.437	1.477
54	5	10	40	0.3	40	1.471	1.427	1.465
55	5	10	50	0.3	40	1.500	1.456	1.496
56	5	10	10	0.3	60	1.497	1.453	1.493
56	5	10	20	0.3	60	1.492	1.450	1.488
58	5	10	30	0.3	60	1.482	1.438	1.478
59	5	10	40	0.3	60	1.472	1.428	1.468
60	5	10	50	0.3	60	1.498	1.454	1.494

Table 89. Factor of safety vs COV of cohesion at medium vertical variability levels at drained condition

Scenario No.	Coefficient of variation			Correlation length		Factor of Safety		
	Unit weight	Friction Angle	Cohesion	Vertical	Horizontal	Bishop simplified	Janbu simplified	Spencer
61	5	10	10	2	20	1.390	1.315	1.385
62	5	10	20	2	20	1.387	1.312	1.376
63	5	10	30	2	20	1.382	1.307	1.372
64	5	10	40	2	20	1.372	1.297	1.360
65	5	10	50	2	20	1.358	1.283	1.349
66	5	10	10	2	40	1.355	1.290	1.348
67	5	10	20	2	40	1.352	1.287	1.342
68	5	10	30	2	40	1.349	1.284	1.339
69	5	10	40	2	40	1.337	1.272	1.325
70	5	10	50	2	40	1.323	1.258	1.313
71	5	10	10	2	60	1.340	1.277	1.330
72	5	10	20	2	60	1.337	1.274	1.327
73	5	10	30	2	60	1.330	1.267	1.320
74	5	10	40	2	60	1.320	1.257	1.310
75	5	10	50	2	60	1.308	1.245	1.298

Table 90. Factor of safety vs COV of cohesion at low vertical variability levels at undrained condition

Scenario No.	Coefficient of variation			Correlation length		Factor of Safety		
	Unit weight	Friction Angle	Cohesion	Vertical	Horizontal	Bishop simplified	Janbu simplified	Spencer
76	5	10	10	5	20	1.310	1.240	1.304
77	5	10	20	5	20	1.305	1.235	1.301
78	5	10	30	5	20	1.297	1.227	1.293
89	5	10	40	5	20	1.290	1.220	1.286
80	5	10	50	5	20	1.280	1.210	1.272
81	5	10	10	5	40	1.254	1.184	1.248
82	5	10	20	5	40	1.247	1.177	1.243
83	5	10	30	5	40	1.239	1.169	1.235
84	5	10	40	5	40	1.232	1.162	1.228
85	5	10	50	5	40	1.222	1.152	1.218
86	5	10	10	5	60	1.230	1.160	1.226
87	5	10	20	5	60	1.223	1.153	1.219
88	5	10	30	5	60	1.215	1.145	1.211
89	5	10	40	5	60	1.208	1.138	1.204
90	5	10	50	5	60	1.198	1.128	1.194

Table 91. Factor of safety vs COV of cohesion at different horizontal variability levels (with high vertical variability)

Scenario No. (Increment No.)	Coefficient of variation			Correlation length		Factor of Safety		
	Unit weigh t	Friction Angle	Cohesi on	Vertical	Horizontal	Bishop simplified	Janbu simplified	Spencer
91 (1)	2	5	20	0.3	20	1.531	1.485	1.527
92 (2)	4	15	30	0.3	20	1.455	1.411	1.454
93 (3)	8	20	40	0.3	20	1.415	1.371	1.417
94 (4)	10	25	50	0.3	20	1.376	1.331	1.38
95 (1)	2	5	20	0.3	40	1.53	1.485	1.526
96 (2)	4	15	30	0.3	40	1.455	1.411	1.454
97 (3)	8	20	40	0.3	40	1.416	1.372	1.417
98 (4)	10	25	50	0.3	40	1.377	1.333	1.38
99 (1)	2	5	20	0.3	60	1.53	1.48	1.526
100 (2)	4	15	30	0.3	60	1.456	1.41	1.455
101 (3)	8	20	40	0.3	60	1.418	1.374	1.419
102 (4)	10	25	50	0.3	60	1.38	1.337	1.384

Table 92. Factor of safety vs COV of cohesion at different horizontal variability levels (with medium vertical variability)

Scenario No. (Increment No.)	Coefficient of variation			Correlation length		Factor of Safety		
	Unit weigh t	Friction Angle	Cohesi on	Vertical	Horizontal	Bishop simplified	Janbu simplified	Spencer
103 (1)	2	5	20	2	20	1.524	1.48	1.52
104 (2)	4	15	30	2	20	1.431	1.38	1.43
105 (3)	8	20	40	2	20	1.379	1.322	1.378
106 (4)	10	25	50	2	20	1.325	1.266	1.325
107 (1)	2	5	20	2	40	1.523	1.479	1.52
108 (2)	4	15	30	2	40	1.431	1.38	1.429
109 (3)	8	20	40	2	40	1.379	1.324	1.377
110 (4)	10	25	50	2	40	1.325	1.267	1.325
111 (1)	2	5	20	2	60	1.523	1.48	1.519
112 (2)	4	15	30	2	60	1.431	1.381	1.429
113 (3)	8	20	40	2	60	1.379	1.325	1.377
114 (4)	10	25	50	2	60	1.326	1.269	1.326

Table 93. Factor of safety vs COV of cohesion at different horizontal variability levels (with low vertical variability)

Scenario No. (Increment No.)	Coefficient of variation			Correlation length		Factor of Safety		
	Unit weigh t	Friction Angle	Cohesi on	Vertical	Horizontal	Bishop simplified	Janbu simplified	Spencer
115 (1)	2	5	20	5	20	1.519	1.475	1.515
116 (2)	4	15	30	5	20	1.417	1.363	1.415
117 (3)	8	20	40	5	20	1.36	1.3	1.359
118 (4)	10	25	50	5	20	1.3	1.23	1.3
119 (1)	2	5	20	5	40	1.518	1.475	1.515
120 (2)	4	15	30	5	40	1.418	1.364	1.415
121 (3)	8	20	40	5	40	1.36	1.3	1.35
122 (4)	10	25	50	5	40	1.3	1.24	1.3
123 (1)	2	5	20	5	60	1.518	1.475	1.515
124 (2)	4	15	30	5	60	1.419	1.366	1.416
125 (3)	8	20	40	5	60	1.36	1.3	1.36
126 (4)	10	25	50	5	60	1.3	1.24	1.3